GENERAL ATOMIC

DIVISION OF

GENERAL DYNAMICS

JOHN JAY HOPKINS LABORATORY FOR PURE AND APPLIED SCIENCE

P.O. BOX 608, SAN DIEGO 12, CALIFORNIA

GA-3542

PHYSICS

INTEGRAL NEUTRON THERMALIZATION

ANNUAL SUMMARY REPORT

October 1, 1961, through September 30, 1962

Contract AT(04-3)-167

Project Agreement No. 2

U.S. Atomic Energy Commission

Work done by:

J. R. Beyster
J. R. Brown
H. C. Honeck
G. K. Houghton
D. H. Houston
G. D. Joanou
J. U. Koppel
W. M. Lopez
Y. D. Naliboff
M. S. Nelkin
D. E. Parks
J. Russell
G. D. Trimble
F. Wikner
J. C. Young

Report written by:

J. R. Beyster
J. R. Brown
H. C. Honeck
D. H. Houston
J. U. Koppel
W. M. Lopez
Y. D. Naliboff
D. E. Parks
G. D. Trimble
F. Wikner
J. C. Young

DISCLAIMER

CONTENTS

I. INTRODUCTION

In September, 1961, a report was issued which contained all results obtained in the Integral Neutron Thermalization program up to that time. In that report (GA-2544), the general methods of attack--experimental, analytical, and theoretical--were explained. Experimental results and the significance of these results for the common moderators--light water, graphite, polyethylene, zirconium hydride, etc. --were discussed. In general, the work described in the present report includes only that which was undertaken during the contract year from October 1, 1961, through September 30, 1962. It is presumed that many of the experimental and analytical procedures are well known by now. Therefore, only new techniques and improvements made in the old procedures are discussed here (GA-2544 contains the background for these discussions). Facility improvements and major-equipment performance during the past year are also described for both General Atomic and Atomic Energy Commission equipment used in the present research program. In addition to summarizing the work done on thermalization at General Atomic, the present document describes much of the current work at other laboratories for purposes of comparison and discussion of specific problems. In many cases, the inclusion of work from other laboratories has stemmed from a cooperative effort to solve particularly difficult problems which have arisen in the present investigations.

The motivation for work in neutron thermalization is quite strong at this time. Reactor technology has been progressing in the direction of higher power density and more heavily loaded systems. Detailed knowledge of neutronic behavior has thus become increasingly important in predictions of reactor lifetime (burnup), temperature coefficient, flux peaking, criticality, and safety. There has been a general tendency in the past to oversimplify and idealize the assumptions regarding neutron thermalization, much to the detriment of reactor calculational procedures. The pulsed techniques developed here and elsewhere are particularly adaptable to studying these problems experimentally in a precise way. Present-day theoretical tools are also capable of shedding much light on these problems.

The current general method of approach in the Integral Neutron Thermalization program includes most of the techniques utilized in the past (experimental and analytical). Experimental techniques were improved during the past year, but this constituted only a minor portion of the program because these procedures had been reasonably well in hand previously.

Studies of neutron spectra under infinite-medium conditions were continued on a reduced scale from that engaged in during other years, since analytical methods have been developed to handle this relatively uncomplex calculation for many practical applications. However, further refinements in our knowledge of the scattering law seem to be necessary before perturbations in neutron spectra due to resonance absorption can be completely described. New moderators and shield materials were studied under infinite-medium conditions to broaden the scope of the program. Specifically, studies of D_2O, polyethylene, and lithium hydride were begun. The main experimental effort during the year was devoted to studying the problems associated with the spatially dependent neutron spectra in water. One-dimensional geometries in which rapid spatial-flux variations were established were studied. This important class of problem is very similar to that which occurs at control rods and fuel-water interfaces in most common reactor designs. Both multiplying and nonmultiplying assemblies were used in the investigations. Theoretical and analytical efforts were intensified considerably, especially regarding evaluation of scattering-law information from the standpoint of its applicability and sensitivity in reactor calculations. Many other problems concerning the time dependence of neutron spectra, energy eigenvalues, heated interfaces, etc., were investigated.

The over-all result of this integrated effort has been to solve some of the difficult problems concerning neutron thermalization which have existed in the past. In addition, some new and interesting problems have been uncovered, and various approaches to solving these have been adopted. The relevance of these matters to specific reactor problems is pointed out in this report where appropriate.

II. RESEARCH EQUIPMENT

This section contains a brief review of changes made during the past year in the General Atomic Linear Accelerator Facility. A more complete discussion of the over-all facility has been presented in GA-2544.

2.1. LINEAR ACCELERATOR

The General Atomic L-band linear accelerator (Linac) shown in Fig. 1 was installed from July through September of 1961 to replace a lower-current S-band accelerator which had been in use for several years. In the first year of actual operation, the new machine has more than equaled its rated specifications. All research performed during the past contract year has benefited greatly from the increased intensities afforded by the new accelerator. The Linac has been used in connection with the high-current, multitarget, beam-switching system which has been developed at General Atomic during the last few years. There are over 12 target areas (see Fig. 2) currently in use in this system, plus a pulsed-magnet system for simultaneous multiple-target experiments and a high-resolution electron-positron spectrometer. The 16- and 50-m neutron flight paths shown in Fig. 2 are being used primarily in the Integral Neutron Thermalization program.

From the standpoint of pulsed-neutron research, the important design parameter of this accelerator is the neutron yield per pulse. Average power considerations very seldom dictate experimental feasibility in neutron-thermalization work. Some typical Linac operating conditions which have been attained during the first year of operation are (1) long-pulse mode ($1\ \mu\text{sec} \leq \tau \leq 14\ \mu\text{sec}$) at 30 Mev and 0.7-amp peak current, (2) short-pulse mode ($0.01\ \mu\text{sec} \leq \tau \leq 1\ \mu\text{sec}$) at 40 Mev and 2 amp, and (3) variable electron energy from 1 to 50 Mev. (Thermalization studies usually require the long-pulse mode, whereas cross-section investigations often demand short-pulse operation of the Linac.) Thus, neutron yields attainable from the General Atomic Linac are within a factor of two of the highest available anywhere today. In addition, beam-spot size (<1 cm in diameter), angular divergence, and energy spectrum in beam extraction from the Linac are such that the electron beam pipes easily to a small spot 90 ft from the machine. Typical current losses are less than a few per cent for most operations, which minimizes spurious and fluctuating sources of neutron background in the target areas, as well as activation

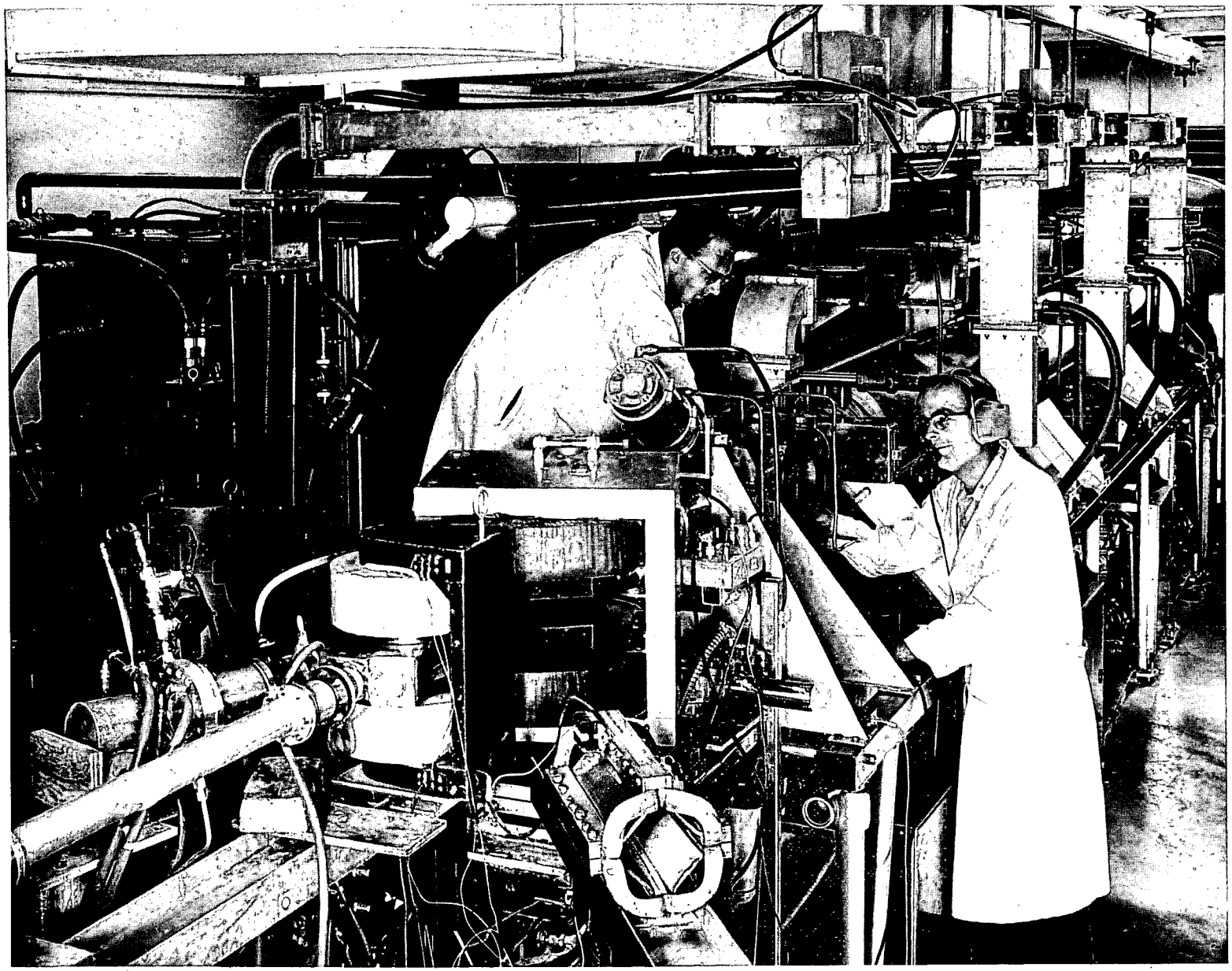

Fig. 1--Installation of the L-band linear accelerator

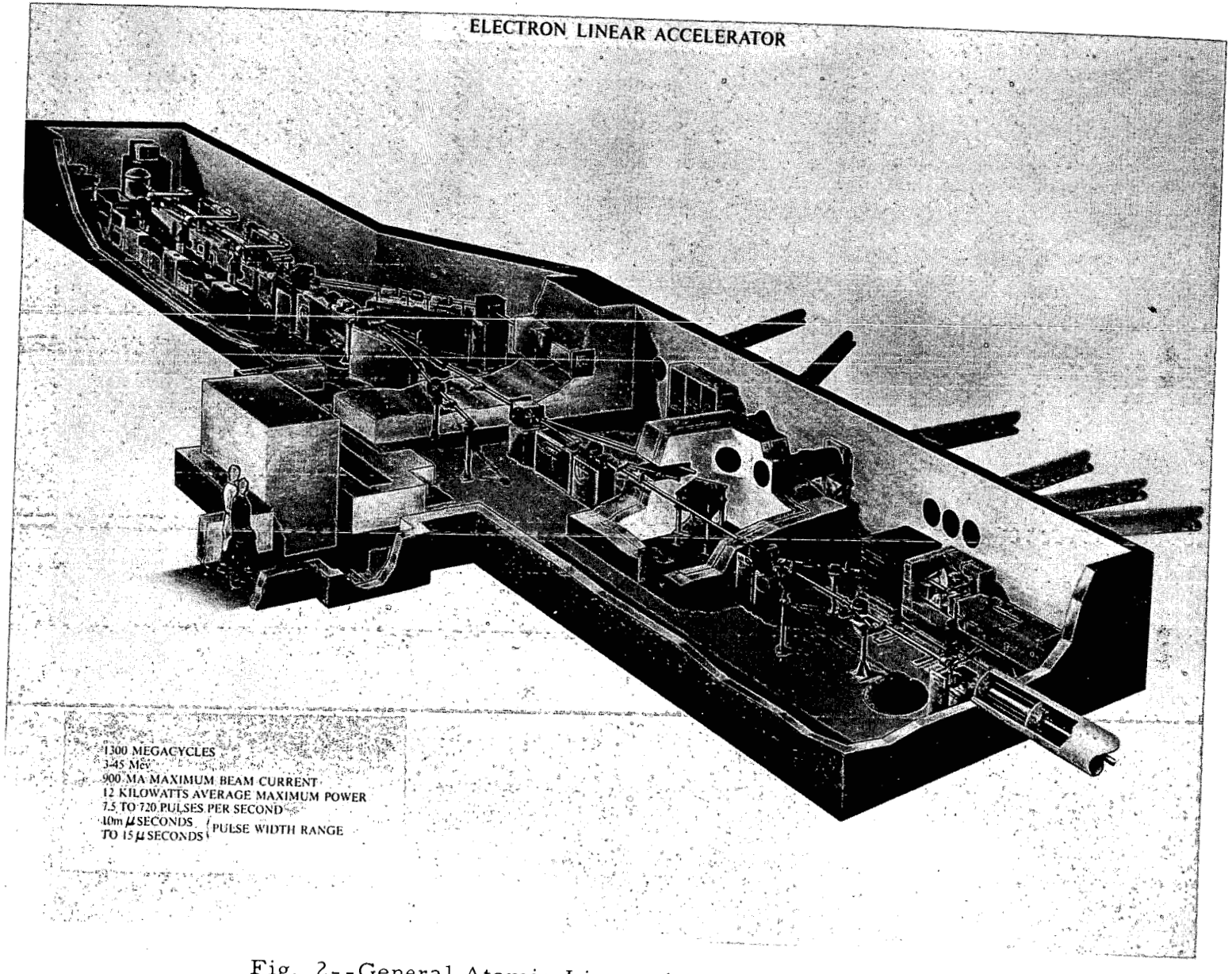

Fig. 2--General Atomic Linear Accelerator Facility

of beam tubes, magnets, and support structures. Other important characteristics of the new machine are the high output current even at low energies (60 ma at 1 Mev) and the fact that stable low values of peak current are readily obtainable (<1 ma) for classes of experiments involving low dose rates.

During the past year, the accelerator has been operated on a three-shift basis, running a total of 3300 operating hours on actual research projects. Major equipment failures have been minimal and only one L-band klystron has been replaced during this period.

A continuous program to improve and upgrade the Linac is being conducted. During the past year, this has involved many alterations to the original factory equipment. Some of these alterations were as follows:

1. Copper traps in the accelerator vacuum system were replaced with molecular sieve traps; as a result, vacuums of 1 to 2×10^{-7} mm Hg are routinely obtained.
2. The r-f driver system was modified extensively to eliminate tube failures and high-voltage breakdown and to obtain greater r-f stability.
3. A high-current positron-producing target was successfully installed and studied in the Linac to obtain a variable-energy, monochromatic gamma-ray source.
4. Injection and electron-gun electronics were considerably stabilized and improved, especially in the 0.01-μsec mode of operation.
5. Optimum beam focusing and tuning conditions for electron energies from 1.0 to 50 Mev were investigated extensively.

2.2. PRESSURE VESSEL

A new feature of the Linac facility which will further extend the scope of neutron-thermalization measurements is the pressure vessel shown in Fig. 3. This vessel will be used to measure neutron spectra in various poisoned solutions for moderator temperatures varying from room temperature to about 600°F. Since the influence of molecular binding in water is still important at normal reactor operating temperatures, this vessel can be used to measure the magnitude of the effect as a function of temperature. Spectra measured under infinite-medium conditions in the pressure vessel will be compared with spectra calculated using Nelkin's and variations of Nelkin's energy-transfer kernel. Special attention will be given to measuring spectra at the temperatures for which Egelstaff,[1] Kottwitz,[2] and others have made differential-scattering measurements in water.

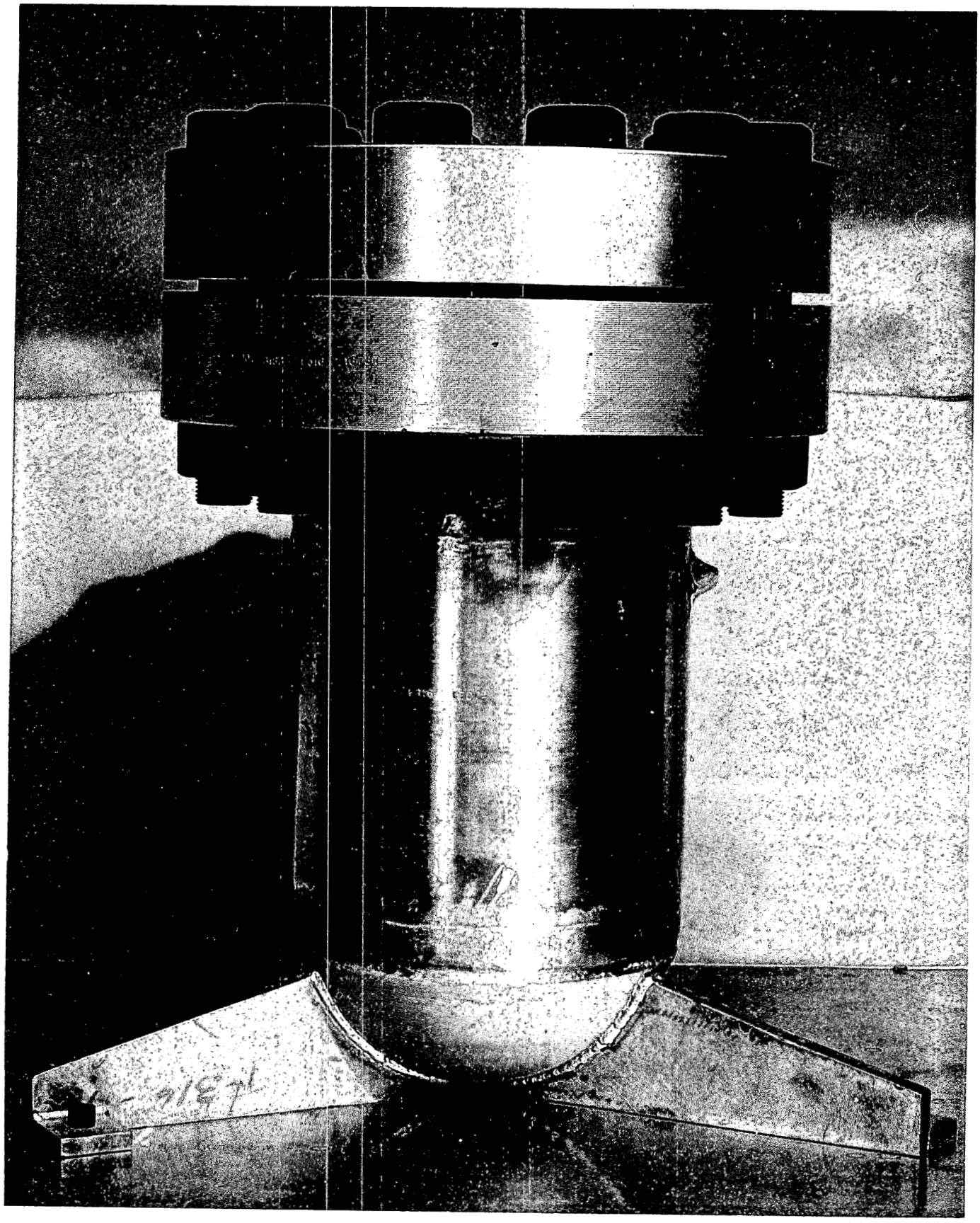

Fig. 3--Pressure vessel for high-temperature neutron-spectrum measurements

The pressure vessel for the present experimental program (Fig. 4) was constructed according to standard ASME-code practices. All welds were carefully radiographed, and the vessel was checked hydrostatically at 3300 psi. The vessel has been certified for operation at 2000 psi and 620°F. The tank wall is of 3/4-in. Type 316 stainless steel. The vessel has an internal diameter of 10 in. and an over-all internal height of 23 in. The bottom of the vessel is hemispherical. The 3-5/8-in.-thick blind-flange head is fastened by twelve 1-5/8-in.-diameter bolts and sealed with a stainless-steel-covered asbestos gasket, using a torque of about 800 ft-lb. The outer surface of the vessel is wrapped with a 2-in. layer of Fiberfrax (an alumina-silica fiber containing B_2O_3), which serves both as an insulation and a thermal-neutron boundary. The vessel is supported by a welded tripod arrangement.

The vessel is self-pressurized by means of a 5-kw immersion-type heater located near the bottom. The temperature of the liquid in the vessel is monitored with stainless-steel-sheathed iron-constantan thermocouples at the heater, near the center of the vessel, and near the top of the vessel. The pressure is monitored with a stand-off type of standard pressure gauge in order to eliminate the need for temperature compensation. The pressure gauge, one thermocouple, and a safety head (rated at 2000 psi and 620°F) are located on the head of the vessel as shown in Fig. 4. A necessary but possibly weak point in the design is the cylindrical tube, or "glory hole," which extends through the center and perpendicular to the axis of the vessel (see Fig. 4). The glory hole is of 0.035-in.-thick Type 316 stainless steel and has a 0.43-in. inside diameter. The wall of the glory hole is made thin to minimize neutron absorption. A scatterer placed at the center of the glory hole is used to extract the neutron beam. The glory hole is considered to be a secondary rupture disk; however, it has successfully passed a 3300-psi hydrostatic test. Because of the glory hole, safety of operation is paramount and every operation, e.g., positioning of the scatterer for signal runs, positioning of the $B_4^{10}C$ plug for background runs, and changing the heater power, is performed completely by remote control.

The pressure vessel is fairly unique in one aspect in that it will contain corrosive salt solutions at high temperatures. Owing to this fact and the small diameter of the pressure vessel, it was felt that cladding techniques would fall short in keeping corrosion products out of solution, and hence that unwanted and unknown neutron absorption might be present. Numerous tests on small cylindrical pressure cells were made to determine the feasibility of using unclad carbon steel to contain the various salt solutions. These tests showed that corrosion formation was very large even after several different solutions were used in the same vessel (to allow for the build-up of an oxide film). Therefore, to minimize corrosion products the entire vessel was constructed of Type 316 stainless steel. One of the tests with the small cylindrical pressure cells indicated that silver, which was to

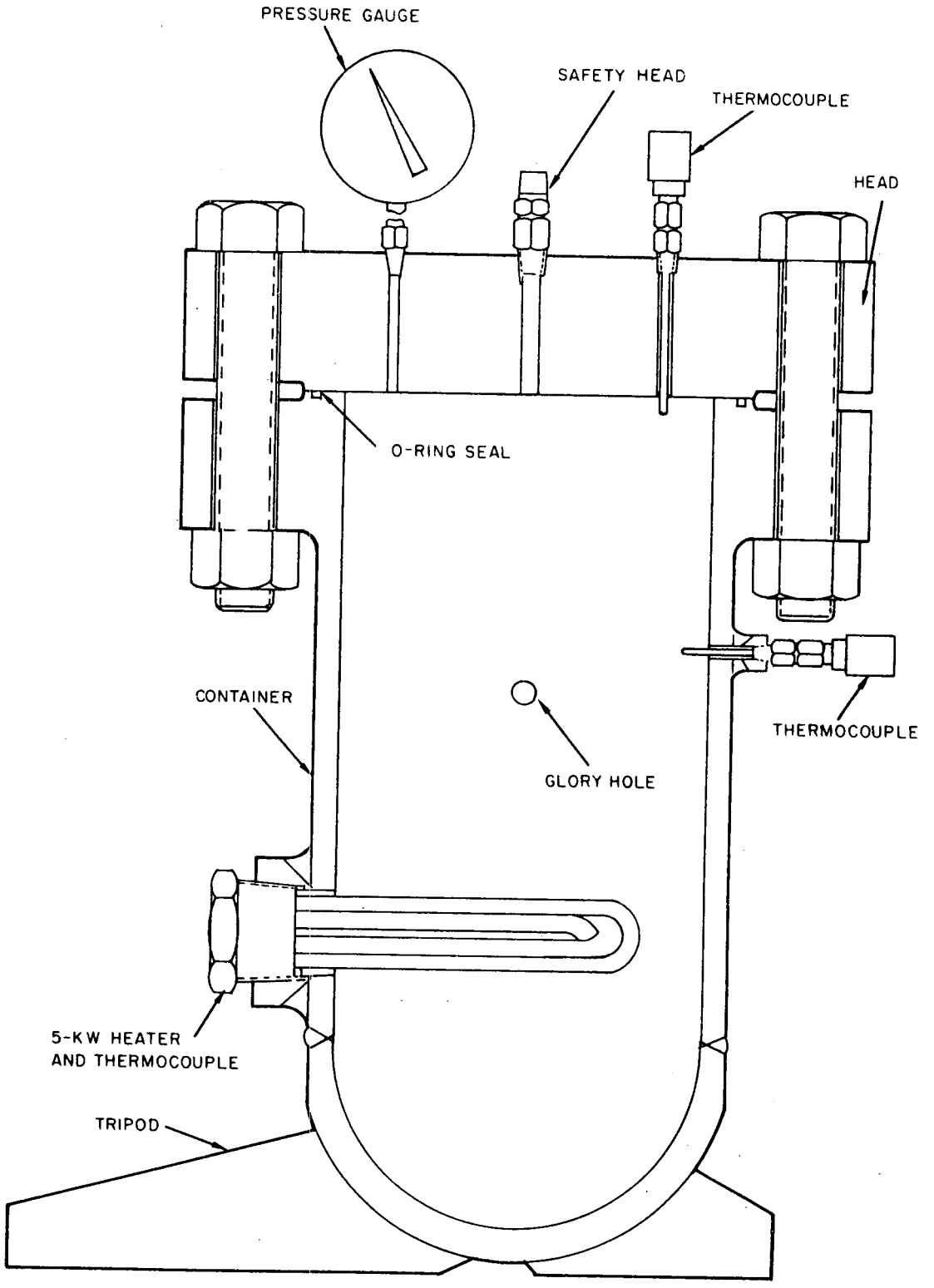

Fig. 4--Schematic diagram of high-temperature pressure vessel

coat the metal O-ring at the large access flange, plated onto stainless steel by an electrolytic corrosion process. Therefore, the O-ring was changed to asbestos clad with Type 316 stainless steel.

The test program involving trial solution runs at the anticipated pressures and temperatures is well under way, and the program of spectral studies will begin after the start of the next contract year.

2.3. COCKCROFT-WALTON NEUTRON GENERATOR

A 150-kv positive-ion accelerator* has been added to the General Atomic Linac facility. It will be used as a 14-Mev and 2.5-Mev neutron generator employing the T(d, n) and d(d, n) reactions. The yield of 14-Mev neutrons is about 10^{11} neutrons/sec.

It is planned to use this generator for calibration of the high-energy-neutron detectors employed in various programs at the Linac. Some of these programs involve measurement of the neutron-spectrum characteristics of fast and intermediate reactors and of neutron spectra at deep penetration through shields. The detectors for neutrons with energies of millions of electron volts are essentially biased liquid scintillation counters utilizing pulse-shape discrimination against gamma radiation.

The generator has been located in an area where it can be operated independently of the Linac, so that conflict in operations of the two is precluded. In addition, it is located close to the 50-m flight station, where the detectors for fast-neutron work are installed. These detectors need only be moved a very short distance for calibration, and the same system of electronics can be used for calibration as for the actual spectral measurements.

The location of the neutron generator and its relationship to other equipment in the area are shown in Fig. 5. Concrete shadow shielding is provided to prevent exposure of personnel and to minimize the interference with any low-background experiment being conducted in the vicinity, e.g. Linac time-of-flight measurements involving neutron and gamma detectors. Figure 6 shows the neutron generator installed in its separate building, and Fig. 7 shows the control console, which is located 50 ft away in another building. The generator has undergone test runs and is now in operation.

*Manufactured by Texas Nuclear Corporation.

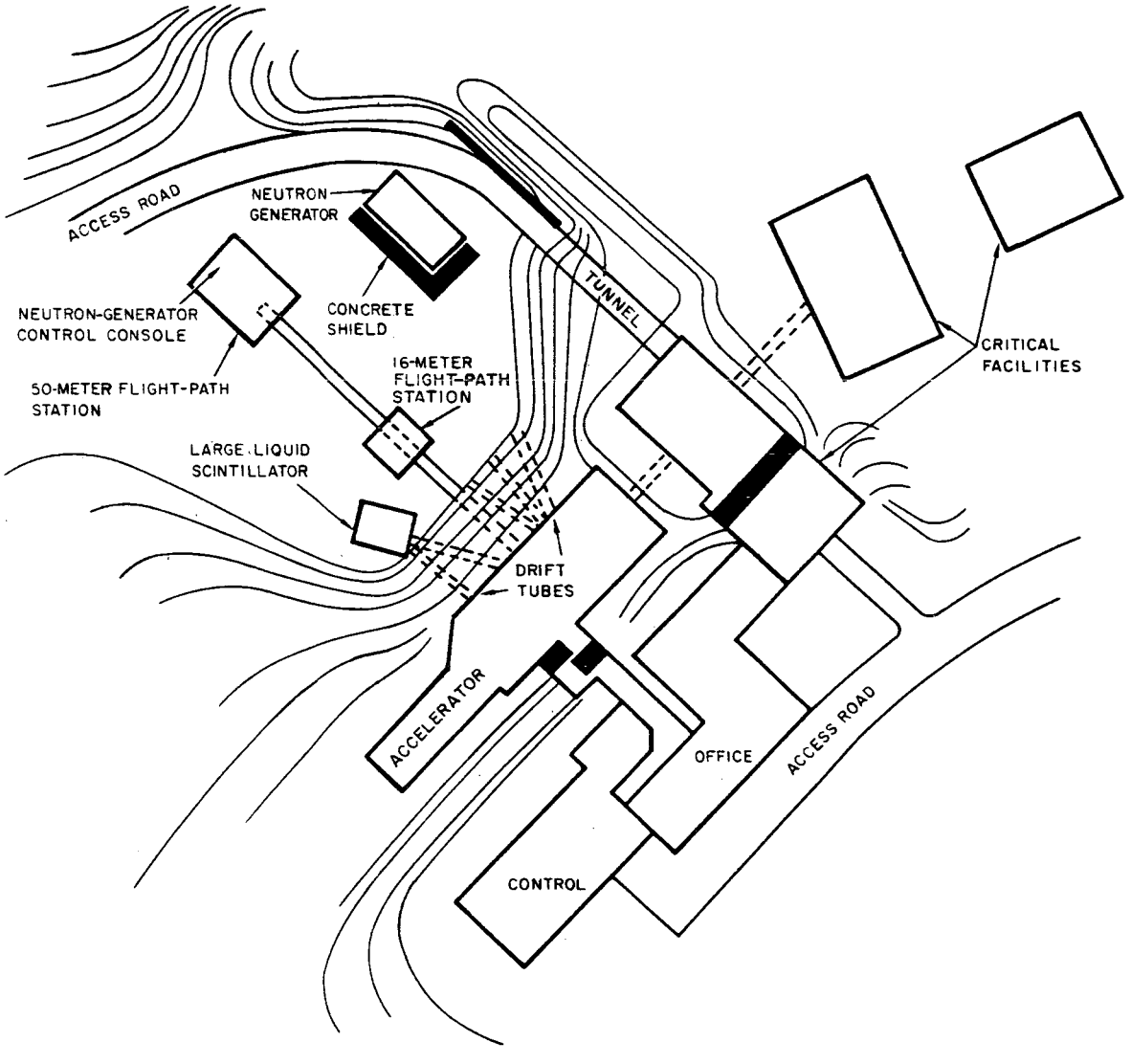

Fig. 5--Top view of linear-accelerator complex, showing location of neutron generator

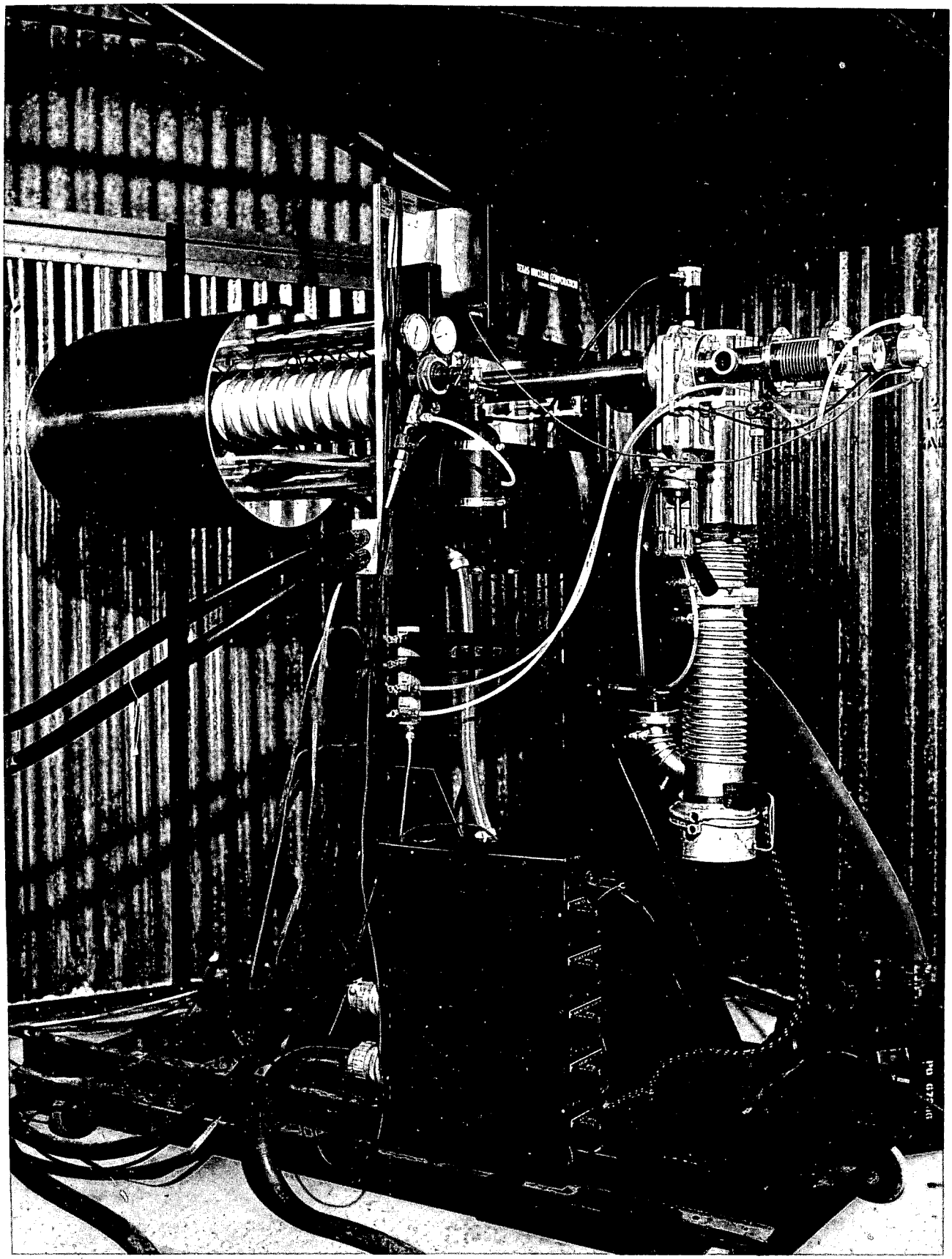

Fig. 6--Neutron generator

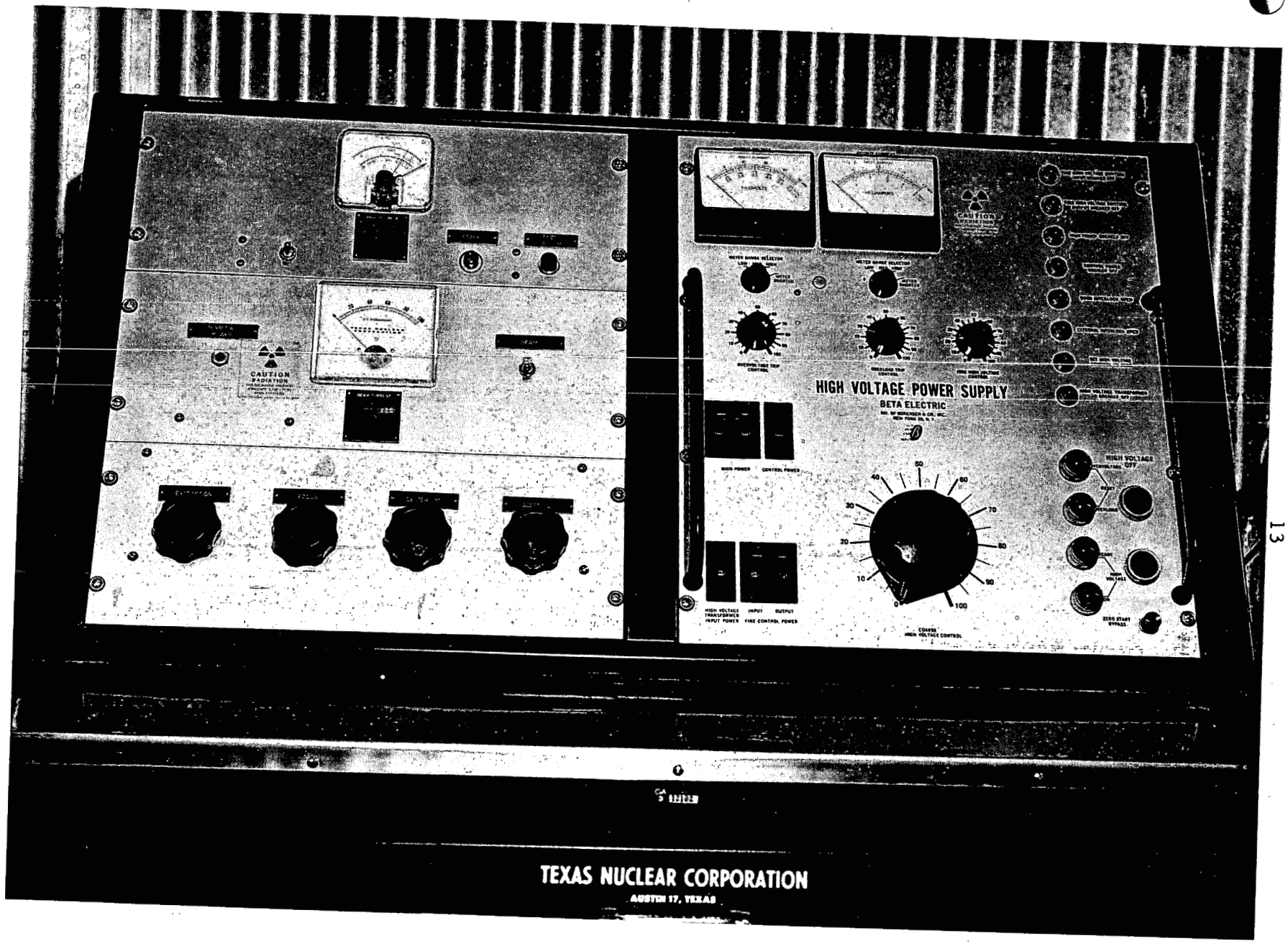

Fig. 7--Control console for neutron generator

2.4. INSTRUMENTATION

This subsection consists of a brief description of the various multichannel analyzers that are currently in use at the Linac facility. Although there is a large amount of additional associated instrumentation, it consists either of standard commercial units or special-purpose instruments of rather limited scope. These devices are more appropriately described later in the report together with the associated experiments.

2.4.1. RCL 256-channel Analyzer, Model 20609

This is an early-model, vacuum-tube, magnetic-core-memory multichannel analyzer. In its original form a pulse-height analyzer, it was subsequently fitted with a transistorized attachment that converts (as an optional mode) the system to a time analyzer. Time-channel widths from 16 μsec to 65.536 msec are provided (by use of a binary system) with an average dead time of 8 μsec.

2.4.2. RCL 256-channel Analyzer, Model 20620

This is a portable, transistorized, multichannel pulse-height analyzer. Its light weight makes it ideal for "on-site" examination of pulse-height spectra. Since most of the critical electronics equipment is situated at the end of long neutron flight paths, a large amount of preliminary investigation can be performed with this instrument while other groups are using the Linac and the more sophisticated analyzers.

2.4.3. TMC 1024-channel Analyzer, Model CN-1024

This is the newest multichannel analyzer in use at the Linac. It has four standard plug-in modules that determine its mode of operation:

1. Pulse-height analyzer logic unit.
2. Pulsed-neutron logic unit.
3. Time-of-flight logic unit.
4. High-speed time-of-flight unit.

The pulsed-neutron logic unit has time channels 10 to 2560 μsec (by use of a binary system) in length, and the pulse pair resolution is approximately 0.2 μsec. The time-of-flight logic unit has time channels from 0.25 to 64 μsec (also by use of a binary system) and a fixed dead time of 16 μsec. The high-speed time-of-flight unit has time-channel lengths of 0.0625 and 0.125 μsec. It can accept only one data pulse per time sweep.

The design of this analyzer is such that its operation can be easily programmed with external routing signals when special applications arise

that cannot be handled with the standard plug-in modules. One of the anticipated applications of this system is a two-parameter study of neutron interactions where time-of-flight versus pulse-height information is stored simultaneously in an M × N array.

III. EXPERIMENTAL TECHNIQUES

During the last few years, low-energy neutron spectra under controlled experimental conditions have been measured at the General Atomic Linac facility. The aim has been initially to obtain infinite-medium conditions in the assemblies used for these investigations and subsequently to perform the measurements where flux gradients of known magnitude exist. Although much of the experimental data is in relatively close agreement with theory, there are now also a sizable number of cases in which several discrepancies between theory and experiment exist and even some cases where experiment is in complete disagreement with theory. It became important last year that every attempt should be made to improve experimental arrangements so as to exclude systematic errors as a cause for the existing discrepancies.

3.1. EXPERIMENTAL ARRANGEMENT

During the past contract year, a number of changes were made in the facilities at General Atomic for measuring neutron spectra. All neutron-detector banks in use over the last several years were completely tested, and detectors of marginal quality were removed. The bank which is normally used at the 16-m flight station was reoriented so that its axis is perpendicular rather than parallel to the neutron beam. This change has eliminated the annoying dip at 5 ev which was caused in all previously measured spectra by the presence of silver solder on the ends of each of the $B^{10}F_3$ detectors.

The instrumentation for time-of-flight work has been materially improved to permit use of the increased beam intensity available from the L-band Linac. A block diagram of the electronics system utilized for a typical neutron-spectrum measurement at 16 m is shown in Fig. 8. The plastic scintillator is used to detect the bremsstrahlung from the source and thereby establish a precise time base to trigger all of the time-of-flight circuitry. The fission chamber shown is used as a neutron monitor. The on-gate circuit allows scaler No. 2 to count only the neutrons which occur between 0.5 and 2.5 msec after the beam pulse. This reduces errors in the monitor caused by variations in room-return neutrons. Scaler No. 3 is used to count the number of times the Linac has pulsed. Two 256-channel time analyzers are used to cover the desired neutron-energy range, and this gives better resolution during a single run. One analyzer is usually run with an 80-μsec channel width, whereas the other is run with a 32-μsec channel width.

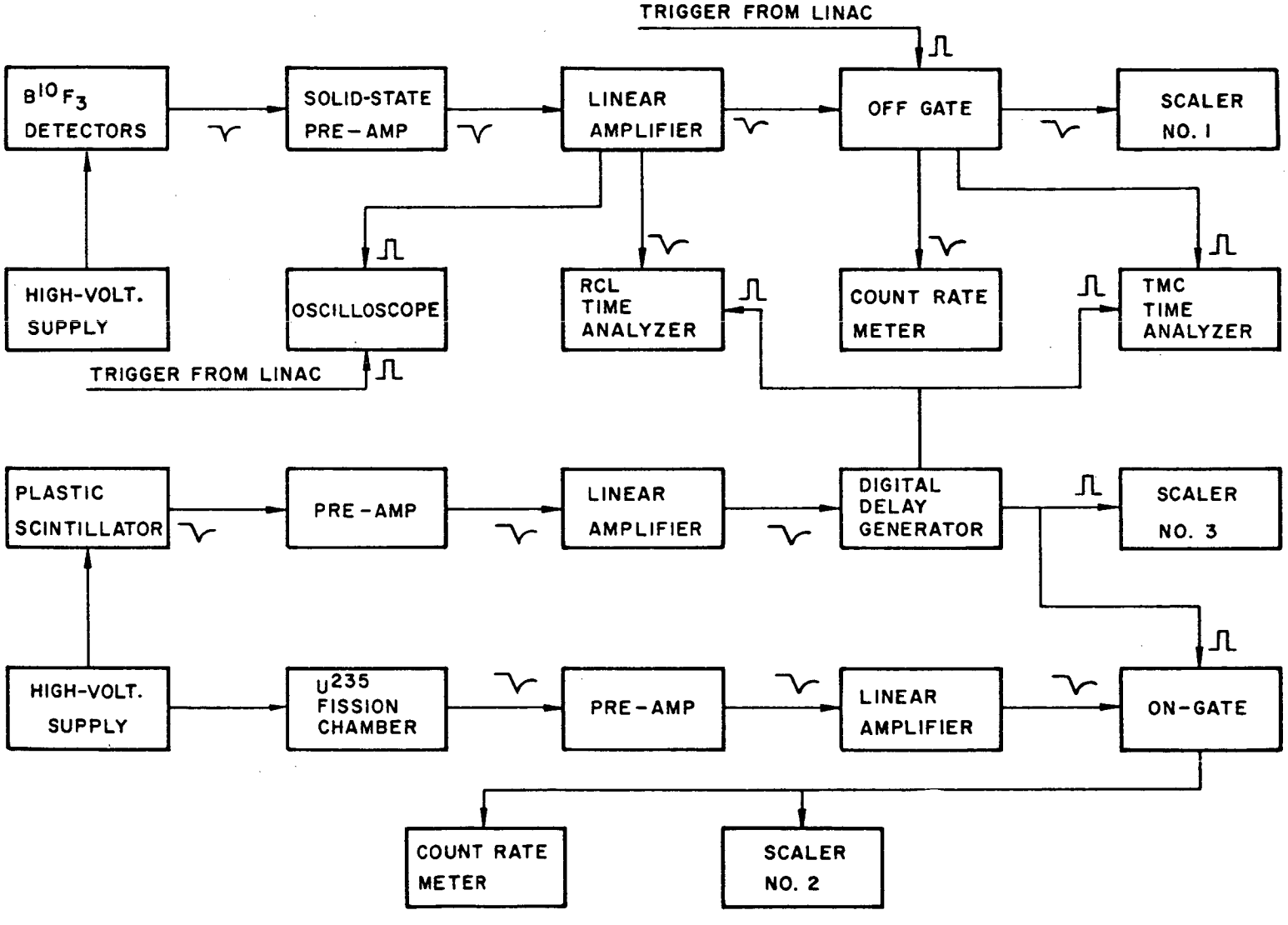

Fig. 8--Block diagram of electronics-system arrangement for a typical neutron-spectrum measurement

New, more precisely constructed nesting collimators have been built and tested, so that it is easily possible to locate an assembly for beam extraction at any angle and position in the shield cave. The collimating system installed on the 16-m flight path has been improved to include a large amount of lead shielding around the collimator for gamma-flash suppression. However, the aperture in the collimator transmits the prompt gamma burst directly from the source. New and reliable methods of decreasing this effect have been found during the present experimental program. Circuitry changes in the amplifiers and preamplifiers to improve the overload characteristics have been helpful in limiting the dead time from the gamma flash to some extent. In addition, it has been found that a 4-in. lead shield between the source and the assembly reduces the electronic dead time due to gamma flash sufficiently that spectra in the kilovolt-neutron-energy region can be measured at the 16-m flight station. This can be accomplished with little or no loss in neutron intensity.

A plan view of the low-room-return neutron cave (where all neutron spectra have been measured) is shown in Fig. 9. The assembly under study is placed in the shielded neutron cave and viewed via the 16- or 50-m flight path (the 50-m flight path being an extension of the 16-m flight path). The 20-m flight path is being used in another program to measure radiative-capture neutron cross sections. The new intensity achieved with the L-band Linac has proved to be too great for the heat-handling capability of the water-cooled lead targets that were previously used. A newly designed, water-cooled fansteel target has proved satisfactory and is presently being used for the neutron-spectrum measurements.

3.2. SENSITIVITY FUNCTIONS OF THE 16- AND 50-METER DETECTOR BANKS

The reorientation of the 16-m detector bank required a remeasurement of the sensitivity of the bank as a function of neutron energy. The sensitivity is determined relative to the known efficiency of a 1/v detector bank. In conjunction with these measurements, the sensitivity of the 50-m detector bank was also remeasured. This more distant detector station is employed in all measurements with multiplying assemblies. The reason for this procedure is that the variation in emission time for neutrons from multiplying systems is longer than that for neutrons from nonmultiplying systems, so that a longer flight path is required for the same resolution.

3.2.1. Derivation of the Sensitivity Function

The sensitivity of the 16-m detector bank, $S(E)_{16}$, can be defined as

$$S(E)_{16} = \epsilon(E)_{16}\, T(E)_{16}\,, \qquad (1)$$

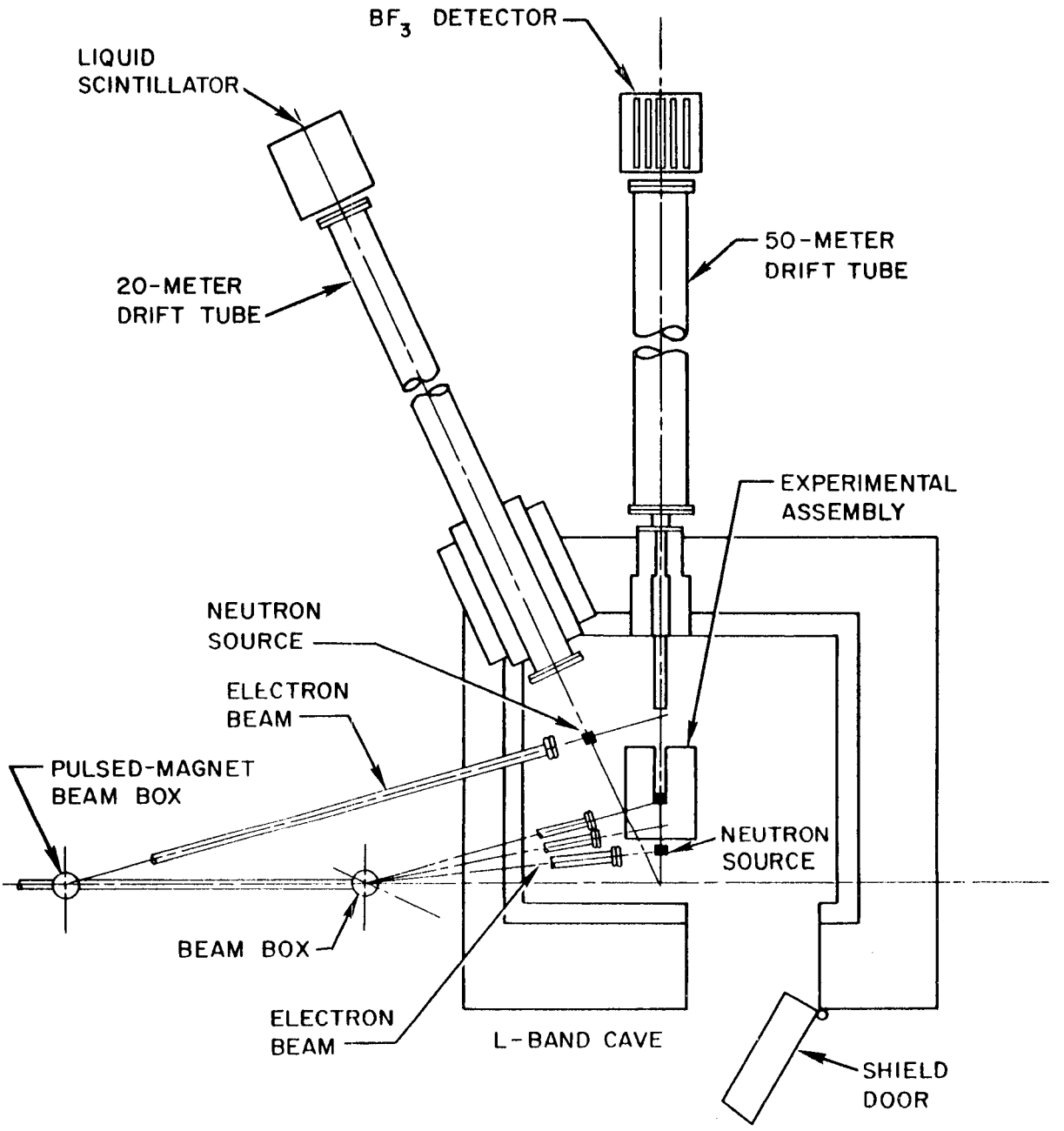

Fig. 9--Plan view of low-room-return neutron cave

where $\epsilon(E)_{16}$ is the efficiency of the 16-m bank and $T(E)_{16}$ is the transmission of the 16-m flight path. Then,

$$C(E)_{16} = S(E)_{16}\,\phi(E)\,, \tag{2}$$

where $C(E)_{16}$ is the counts per channel from the 16-m detector bank for a given assembly with a spectrum $\phi(E)$.

For a bank of 1/v detectors,

$$C_0(E) = \frac{K}{\sqrt{E}} \cdot T_0(E) \cdot T_{16}(E)\,\phi(E)\,, \tag{3}$$

where K is a normalizing constant and $T_0(E)$ is the transmission of the copper wall on the 1/v detector bank. Dividing Eq. (2) by Eq. (3), it can be seen that the sensitivity function is

$$S(E)_{16} = \frac{K}{\sqrt{E}} \cdot T(E)_{16} \cdot T_0(E)\,\frac{C_{16}(E)}{C_0(E)}\,. \tag{4}$$

$S(E)_{16}$ is given in Table 1 and is used in the code ECTOPLASM for the 16-m data.

The transmission of the copper wall of the 1/v detector is given by

$$T_0(E) = e^{-N_{Cu}\sigma(E)t}\,,$$

$$N_{Cu}t = \frac{(8.96)(6.02 \times 10^{23})(2.54)(0.031)}{63.54} = 6.6836 \times 10^{21}\,,$$

$$T_0(E) = e^{0.00668\sigma_{Cu}(E)}\,.$$

The end plates on the flight path are a total of 0.189 in. of aluminum. Thus,

$$T_2(E) = e^{-N_{Al}\sigma_{Al}(E)t}\,,$$

$$N_{Al}t = \frac{(2.7)(6.02 \times 10^{23})(2.54)(0.187)}{26.98} = 2.861 \times 10^{22}\,,$$

$$T_2(E) = e^{-0.02861\sigma_{Al}(E)}\,,$$

where $T_2(E)$ is the transmission of the end plates. For the transmission

Table 1

SENSITIVITY OF 16-METER DETECTOR BANK

E	S(E)	E	S(E)	E	S(E)
10000	0. 001135	220	0. 007155	0. 09	0. 241
9100	0. 001187	200	0. 007529	0. 08	0. 250
8000	0. 001260	150	0. 008650	0. 07	0. 261
7300	0. 001315	100	0. 01056	0. 06	0. 271
6300	0. 001399	70	0. 0128	0. 05	0. 287
6100	0. 001404	50	0. 0149	0. 04	0. 306
5700	0. 001467	30	0. 0191	0. 03	0. 329
5500	0. 001504	20	0. 0233	0. 025	0. 339
5000	0. 001576	15	0. 0267	0. 02	0. 351
3000	0. 002024	10	0. 0331	0. 018	0. 359
2100	0. 002389	9	0. 0348	0. 015	0. 360
1500	0. 002813	8	0. 0369	0. 013	0. 359
1000	0. 003478	7	0. 0391	0. 011	0. 359
900	0. 003656	6	0. 0420	0. 01	0. 356
800	0. 003860	5	0. 0459	0. 0095	0. 352
700	0. 004066	4	0. 0505	0. 009	0. 352
660	0. 004129	3	0. 0575	0. 008	0. 357
640	0. 004129	2	0. 0675	0. 007	0. 361
620	0. 004114	1. 5	0. 0763	0. 006	0. 369
600	0. 003923	1	0. 0919	0. 005	0. 378
590	0. 003589	0. 9	0. 0971	0. 004	0. 390
580	0. 003285	0. 8	0. 1015	0. 0035	0. 391
570	0. 004142	0. 7	0. 109	0. 003	0. 388
560	0. 004516	0. 6	0. 116	0. 0025	0. 379
550	0. 004701	0. 5	0. 126	0. 002	0. 359
500	0. 004900	0. 4	0. 137	0. 0015	0. 320
400	0. 005401	0. 3	0. 155	0. 001	0. 254
300	0. 006178	0. 2	0. 181	0. 0005	0. 180
245	0. 006806	0. 15	0. 203		
230	0. 006375	0. 1	0. 236		

of air, assume standard temperature and pressure and 50% relative humidity. The thickness (t) of air is 138.8 cm, so that T_3, the transmission of air, is given by

$$T_3 = e^{-\sum_i N_i \sigma_i t},$$

$$\sum_i N_i \sigma_i t = \left[\frac{(2)6.02 \times 10^{23}}{22.4 \times 10^3}\right](138.8)$$

$$\cdot\left[0.7803\sigma_N + 0.2099\sigma_O + \frac{12}{760}\sigma_H + \frac{12}{(760)2}\sigma_O\right],$$

$$T_3 = \exp -[7.4605 \times 10^{21}]\,[0.7803\sigma_N + 0.2178\sigma_O + 0.01578\sigma_H].$$

Since

$$T_{16}(E) = T_2(E)T_3(E),$$

then

$$T_{16}(E)\,T_0(E) = \exp -[0.00668\sigma_{Cu}(E) + 0.02861\sigma_{Al}(E) + 0.00582\sigma_N(E)$$

$$+ 0.00162\sigma_O(E) + 0.000118\sigma_H(E)],$$

where all cross sections are in barns and are taken from BNL-325. Then $S(E)_{16}$ per channel for the 16-m bank is given by

$$S(E)_{16} = \frac{C_{16}}{C_0} \cdot \frac{K}{\sqrt{E}} \cdot \exp -[0.00668\sigma_{Cu}(E) + 0.02861\sigma_{Al}(E) + 0.00582\sigma_N(E)$$

$$+ 0.00162\sigma_O(E) + 0.000118\sigma_H(E)].$$

The 50-m detector bank was calibrated by comparison with the 16-m BF_3 bank (to save machine time by avoiding the use of the 1/v detectors). The 50-m flight path is an extension of the 16-m flight path, consisting of the evacuated 16-m flight path plus two helium-filled gas bags which have four 0.020-in. aluminum windows. Given that

$$C_{16} = S(E)_{16}\phi(E), \qquad (5)$$

using a standard assembly, there is a sensitivity, $S(E)_{50}$, at 50 m for the same assembly such that

$$C_{50} = S(E)_{50}\phi(E) . \tag{6}$$

Using this and Eq. (5), we have

$$S(E)_{50} = \frac{C_{50}}{C_{16}} S(E)_{16} . \tag{7}$$

Reducing the raw data obtained at both the 16- and 50-m flight paths with the 16-m sensitivity will give

$$C_{50} = S(E)_{16}\phi(E)_{50} ,$$

$$C_{16} = S(E)_{16}\phi(E)_{16} ;$$

and since

$$\phi(E)_{16} \equiv \phi(E) ,$$

then

$$\frac{C_{50}}{C_{16}} = \frac{\phi(E)_{50}}{\phi(E)_{16}}$$

or

$$S(E)_{50} = \frac{\phi(E)_{50}}{\phi(E)_{16}} S(E)_{16} ,$$

where $S(E)_{50}$ is as given in Table 2 and is used in the code ECTOPLASM for the 50-m data.

The energy sensitivity of the reoriented 16-m detector bank has been established with increased precision over six energy decades. A relative accuracy of about 3% has been achieved. Between 100 and 1000 ev, the gas in the detector bank acts like a thin 1/v absorber, so that the sensitivity can be easily calculated. The resonances indicated in Table 1 are in the copper walls of the counter. The measured quantity S(E) is, of course, very vital, since all experimental time-of-flight data must be adjusted by this function to obtain the neutron spectrum.

After the energy sensitivity of the improved detector bank was

Table 2

SENSITIVITY OF 50-METER DETECTOR BANK

E	S(E)	E	S(E)	E	S(E)
10000	0.014	30	0.0414	0.125	0.129
2100	0.0177	20	0.045	0.11	0.133
1500	0.0193	15	0.0475	0.1	0.132
1000	0.021	10	0.0536	0.09	0.128
900	0.021	9	0.054	0.08	0.124
800	0.0216	8	0.055	0.07	0.127
700	0.0216	7	0.0566	0.06	0.132
660	0.0216	6	0.0585	0.05	0.144
640	0.0213	5	0.058	0.04	0.150
620	0.0212	4	0.062	0.03	0.160
600	0.0199	3	0.0655	0.025	0.164
590	0.0183	2	0.0675	0.02	0.169
580	0.0168	1.5	0.0695	0.018	0.171
570	0.212	1	0.0765	0.015	0.173
560	0.0228	0.9	0.0798	0.013	0.172
550	0.0238	0.8	0.0805	0.011	0.173
500	0.0238	0.7	0.0845	0.01	0.170
400	0.0250	0.6	0.0885	0.0095	0.163
300	0.0260	0.5	0.0945	0.009	0.166
245	0.0273	0.4	0.099	0.008	0.168
230	0.025	0.3	0.105	0.007	0.168
220	0.028	0.25	0.114	0.006	0.174
200	0.0284	0.225	0.111	0.005	0.181
150	0.0301	0.21	0.124	0.004	0.181
100	0.0296	0.2	0.131	0.0035	0.181
70	0.0337	0.175	0.129	0.003	0.173
50	0.0376	0.15	0.122	0.001	0.160

established, the spectrum in a standard, reference, borated-polyethylene geometry (~5 barns of absorption per hydrogen atom) was remeasured. A comparison of the results of this measurement with a spectrum measured with the old detector bank is given in Fig. 10.

A secondary check of the 16-m detector bank was attempted by measuring the transmission of this bank. However, it was found that the effect was masked by the scattering of the copper walls, and the efficiency could not be determined without using elaborate experimental techniques.

3.3. EFFECT OF SCATTERER ON NEUTRON SPECTRA

At the Brookhaven Thermalization Conference,[3] a criticism of an experimental technique often used in the present program was voiced. It was suggested that the scatterer technique of extracting beams from our assemblies was leading to spurious answers. The scatterer, usually zirconium, which is a coherent scatterer, is placed in a small glory hole which penetrates the assembly, and the neutrons scattered in the direction of the detector system are observed. The heavy scatterer essentially performs the following angular integral:

$$\Phi(X, E, \mu = 1) = \int_0^{\infty} \int_0^{4\pi} \phi(X, E', \mu') \Sigma_s(\mu' \rightarrow \mu, E' \rightarrow E)\, dE' d\Omega ,$$

where $\Sigma_s(\mu' \rightarrow \mu, E' \rightarrow E)$ is the scattering kernel for the zirconium scatterer, whereas the desired measurement is the scalar flux,

$$\int \phi(X, E, \mu)\, d\Omega .$$

The conditions for an ideal scatterer are severe:

1. Very low absorption cross section,
2. Σ_s not a function of energy,
3. Σ_s an isotropic scatterer, so that no angular region is especially emphasized,
4. Only elastic scattering $\Sigma(E' \rightarrow E) = \Sigma_s\, \delta(E' \rightarrow E)$.

Zirconium would appear to be fairly ideal, but Poole (at BNL) had experimental evidence of coherent effects in the scattering at low energies.

At the time of the adoption of this technique, the method had been tested against the standard re-entrant-hole extraction technique, and both methods should ideally have given the same result (no flux gradient). Agreement within the experimental errors had been obtained, but experimental intensities were much lower than they are at present. For these reasons,

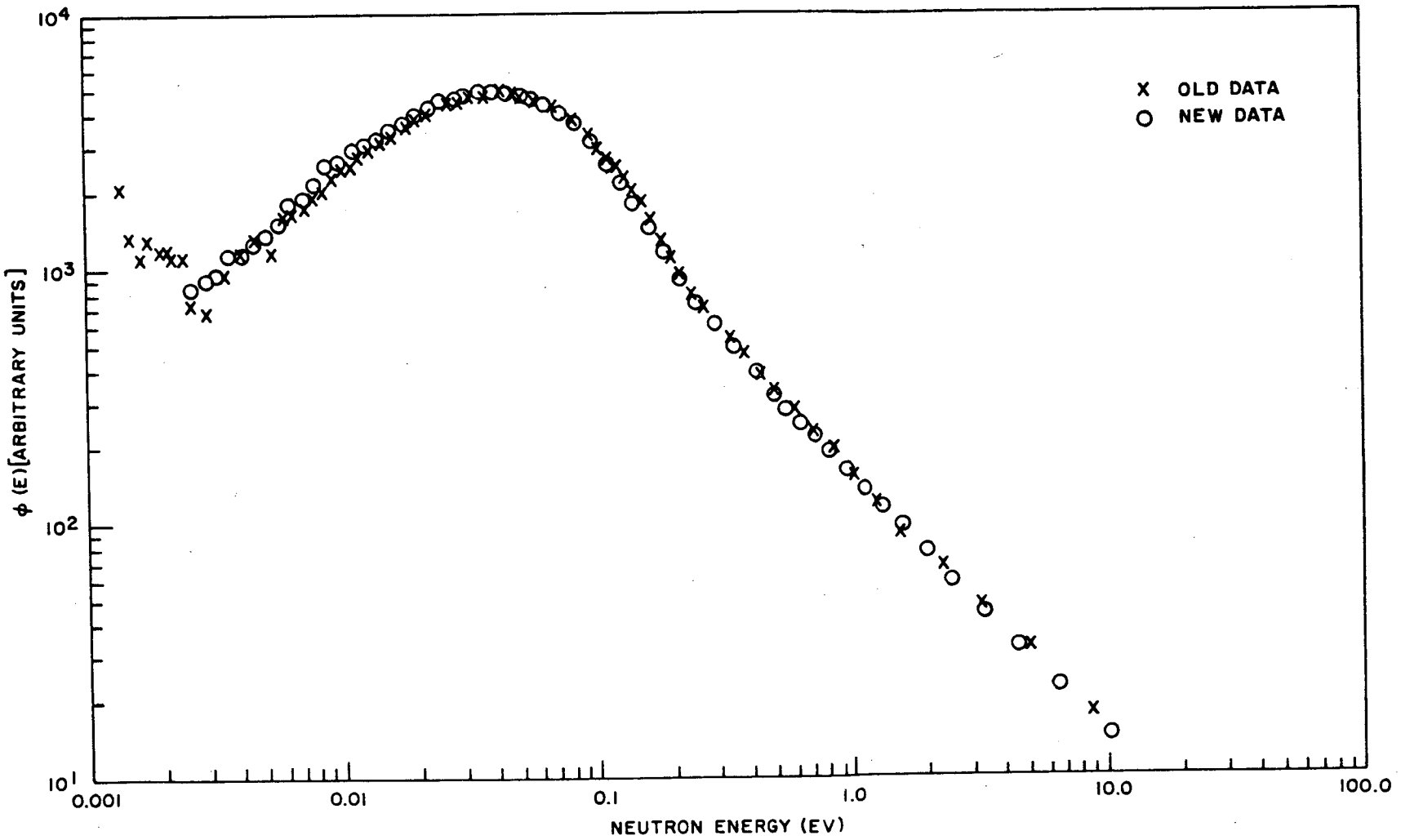

Fig. 10--Comparison of spectra measured with old and new 16-m detector banks

a new and more severe test of the scatterer method was devised. It was decided to test scalar-flux determinations at a point where a large flux gradient existed in a poisoned polyethylene assembly. Two scatterers, lead and zirconium, were compared, since both satisfy conditions 1 and 2 above but could be expected to exhibit considerably different scattering angular distributions. The results of these measurements are shown in Fig. 11. As can be seen, the same spectrum under the above conditions was observed for neutron energies from 10 to 0.01 ev. It is therefore thought, as before, that there is no reason to disqualify spectral data obtained by the beam-scatterer technique. In fact, this technique may turn out to be very useful for high-energy beam extraction since Pb^{206} appears to be an effective scatterer up to neutron energies of 100 kev.

An experiment was conducted to determine the minimum-thickness beam scatterer which could be used in a glory-hole neutron-beam-extraction system. Figure 12 shows the relative intensity of the counts in the 16-m detector bank as a function of scatterer size in a given geometry.

Spectra were measured in a 25 g per liter boric acid solution with a 3/8-in.- and a 1/16-in.-thick zirconium scatterer. The results of these measurements are shown in Fig. 13. The 1/16-in.-thick zirconium scatterer permitted very good measurement of the neutron spectrum in the assembly studied. This is an important observation because it is desirable in future lattice experiments to measure spectral variation over short distances, e.g., in narrow water gaps.

3.4. EFFECT OF LOCATION OF PULSED NEUTRON SOURCE ON SPECTRA

An experiment was conducted to determine the sensitivity of spectra, using a particular slab geometry, to source location in a direction parallel to the slab. A typical arrangement for slab measurements is shown in Fig. 14. The geometry chosen was an 18 in. by 18 in. by 4 in. slab of 1 wt-% borated polyethylene. This was essentially a check on the validity of our assumption of a one-dimensional geometry. Surface-leakage spectra were measured using a 1/2-in. precollimator 1-1/8 in. from the surface of the assembly. The source was located on the axis of the precollimator, 3-3/4 in. off axis, and 6-7/8 in. off axis. The results of these measurements are shown in Fig. 15, where it can be seen that there is no detectable difference in the spectra obtained with the three source positions.

3.5. EFFECT OF PRECOLLIMATOR OPENING AND LOCATION ON SPECTRA

Studies of the effect of precollimator location (see Fig. 14) on surface-leakage spectra were made using an 18 in. by 18 in. by 4 in. slab of 1 wt-%

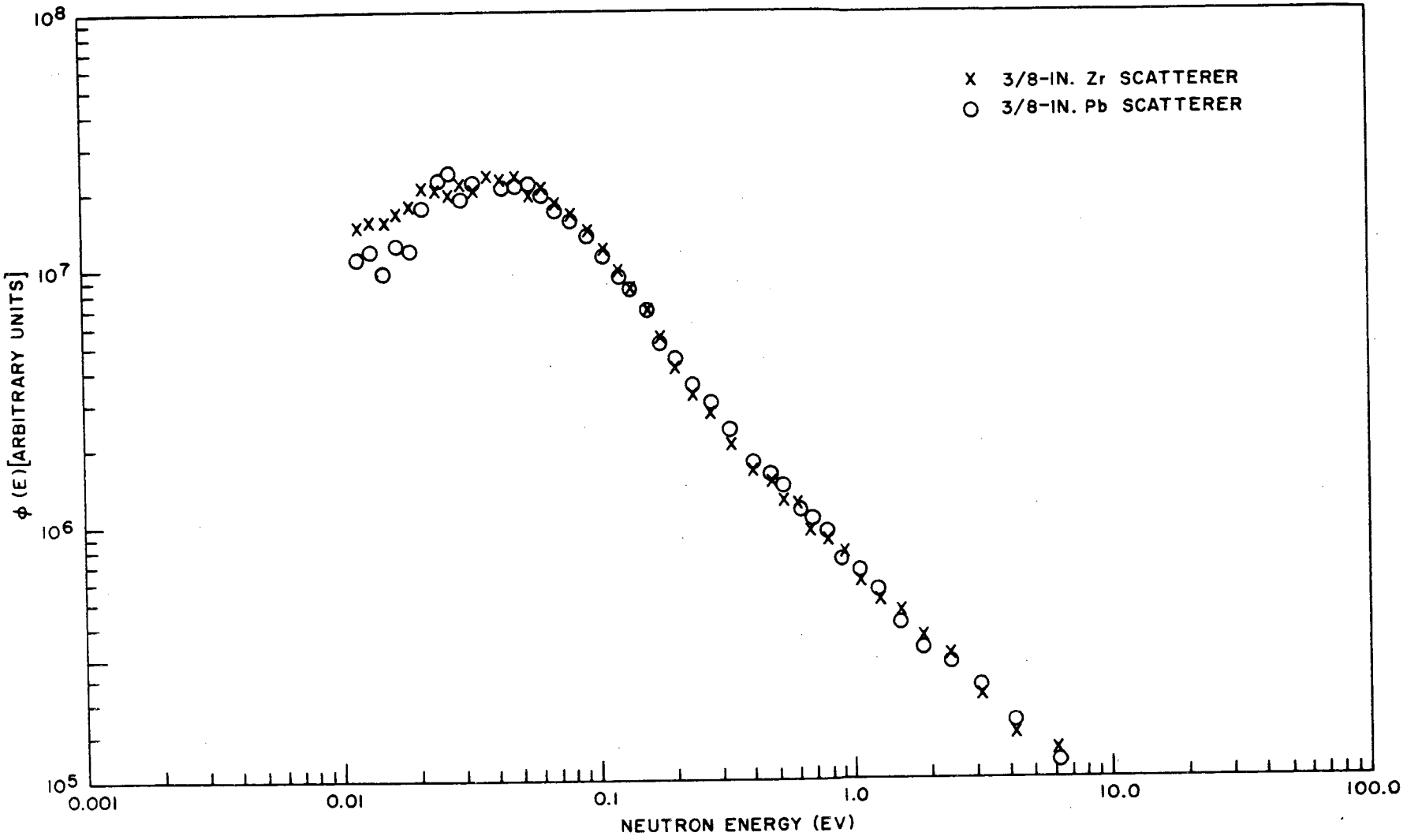

Fig. 11--Comparison of spectra measured with a zirconium and a lead scatterer

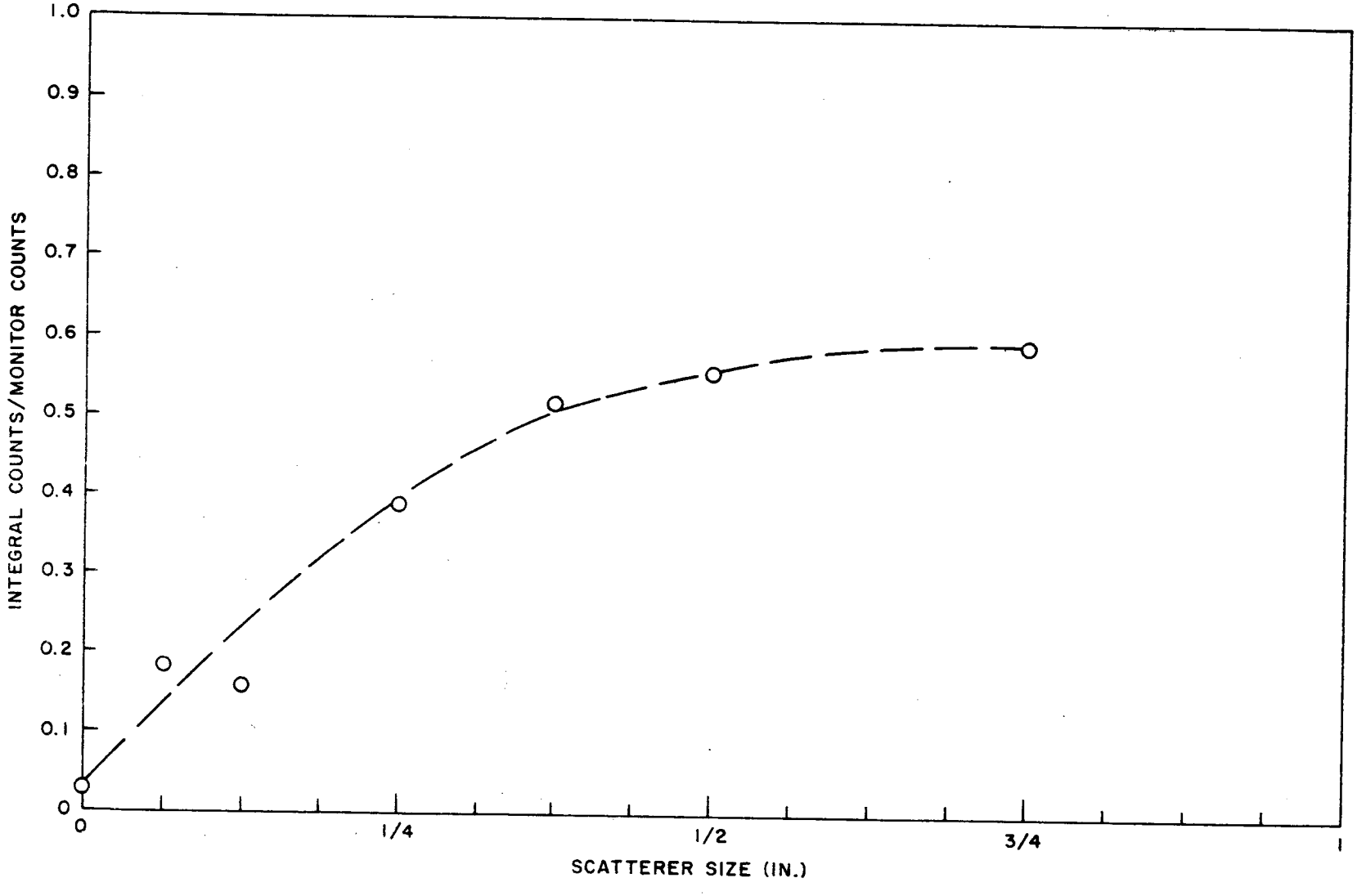

Fig. 12--Relative neutron intensity versus scatterer thickness

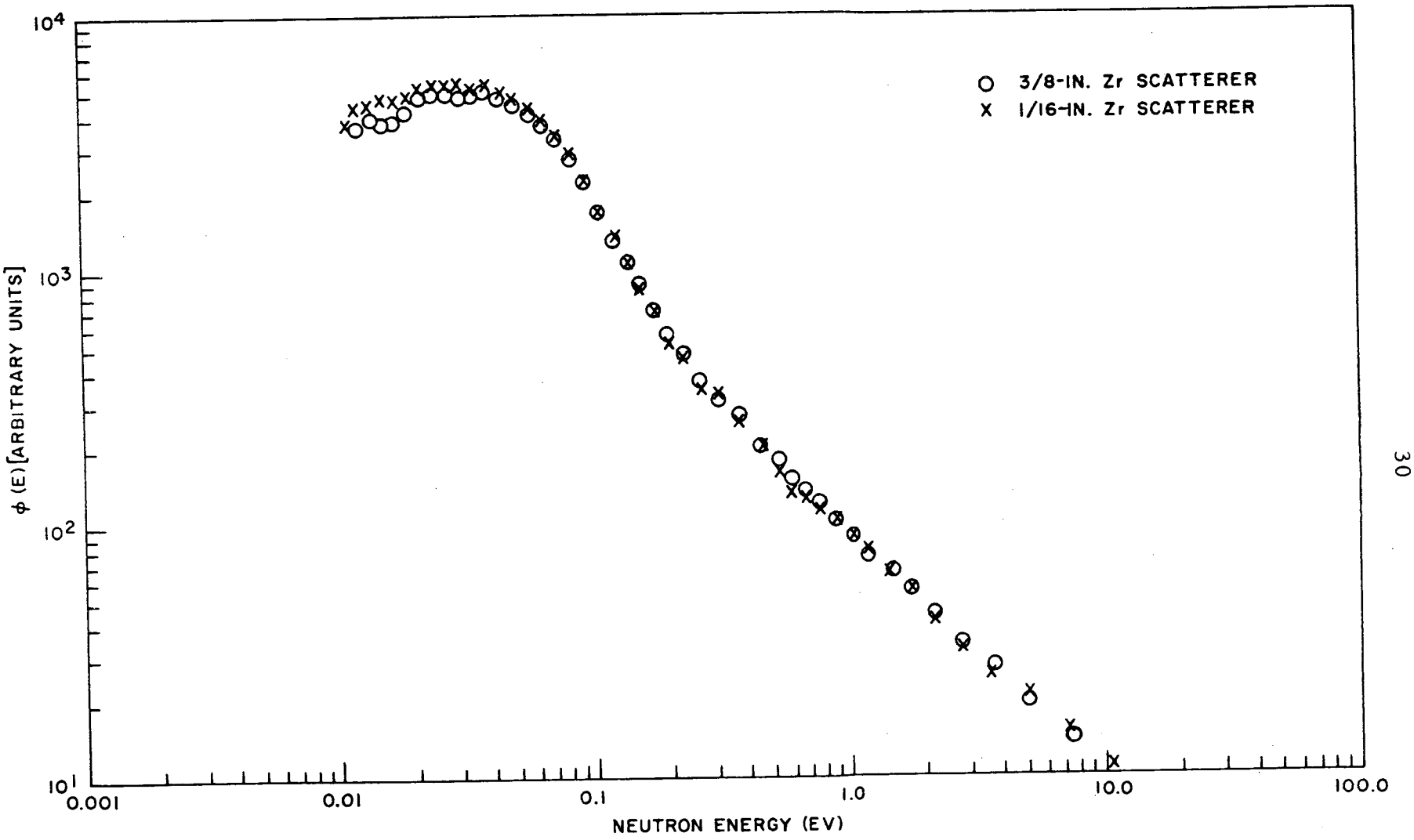

Fig. 13--Comparison of spectra measured with a 3/8-in. -thick and a 1/16-in. -thick zirconium scatterer

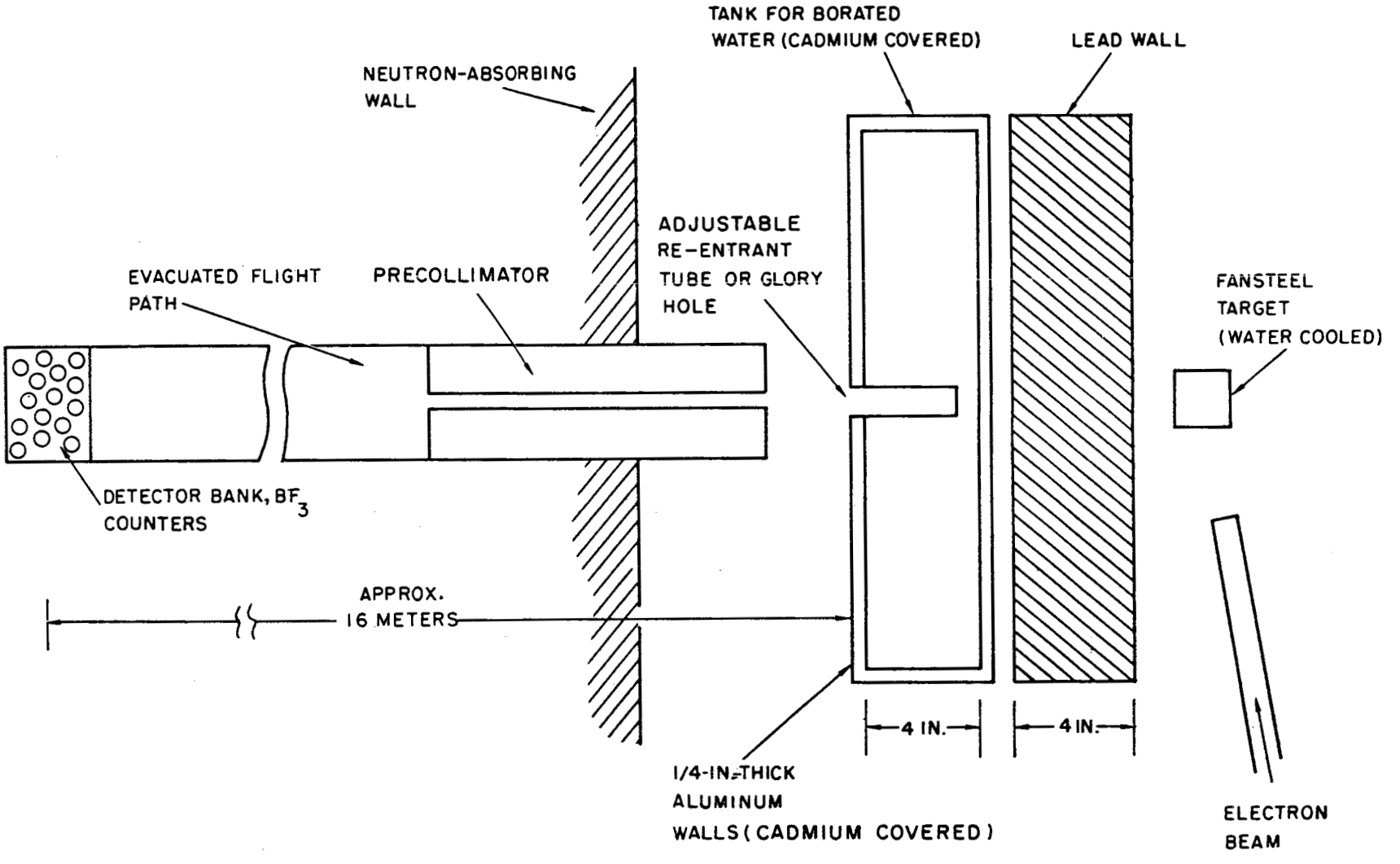

Fig. 14--Typical experimental arrangement for measuring spatially dependent neutron spectra

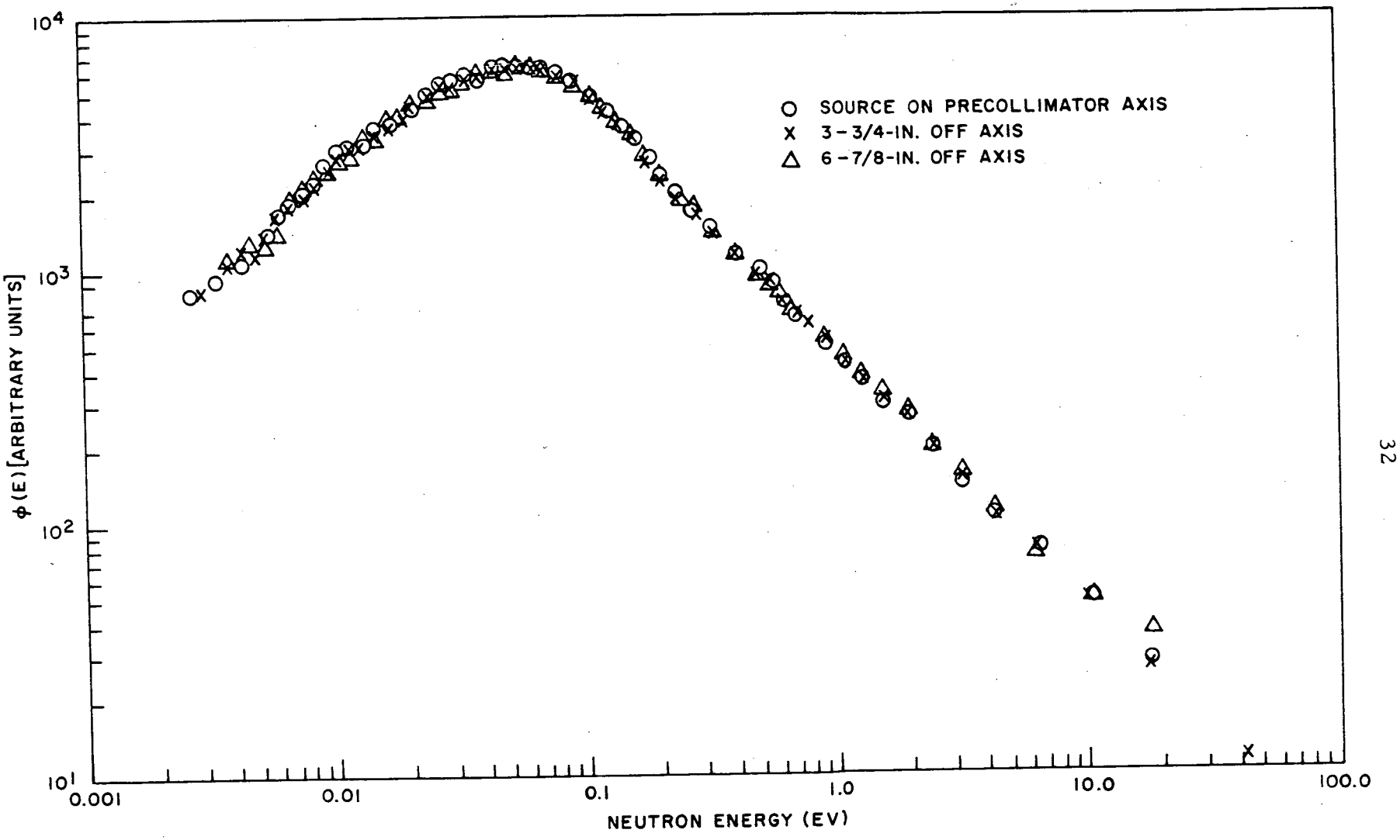

Fig. 15--Comparison of spectra obtained with pulsed neutron source on and off axis of the precollimator

borated polyethylene. Spectra were measured with a 1/2-in.-diameter precollimator at 1-1/2 in. and 8-5/8 in. from the surface of the assembly. In addition, a 1-in.-diameter precollimator was used 1-1/2 in. from the surface of the assembly. The results of these measurements (shown in Fig. 16) indicate that there is no perturbation of the leakage spectra as a result of precollimator positions used in the experimental arrangement. Thus, backscattering from the precollimator into the assembly does not appear to perturb spectra.

Spectra were also measured in a reference boric acid solution with a 0.43-in.-diameter re-entrant tube and a 0.30-in.-diameter borated-epoxy precollimator and in the same solution with a 1-in.-diameter re-entrant tube and a 1/2-in. $B_4^{10}C$ precollimator. The results of these measurements (shown in Fig. 17) indicate that no perturbation results from re-entrant hole size or precollimator diameter.

3.6. EFFECT OF LINAC INTENSITY ON SPECTRA

Spectra were measured in an 18 in. by 12 in. by 12 in. borated-polyethylene (1% by weight) assembly to check for any possible effect due to measuring spectra at widely different Linac intensities. It was thought that saturation or pile-up effects might be leading to small spectral distortions. The machine intensity was changed a factor of 10 for these measurements. The results (shown in Fig. 18) revealed no perturbation of the spectra under the conditions cited.

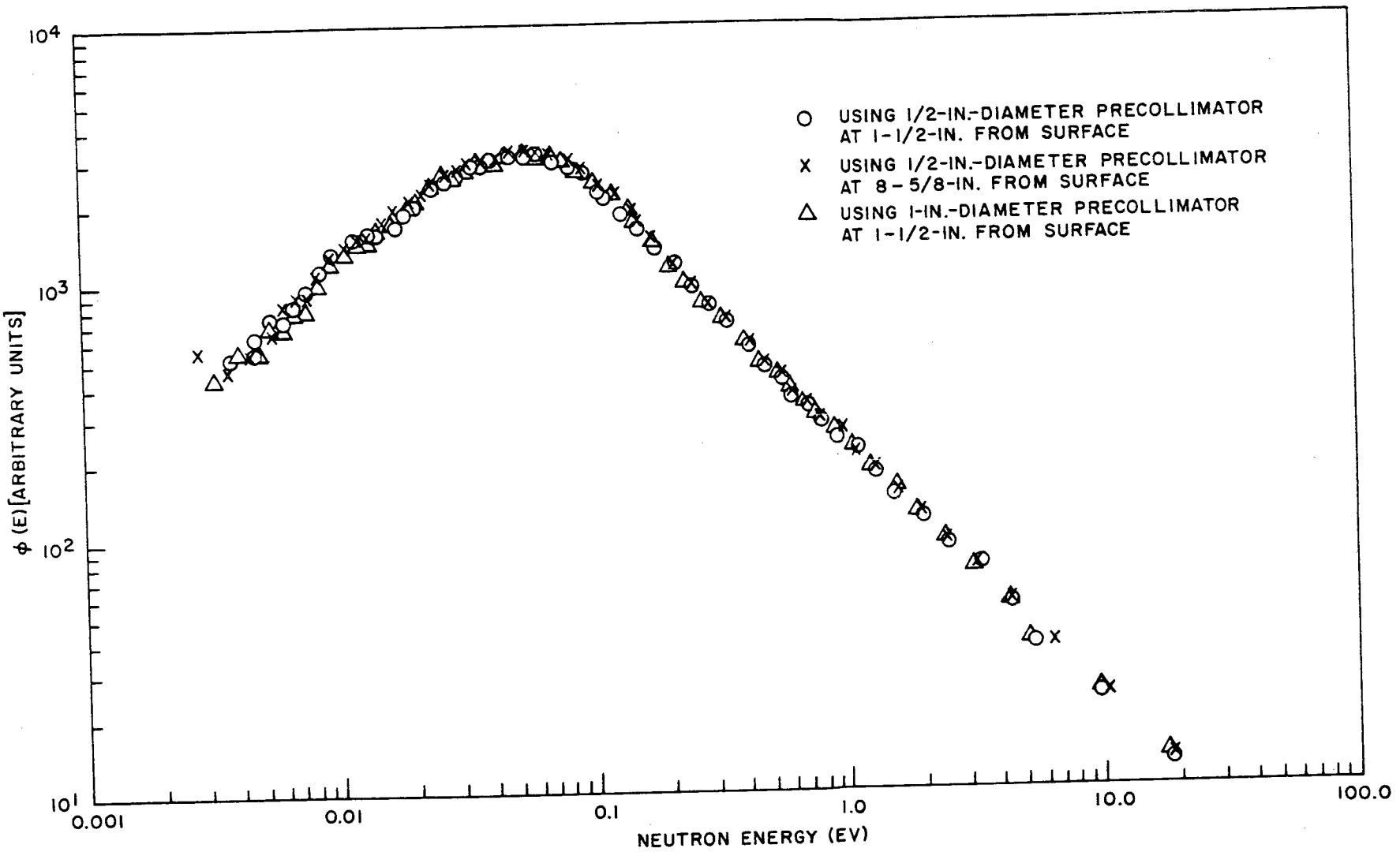

Fig. 16--Comparison of spectra obtained with two precollimators at two different positions

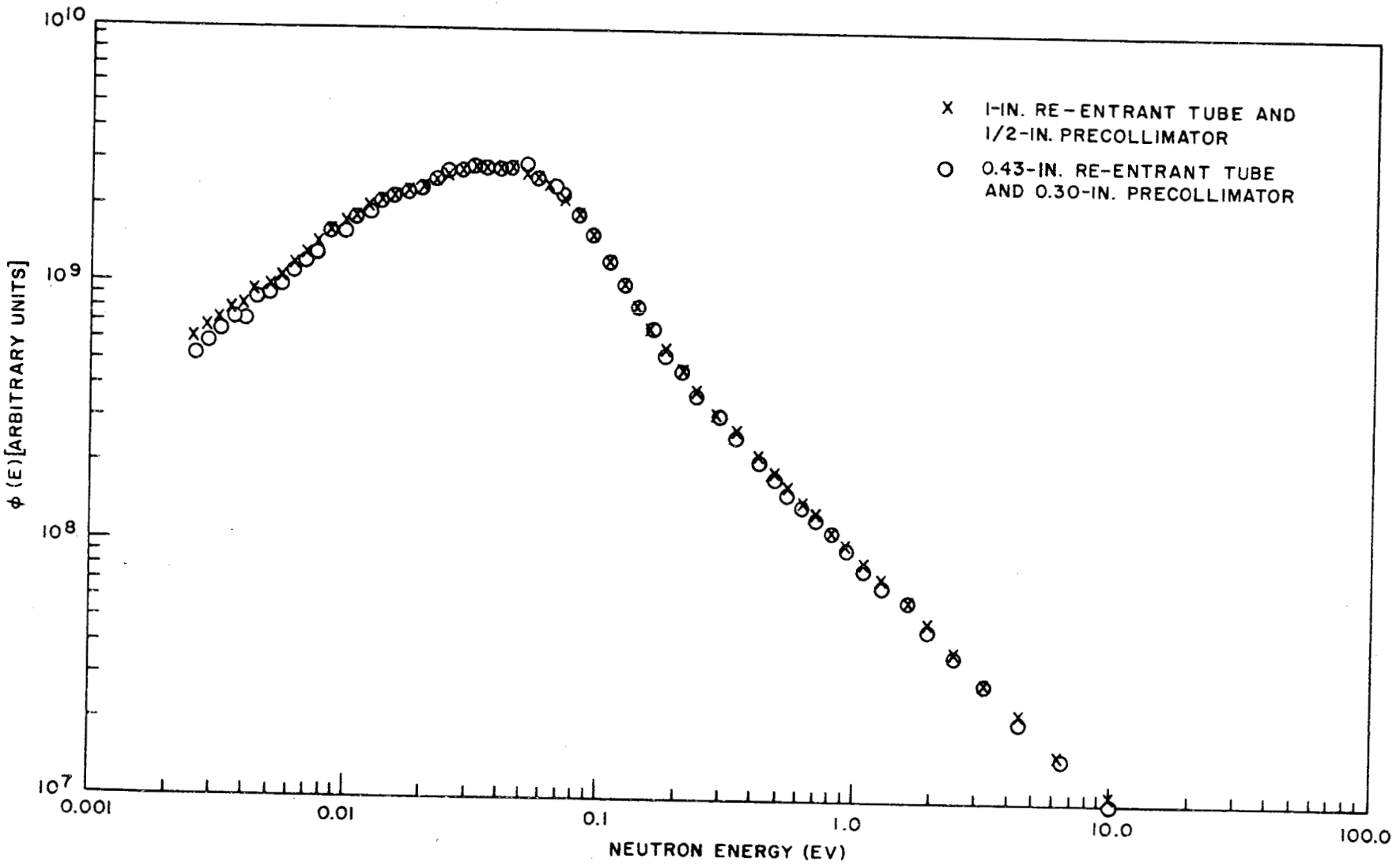

Fig. 17--Comparison of spectra obtained with precollimators and re-entrant tubes of different sizes

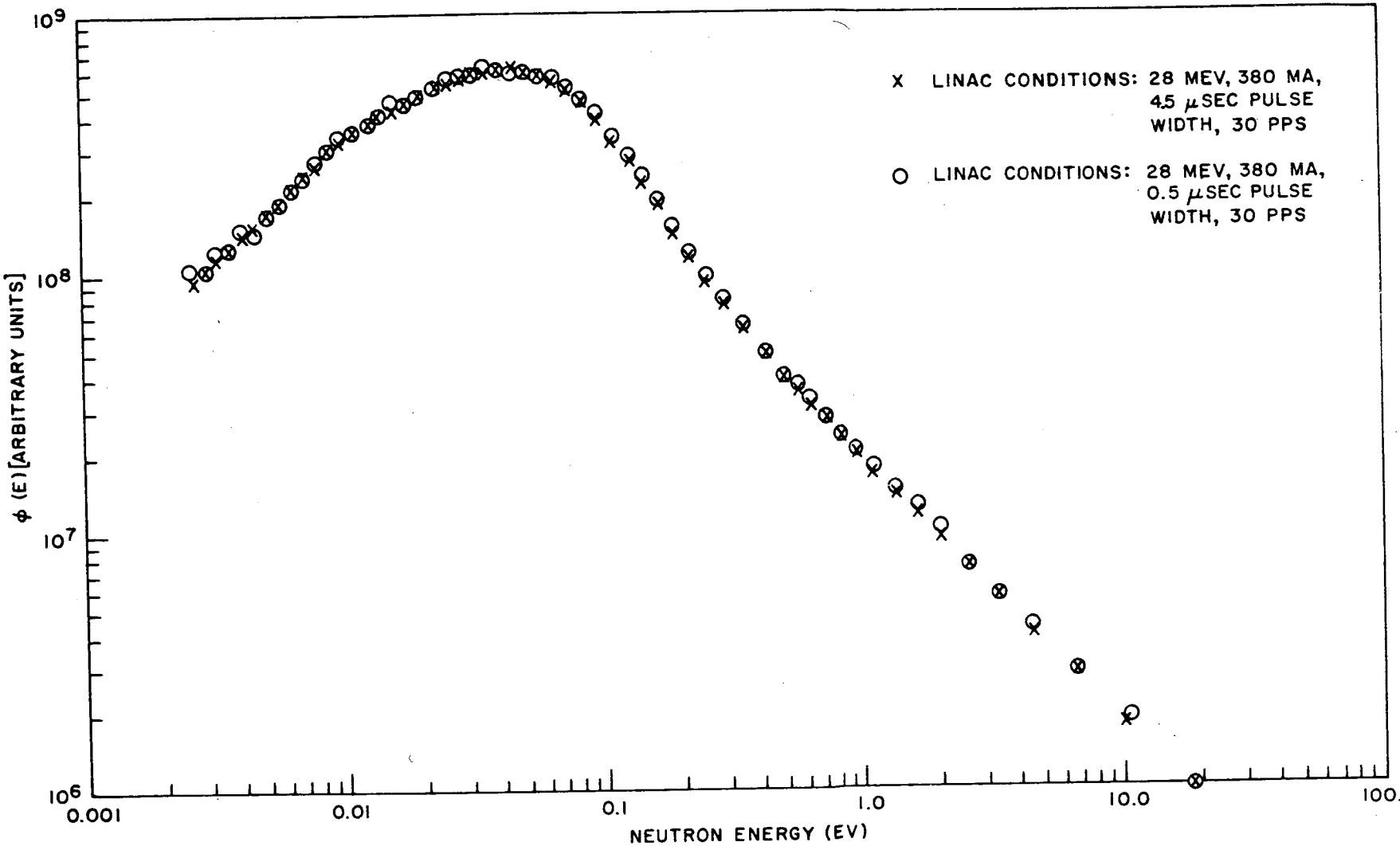

Fig. 18--Comparison of spectra measured at different Linac intensities

IV. SPATIALLY DEPENDENT, FINITE-MEDIUM SPECTRA IN NONMULTIPLYING SYSTEMS

The important practical problem of understanding neutron spectra in finite media was heavily emphasized during the past contract year. Most of the experimental and analytical work was conducted for water-moderated systems, although some supplementary studies were performed for polyethylene. Large flux gradients were intentionally established in the test systems through location of the external neutron source and choice of boundary conditions. Both angularly dependent and scalar-flux measurements were made. The objective is to compare measured fluxes with theoretical predictions based on the standard transport-theory approach common to reactor analysis and to resolve or understand any discrepancies brought to light. As was described in Section III, many experiments have been performed to verify that the experimental procedures do not introduce systematic errors.

Earlier experience had pointed up the value of having all spectral measurements for a given geometry (e. g. , a 4 by 18 by 18 in. tank) obtained for the same poison concentration. Data had been previously taken (1961) over a long period of time and with varied poison concentrations, necessitating separate and costly numerical computing work for each of the concentrations. These data had served to point up the difficulty of understanding spectra measurements, but were not precise enough for definitive comparisons. Consequently, the most recent and most precise measurements on water poisoned with boric acid have all been made with a concentration of 43. 7 g per liter of solution.

A typical experimental setup for measurement of spectra in a finite, one-dimensional medium is shown in Fig. 14. In the thin dimension, flux plots are taken to determine the flux shape. A 1-in. -diameter re-entrant tube with a thin (0. 020-in.) aluminum end can be positioned at any depth in the thin dimension to determine the zero-degree angular spectra at various points. A 0. 430-in. -diameter glory hole through the tank in the thin dimension provides for the placement of a cylindrical zirconium scatterer (usually 3/8 in. long) at any position to determine the scalar spectrum at that position, since the scattering from zirconium integrates over all angles. For each spectrum measurement, a background is subtracted. For background runs, a 1-in. cube of $B_4^{10}C$ is placed on the end of the re-entrant tube for the angular-spectra measurements and is placed on the source side of the tank covering the end of the glory hole for the scalar-spectra measurements. The precollimator opening on the

entrance to the flight path is sized to view only the end of the re-entrant tube or the end of the zirconium scatterer. Neutrons from the wall of the re-entrant tube or the glory hole will markedly disturb the spectrum being measured and must be excluded. The assembly whose spectrum is being measured is located in a small room (the neutron cave shown in Fig. 9) with neutron-absorbing walls so that the neutrons seen by the assembly are those from the target only and not from room return.

4. 1. FOUR-INCH-THICK SLAB

A 4-in. -thick slab was the geometry chosen for the detailed studies undertaken for the finite-medium spectrum measurements. A large number of measurements were made in this geometry, since it was big enough to provide a nearly asymptotic spatial flux distribution far from the source and yet was not so big as to make the numerical computations performed with the transport-theory codes THERMOS and DSN impractical. It should be pointed out that in many ways the geometry chosen is close to that for the standard Milne problem and is thus a very important test of transport methods.

The 4-in. -thick slab was 18 in. wide and 18 in. high. Two boric acid concentrations were used: 43. 7 g per liter of solution and 50. 5 g per liter of solution. The 50. 5 g per liter of solution was used as an independent check to make certain that there was no contamination in the standard 43. 7 g per liter of solution and to ensure reproducibility of the measurements. The spectral measurements obtained in the two solutions were consistent, with only a slight hardening of the spectra in the 50. 5 g per liter of solution owing to the additional absorber present.

Since the codes used to calculate these spectra require the specification of the epithermal source term, several flux plots were taken in this assembly. Figure 19 shows the results obtained with cadmium-covered indium ($\sim$ 1. 4 ev) foils, bare indium (thermal) foils, and cadmium-covered gold ($\sim$ 5 ev) foils. As can be seen, the build-up on the source side of the tank varies for each neutron energy even though the solution is heavily poisoned. Thus, on this side of the tank we are definitely contending with transient flux conditions. It should be noted that the flux for each neutron energy peaks at about the same location in the slab and then falls off with about the same slope to the opposite boundary. If the slab boundary were black to neutrons (i. e. , if the vacuum-interface condition were met there), one would expect a dip of the flux near the boundary. However, the flux plots taken showed no indication of this effect. The cause of this is not known at present, but room return is strongly suspected.

The lead wall between the source and the slab (Fig. 14) also affected the spatial distribution of the epithermal neutrons in the slab. The effect

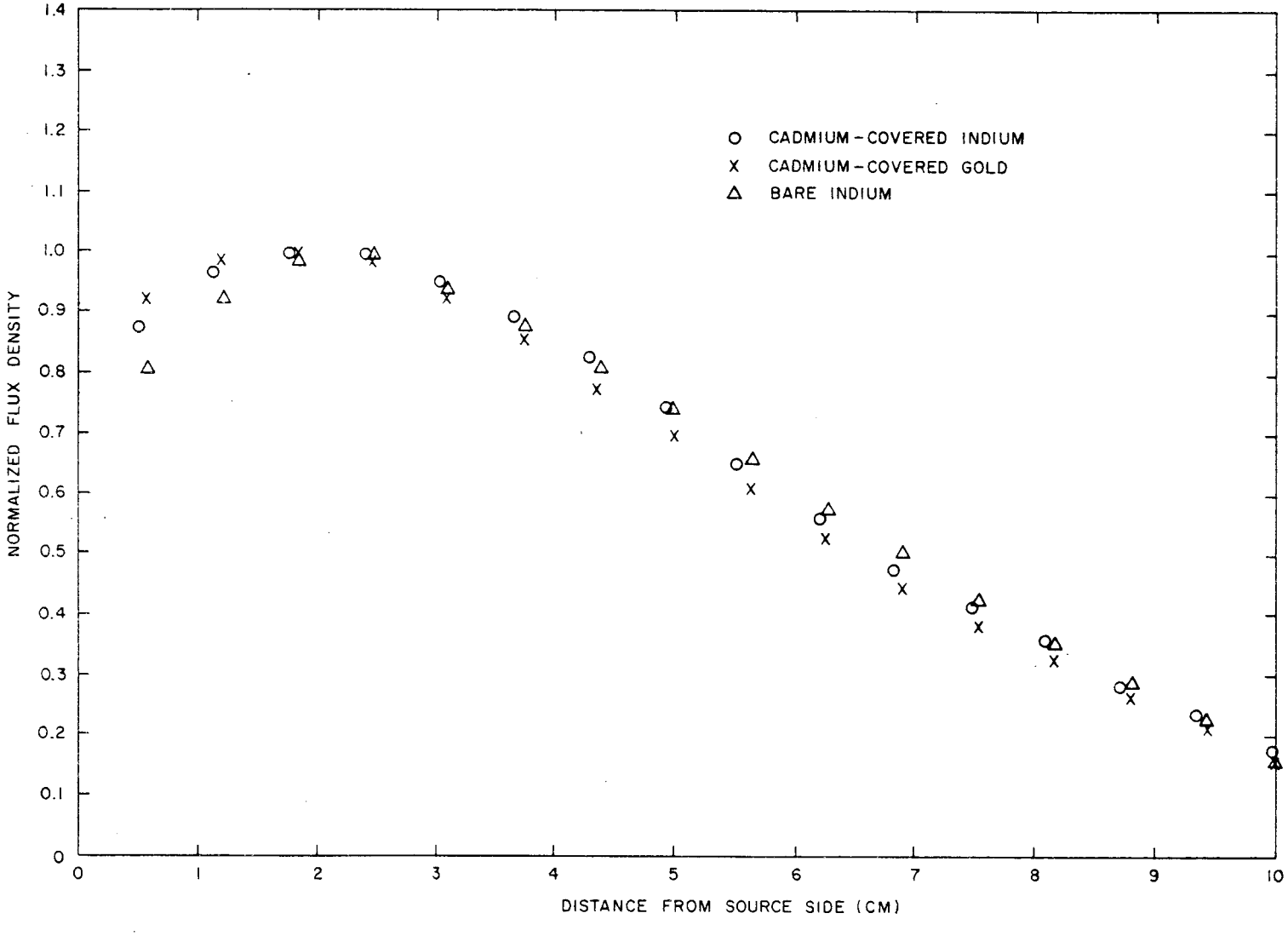

Fig. 19--Spatial distribution of neutron flux in 4-in. slab

of the lead wall on the cadmium-covered-indium flux plots was to shift the peak of the flux closer to the source (see Fig. 20). All spectrum measurements described in this section were taken with the lead wall present.

The spectrum measurements taken in the 4-in. slab consisted of two scalar measurements and six zero-degree angular measurements. The two scalar fluxes were measured at 2.5 cm (zero gradient) and 6.35 cm (strong gradient) from the source side. The results of these measurements are compared with transport-theory (DSN) calculations in Fig. 21. The relative intensity between 2.5 and 6.35 cm has been preserved in the experimental measurement technique and is shown in comparison with the change in intensity predicted by DSN. The theoretical calculations have been normalized at 1 ev to the measurement taken at 2.5 cm only for comparison. As can be seen, for the relative intensity at 1 ev, the agreement between theory and experiment is good. However, there still appears to be some discrepancy in the spectral indices between 1 and 0.025 ev. The agreement between theory and experiment in this scalar-flux case is not as good as that obtained under infinite-medium conditions. The agreement seems to be considerably better at 6.35 cm, where the measurement is made under more nearly asymptotic conditions. These discrepancies can possibly be reduced by going to higher-order (P_2, P_3) terms in the scattering matrix for H_2O. The scalar measurement (3/8-in. zirconium scatterer) at 2.5 cm was compared with the zero-degree angular measurement (re-entrant tube) at 2.5 cm. Figure 22 shows the results of this comparison. As was expected, these two measurements are in good agreement owing to the zero-gradient condition at the peak of the flux.

The zero-degree angular measurements in the 4-in. slab were made at 1.59, 2.5, 4.0, 6.5, 8, and 10.2 cm from the source side. The results of these measurements are shown in Figs. 23, 24, and 25. Here again, comparison of relative intensities at 1 ev shows that experiment and theory are in good agreement. However, between 1 ev and 0.025 ev, there is a consistently greater disagreement between experiment and theory for the angular-flux measurements than for the scalar measurements. An exception is the one angular-flux measurement at 10.2 cm of the leakage from the surface of the slab, which must be considered in a different light from the other angular measurements. As was pointed out previously, the spatial flux distribution of the epithermal neutrons (Fig. 19) used to calculate the source term for the codes did not show the expected flux depression at the surface. Since DSN is used to calculate the distribution with the assumption that a vacuum interface exists at the boundary, the odd shape of the calculated surface-leakage spectrum is probably due to a thermal-flux depression calculated with the code but not observed experimentally. The theoretical and experimental spectral indices are thus apparently in better agreement at the surface than internally in the slab. In the angular-flux

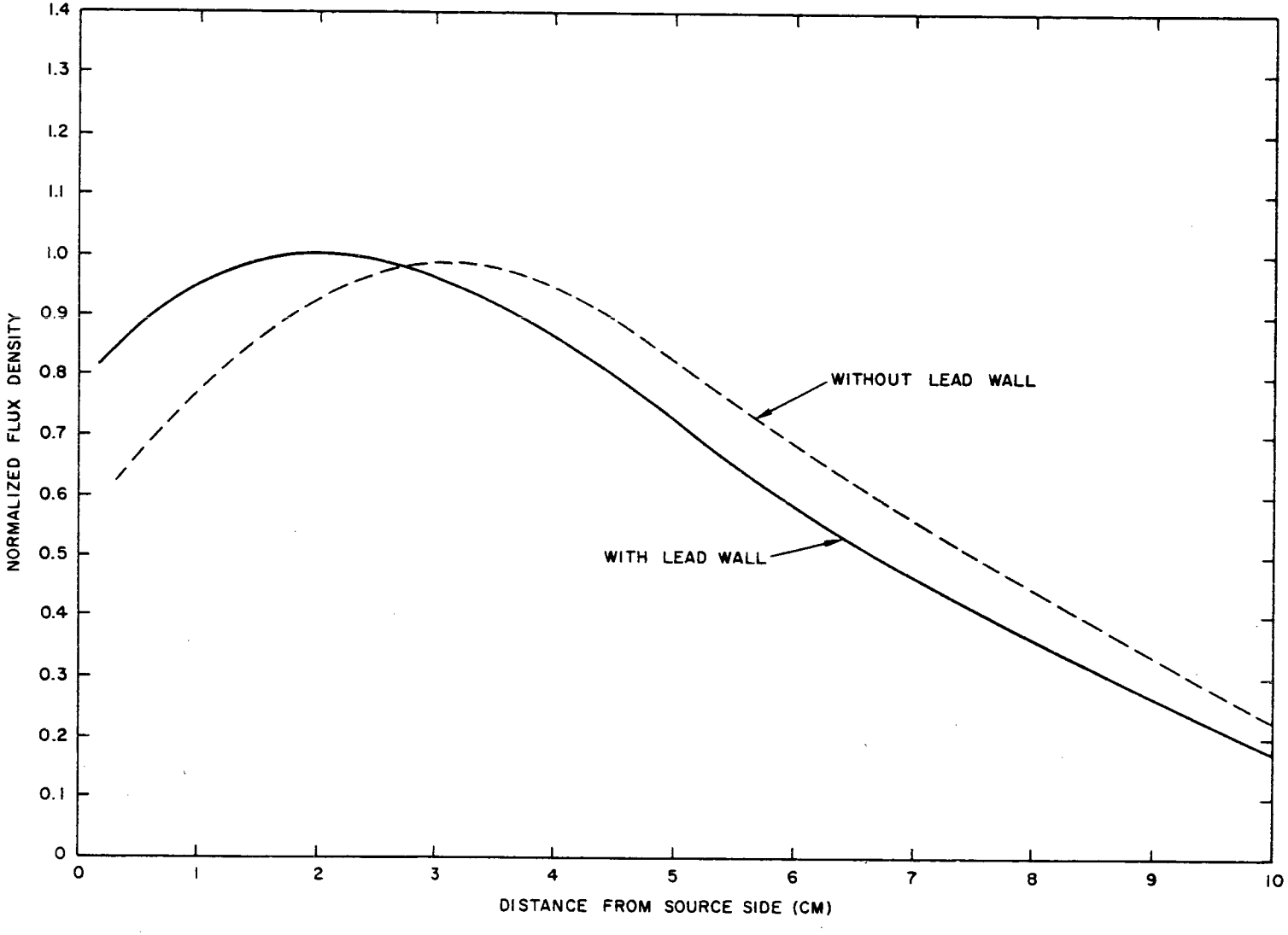

Fig. 20--Effect of lead wall on cadmium-covered-indium flux plot in 4-in. slab

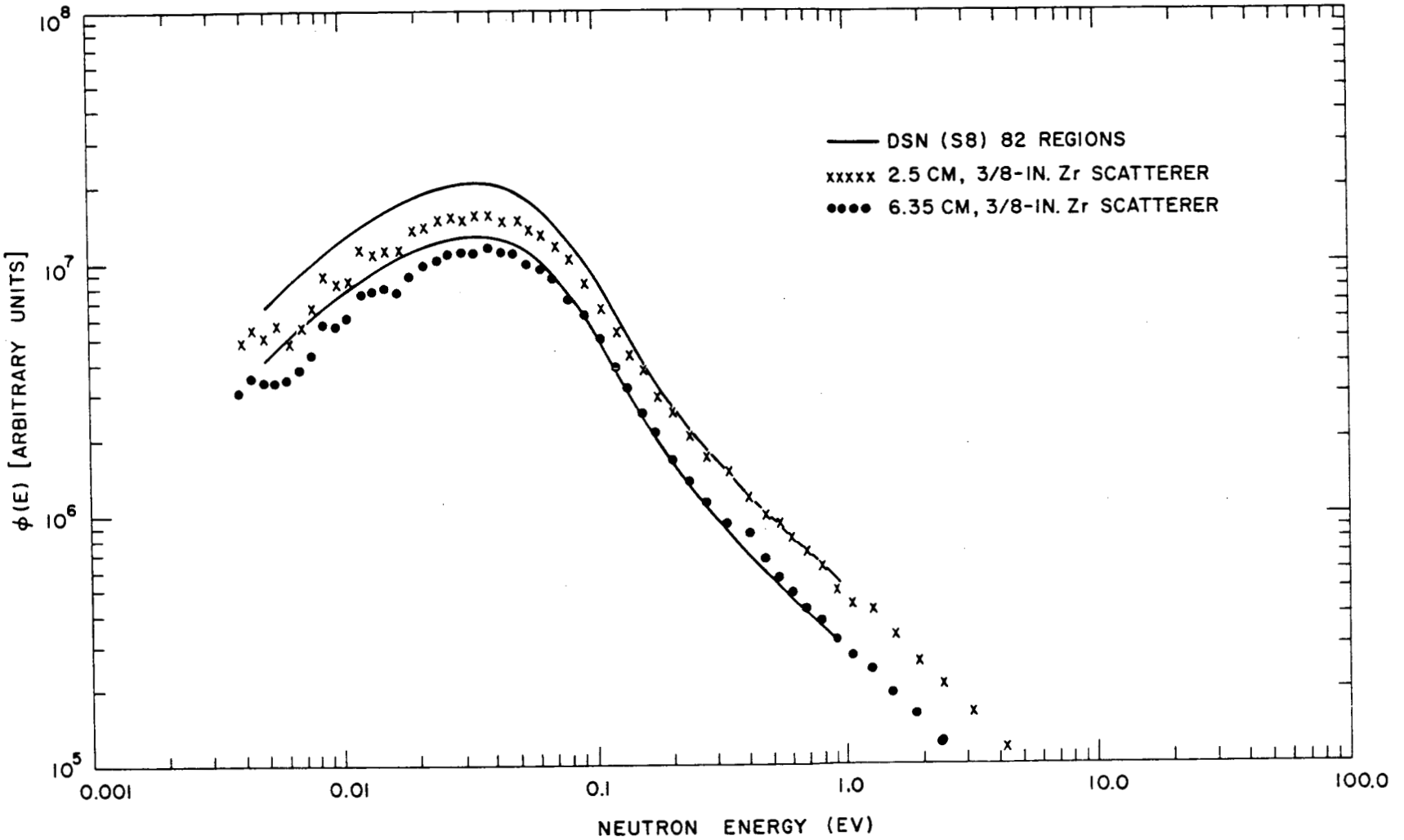

Fig. 21--Scalar neutron spectra in a 4-in. slab of H_3BO_3

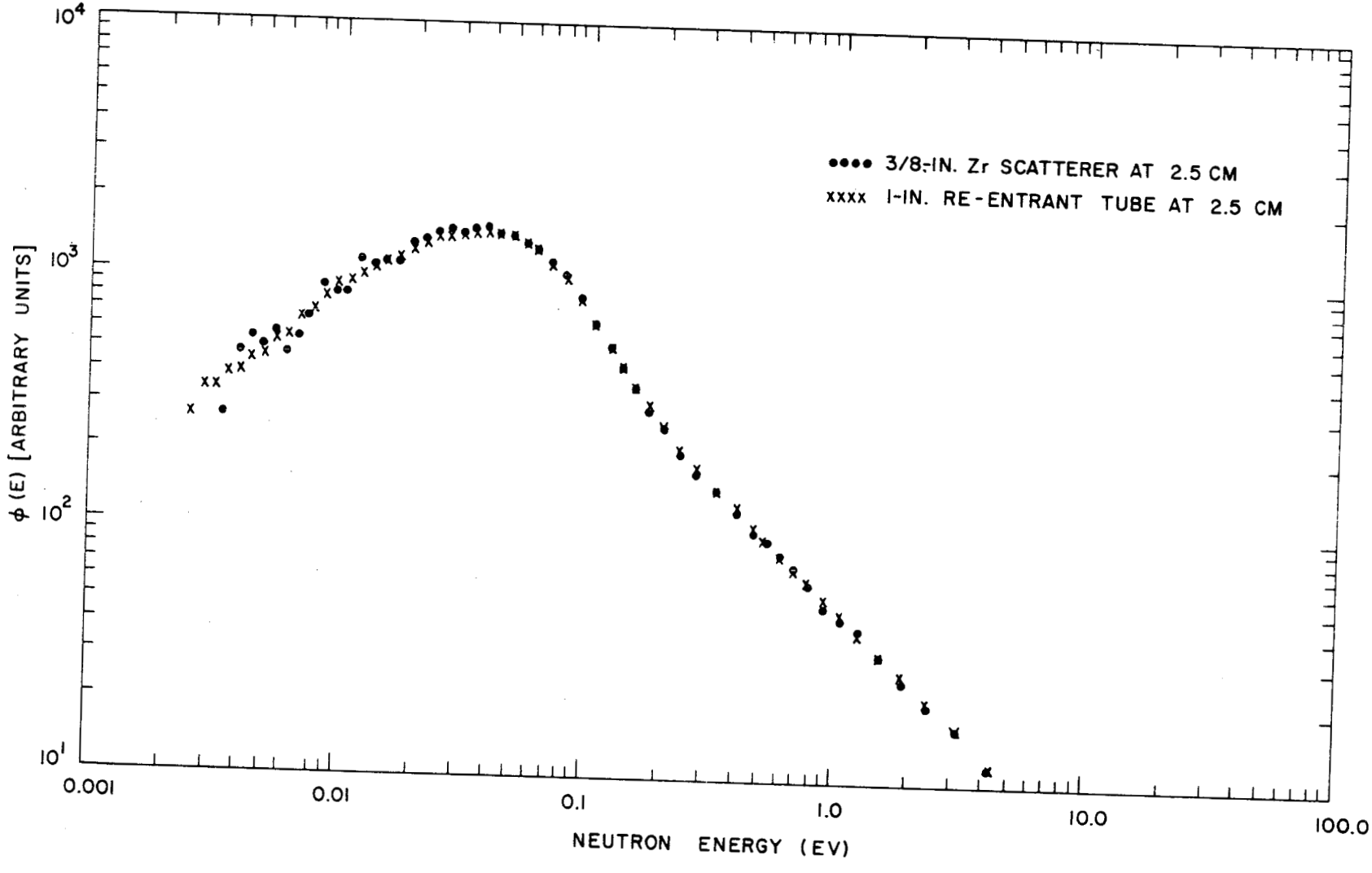

Fig. 22--Comparison of spectra measured with zirconium scatterer and with re-entrant tube at neutron flux peak in 4-in. slab

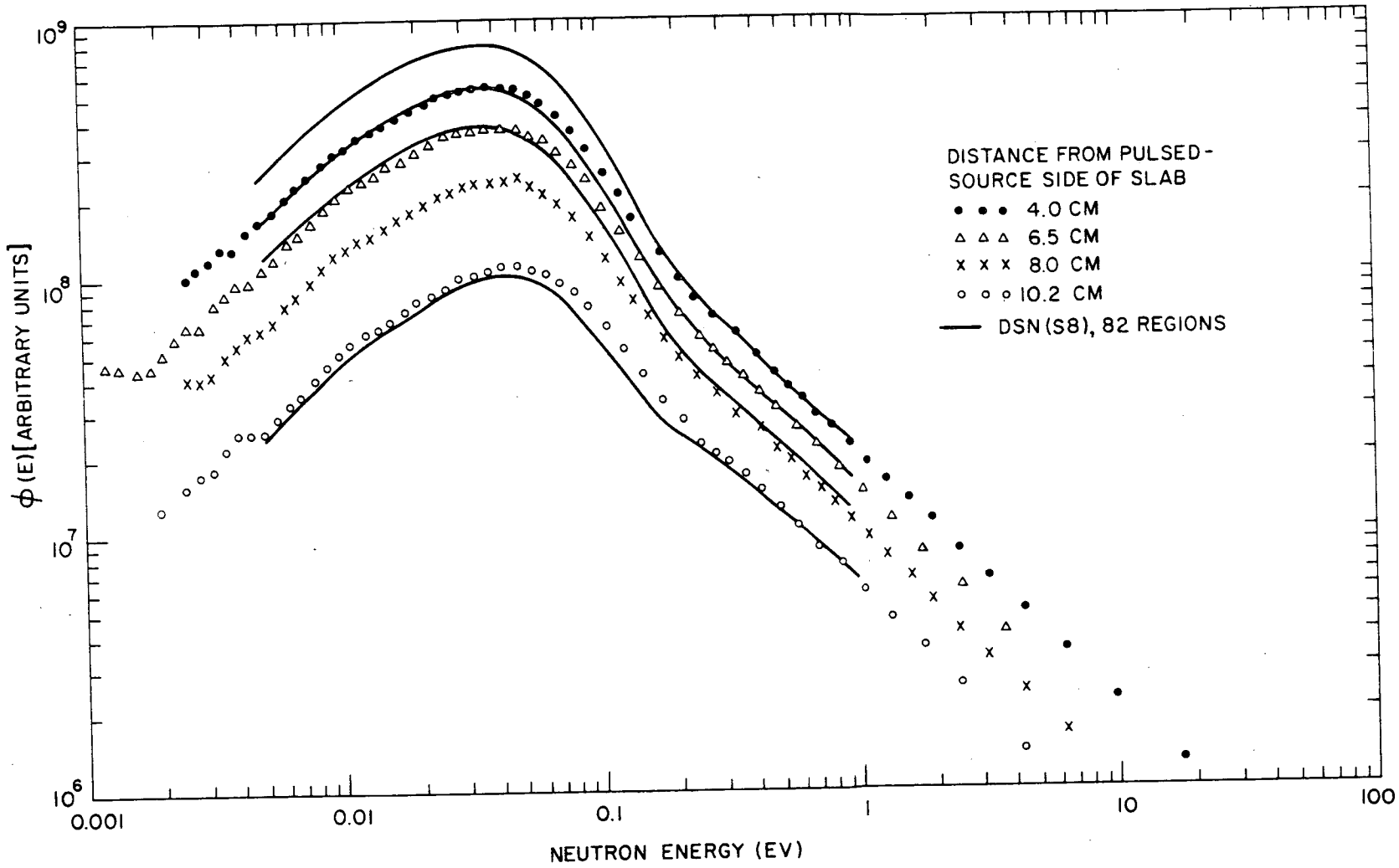

Fig. 23--Zero-degree angular-flux spectra in a 4-in. slab at 4, 6.5, 8, and 10.2 cm

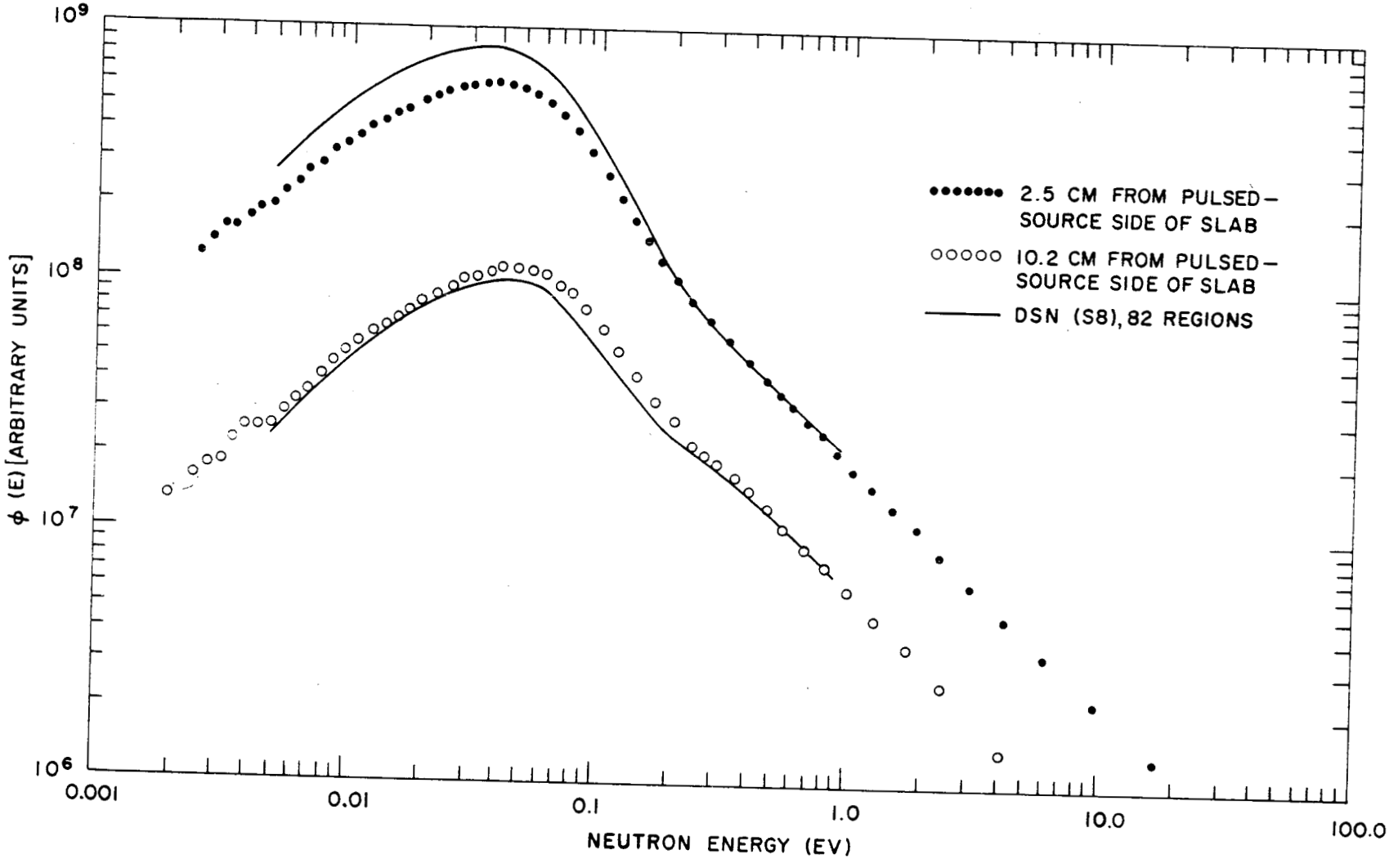

Fig. 24--Zero-degree angular-flux spectra in a 4-in. slab at 2.5 and 10.2 cm

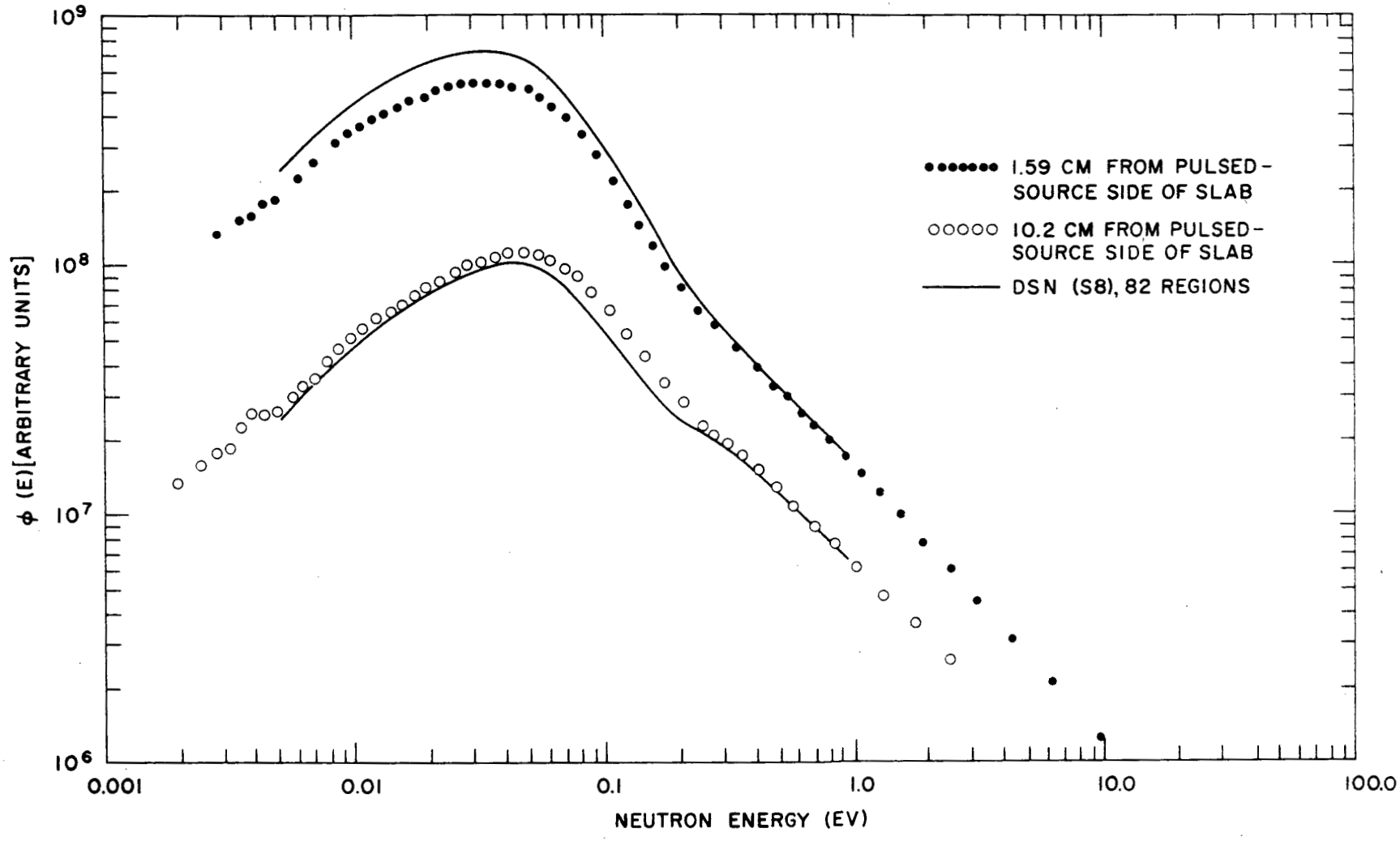

Fig. 25--Zero-degree angular-flux spectra in a 4-in. slab at 1.59 and 10.2 cm

comparisons, it is expected that the discrepancies will also be reduced by inclusions of higher-order terms in the scattering matrices and by refinements in the DSN approximations. What should be stressed here is the calculational precision which has been necessary for understanding this typical experiment in the transport of essentially reactor spectrum neutrons.

In Subsection 4.3, more detail will be given on what contribution has been made by each change in the transport calculation. In general, it appears that accurate predictions of spectra near discontinuities in water-reactor experiments must be accomplished by DSN (or its equivalent) working in at least the S8 mode with inclusion of a very fine spatial mesh and higher-order (P_2, P_3) terms in the scattering matrix for the bound-hydrogen moderator. As will be made apparent in Section V, the sensitivity to these effects is reduced somewhat by using a distributed neutron source rather than an external source, but large transport effects are still present for multiplying systems.

4.2. TWO-INCH-THICK SLAB

Measurements of neutron spectra were made in borated water in a slab with a critical dimension of 2 in., an 18-in. width, and an 18-in. height. A lead wall was inserted between the slab and the pulsed neutron source as shown in Fig. 14. The H_3BO_3 concentration used was the standard 43.7 g per liter of solution. To specify the epithermal spatial source distribution for transport theory, cadmium-covered indium foils were used to measure the flux in the 2-in. slab with boric acid solutions. The results of these measurements are shown in Fig. 26.

The neutron spectra measured in this slab consisted of a scalar flux at the center, a zero-degree angular flux at the center, and a zero-degree surface leakage. The results of these measurements are shown in Figs. 27 and 28 together with DSN (S8) calculations for comparison. Here again, the relative intensity between the zero-degree angular measurements was preserved and the theoretical calculation was normalized at 1 ev for the surface leakage only. Once again, the relative intensity predicted by theory agrees with experimental measurements. However, the spectral indices between 1 ev and 0.025 ev show better agreement than did the comparable indices for the 4-in. slab. It should be noted that the surface-leakage measurements for the 2-in. slab (Fig. 28) are in much better agreement than those in the 4-in. slab (Fig. 23). The two slabs differed in the boundary termination in the following way. The 2-in. aluminum tank was terminated internally with heavily borated polyethylene, whereas the 4-in. aluminum tank was terminated externally with cadmium. It is believed that inclusion of the aluminum wall in the DSN calculations for the 4-in. tank will correct the discrepancy in the surface leakage. Further comparison awaits the new improvements being introduced into DSN.

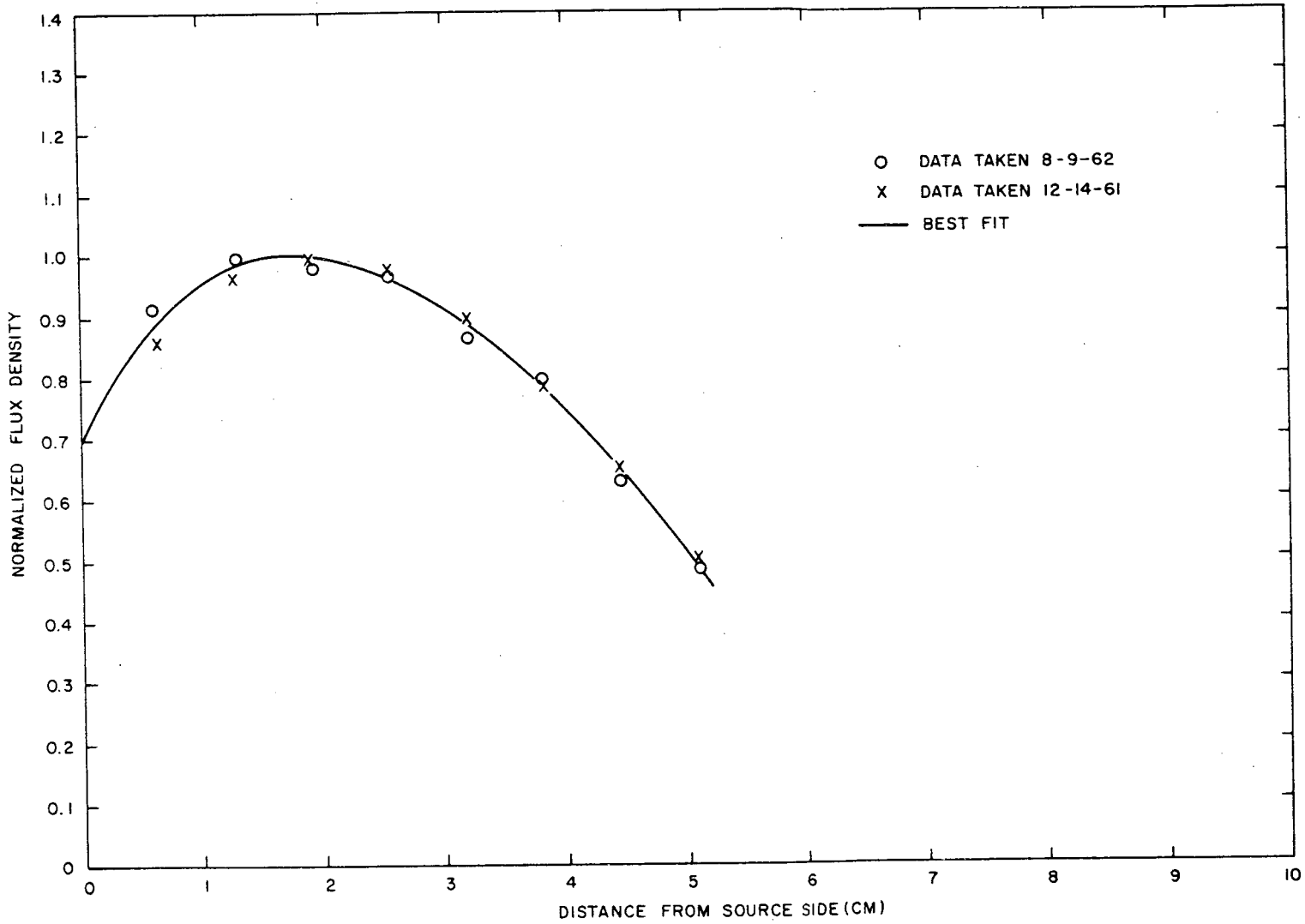

Fig. 26--Cadmium-covered-indium flux plots in a 2-in. slab

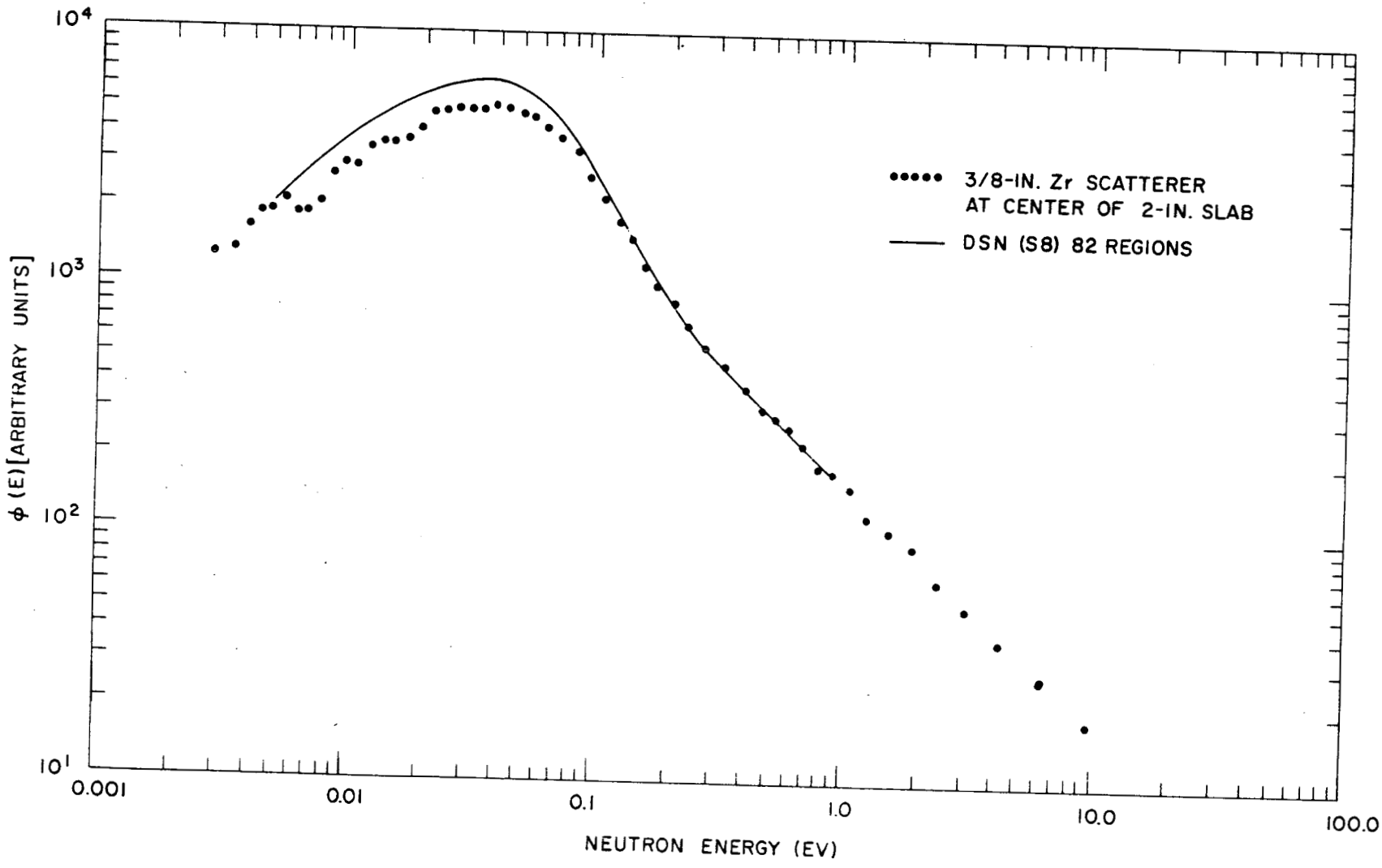

Fig. 27--Scalar neutron spectrum at center of 2-in. slab

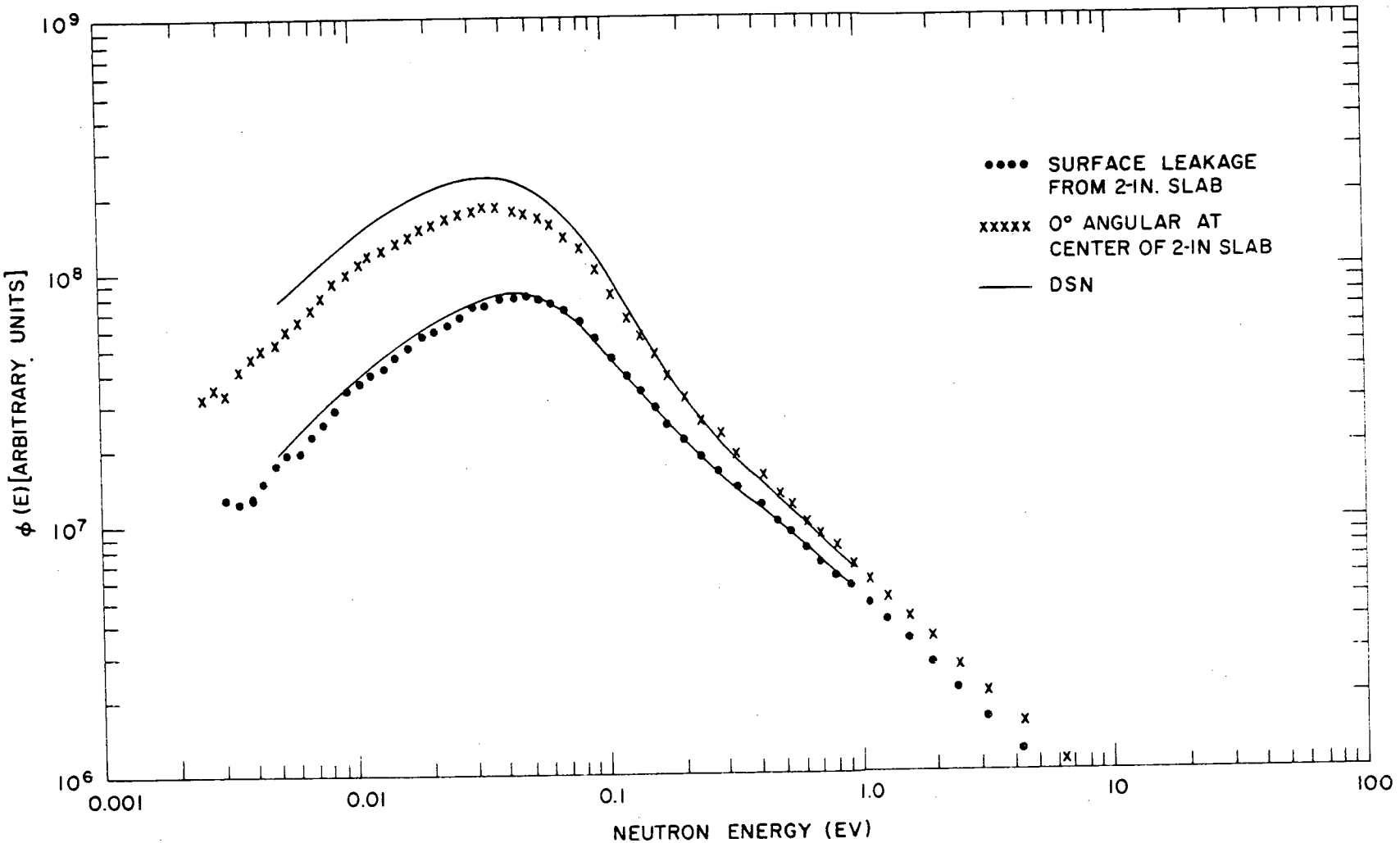

Fig. 28--Zero-degree angular-flux spectra at center and surface of 2-in. slab

In general, the studies with the 2-in. slab indicate the extreme sensitivity to the refinements in the transport-theory analysis, as was the case for the 4-in. slab.

4.3. FINITE-MEDIUM (NONMULTIPLYING) ANALYSIS

The analysis of finite, one-dimensional slab measurements has been performed with the codes THERMOS (integral transport theory) and DSN (differential transport theory). These measurements were made in a water solution poisoned with boric acid, which is typical and experimentally convenient. In both codes, the source term was calculated from the measured epicadmium flux plot with the energy dependence given by the free-gas scattering law. THERMOS scattering kernels are generated by a library program for the free-gas model and by a special code written for the Nelkin bound-hydrogen kernel,[4] whereas DSN uses any desired kernel,* group-averaged over some suitable spectrum.

Both codes have been modified to include anisotropic scattering. These modifications are a diagonal P_1 component of the scattering kernel for THERMOS and a full P_1 kernel and, later, P_2 and P_3 kernels for DSN. The modifications to THERMOS are described in detail in Section IX; those to DSN are given in Ref. 9. The local version of DSN was further modified to include a P_1 component of the source.

Investigations of the spatial convergence of the codes were first made with the original isotropic version of THERMOS, and it was found that an isotropic 50-region solution gave results not significantly different from a 20-region solution. The original 20-region THERMOS was then expanded to include anisotropic scattering and source terms, on the assumption that 20 regions were sufficient to describe the problem fully. The conclusion that spatial convergence had been reached was unfounded, as studies with DSN have indicated. In the DSN studies, because of the differential nature of the method, enough machine memory was available to permit an examination of the effects on the solution of an increased number of regions with anisotropic (P_1) scattering and source. Significant improvements in the spectra were observed when a larger number of regions (~80 rather than 20) was used. Since the anisotropic versions of DSN and THERMOS agree for 20 regions, it must be concluded that the solution for the anisotropic problem is considerably different from that for the isotropic one and requires increased spatial detail for convergence. Calculations for the case of a boundary-free exponential-source distribution[10] indicate the need for including P_2 and P_3 components of the scattering kernel.

*Some available kernel-generating codes are KERNEL, ISGM-GAS, and KRYOS-II (described in Ref. 5); ROBESPIERRE (described in Ref. 6); THERMIDOR (described in Ref. 7); and SUMMIT (described in Ref. 8).

Numerical experiments with the slab calculations have led to some important operational conclusions: (1) Measurements must be made in a reproducibly poisoned solution, since the expense of the calculations makes it undesirable to calculate spectra at many positions within the slab for different poison concentrations; (2) the epicadmium flux plot, which determines the source shape, must be measured with good accuracy and in considerable detail, since quite small variations in the shape can introduce fairly large changes in the spectrum near the region of variation.

The latest calculations, which were compared with experimental results in Subsections 4. 1 and 4. 2, have been made with DSN, using many regions (~80 for a 4-in., poisoned boric acid slab), full P_1 scattering kernel, and P_1 source. The next step will be the inclusion of the P_2 and P_3 components of the scattering kernel. The effect of the transverse buckling may be accounted for by a fictitious absorber (Σ_a (E) = D(E) $B^2_{transverse}$) when the discrepancies between theory and experiment become sufficiently small for this effect, which is of the order of a few per cent, to be noticeable.

In Fig. 29, the effects of the anisotropic (P_1) components of the scattering kernel and the distributed source on the surface leakage are shown. The calculation is for a 2-in. slab of the standard (43. 7 g per liter) H_3BO_3 solution. Twenty-three energy groups and 47 regions were used in the DSN calculation. On the curve, A indicates anisotropic and I isotropic; the letters before and after the dash refer to the scattering and the source, respectively. (A-I, for example, means anisotropic scattering with isotropic source.) The curve is typical of the zero-degree angular spectra; smaller effects are observed in the scalar fluxes, particularly in the region of the flux peak.

It can be seen that the anisotropic component of the scattering kernel is by far the most important refinement to the isotropic calculation, accounting for a deviation of about 30% from the isotropic solution at 0. 9 ev. The anisotropic source component has a smaller effect, principally in the region of transition to a 1/E spectrum.

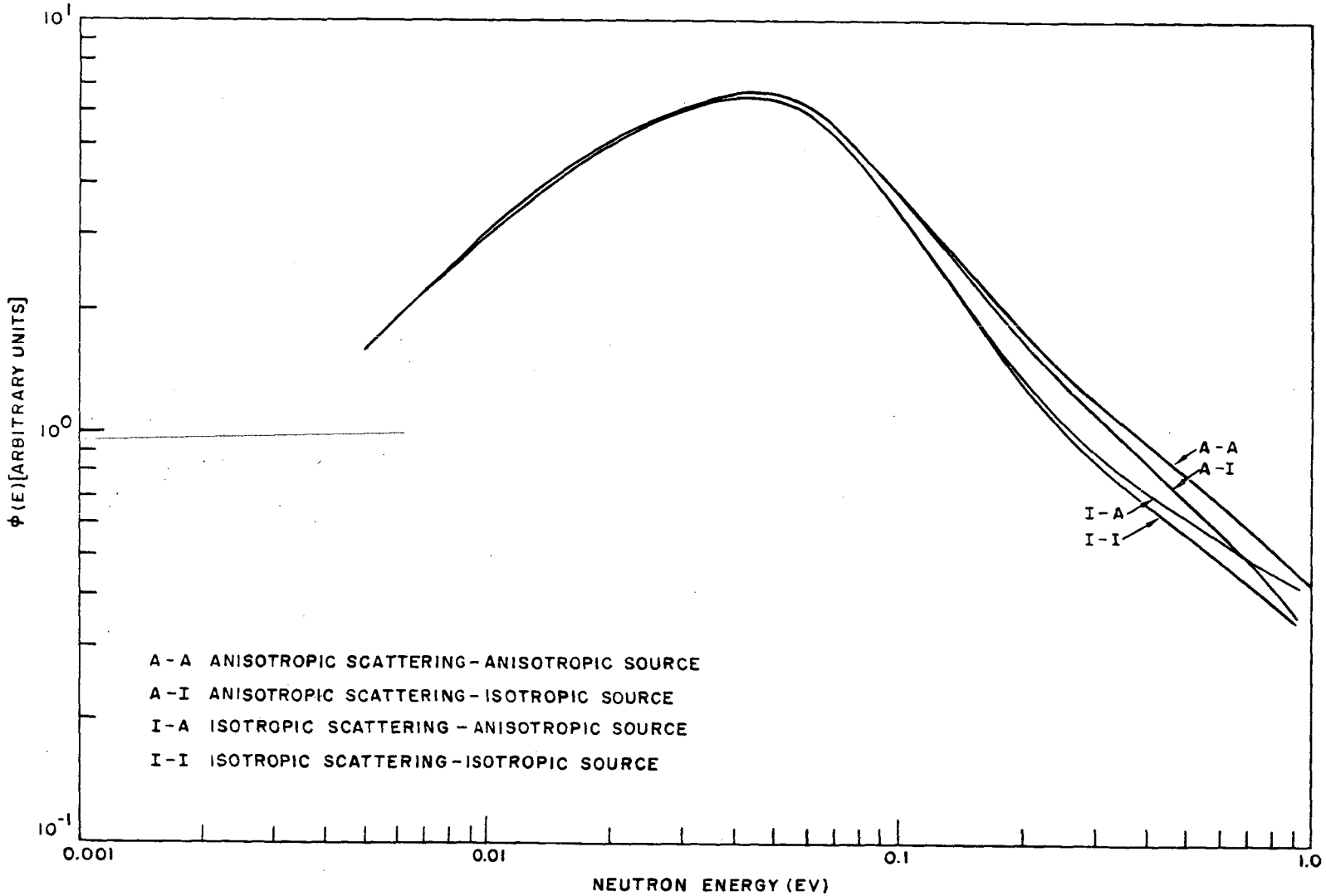

Fig. 29--Comparison of the effects of anisotropic source and scattering on surface leakage from a 4-in. slab

V. SPATIALLY DEPENDENT, FINITE-MEDIUM SPECTRA IN MULTIPLYING ASSEMBLIES

5.1. EXPERIMENTAL

In designing experiments of infinite- or finite-medium neutron spectra in nonmultiplying assemblies, it has not usually been possible to obtain a spatially flat or slowly varying neutron-flux distribution. Instead, quite strong flux gradients have often existed in the assemblies. It is known that under certain geometrical conditions and with high absorption introduced into the assemblies, the effects of these gradients can be rendered insignificant. However, in many other circumstances the spectral effects due to strong gradients are very large and hard to calculate (as was demonstrated in Section IV). The primary purpose of the multiplying-assembly project has been to construct an environment more nearly free of the large spatial effects induced by the external source. Spectra could then be measured under distributed source conditions and compared with one-dimensional transport-theory calculations. A secondary objective was to study neutron lifetime, or die-away time, as a function of loading of the multiplying assembly and to attempt to correlate this with the multiplication constant for the system. A third purpose was to determine the feasibility of obtaining spectral measurements (eventually within cell lattices) by time-of-flight techniques in a system with a relatively long neutron die-away time.

The multiplying assembly developed for this work was made by accurately spacing thin plates of uranium-aluminum alloy 1/8 in. apart in a water tank. The assembly was designed for the study (initially) of bare, homogeneously poisoned systems. An over-all view of the assembly is shown in Fig. 30. An axial glory hole traversing the assembly is lined up with the pulsed neutron source to permit extraction, by conventional techniques, of the beam of neutrons for neutron-spectrum measurements. For the pulsed die-away experiments, a small U^{235} fission detector (1/4-in. diameter and 1/4-in. active length) was remotely positioned in this hole at several locations through the core. Figure 31 is a top view of the geometrical arrangement. The electron beam from the Linac is directed into the assembly from the left. The core is surrounded by a 6-in.-thick lead wall to permit access to the work and loading areas after the assembly has been run at high power levels (~100 w). Figure 9 in Section III is a diagram of the low-background neutron cave which, in turn, surrounds the lead-shielded core.

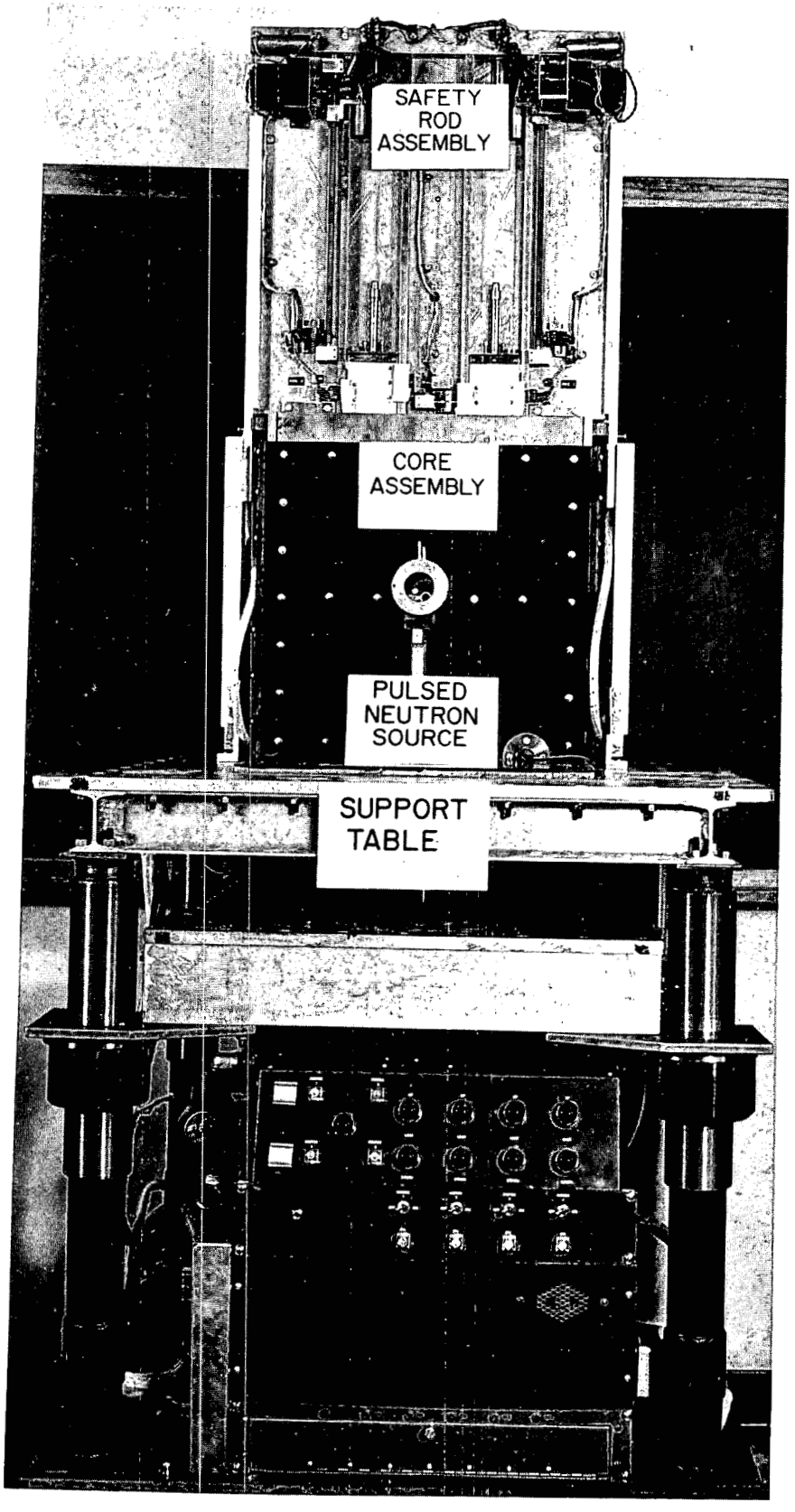

Fig. 30--Over-all view of subcritical assembly

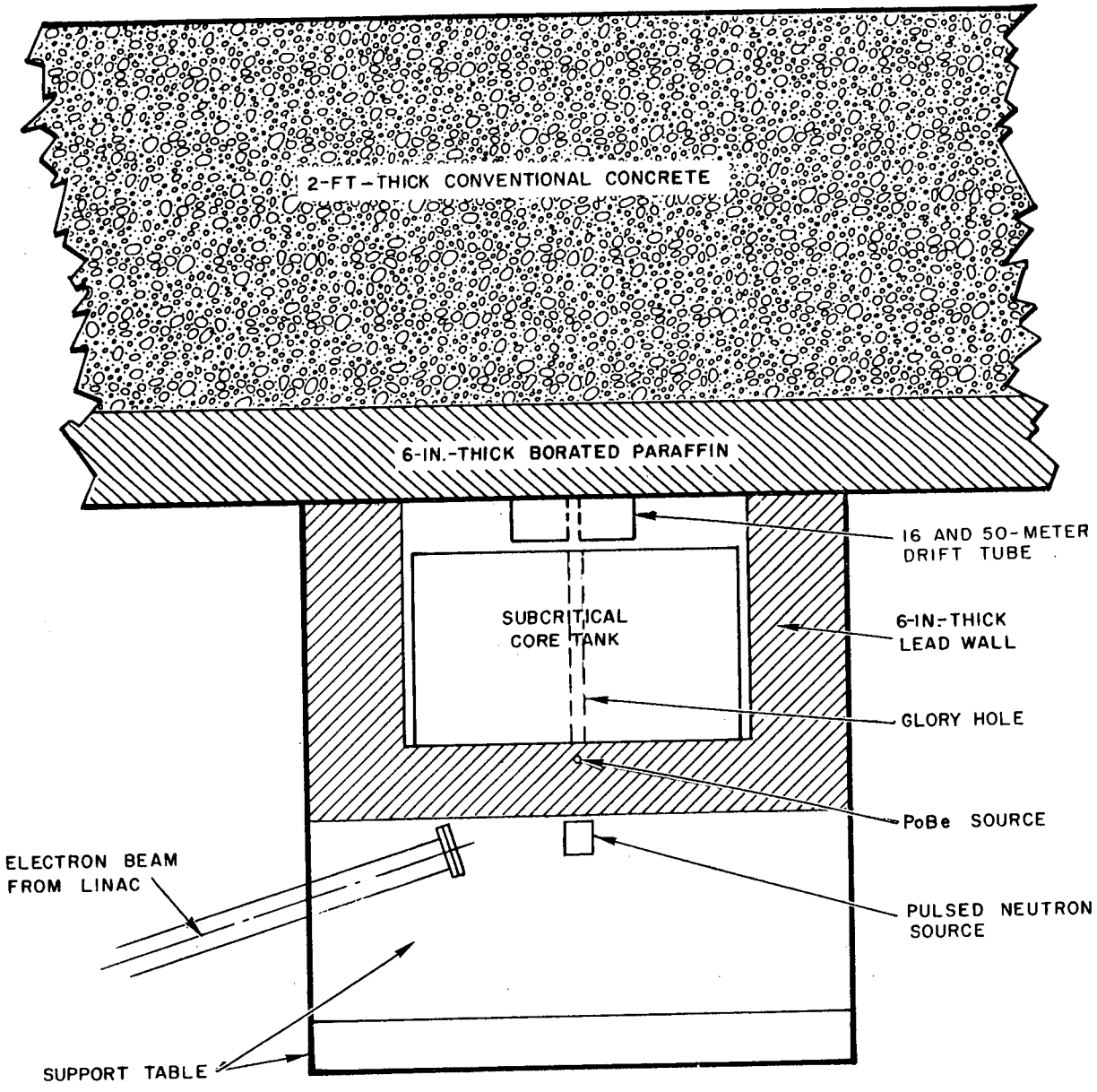

Fig. 31--Plan view of geometrical arrangement for multiplying-assembly measurements

During the loading of the plates into the assembly, typical inverse-multiplication curves were plotted by means of four different neutron-detector channels. Several of these curves are shown in Fig. 32. These curves have been extrapolated from the final loading to the critical mass. The experimental value agrees to within 2% of the calculated mass.

5. 1. 1. Flux-distribution Measurements

Spatial neutron distributions were obtained in the subcritical assembly to provide the input spatial source necessary for calculating the thermal space problem by transport theory.

Figure 33 shows the thermal-neutron-flux distribution in the axial dimension measured with a U^{235} fission counter for the final loading. The neutron source was located at the left. Data were obtained with and without the lead shield wall in place. Indium-foil flux plots were made with the shield wall in place for purposes of comparison. The average flux distribution for the assembly was also obtained with cadmium-covered indium foils (~1. 4 ev), bare indium foils (thermal), and sulfur foils (~3 Mev). The distributions obtained are close to a normal-mode distribution. Hence, the multiplying assembly accomplished the desired result, namely, that of redistributing both the thermal and epithermal neutrons spatially in approximately the normal-mode distribution. The three foil mappings are shown in Fig. 34. This figure also illustrates the effect of having the 4-in. lead wall placed next to the pulsed-source side of the assembly. The epithermal flux shows a definite perturbation owing to the reflection of fast neutrons from the lead wall. The shape of the thermal flux is probably not as strongly affected by the fast-neutron reflection as by the thermally black borated polyethylene forming the boundary of the assembly. As can be seen from Fig. 34, except for the source-perturbed side, the thermal flux follows the epicadmium flux. The fast-neutron flux does not appear to be nearly as perturbed by reflected neutrons as the epicadmium flux, but does exhibit a large extrapolation distance on the side opposite the pulsed source. The effect of the reflected neutrons has been detected by die-away measurements, which indicate that the lead wall can increase the die-away time by as much as 50%. This points up the extreme difficulty of obtaining a truly bare multiplying assembly.

5. 1. 2. Measurement of Decay Constants

From the time-dependent neutron decay, one can determine the die-away time of the fundamental mode and the higher harmonics. A typical decay curve is shown for the last loading in Fig. 35. The time-dependent spatial flux distributions were Fourier-analyzed to determine at each time point the amplitude of each mode. One essentially fits each spatial flux

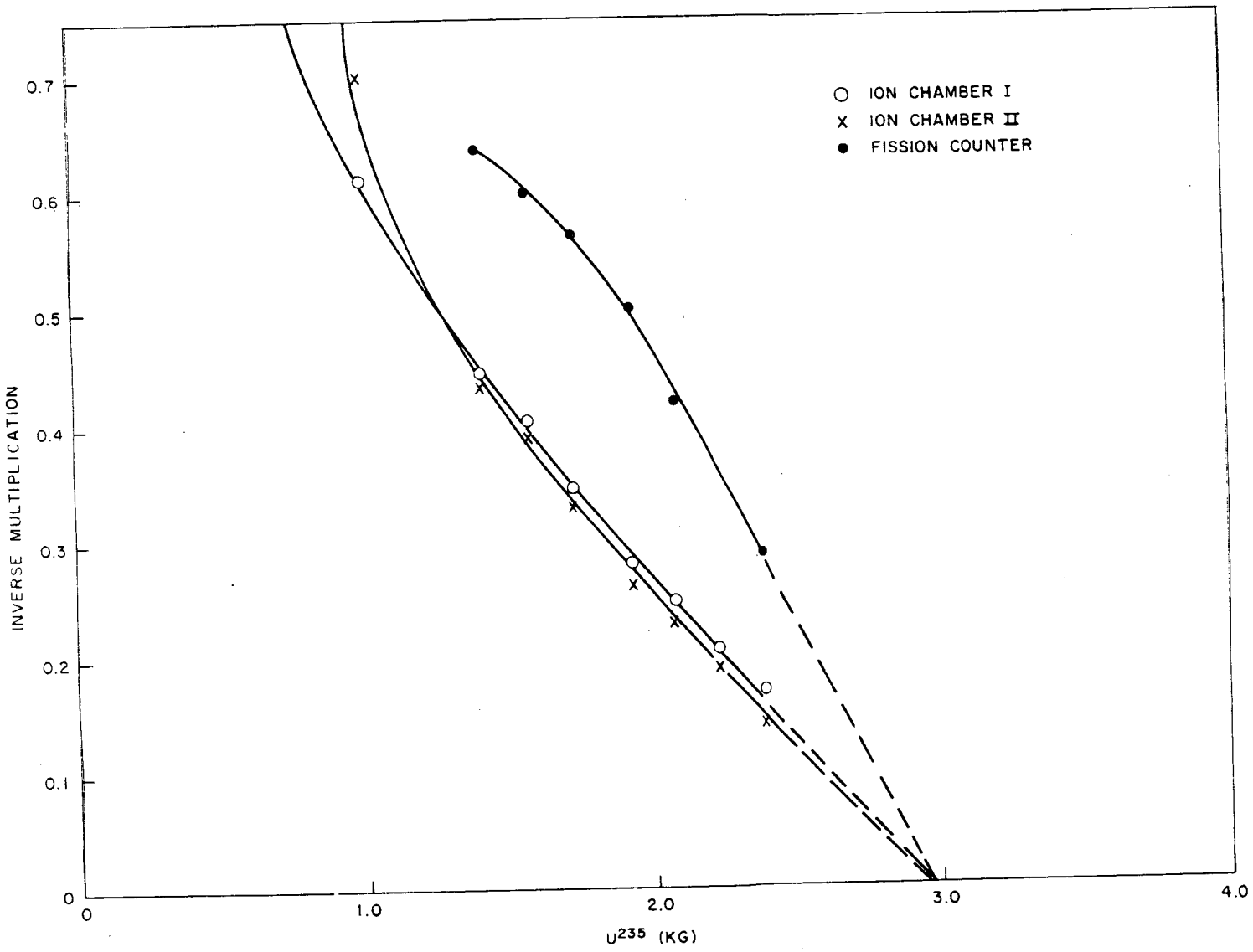

Fig. 32--Inverse multiplication versus kilograms of U^{235} in multiplying assembly

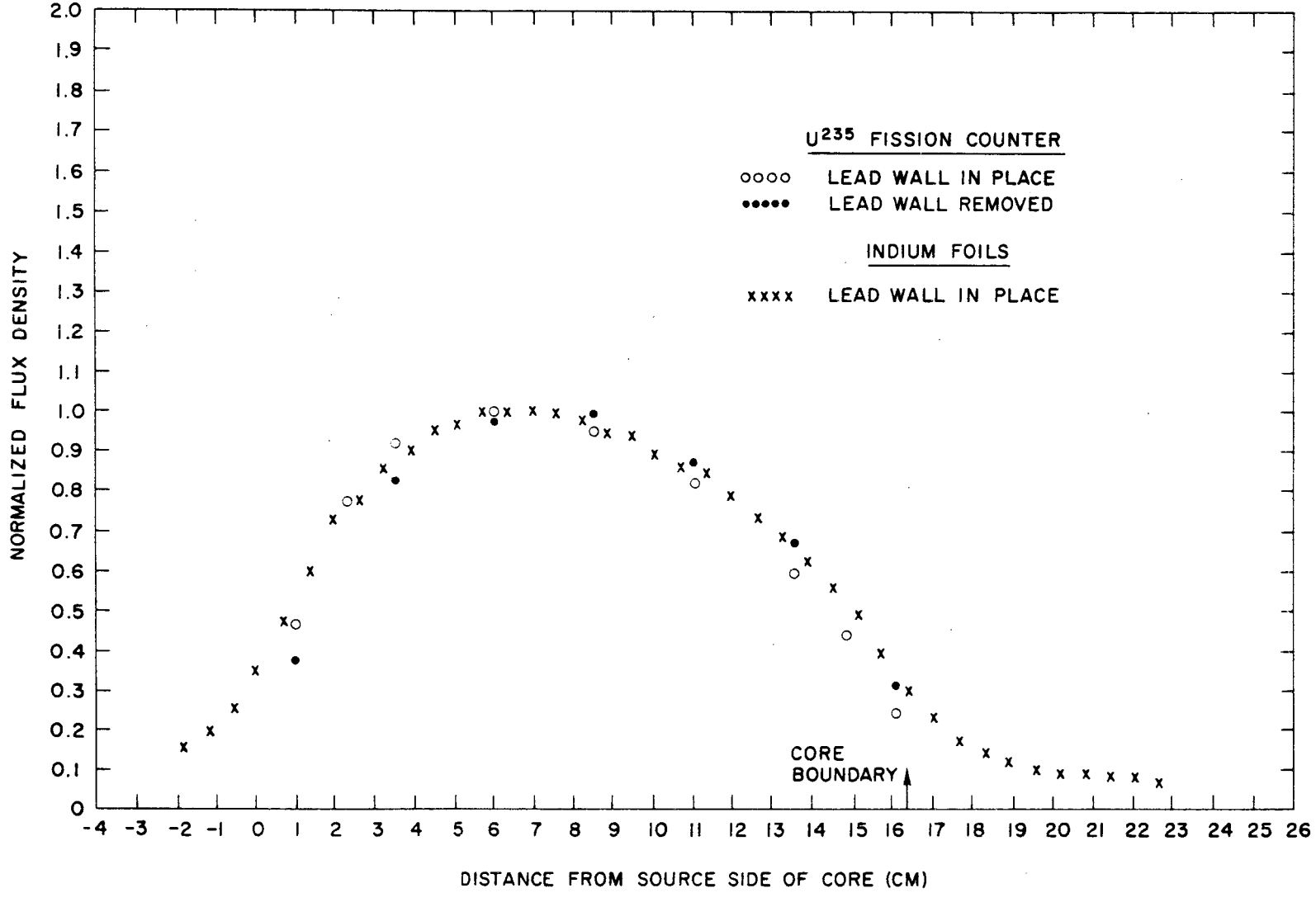

Fig. 33--Spatial flux distribution obtained using a U^{235} fission counter with and without a lead wall compared with a flux plot obtained using bare indium (thermal) foils

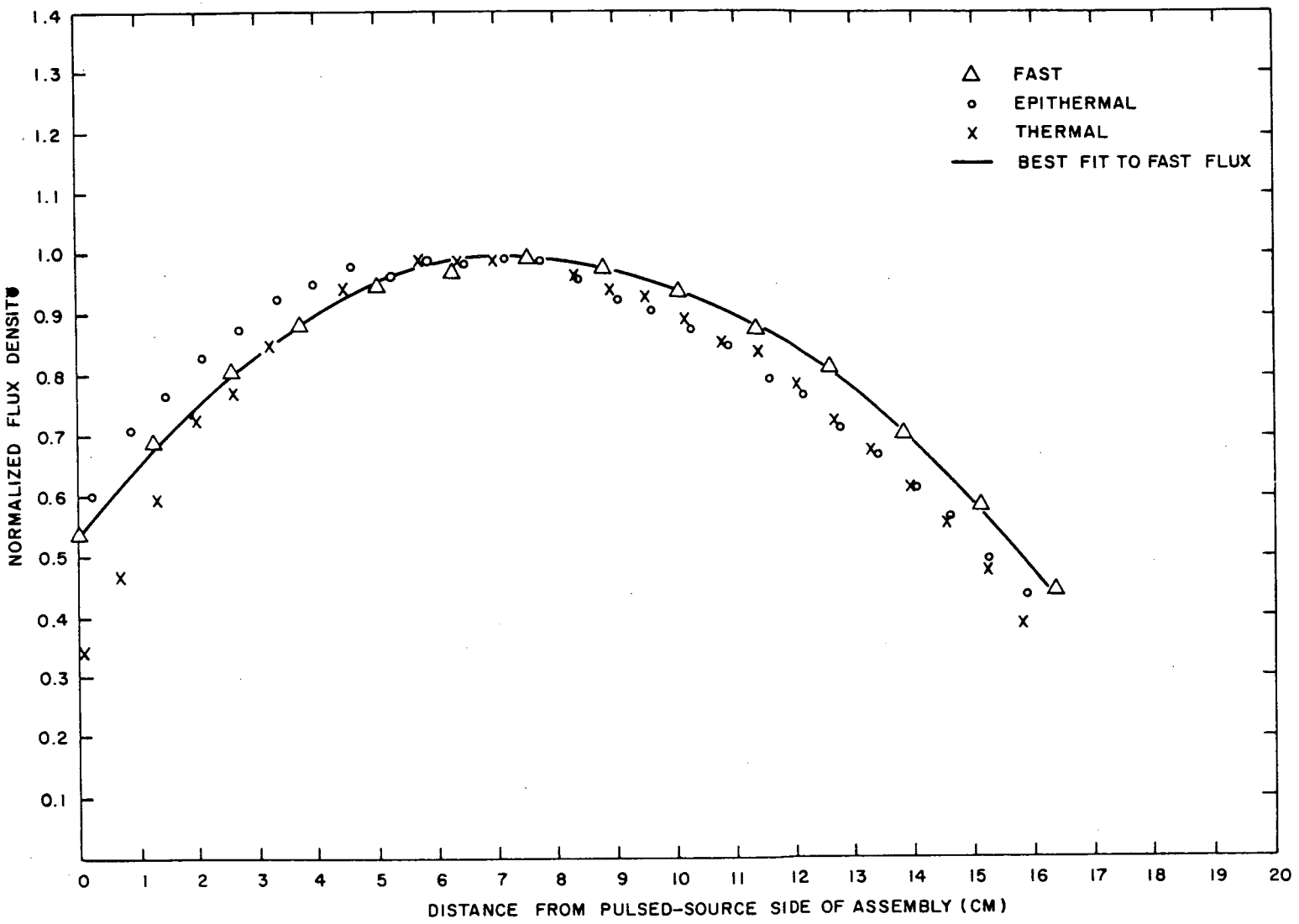

Fig. 34-- Thermal, epithermal, and fast neutron spatial distribution in the subcritical assembly

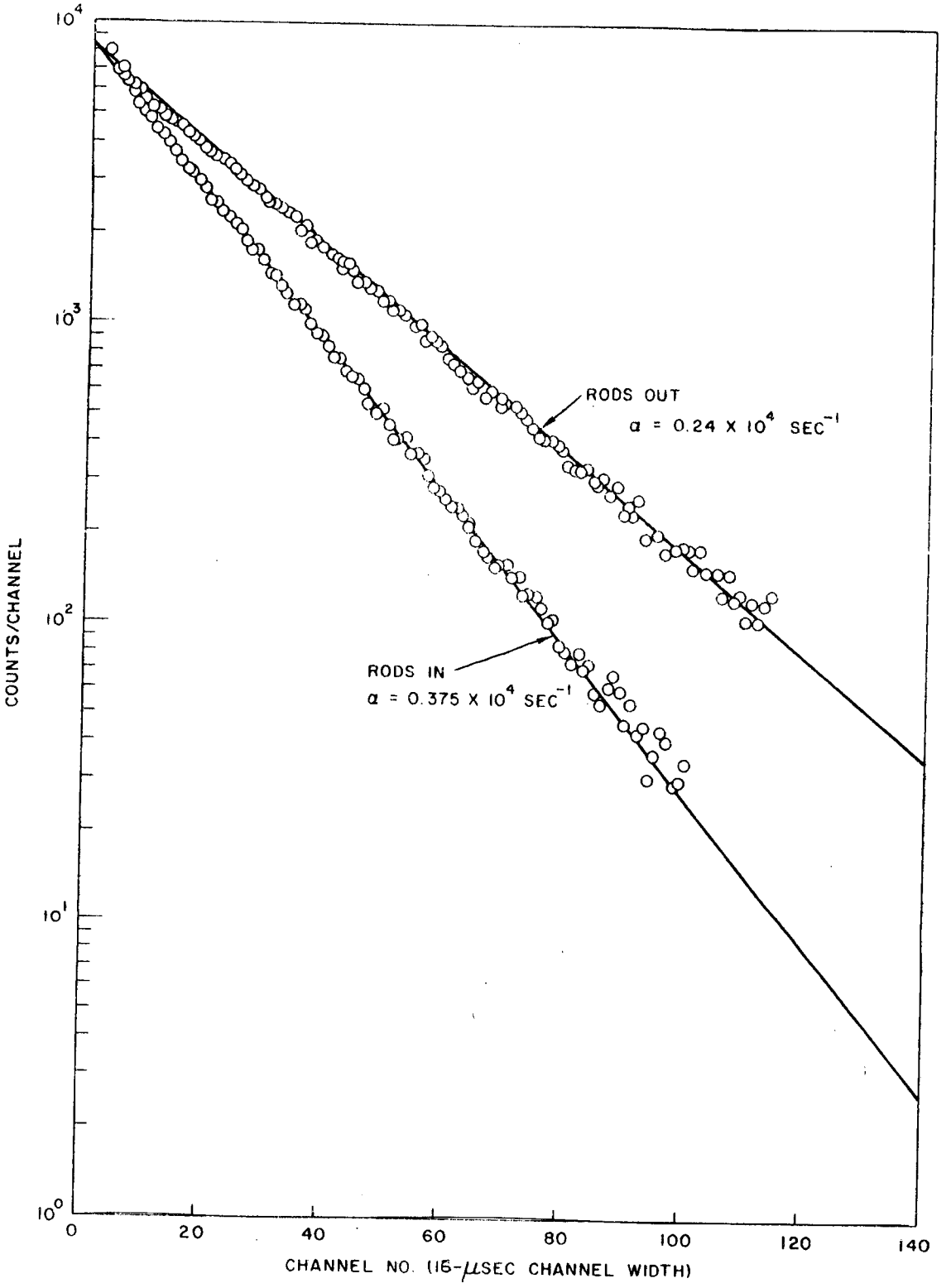

Fig. 35--Typical decay plot of thermal neutrons in subcritical assembly

plot with

$$\phi(X) = \sum_n A_n \sin \frac{n\pi X}{a} ,$$

where a includes the extrapolation length. It was found that the fundamental mode decays with a 409-μsec die-away time, while the second harmonic has about a 40-μsec die-away time. The ratio of the first to the second is much higher than would be obtained for a nonmultiplying system. The reason for this is that the effective multiplication constant for the second harmonic is still very small, signifying that harmonic-mode suppression in a multiplying system is greatly improved over that in a nonmultiplying system--which makes the subcritical assembly an excellent place to study neutron spectra.

During the multiplying-assembly investigation, the time dependence of the amplitude of the fundamental mode was studied experimentally, and a build-up was noted which peaked around 20 μsec. (This has been discussed in another report.[11]) A build-up is not to be expected since the neutron density and the thermal-neutron flux are what was actually being measured with the 1/v fission detector used. Obviously, in a subcritical assembly the total neutron density can only decrease with time. Experiments performed with and without the lead shield wall surrounding the assembly indicated that this build-up could be caused by the lead wall, which is essentially feeding neutrons to the assembly many microseconds after the accelerator pulse. A further discussion of the current thinking on this problem is included in Appendix I. The experimental measurements will be repeated in the near future, at which time the multiplying assembly will be taken critical and a complete study of the assembly will be made in as nearly a bare configuration as possible, since a fast-neutron reflection from the lead shield surrounding the core is obviously important. Flux traverses in the axial direction of the subcritical core were taken at each loading in the approach to full multiplication. A U^{235} fission counter was used for these measurements. Preliminary reduction of these data indicates that for the first few loadings (i. e., when the core is very thin in the axial dimension), the modal analysis is very sensitive to both extrapolation lengths and the number of harmonics used to reduce the data. Procedures for calculating the time constant for pulsed systems are under study; these will be discussed in Subsection 5. 2.

5. 1. 3. Spectra

A scalar neutron spectrum was measured in the assembly for comparison with the spectrum measured in July, 1961, and with theoretical predictions. Both the infinite-medium code SPECTRUM and the transport code DSN were used to calculate spectra. The scattering kernel for DSN

included the P_1 anisotropic refinement. The results of this recent measurement are shown in Fig. 36 along with the earlier DSN calculation. Agreement with the previous data is good. Another scalar spectrum was taken in the presence of a strong gradient and compared with the DSN calculation using Nelkin's bound-hydrogen kernel. The results of this measurement are shown in Fig. 37. The scalar spectra measured in the multiplying assembly appear to be in considerably better agreement with theory than those measured in the nonmultiplying slabs. Two internal zero-degree angular spectra were also measured in the core. One was measured at 5 in. from the source side of the core (Fig. 38) and the other was measured at 5.69 in. from the source side of the core (Fig. 39). In addition to these two measurements, a leakage spectrum (Fig. 40) from the surface of the core (which was 6.43 in. thick) was measured. These three measurements appear to be in somewhat better agreement with the DSN calculation than are the results for the nonmultiplying assembly, but as yet a refined fine-mesh DSN calculation has not been performed for the former case.

The measurements appear to be perturbed for energies lower than about 0.02 ev. It is believed that this is due to a low-energy-background subtraction problem associated with the 50-m flight path. A complete study of the 50-m flight path is presently under way, and the measurements will be repeated to further check reproducibility as soon as the study is completed.

In conclusion, the subcritical assembly has been shown to be a practical tool for experimental spectral investigations and will be used extensively in the future. The assembly does not appear to be necessary for infinite-medium spectral studies, but it is highly desirable for many investigations of spatially dependent spectra, such as spectra near control rods. Predictions of spatially dependent spectra in the subcritical assembly, where a distributed epithermal source is used, seem to be more accurate than predictions of those in the one-dimensional finite-medium case, where an external point source is used.

5.2. ANALYSIS OF EXPERIMENTS

5.2.1. Decay Constant of Multiplying Assemblies

The fundamental prompt decay constant of subcritical multiplying assemblies can be calculated quite accurately if the corresponding asymptotic neutron spectrum is assumed to be separable in space and energy. In this case, without considering the delayed neutrons, the neutron-balance equation is as follows:

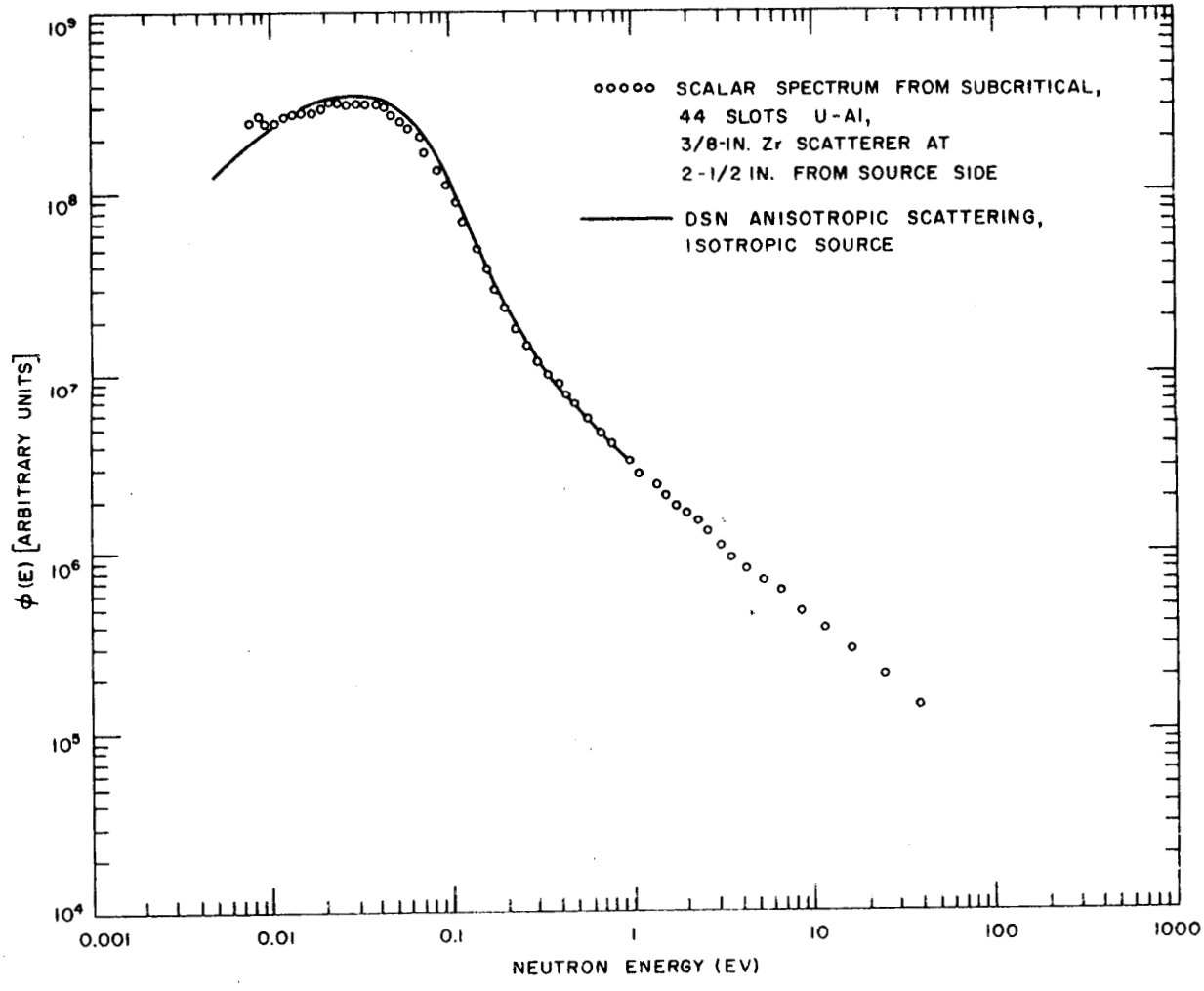

Fig. 36--Scalar neutron spectra in subcritical assembly at flux peak

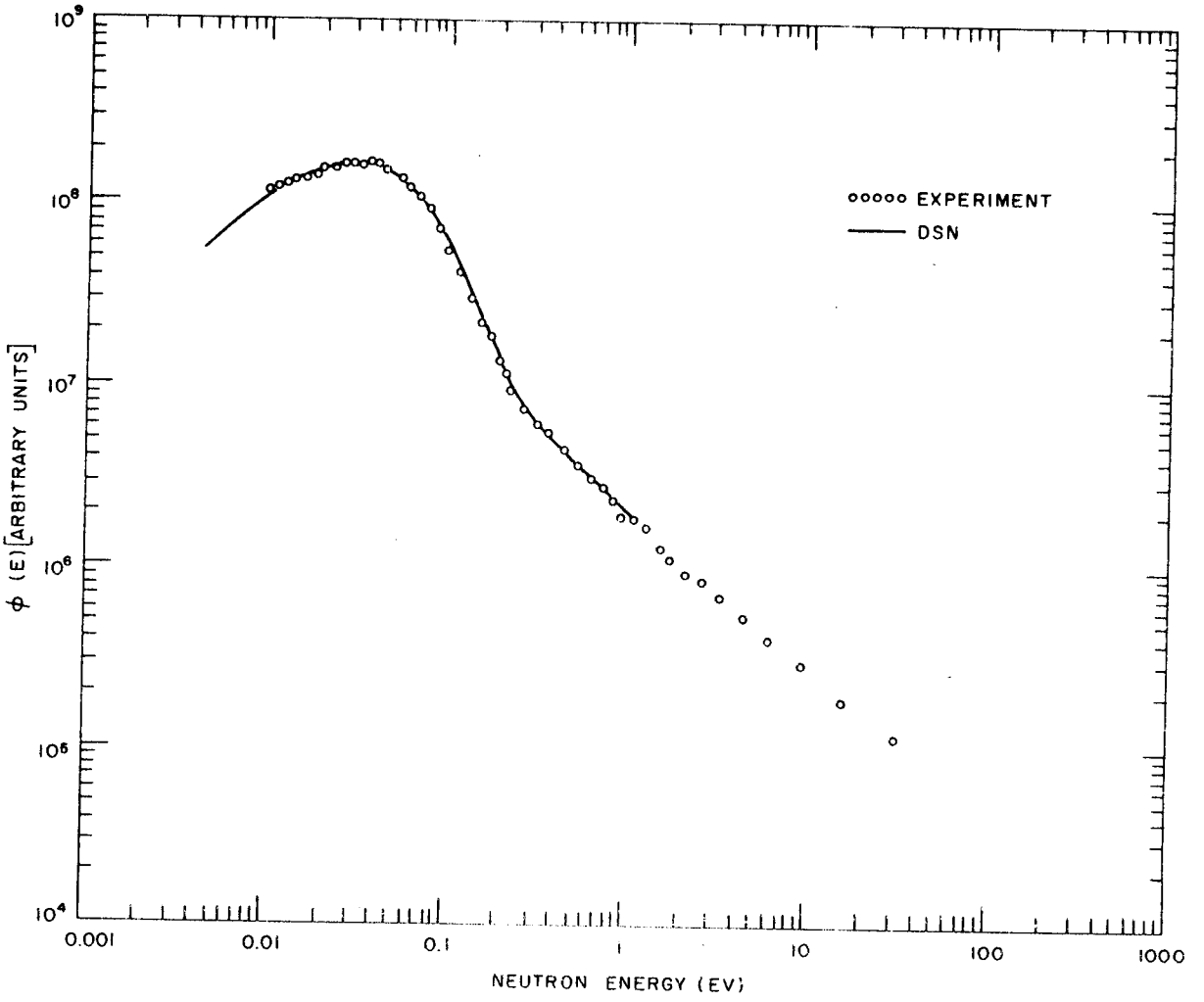

Fig. 37--Scalar neutron spectra in subcritical assembly in presence of a gradient

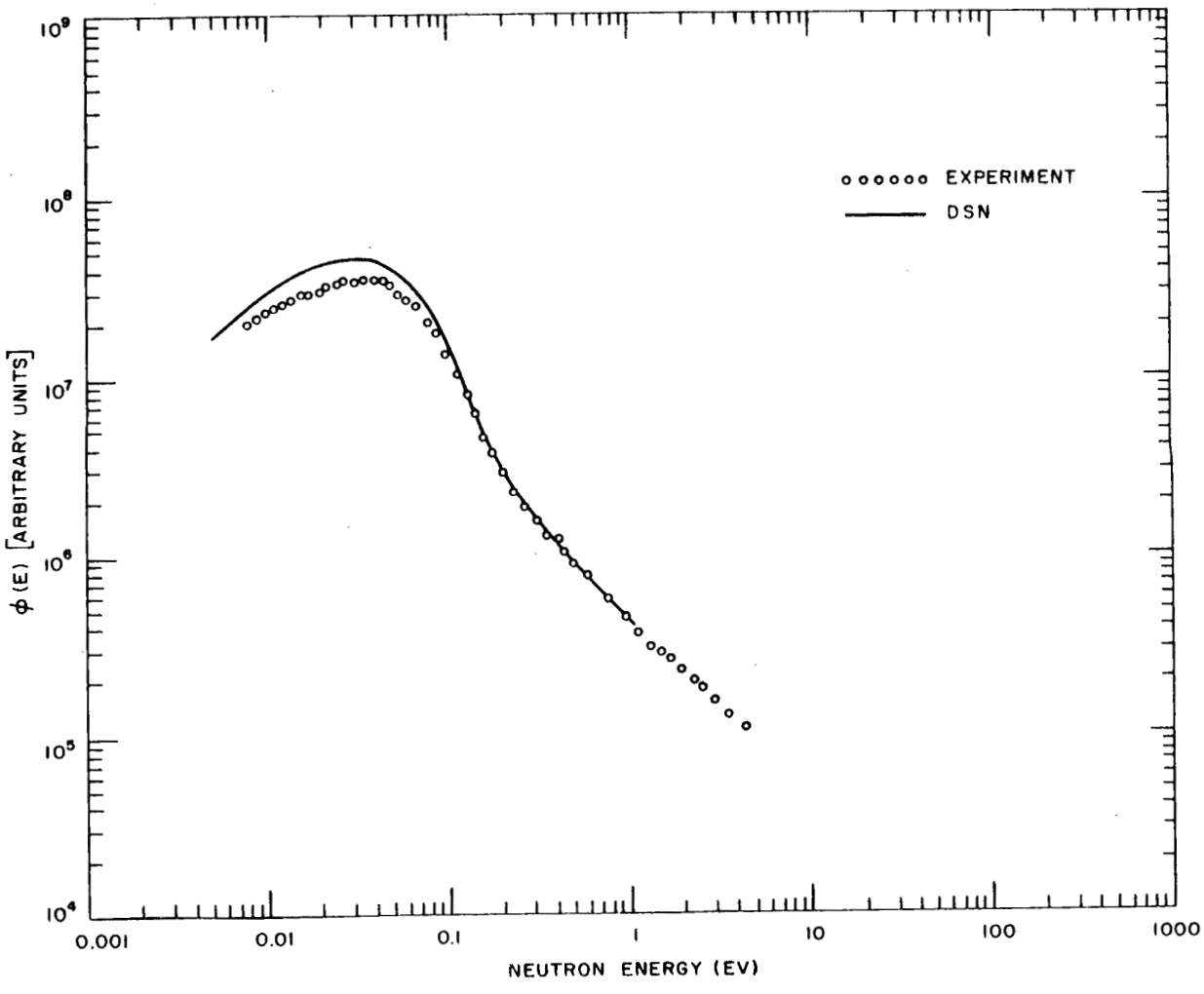

Fig. 38--Zero-degree angular flux at 5 in. in subcritical assembly

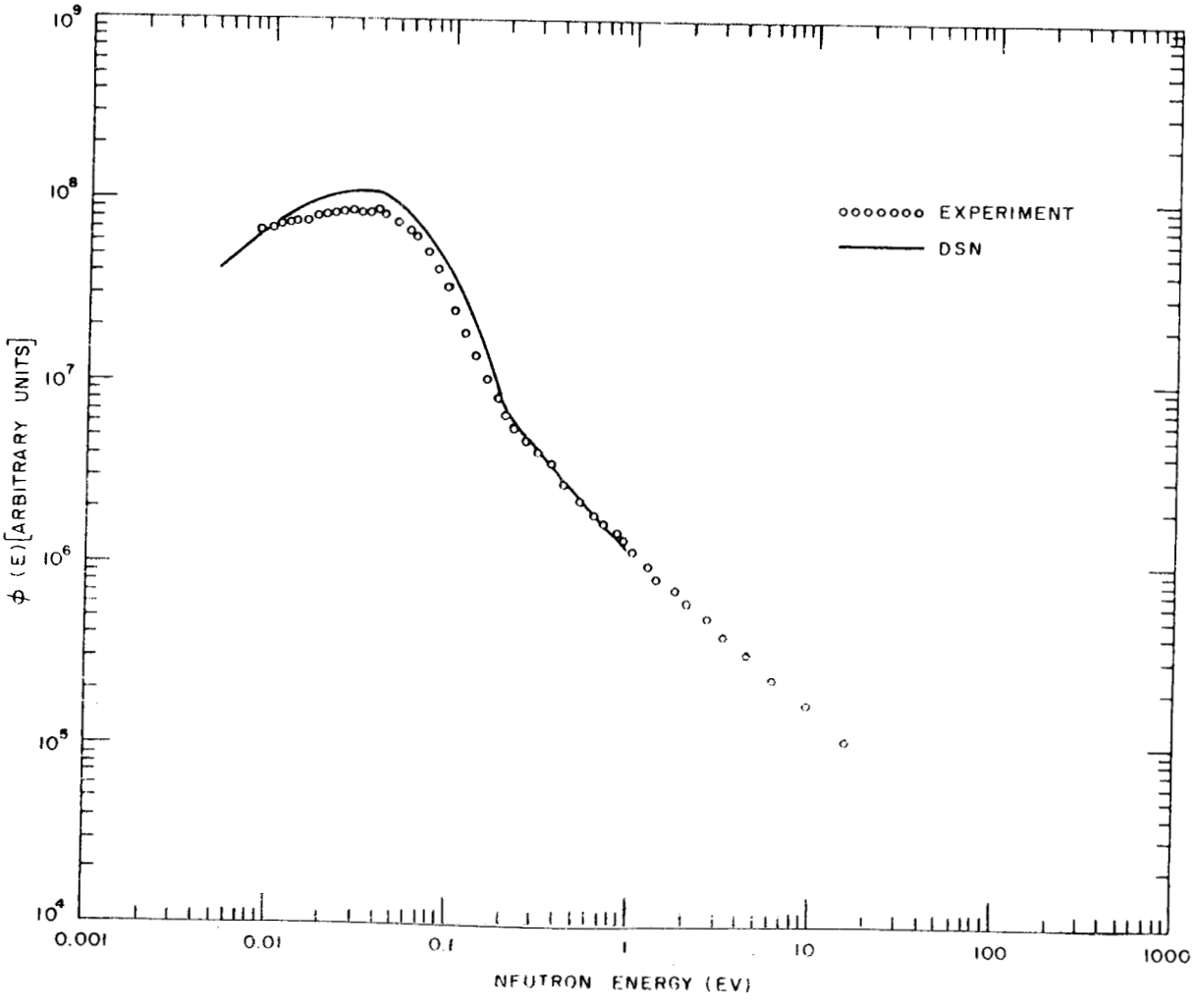

Fig. 39--Zero-degree angular flux at 5.69 in. in subcritical assembly

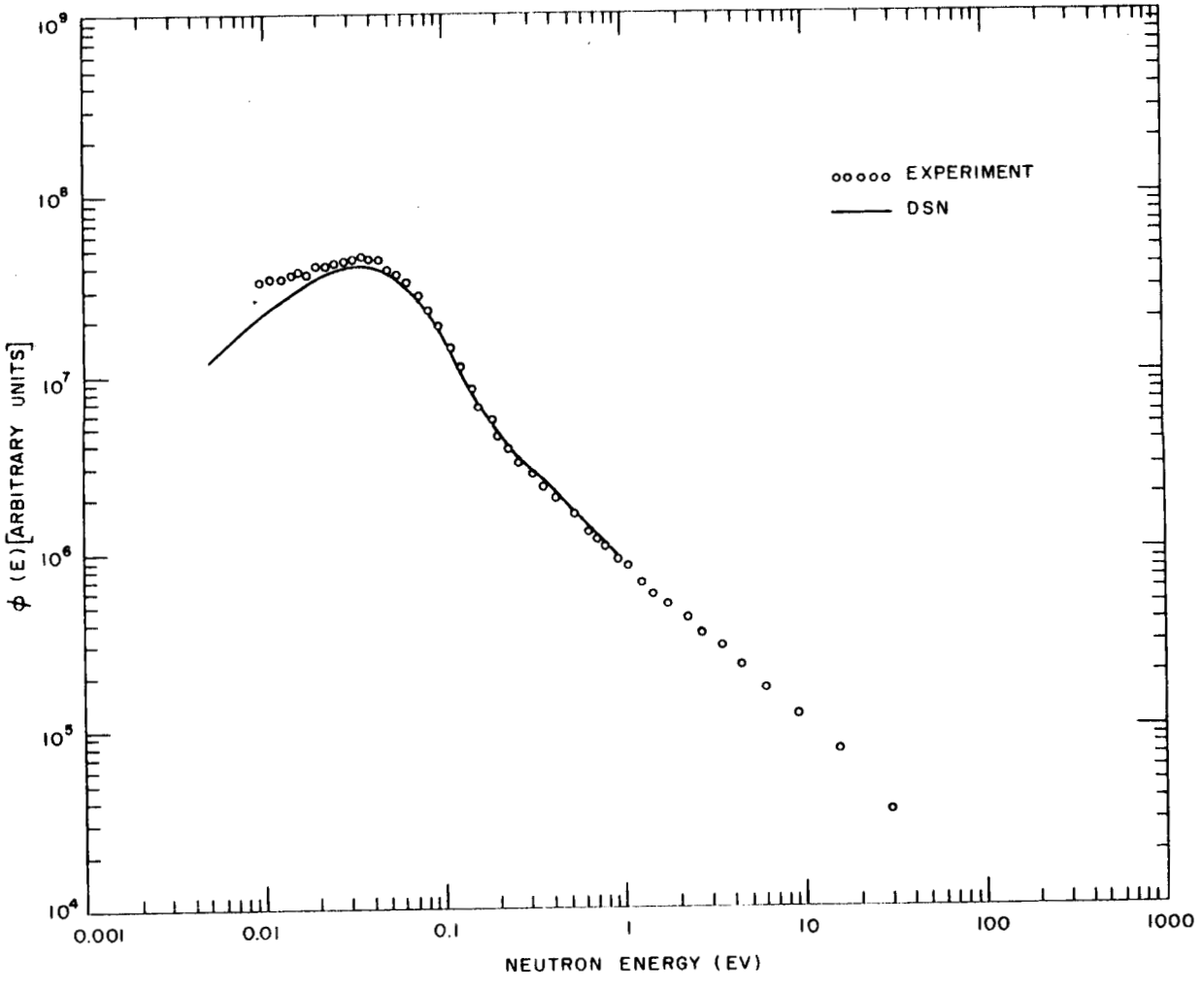

Fig. 40--Zero-degree angular flux at surface of subcritical assembly

$$\frac{\partial \Psi(E,t)}{v\partial t} = \int_0^\infty \Psi(E',t)\,\Sigma(E' \to E)\,dE' - \Psi(E)[\Sigma(E) + B^2 D(E)]$$

$$+ (1-\beta)\,f(E) \int_0^\infty \Psi(E',t)\,\Sigma_f(E')\nu dE' , \qquad (8)$$

where $f(E)$ is the normalized fission spectrum, B^2 is the geometric buckling of the assembly, $D(E)$ is a suitably computed diffusion constant yielding the correct leakage at all energies, and $\Sigma(E)$ is the total cross section. Equation (8) has an asymptotic solution of the form

$$\Psi(E,t) = e^{-\alpha t}\,\phi(E) , \qquad (9)$$

where α is the decay constant to be calculated.

Substituting (9) into (8), we obtain

$$\int_0^\infty \phi(E')[\Sigma(E' \to E) + f(E)(1-\beta)\nu\Sigma_f(E')]\,dE' = \phi(E)[\Sigma(E) + B^2 D(E) - \frac{\alpha}{v}] . \qquad (10)$$

This equation is an eigenvalue problem for α. It is seen that α can be interpreted as a negative $1/v$ absorber which makes the system just (prompt) critical.

Integrating Eq. (10) over all energies, it is found that

$$\alpha = \frac{\int_0^\infty \phi(E)[\Sigma_a(E) + B^2 D(E) - (1-\beta)\,\nu\Sigma_f(E)]\,dE}{\int \phi(E)\,\frac{dE}{v}} , \qquad (11)$$

where Σ_a includes both capture and fission cross sections. Equations (10) and (11) must be solved by iteration. A simple iteration scheme is as follows. We split the spectrum into a fast and a thermal part, choosing a cut-off energy E_c such that up-scattering and binding effects can be neglected above E_c and

$$f(E) = 0 \qquad \text{for } E \leq E_c .$$

Hence, the equations for the fast and the thermal spectra are, respectively,

$$\int_{E_c}^{\infty} \phi(E')\,\Sigma(E' \to E)\,dE' + Q_{f0}\,f(E) = \phi(E)\left[\Sigma(E) + B^2 D(E) - \frac{\alpha}{v}\right] , \tag{12}$$

$$\int_{0}^{E_c} \phi(E')\,\Sigma(E' \to E)\,dE' + S(E) = \phi(E)\left[\Sigma(E) + B^2 D(E) - \frac{\alpha}{v}\right] , \tag{13}$$

where Q_{f0} is the integrated source of fission neutrons and

$$S(E) = \int_{E_c}^{\infty} \phi(E')\,\Sigma(E' \to E)\,dE' . \tag{14}$$

The thermal source term, $S(E)$, depends on the properties of the moderator. For the case of water, the free-hydrogen gas model yields[12]

$$S(E) = \text{const}\ \text{erf}\left(\sqrt{E/\bar{E}}\right) , \tag{15}$$

which is a fair approximation if $\bar{E}$ is calculated from the bound-hydrogen model: $\bar{E} = 0.117$ ev.

Integrating (12) from E_c to ∞ and (13) from 0 to E_c, it follows that

$$Q_{f0} = Q_{th} + \int_{E_c}^{\infty} \phi(E)\left[\Sigma_a(E) + B^2 D(E) - \frac{\alpha}{v}\right] dE \tag{16}$$

and

$$Q_{th} = \int_{0}^{E_c} \phi(E)\left[\Sigma_a(E) + B^2 D(E) - \frac{\alpha}{v}\right] dE , \tag{17}$$

where

$$Q_{th} = \int_{0}^{E_c} S(E)\,dE = \int_{0}^{E_c} dE \int_{E_c}^{\infty} \phi(E')\,\Sigma(E' \to E)\,dE' . \tag{18}$$

Q_{th} is obviously the integrated source for the thermal spectrum.

Next, a first guess α_0 has to be made for α. Introducing this guessed value into Eqs. (12) and (13), it is possible by means of suitable codes to calculate a first approximation $\phi_0(E)$ for the asymptotic spectrum. In order to get a consistent normalization of the fast and the thermal portion of this spectrum, Eqs. (16) and (17) must be satisfied simultaneously.

This yields Q_{th} once Q_{f0} has been chosen arbitrarily.* Next, we calculate the number of (prompt) fission neutrons produced by $\phi_0(E)$:

$$Q_{f1} = (1 - \beta)\int_0^\infty \phi_0(E)\nu\Sigma_f(E)\, dE \quad . \tag{19}$$

If α_0 and therefore $\phi_0(E)$ were the exact solution of the eigenvalue problem, Eq. (10), Q_{f1} would turn out to be equal to Q_{f0}. The ratio Q_{f1}/Q_{f0} is obviously the multiplication factor of the fictitious system which includes the negative poison $-(\alpha_0/v)$. When the system is just critical, $Q_{f1}/Q_{f0} = 1$. Otherwise,

$$\left(1 - \frac{Q_{f1}}{Q_{f0}}\right)\Sigma_a(v_0)v_0 = \Delta\alpha \tag{20}$$

is a correction which when added to α_0 yields an improved value α_1. $(1/\Sigma_a(v_0)v_0)$ is the infinite-medium thermal-neutron lifetime, and is close enough to the true lifetime in the assembly to make this iteration procedure converge very fast (one or two iterations are usually sufficient). Equation (11) provides a check on the value obtained for α. However, the converged spectrum has to be used in the integral.

For the special case of 1/v absorption and fission cross sections, Eq. (11) becomes

$$\alpha = \Sigma_a(v_0)v_0 - (1 - \beta)\nu\Sigma_f(v_0)v_0 + B^2\overline{Dv} \quad , \tag{21}$$

or

$$\alpha = \Sigma_a(v_0)v_0(1 + B^2\overline{L}^2)\left(1 - \frac{k}{1 + B^2\overline{L}^2}\right) , \tag{22}$$

---

*This normalization method seems to be the most accurate. It can be checked by the approximate relation, known from slowing-down theory:

$$Q_{th} = \phi(E_c)\left\{\zeta\Sigma_s(E_c) + \gamma\left[\Sigma_a(E_c) + B^2D(E_c) - \frac{\alpha}{v_c}\right]\right\} \quad .$$

For hydrogen, this relation is exact and $\zeta = \gamma = 1$. Another check is, of course, that the fast and the thermal fluxes have to match properly at the cutoff energy, E_c.

where

$$k = \frac{(1 - \beta)\nu\Sigma_f(v_0)}{\Sigma_a(v_0)} ,$$

$$\overline{L}^2 = \frac{\overline{Dv}}{\Sigma_a(v_0)v_0} , \qquad (23)$$

$$\overline{Dv} = \frac{\int_0^\infty \phi(E)D(E)\,dE}{\int_0^\infty \phi(E)\,\frac{dE}{v}} .$$

5. 2. 2. Numerical Calculation

The calculation of the fast spectrum (Eq. (12)) was performed with the B_1 code GAM.[13] The thermal spectrum (Eq. (13)) was computed with GATHER[14] by assuming that $D(E) = [1/3\Sigma_{tr}(E)]$. The different integrals over $\phi(E)$ were computed by GATHER from 0 to E_c and by GAM from E_c to ∞. Actually, the integral $\int_0^\infty \phi(E)D(E)\,dE$ computed by GAM is such that B^2 times this integral yields the fast leakage within the B_1 approximation. Since the thermal leakage is usually small, the results may thus be considered accurate within the same approximation.

The method was used to calculate the decay constant corresponding to an H_2O–U^{235} assembly with $B^2 = 0.025\ cm^{-2}$. The result was $1/\alpha = 331\ \mu sec$, which is to be compared with a measured inverse decay constant of $410\ \mu sec$.

The value $0.025\ cm^{-1}$ is the experimental buckling[11] corresponding to a loading with a core width of 6. 88 in. ($K_{eff} = 0.9$). No attempt has been made to normalize input data in this calculation. Only differential data have been utilized. As the leakage fraction is more than 50% for this assembly, a small error in B^2 means a very large error in $1/\alpha$.

Therefore, it is felt that further improvement of the calculations may require a better theoretical or experimental knowledge of the extrapolation distance. A theoretical approach to this problem by Parks is given in Appendix II.

VI. INFINITE-MEDIUM STUDIES

This section is primarily concerned with new experimental information obtained on the behavior of infinite-medium neutron spectra for the various common moderators. The influence of various types of absorption, 1/v or resonance, has been studied during the past year. The motivation for this work has been to check questionable data taken previously, to improve precision of measurement for critical cases, and to evaluate our over-all precision of measurement by determining reproducibility. In Section VII, some theoretical calculations of spectra which have stemmed from recent scattering-law studies will be discussed.

6.1. SAMARIUM

Because of the long-standing disagreement between theoretical and measured neutron spectra in solutions heavily poisoned with samarium, a number of measurements with $SmCl_3$ and water were repeated with improved geometrical arrangements and greater Linac intensity. In Fig. 41, measurements of $SmCl_3$ made in April, 1960, and February, 1962, are compared. There is a 7% difference in the concentration of these two solutions. Figure 42 is a comparison of two infinite-medium spectra, one taken in $SmCl_3$ in April, 1960, using a water solution of 42.9 g of $SmCl_3$ per liter and a more recent measurement, using higher Linac intensities and a water solution of 54.2 g of $Sm(NO_3)_3$ per liter. The number density for the $SmCl_3$ solution is 3.5% greater than that for $Sm(NO_3)_3$ solution. Even though the difference in the concentration of the solutions for Figs. 41 and 42 are slightly different, it can be seen that this cannot account for the 20% discrepancy between measurement and theory.

There are a number of possible explanations for the discrepancy between theory and experiment. Some of these are discussed below:

1. Absorption cross section. The total cross section as given by BNL-325 might be incorrect. Adjustment of the energy-dependent parameters, e.g., the total cross section, does not improve the agreement between theory and experiment in the proper manner. Remeasurements of the total cross section of samarium have been made at General Atomic and these agree well enough with values reported in BNL-325 so that this explanation cannot be taken seriously.

2. Concentration. If the samarium concentration in the water solution or the isotopic composition of samarium is adjusted, a fairly good fit to

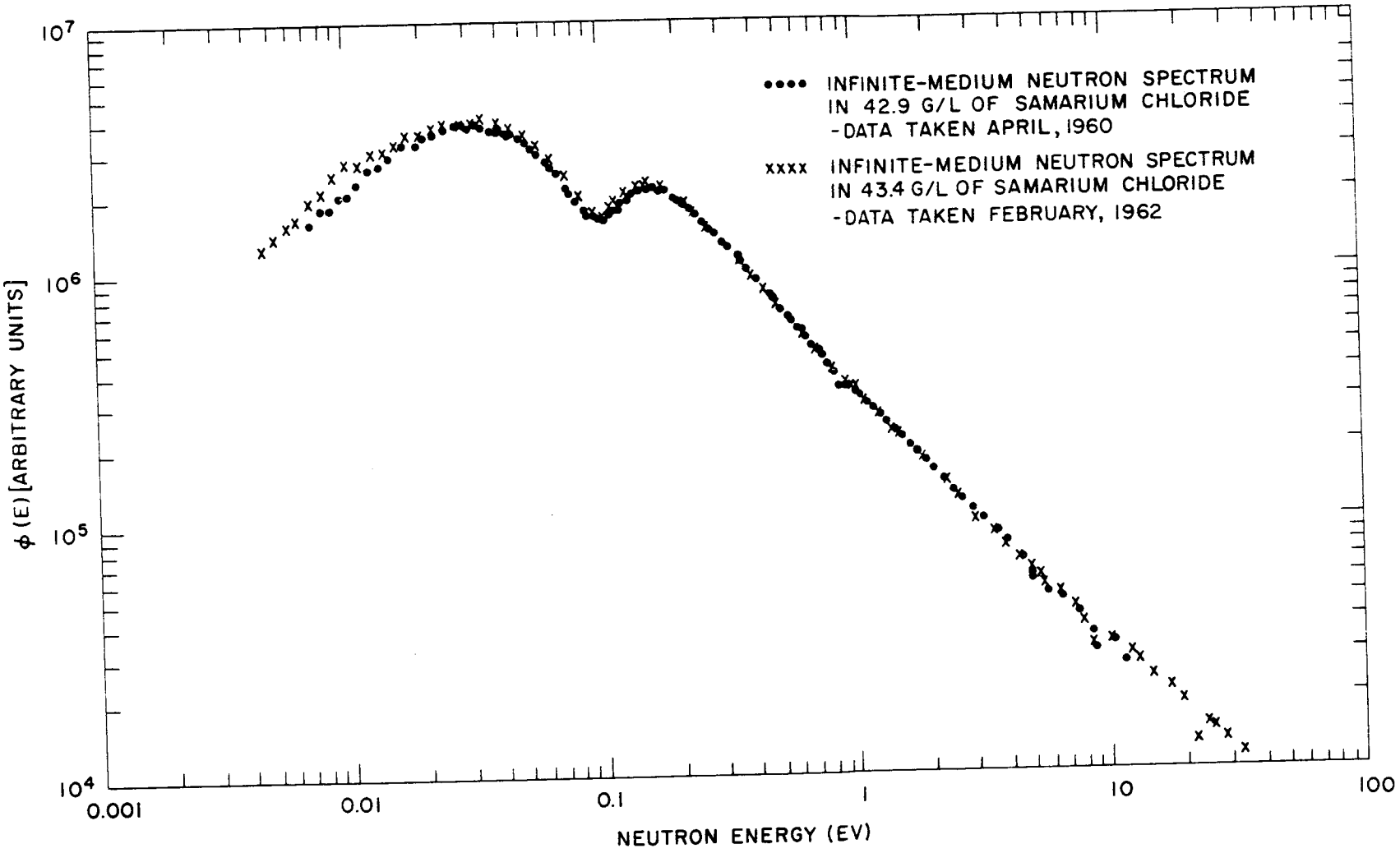

Fig. 41--Comparison of old and new spectra measurements in a heavily poisoned samarium solution

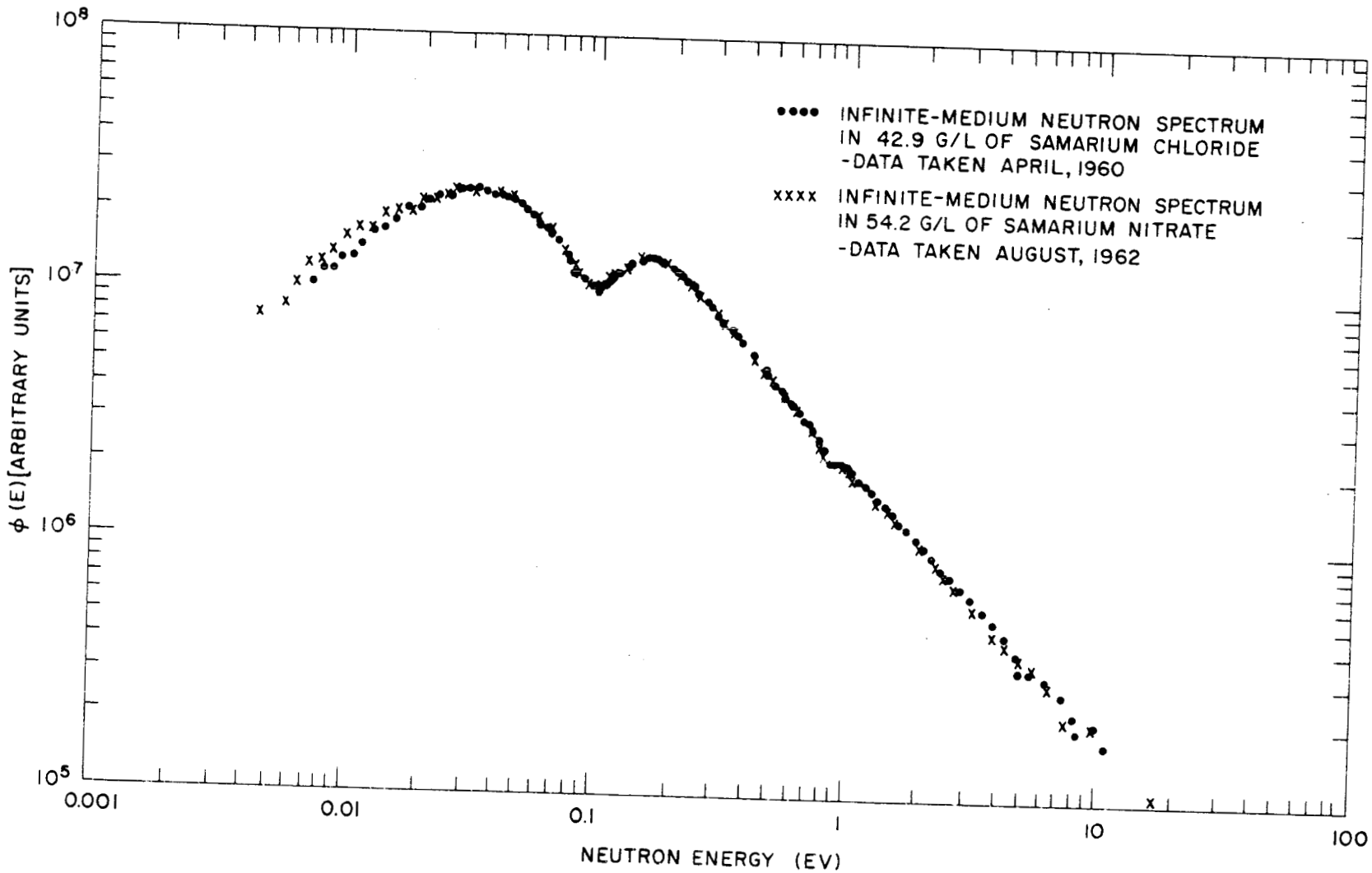

Fig. 42--Comparison of an old spectrum measurement in samarium chloride solution and a recent spectrum measurement in a samarium nitrate solution

the measured spectrum can be obtained. Figure 43 illustrates this point through a comparison of the infinite-medium spectrum of a 41.76 g per liter samarium nitrate solution and a theoretical spectrum with an adjusted atom density equivalent to a 50.0 g per liter solution of samarium nitrate. The agreement is fairly good if the two spectra are normalized as they have been in the figure.

To ensure that chemical analysis of the samarium solutions was correct, duplicate samples were analyzed by General Atomic and Truesdail Laboratories, Inc. Two separate methods were used at General Atomic, i.e., oxalate and hydroxide precipitation. The results are listed below:

General Atomic	40.3 g/l (oxalate precipitate)
General Atomic	40.7 g/l (hydroxide precipitate)
Truesdail Laboratories, Inc.	40.33 g/l

Solutions which were diluted by half also gave the expected result. Therefore, the chemical analysis of the concentration of samarium is not very suspect.

3. Isotopic composition. A sample of the samarium chloride used to prepare the solution for the spectra measurements was sent to Tracerlab, Inc. An isotopic analysis revealed that the samarium isotopes were present in the normal abundances.

4. Purity. It is possible that some rare-earth element similar in cross section to samarium is present in the solutions. Therefore, a spectroscopic analysis was made for rare-earth elements. The only significant rare earth was europium, which was present in the ratio of less than 500 ppm. This is not enough to influence the neutron absorption by a measurable amount.

5. Deposits on the end of the re-entrant tube. There is a small probability that some samarium could plate out on the end of the aluminum re-entrant tube. Therefore, aluminum strips were submersed in a samarium chloride solution for three weeks, after which time the samarium concentration on the strips was determined by X-ray emission spectroscopy. The largest amount of samarium found on either side of the eight strips was 0.12 mg/cm^2. The end of the re-entrant tube is 1 in. in diameter and has an area of about 5 cm^2, so the total amount of samarium which could plate on the end of the tube is 0.6 mg. As further evidence that plating is not important, the same tank which was used for measurement of the samarium spectra was used to measure the infinite-medium spectrum of a 43.7 per liter boric acid solution. A comparison of this spectrum and the predicted theoretical spectrum is shown in Fig. 44, along with a theoretical spectrum obtained using the scattering-law parameters recently suggested by Egelstaff.(15)

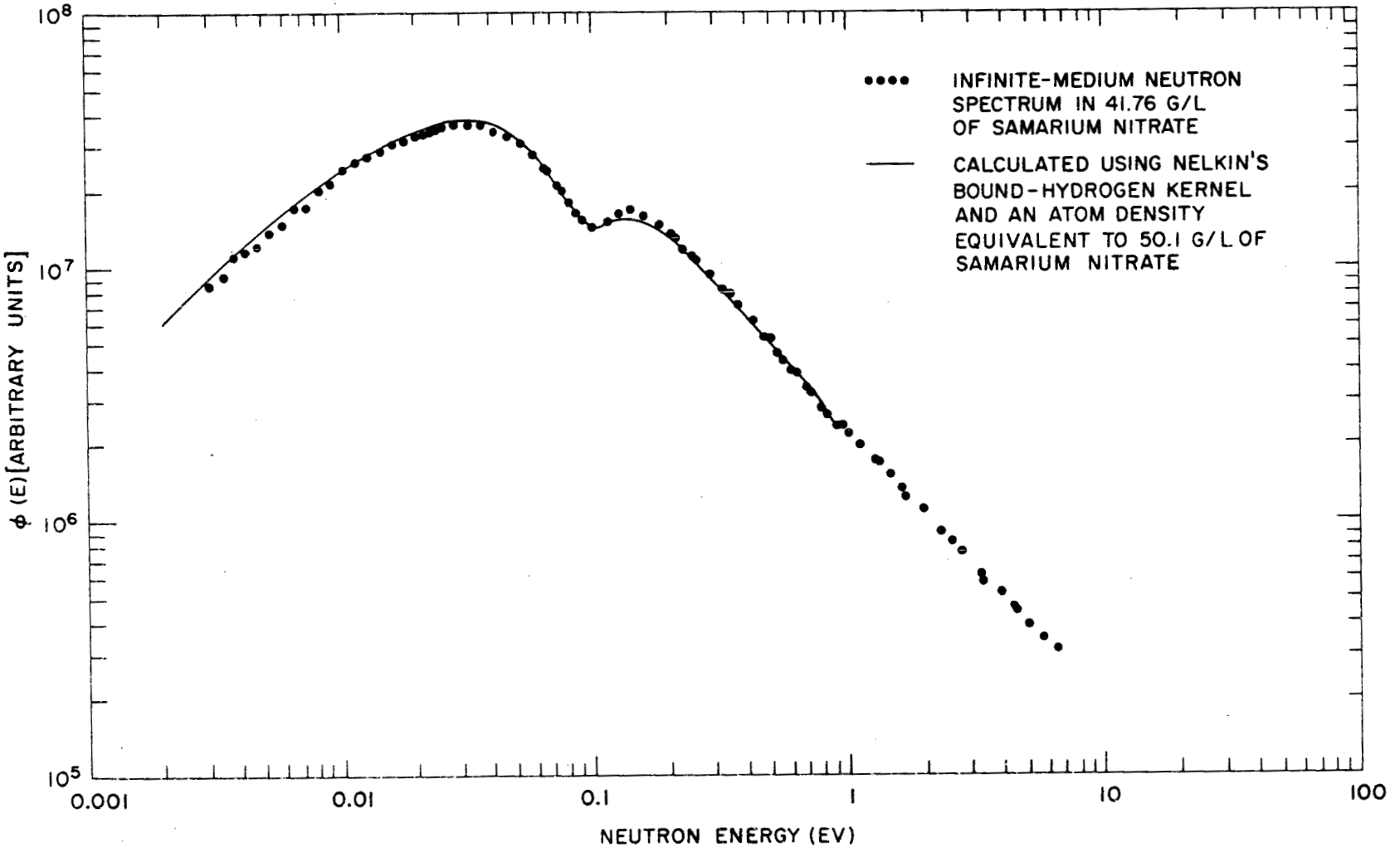

Fig. 43--Comparison of spectra in a 41.76 g per liter samarium nitrate solution with a theoretical spectrum in the equivalent of a 50.1 per liter samarium nitrate solution

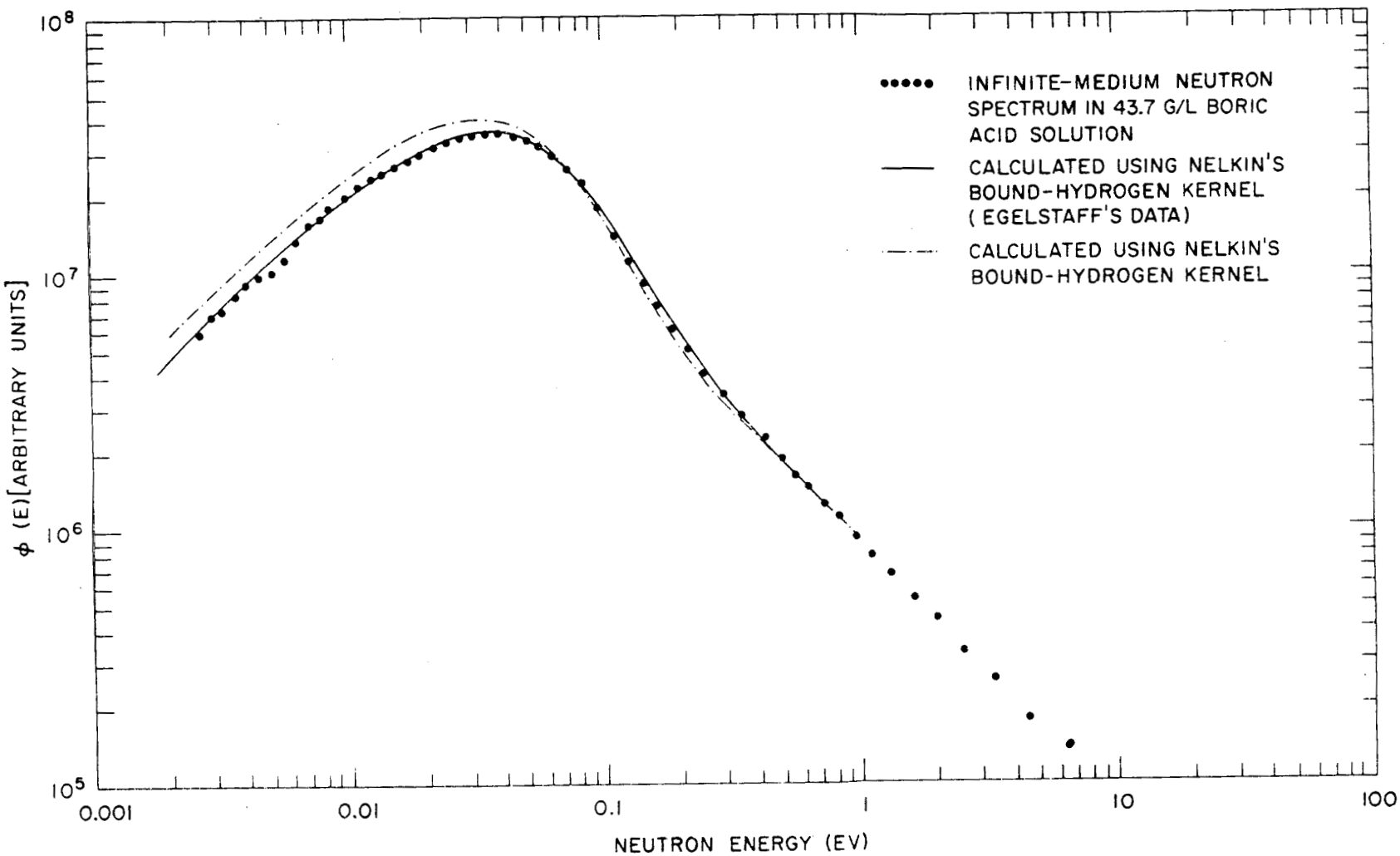

Fig. 44--Infinite-medium spectrum of a 43.7 g per liter boric acid solution compared with theoretical spectrum

6. Build-up of a radioactive isotope of samarium with a high absorption cross section. The geometry for the infinite-medium scalar spectrum measurements of samarium is shown in Fig. 45.

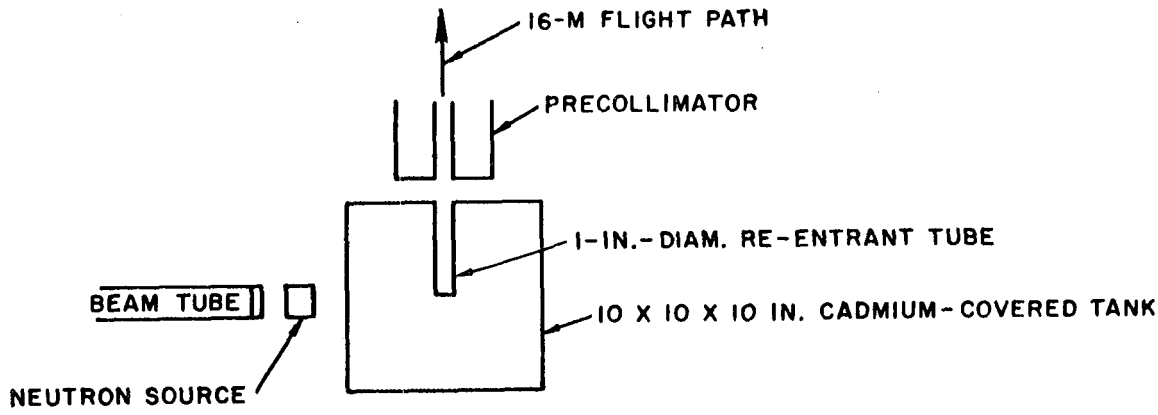

Fig. 45--Geometrical arrangement for infinite-medium measurements

The electrons from the linear accelerator strike a high-atomic-number target, which produces neutrons and a copious supply of bremsstrahlung. The slowed-down neutrons are then sampled by means of a re-entrant tube and time-of-flight techniques. Hence, it is quite possible that through either an (n,γ) or, more likely, a (γ, n) reaction Sm^{153} and Sm^{155} are produced. These radioactive isotopes could conceivably have very large cross sections and if produced in large enough quantities could result in appreciable absorption. An experiment was made to determine the contribution of these radioisotopes to the total absorption. This was accomplished by measuring a spectrum with and without a lead wall between the target and tank. The lead wall considerably reduced the amount of bremsstrahlung reaching the tank, but not the number of neutrons. These two spectra are shown in Fig. 46, where it can be seen that they are in reasonably good agreement. A small hardening of the spectrum obtained in the unshielded geometry is evident, but this is probably due to a small difference in geometry.

In addition, a sample of the samarium nitrate solution was qualitatively analyzed with a multichannel gamma-ray spectrometer. Two known gamma rays of Sm^{153}, which has a 46.7-hr half life, were detected. This isotope apparently is not produced in large enough quantities or does not have a large enough cross section to contribute appreciably to the total absorption.

An attempt has been made to fit the measured neutron spectrum by adjusting various parameters in Nelkin's kernel on the basis of recent considerations of inelastic neutron scattering in water by Egelstaff (refer to Subsection 7.4). These adjustments in the scattering kernel were a

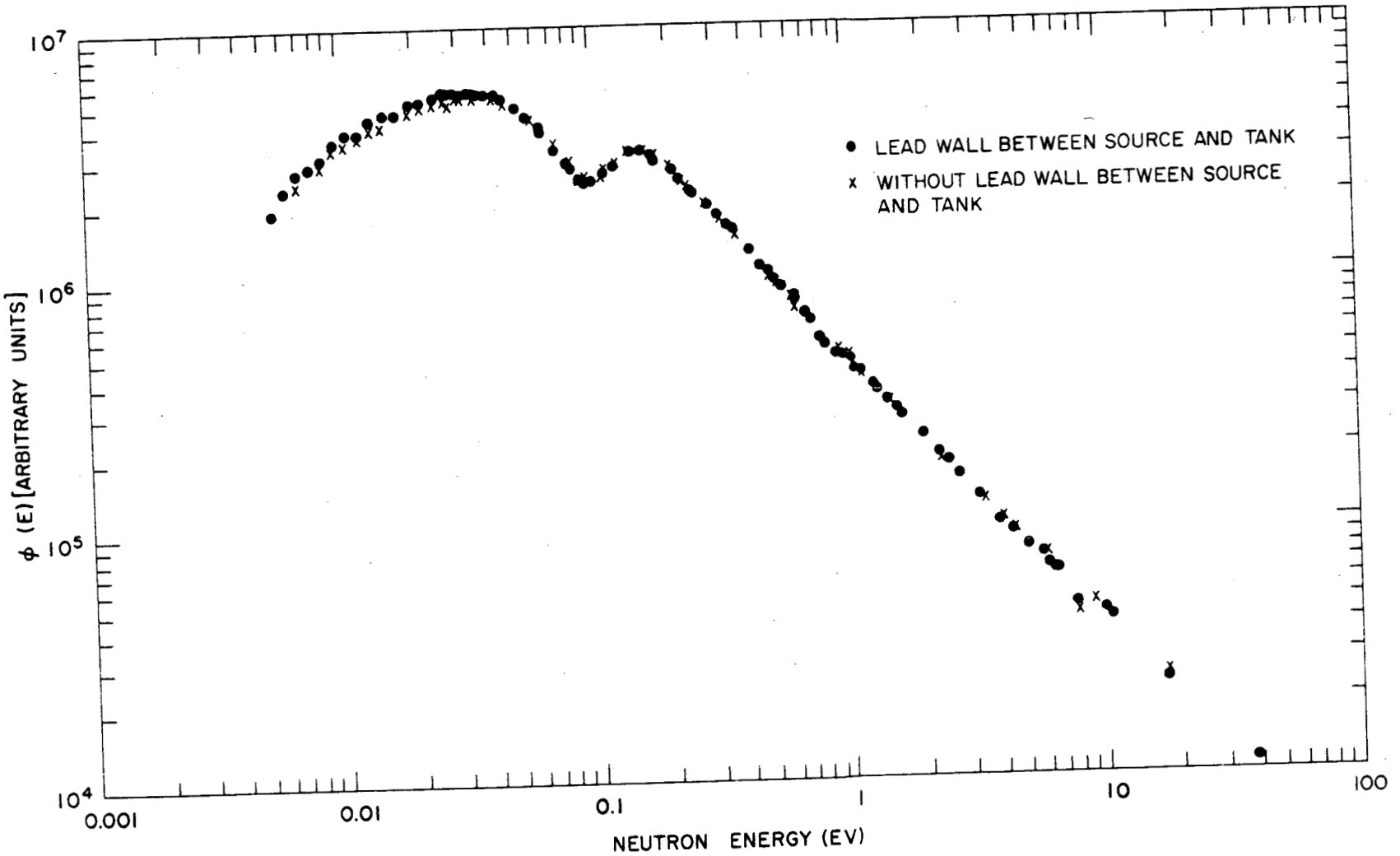

Fig. 46--Spectra in a heavily poisoned samarium nitrate solution with and without lead wall between tank and pulsed source

reduction of the weighting of the rotational level and an increase of the weighting of the highest vibrational level. A comparison of Nelkin's kernel, Nelkin's kernel using Egelstaff's parameters, and the experimental data is given in Fig. 47. This approach is only a first attempt and much more thought is needed on parameter selections. For example, although a very good fit to the experimental spectrum has been obtained by following Egelstaff's recommendations, the calculated total cross section for water is in large disagreement with experiment (see Fig. 48).

There are a few other adjustments which can be made in the weights assigned to various degrees of freedom in the water molecule within the framework of Nelkin's model. It is possible that all experimental data can be explained in a consistent manner without resorting to the more elegant descriptions of the physical processes. This approach will be tried before an attempt is made to specify a more elaborate scattering law than that given by Nelkin.

The neutron-conservation condition for a hydrogenous medium is

$$\int_0^{E_c} \Sigma_a(E)\phi(E)\,dE = E\phi(E)(\Sigma_s + \Sigma_a)\,, \qquad (24)$$

where Σ_a is the macroscopic absorption cross section. Spectra of cadmium-sulfate-poisoned water varying up to 30 barns/hydrogen atom of absorption have already been measured and were reported in GA-2544. The cadmium sulfate spectra have for all poison concentrations satisfied Eq. (24) to within 5%, although the theoretical fit to these spectra is not exceedingly good (possibly owing to the inadequacies of the scattering law). However, for samarium, neutron conservation for absorption of 9 barns/hydrogen atom, is not satisfied to within 25% if E_c is chosen as 1 ev. One of the main differences between cadmium and samarium is the epithermal-resonance structure. Cadmium has a large resonance at 0.17 ev, then drops sharply to a cross section of a few barns at an energy of 10 ev, with a few very sharp resonances at higher energies. Samarium, on the other hand, has a large resonance at 0.098 ev with a smaller resonance at 0.88 ev, then drops to a cross section of about 30 barns with a subsequent moderately broad resonance at 8 ev. These resonances are evident in Fig. 41. However, because of the fairly poor resolution, they are not as pronounced as would be expected. These resonances are all located in the slowing-down region and thereby perturb the neutron source feeding the lower energies and hence the slowing-down source. Therefore, the above conservation equation is not strictly valid for this situation.

Strictly speaking, neutron conservation should be tested for the

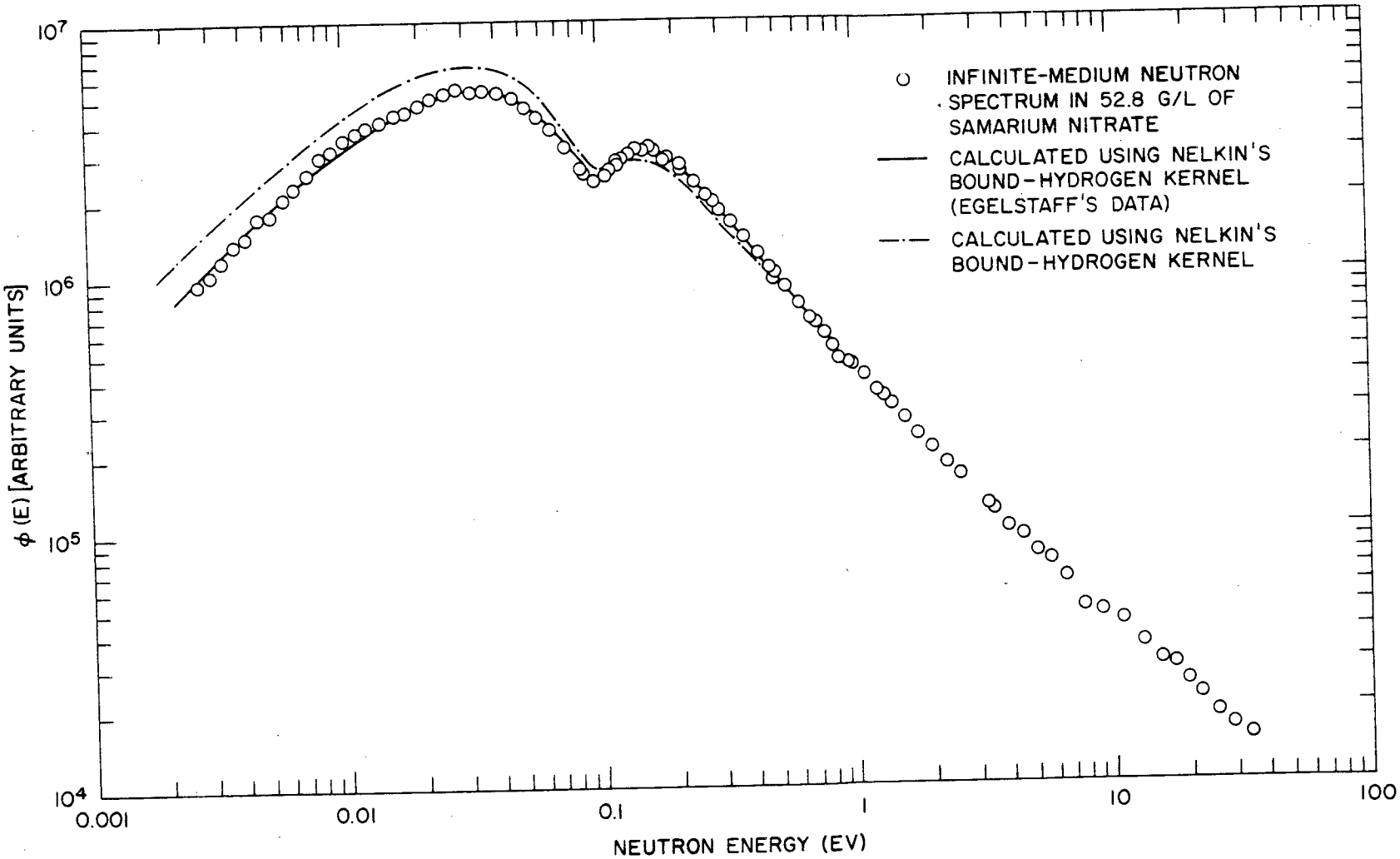

Fig. 47--Comparison of a spectrum in a heavily poisoned samarium nitrate solution and theoretical spectra obtained using Nelkin's kernel and Nelkin's kernel with Egelstaff's data

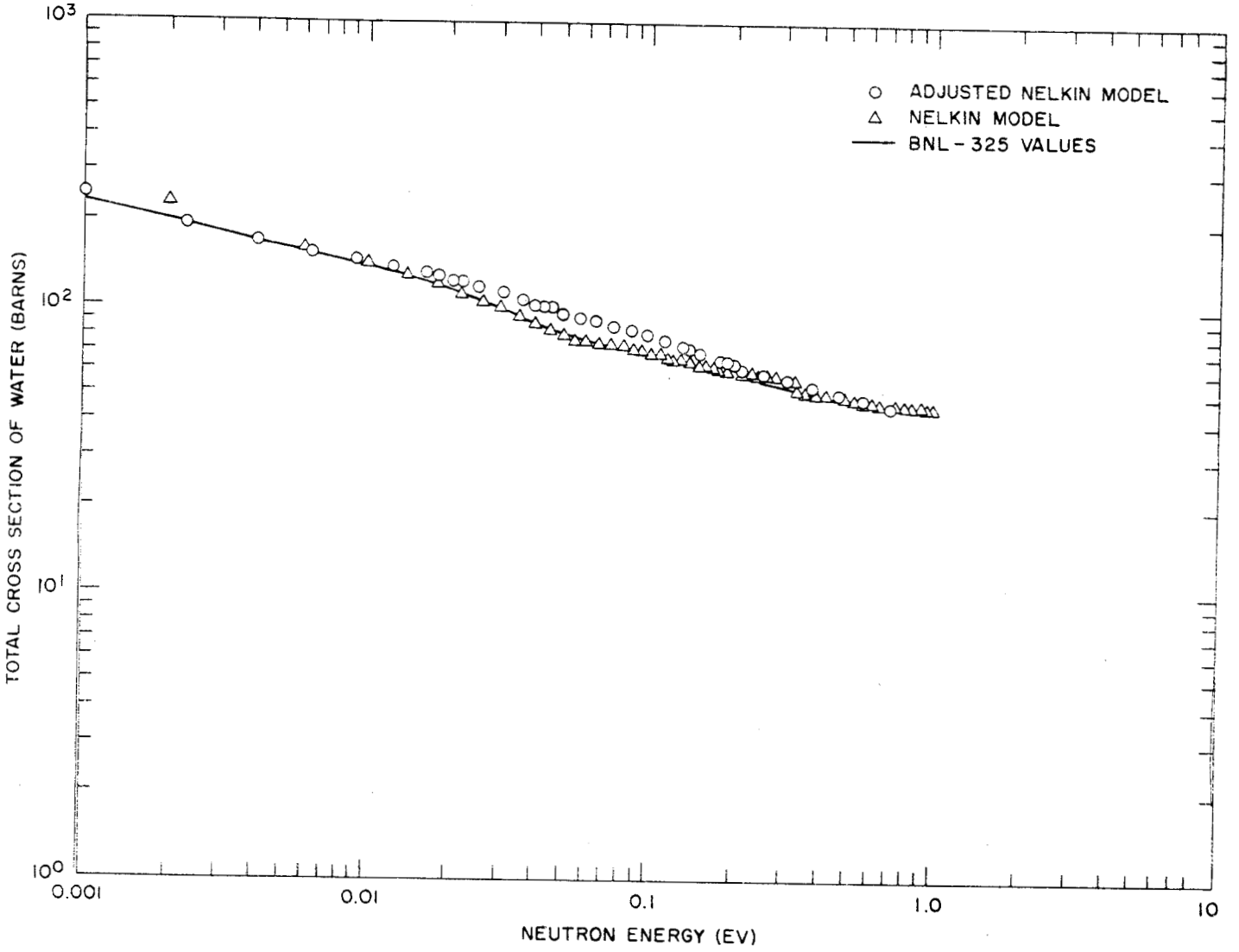

Fig. 48--Comparison of the total cross section of water obtained using Nelkin's kernel and Nelkin's kernel with Egelstaff's data

experimental spectrum by satisfying the equation

$$\int_0^{E_c} \phi_m(E)\Sigma_a(E)\,dE = \int_{E_c}^{\infty}\int_0^{E_c} \phi_m(E')\Sigma_s(E' \rightarrow E)\,dE\,dE', \qquad (25)$$

where $\phi_m(E)$ is the measured spectrum. However, some additional statements can be made concerning neutron conservation for the samarium spectra. If we normalize the old Nelkin theory and experiment at, say, 1 ev (Fig. 47), we are approximately normalizing the slowing-down sources in the two cases. If we then compare the absorption below 1 ev in both cases, the disagreement is cut in half (about 14%) in the worst case. Furthermore, it is quite evident, using Nelkin's kernel with Egelstaff's parameters (Fig. 47), that theory and experiment would have the same number of absorptions to within a very few per cent. The conclusion to be drawn is that the simple neutron-conservation condition should not be applied blindly to the evaluation of all neutron spectra. It definitely fails in the case of large, unresolved epithermal absorption. Thus, experimental data should not be subject to suspicion on this basis alone. In the case of the samarium spectra, it seems likely that the conservation condition, when properly applied to the data, will be satisfied. Therefore, the disagreement between theory and experiment shown in Fig. 47 should be taken seriously, and methods consistent with other experimental data (total and differential scattering data) should be investigated to introduce improvements in the theory for predicting neutron spectra in water systems, primarily into the scattering law for water.

6.2. GADOLINIUM

During the last few years, an extensive series of experiments on infinite-medium spectra in poisoned water-moderated assemblies has been conducted. The absorbers used have been boron, cadmium, samarium, and erbium. These experiments have served as integral checks on proposed energy-transfer kernels for thermalization in water. In addition, the stationary spectrum is the quantity which it is desired to be able to predict for practical problems. Since the characteristic discrepancies between theory and experiment appear to depend on the nature of the absorber, it was considered worthwhile to try a distinctively different absorber. Gadolinium was chosen because it is an important reactor poison, its absorption being attributable partly to a negative energy resonance. It also possesses absorbing properties which are not unlike those of xenon. The infinite-medium spectra for a 12.3 g per liter water solution of gadolinium chloride is shown in Fig. 49. This spectrum, which was taken with a higher-intensity source from the new L-band Linac, agrees with theory over much of its energy range but disagrees at lower energies. Neutron conservation is

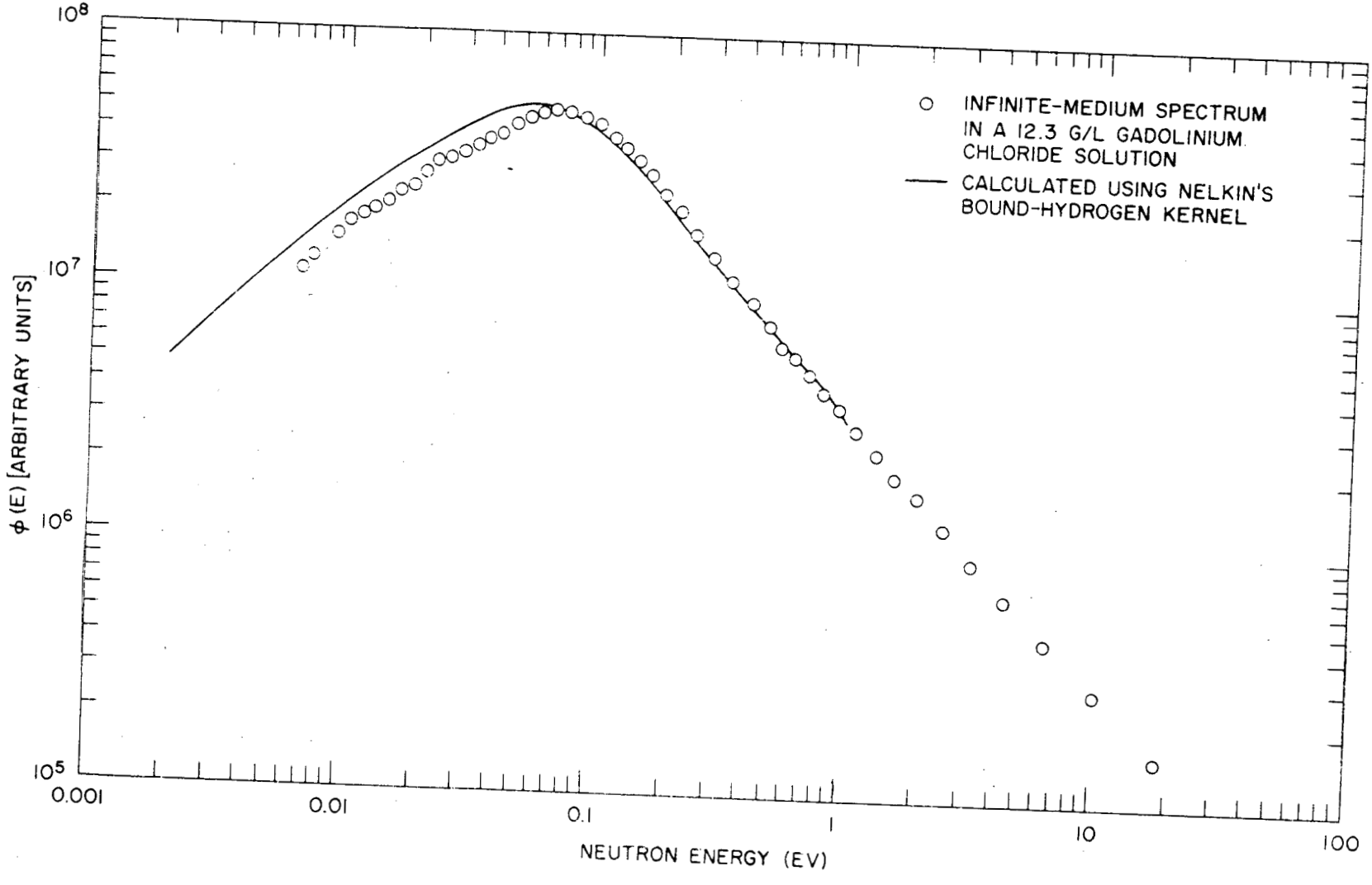

Fig. 49--Comparison of theory and experiment for a 12.3 g per liter solution of gadolinium chloride

satisfied in this case about as well as for all resonance absorbers. The disagreement at low energies tends to indicate, as it did with the samarium spectra, that further refinements and adjustments in the scattering model for predicting water spectra should be made. One of these refinements has already been discussed in Subsection 6.1, i.e., the weighting of the rotational and vibrational levels. Therefore, this procedure will be applied to the data for gadolinium as well as for samarium in the very near future in an attempt to understand the spectral variations being observed.

6.3. POLYETHYLENE

The moderating properties of polyethylene are interesting for two reasons. From a practical standpoint, polyethylene is a convenient material for use in mocking up critical configurations of proposed water reactors. In this capacity, one assumes that its moderating properties are not too dissimilar from those of water and that simple ways can be found to account for any possible small variations between the two moderators. Also, polyethylene is an example of a long-chain organic molecule, which has been studied to some extent. Information on the vibrational molecular-frequency spectrum is available from the work of Nielsen and Woolett.[16] Other auxiliary information on low-energy neutron inelastic scattering is also available. Thus, there is actually a backlog of information on which to base a good approximate representation of the low-energy scattering law for neutrons. For these reasons, it was decided to measure spectra in poisoned polyethylene in clean geometries under infinite-medium conditions as an over-all check on our ability to predict neutron thermalization for this typical hydrogenous moderator.

Measurements of spectra in polyethylene under infinite-medium conditions were obtained some years ago with the old Linac. These measurements were repeated during the past contract year as a confirmation of the accuracy of the new experimental arrangement. In addition, Goldman's spectral predictions[17] based on a realistic scattering kernel have become available. Experimental measurements and theoretical calculations at 10.45 and 5.74 barns/hydrogen atom are shown in Figs. 50 and 51. At 5.74 barns/hydrogen atom, measurements were made 2.5, 4.5, and 5-3/4 in. from the pulsed source side of the slab geometry. All three measurements are in agreement. Goldman's kernel (scattering law) is essentially an extension of the kernel developed for water by Nelkin. The frequency spectrum assumed by Goldman has vibrational energy levels at 0.533, 0.354, and 0.187 ev and a hindered rotational level at 0.89 ev.

It can be seen that the approximate representation proposed by Goldman does a fair job of reproducing the hardened neutron spectrum. Thus, even though the method treats very superficially the acoustical molecular-frequency band, no serious spectral distortions result.

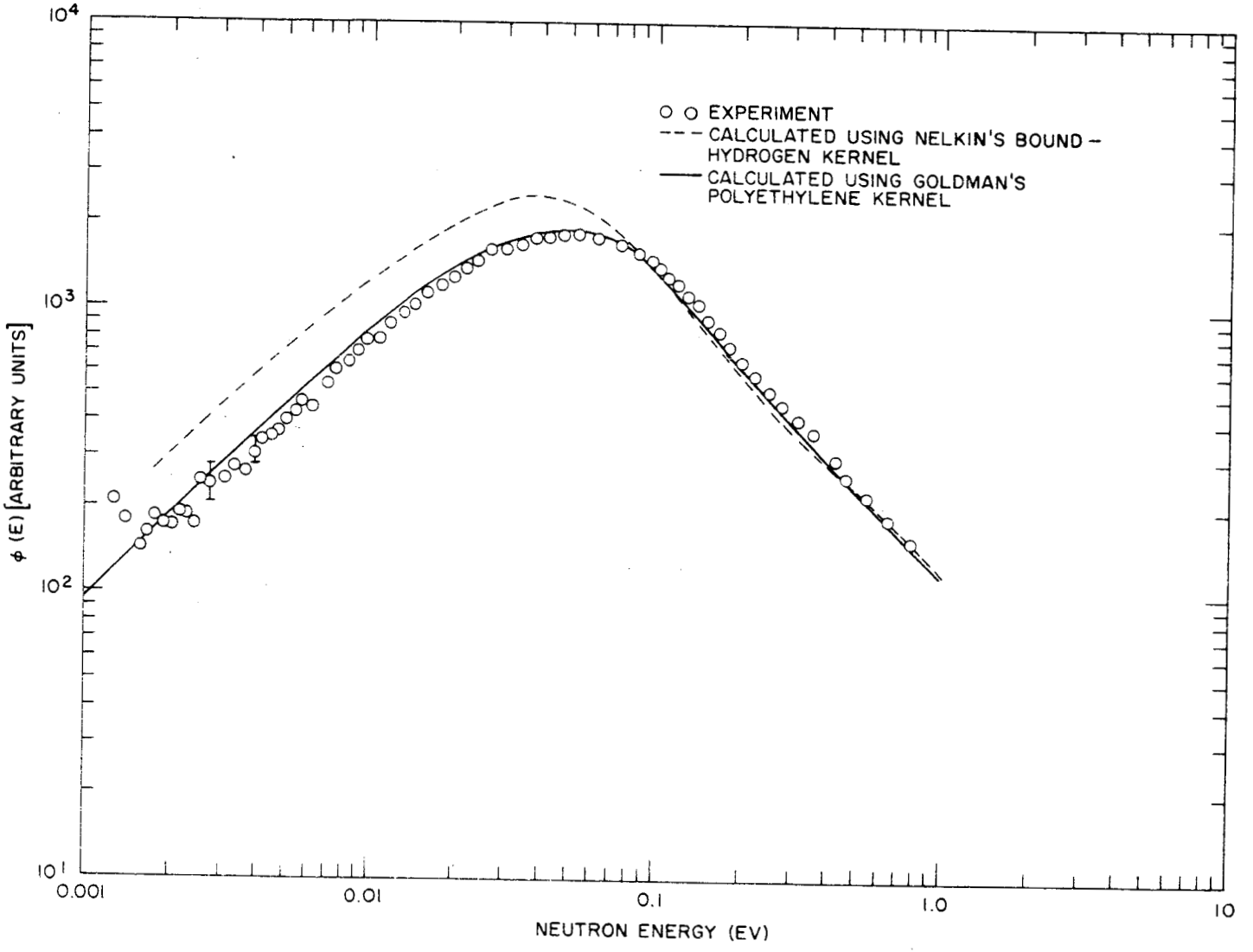

Fig. 50--Infinite-medium spectrum measurement in polyethylene poisoned with 10.45 barns/hydrogen atom compared with calculations performed with Goldman's kernel

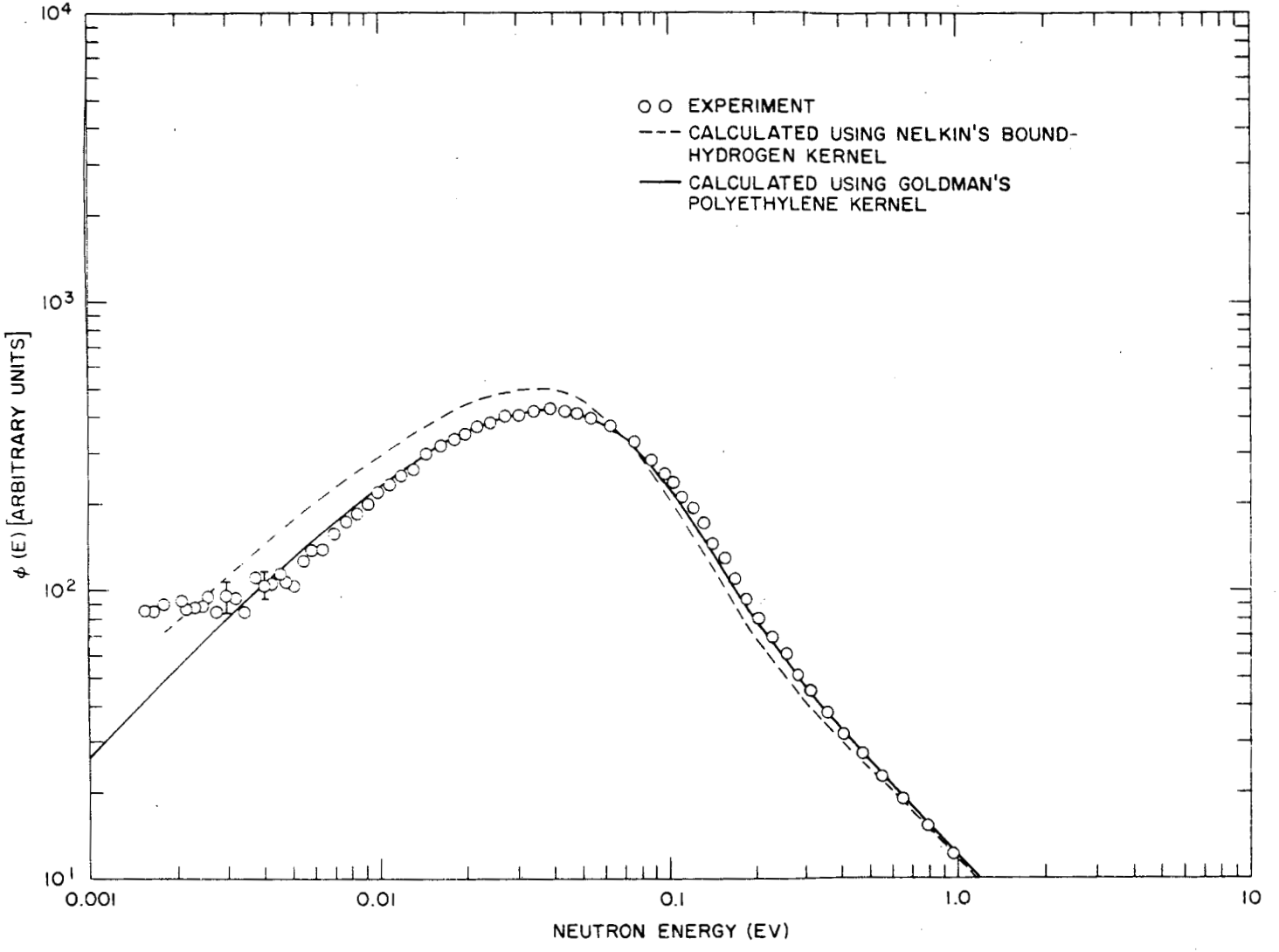

Fig. 51--Infinite-medium spectrum measurement in polyethylene poisoned with 5.74 barns/hydrogen atom compared with calculations performed with Goldman's kernel

As a further integral check of Goldman's procedure and also as an introductory cryogenic spectral experiment, spectra were measured in borated polyethylene at liquid-nitrogen temperatures. The experimental setup is shown in Fig. 52, and the results, together with results obtained at room temperature, are shown in Fig. 53. At liquid-nitrogen temperatures, the spectrum should be far more sensitive to the physical description for the acoustical modes of vibration of the polyethylene molecule. Goldman has also performed preliminary calculations of the infinite-medium spectra to be expected in this case. Results from both experiment and theory are shown in Fig. 54. The agreement again appears to be very good, indicating that detailed knowledge of the acoustical molecular-frequency spectra may not be necessary for good spectral predictions. It seems possible that an adequate description of the scattering processes for most practical purposes can be obtained by merely specifying approximately the correct weighting factors for the various degrees of freedom of the polyethylene molecule.

6.4. D_2O

The study of neutron spectra in D_2O systems has essentially not advanced beyond rather primitive experiments. There are several reasons for this situation: (1) Spectra in D_2O reactors are in general quite thermal and relatively insensitive to the details of the liquid-state scattering law for the molecule; (2) methods for studying spectra in D_2O which involve chopper techniques have utilized rather complicated unclean geometries, so that the results have been ambiguous; (3) it has been felt by many that the pulsed-source method (Poole technique) of spectral investigation is not adaptable to D_2O systems since the neutron slowing down and lifetime in this moderator are so long. Nevertheless, many studies of reactor lattices with D_2O moderation are being conducted both in this country and Canada, and it appeared desirable to obtain an integral check on the importance of the scattering law for this moderator in reactor spectral calculations as soon as possible.

The situation is currently ideal for clean integral studies of D_2O spectra. A general knowledge of the molecular-frequency spectrum from which to calculate the scattering kernel is available. First, the vibrational frequencies of the molecule are known from Herzberg[18] and the rotational energy is known from Hughes, et al.[19] Second, neutron scattering-law measurements have been performed by Egelstaff,[1] et al., over a large range of energy and momentum transfers. (These were recently compiled and reported by Brugger.[20]) Thus, much data exists for the construction of a realistic scattering law for this moderator.

It is usually highly desirable to utilize the pulsed technique for measuring neutron spectra where possible, since this permits a great

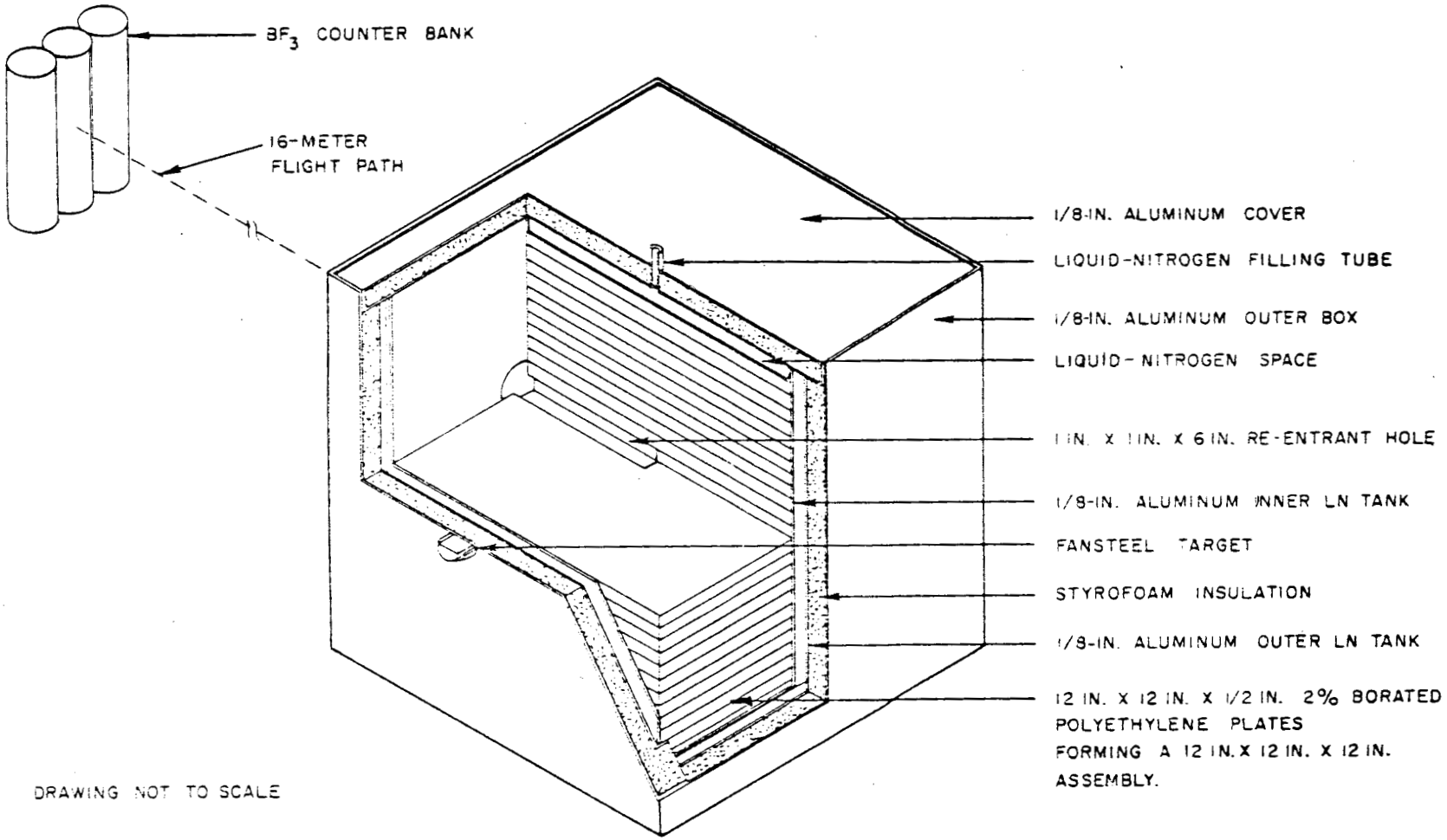

Fig. 52--Experimental arrangement for measuring infinite-medium spectra in borated polyethylene at both liquid-nitrogen and room temperatures

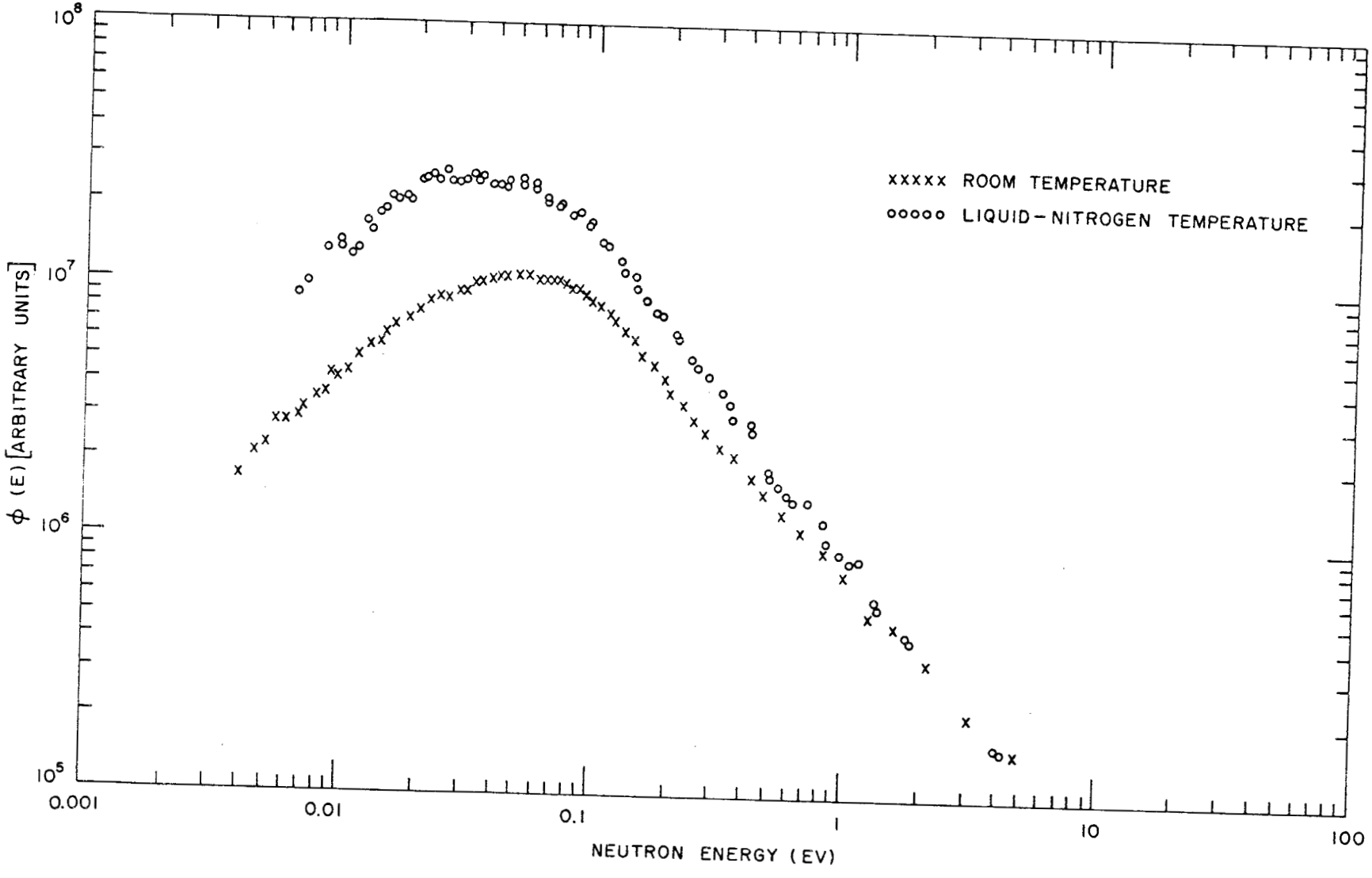

Fig. 53--Infinite-medium neutron spectra in a 12-in. cube of borated polyethylene at room and liquid-nitrogen temperatures

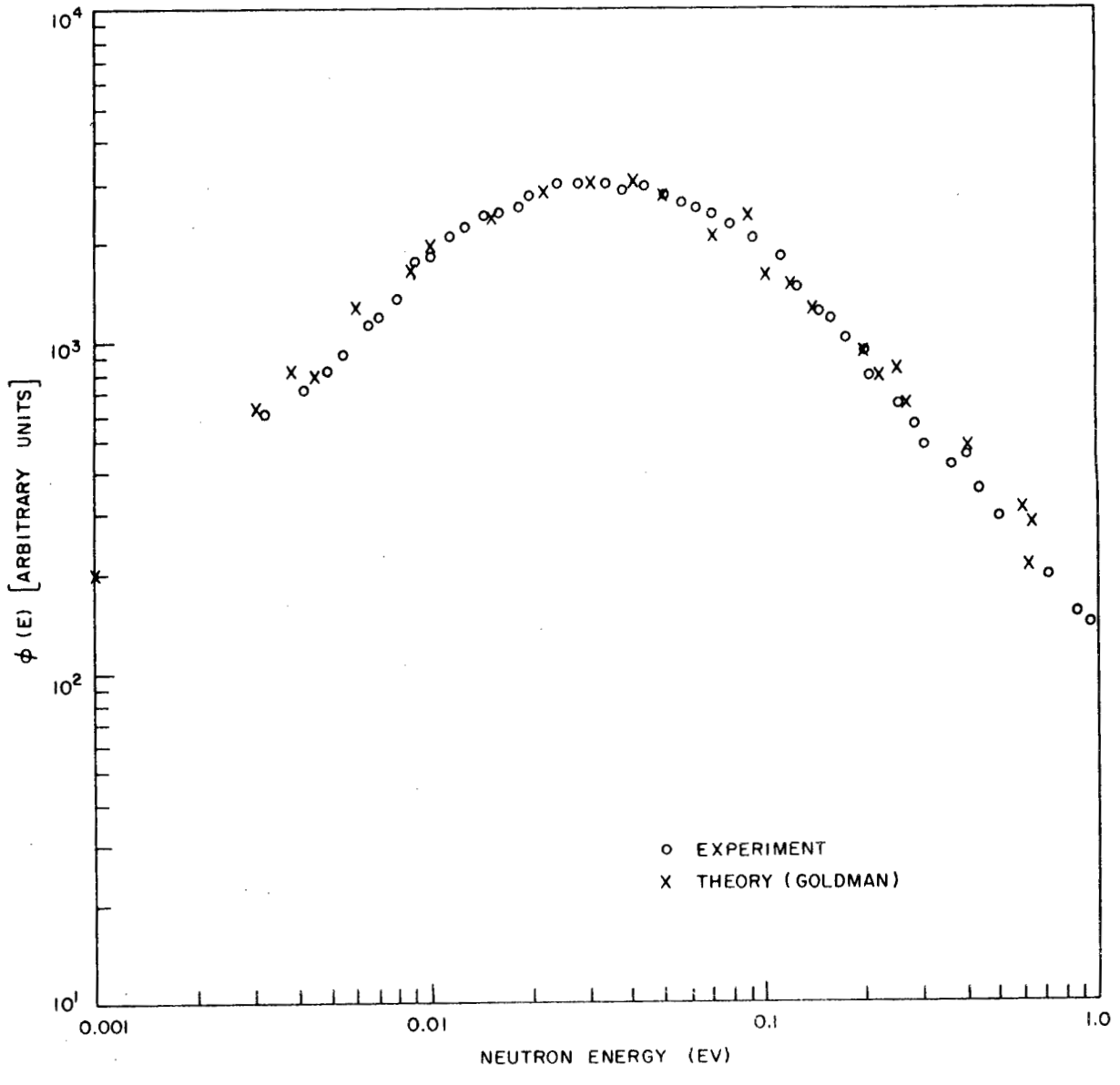

Fig. 54--Liquid-nitrogen-temperature spectrum in borated polyethylene compared with Goldman's theoretical calculations

deal of experimental flexibility. For example, most of the investigations of spectra involving chopper techniques which have been reported in the literature have been seriously complicated by undesirable geometrical effects, i.e., large flux gradients, large leakage corrections, and two-dimensional heterogeneities, not to mention the additional uncertainties introduced by energy-dependent chopper transmission functions. The extreme flexibility and precision of the pulsed-source technique has by now been demonstrated. There is, however, a misconception concerning the applicability of the pulsed-source method to studies of spectra in moderators having long thermal and epithermal lifetimes. The investigations for graphite moderators discussed in GA-2544 demonstrated the success of this straightforward approach. The technique which is used to circumvent the long lifetime inherent in the moderator is to poison the assembly with boron or resonance absorber. Thus, the thermal lifetime is decreased to a manageable value for a long-flight-path experiment. The moderation times, although rather long, are also not a serious problem, since these times can be accurately calculated and a correction to the measured time spectra can be precisely made. With our latest techniques, this correction in a pulsed spectral study is less than 5%. Fortunately, the addition of thermal poison (increasing $\Sigma_a/\xi\Sigma_s$) improves the experiment from the physics standpoint. It is well known that neutron spectra for both very small and very large amounts of absorber are quite insensitive to scattering law. However, at the intermediate poison concentrations typical of many reactor applications, the sensitivity is large. Fortunately, poison concentrations required to test scattering-law sensitivity in an integral fashion are approximately those desired to reduce the thermal lifetime for practical pulsed spectrum experiments.

The pulsed spectrum experiments performed on D_2O were conducted in the neutron cave (Fig. 9, Section III) with the 16-m flight path and the calibrated detector bank. The experiments were performed in slab configuration using the core tank for the subcritical assembly (Fig. 55). The D_2O had a light-water contamination of 3.6% by weight. The poison (boron) was introduced in the form of impregnated aluminum plates spaced 0.125 in. apart in the subcritical tank. This is a very good approximation of a homogeneous situation, since the absorbers are placed less than 1/10 of a mean free path apart. The poison concentration was 2.4 barns/deuterium atoms.

Two flux plots were made in the D_2O assembly. The cadmium-covered-indium axial flux mapping was used to determine the position where the gradient of the flux was zero (the best place for a meaningful spectrum measurement). These data were also used to determine the spatial variation of the epithermal-neutron source for spectrum measurements. Sulfur pellets were used to determine the primary fast source input. The results of these measurements are shown in Figs. 56 and 57. All the above flux data were employed in making the small spatial corrections to the measured spectra.

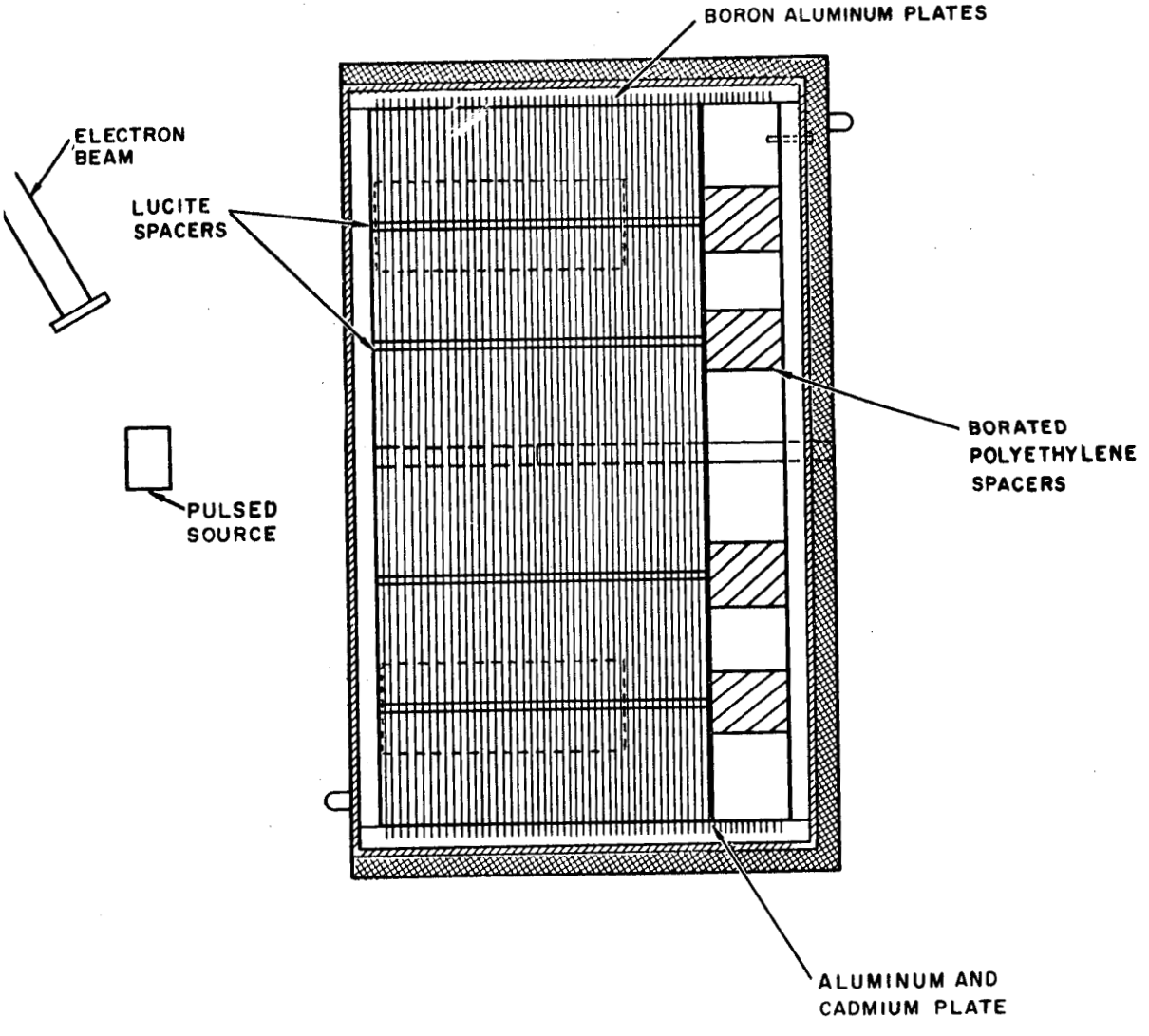

Fig. 55--Plan view of geometrical arrangement for spectral measurements in poisoned D_2O

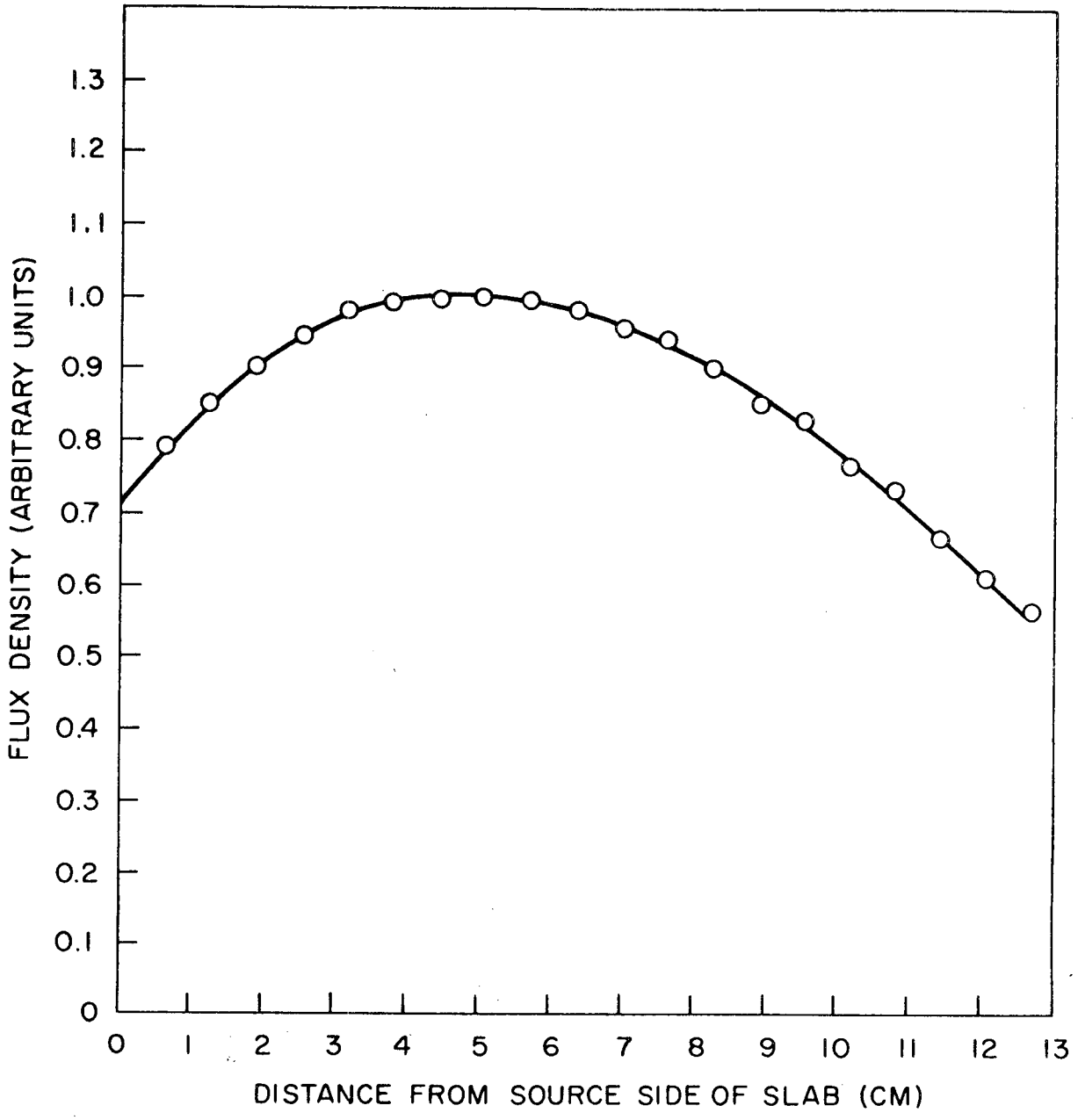

Fig. 56--Axial flux mapping using cadmium-covered indium foils in borated D_2O

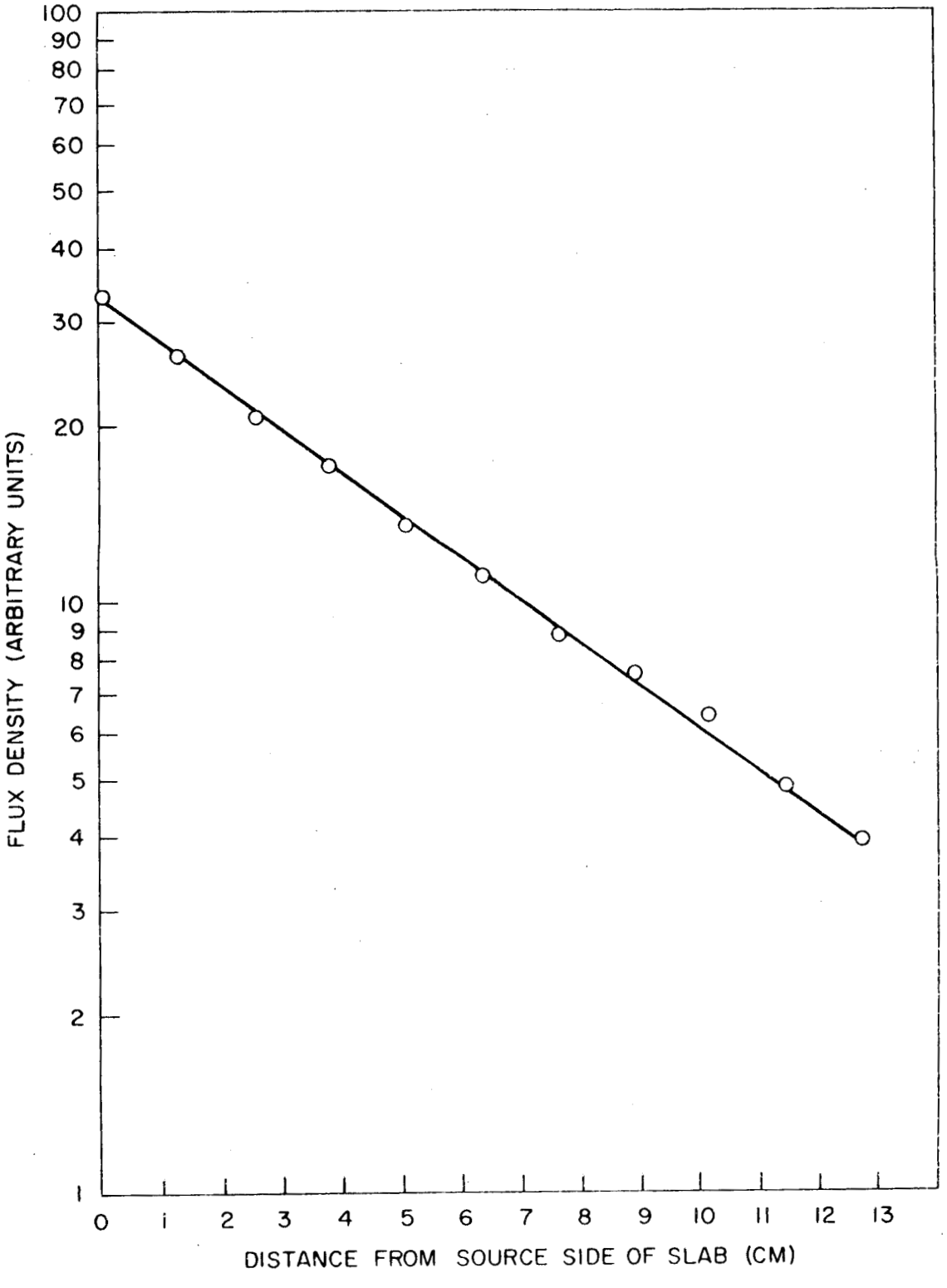

Fig. 57--Axial flux mapping using sulfur pellets to determine primary fast source in borated D_2O

The die-away (neutron lifetime), τ, of the assembly was measured using a U^{235} fission chamber (with a 1/4-in. active length) placed 5 cm from the source side of the assembly. The results of this measurement are shown in Fig. 58. These data are essential for establishing the mean-emission-time correction in the analysis of the spectral data. The mean-emission-time correction was calculated by a method developed by Parks[21] for determining the first time moment of the time-dependent spectrum, namely,

$$\bar{t}(E) = \frac{\int \phi(E, t) t \, dt}{\int \phi(E, t) \, dt} = \frac{\Psi(E)}{\phi(E)}$$

Both $\Psi(E)$ and $\phi(E)$ satisfy the infinite-medium steady-state diffusion equation. The scattering kernel used for this correction was that for a free gas of deuterium. This kernel, along with the epithermal source, absorption, and scattering cross sections, was placed on a binary tape for the code GATHER, which was used to calculate both $\phi(E)$ and $\Psi(E)$. Since the free-gas kernel affords relatively good agreement between the measured and theoretical spectra, little error should occur in using it instead of a more exact expression in this correction procedure. The calculated mean emission time is shown in Fig. 59.

The measured scalar neutron flux was obtained by the standard beam-scatterer technique; measurement was made at the spatial flux peak to eliminate gradient effects. A comparison between the D_2O spectrum and that for identically poisoned H_2O and various simple infinite-medium spectral calculations is given in Fig. 60.

The results of refined theoretical analyses for the same experimental data are plotted in Fig. 61. This figure includes a free-gas calculation for an infinite medium using a DB^2 correction and a DSN calculation using a free-gas model and a transverse DB^2 correction. A calculation employing a bound-deuterium scattering kernel is also given. This kernel (constructed by H. Honeck of Brookhaven National Laboratory) is patterned after that for Nelkin's light water. The molecular-frequency spectrum is assumed to be described by various vibrational, rotational, and translative degrees of freedom. The vibrational oscillators are chosen at energies $\omega_{v1} = 0.15$ ev and $\omega_{v2} = \omega_{v3} = 0.35$ ev; a hindered rotation of effective mass $m_v = 4.11$ is assumed at $\omega_v = 0.05$ ev; and free translation is assumed. Then the kernel is generated in the incoherent approximation by procedures analogous to those used for light water. For light water, a free-hydrogen kernel does not permit good spectral predictions to be made. For D_2O, the experimental spectrum is in very good agreement with free-gas predictions and in somewhat poorer agreement with results based on a much more realistic description of the scattering process. The discrepancies reported here should not be considered final insofar as experimental results

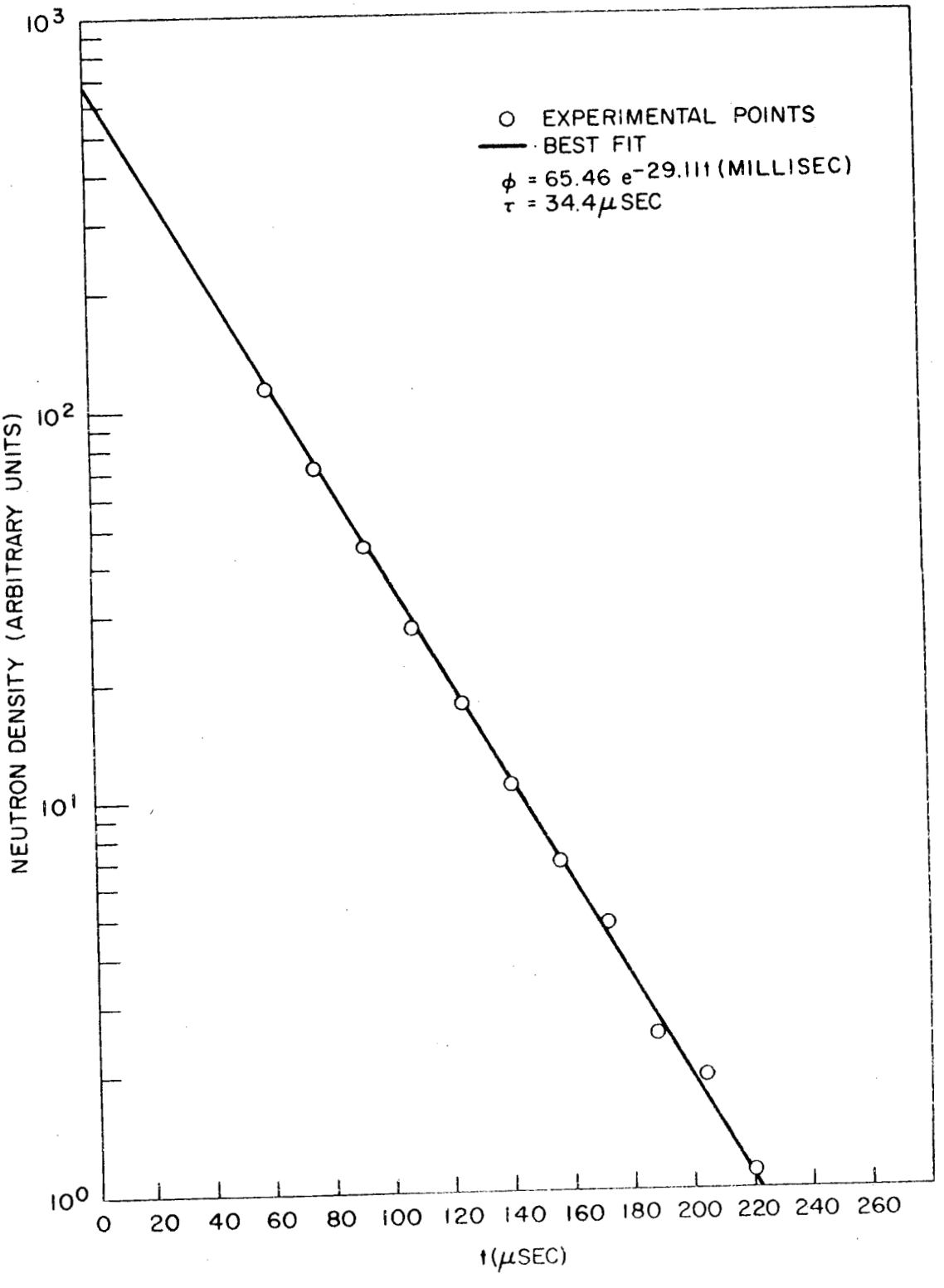

Fig. 58--Die-away of thermal neutrons in a 5-in. slab of borated D_2O

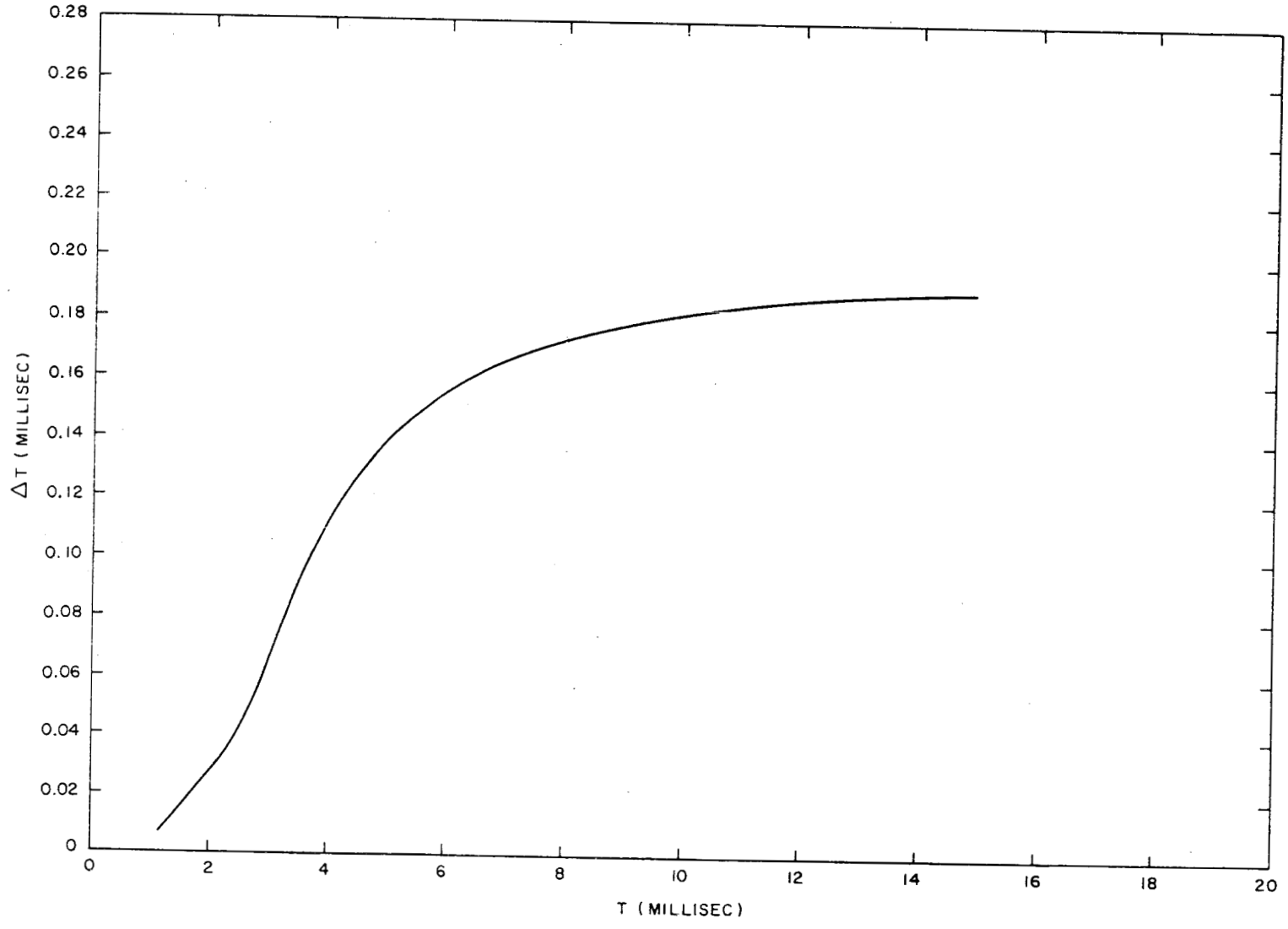

Fig. 59--Calculated mean emission time for borated D_2O

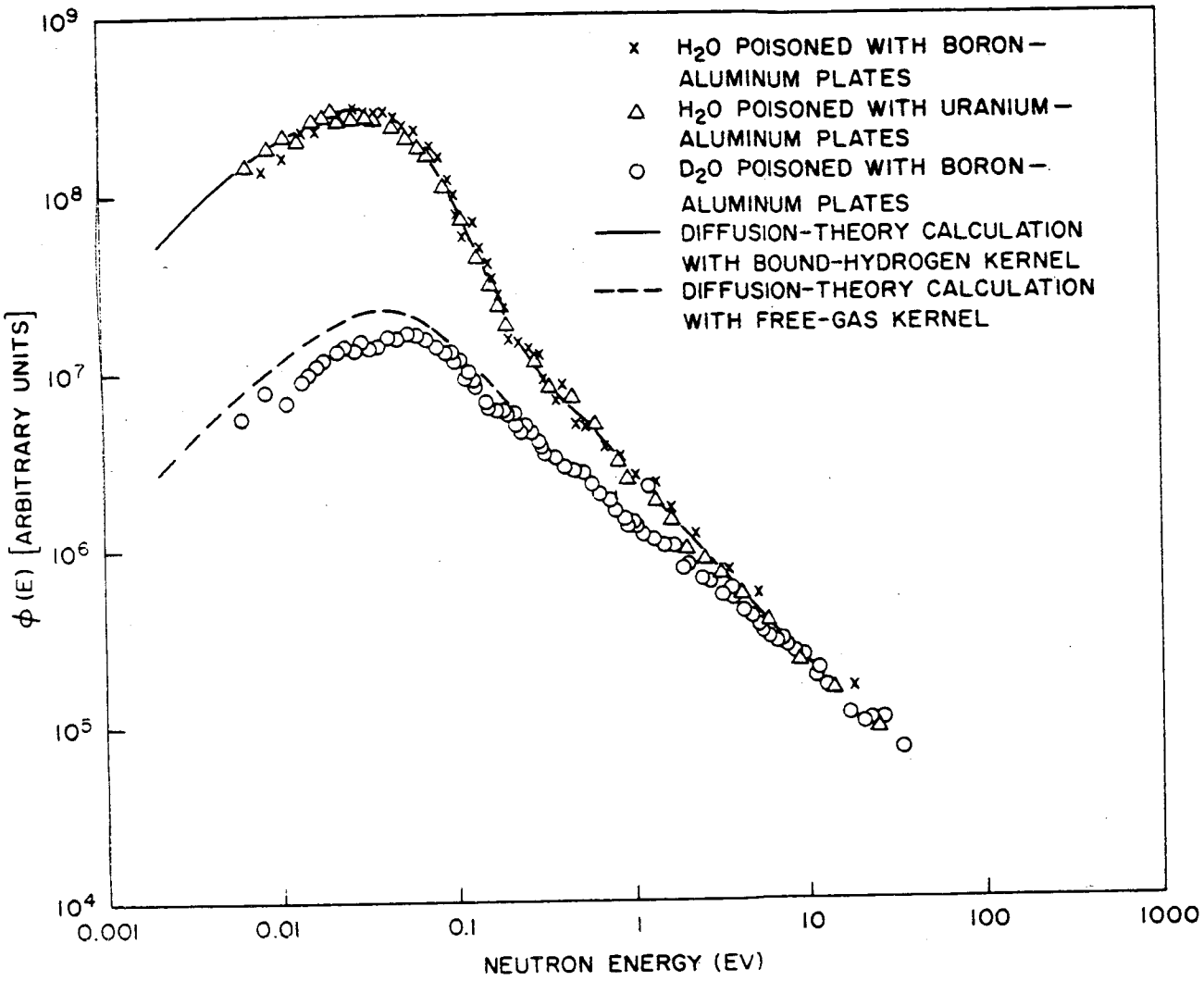

Fig. 60--Comparison of scalar neutron spectra in borated H_2O, D_2O, and H_2O poisoned with uranium-aluminum

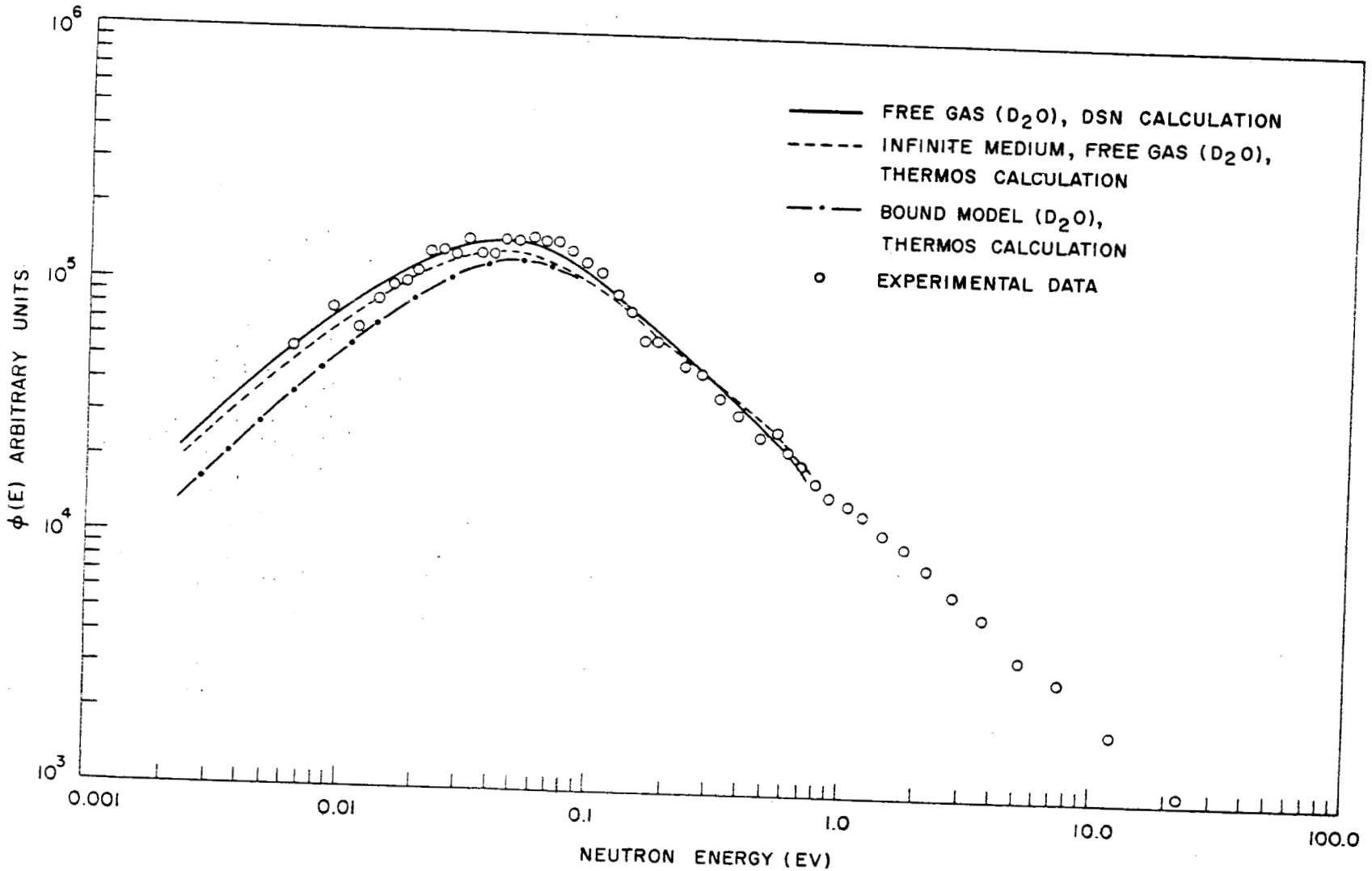

Fig. 61--Spectrum measurement in borated D_2O compared with three theoretical calculations

are concerned, since a detailed programmatic spectral study is still needed for poisoned D_2O systems. However, it should be noted that in the past disagreements between theory and experiment have always been in a direction such that experimental spectra were harder (more epithermal) than theoretical spectra. Usually, this has occurred in studies conducted under nonequilibrium or nonasymptotic conditions. It is hard to conceive of an experimental mechanism to explain the softer spectrum observed in D_2O. Further studies of the scattering kernel and the importance of the coherent scattering are clearly indicated. However, one important significance of the experimental results shown in Fig. 61 should be emphasized. Namely, from the standpoint of reactor design, predictions of scalar spectrum in D_2O systems can be made rather well by crude methods even now. D_2O spectra appear to be far less sensitive to the details of the scattering process than spectra for light water, graphite, polyethylene, or zirconium hydride. Whether the spectra of the angular flux can be equally well predicted through simple procedures remains to be seen.

A final comment should be made about the comparison of theory and experiment. Other experiments in D_2O lattices (namely, those concerned with foil activation, disadvantage studies, etc.) have indicated that the Brown–St. John model[22] for scattering in D_2O gives good results. Although our calculations made with this model are not yet available, the same result will undoubtedly be apparent. Molecular binding is included in the Brown–St. John model, which uses an effective mass of 3.6. Thus, it is expected that the result would be a spectral prediction roughly between the bound-model and free-gas D_2O curves shown in Fig. 61. A further qualitative indication that the Brown–St. John model for D_2O will be fairly good at least for scalar spectra is obtained if one calculates the neutron temperature of the spectrum for comparison with experiment. According to this model,

$$T_n = T_m \left(1 + 1.92 \frac{\Sigma_a}{\Sigma_s}\right) .$$

This gives for our case a T_n corresponding to 0.044 ev, which is very nearly the temperature of our hardened experimental spectrum. Of course, the complete test of the scattering law for practical applications should involve studies not only of scalar spectra but also of angular flux. Coherent effects and transport considerations may render the predictability of angular-flux spectra far more difficult than that of scalar-flux spectra.

6.5. THERMAL SPECTRA IN LITHIUM HYDRIDE

The measurements discussed in this subsection did not arise from any deliberate attempt to measure infinite-medium spectra in lithium hydride,

but occurred as part of a one-dimensional study of lithium hydride shielding The measurements are interesting, however, from the standpoint of integral studies of the scattering law.

Lithium hydride is currently considered a very promising light-weight shield material. It combines the high slowing-down power of hydrogen with the strong absorption properties of Li^6. In addition, the absorption process produces no secondary residual gamma-ray sources which would require shielding. Despite its extremely high absorption properties, lithium hydride is still interesting from the neutron-thermalization standpoint. The infrared measurements of spectra for phonons with wave number $\vec{g} = 0$ show transverse and longitudinal normal modes with frequencies at 0. 098 and 0. 13 ev. The rest of the optical band in this ionic crystal has been observed. Furthermore, information on the specific heat of lithium hydride is also available. Thus, information on which to base an approximate scattering law for this material exists.

Transmission experiments on large pieces of lithium hydride have been carried on for some time by the Oak Ridge National Laboratory (ORNL) shielding group using the General Atomic Linac facility. In addition to these angular-flux measurements, several studies of the scalar flux in this material have been conducted both by ORNL and General Atomic. This neutron spectrum is in principle simpler to calculate than the angular flux and should depend primarily on the absorption and energy exchange properties of the neutron scattering in lithium hydride, whereas the angular flux depends strongly on the transport properties. The present report covers only the attempts made to study the scalar flux (essentially infinite-medium spectrum) in this moderator. Any studies of the angular-flux measurements made during the past year at General Atomic will have to await the solutions of the same one-dimensional problem for water geometries. When our transport codes are fully able to handle that problem, the lithium hydride data will also be calculated.

The experiments were performed in much the same manner as similar experiments conducted for water spectra (refer to Section III, Fig. 14). The scalar-flux spectra were measured at various distances from the source by the zirconium-beam-scatterer technique. Background was measured as usual by removing the beam scatterer. The collimator system then viewed only sources of background plus a $B_4^{10}C$ plug which backs up the glory hole through the assembly. Essentially, five scalar-flux studies have been conducted during the last year in a 10-cm-thick slab of lithium hydride. Two measurements were made by the scatterer technique at 3 cm from the edge of the slab, where the flux peaked. These measurements are in fair agreement, but both differ by approximately 25% with a zero-degree angular flux measured at the same point by the re-entrant-tube technique. Normally, for water systems the scalar flux and the zero-degree angular flux always

agree at the flux peak. However, accurate subtraction of background is very essential but difficult when working with highly absorbing assemblies. Scalar-flux measurements obtained by the scatterer technique at 5 and 7.5 cm from the source agreed approximately with the zero-degree angular-flux measurements made at 3 cm from the source. This may indicate that the scalar-flux measurements at the peak are inaccurate. An angular-flux measurement at 7.5 cm was also performed, and Verbinski[23] used the Purohit relation to reconstruct the scalar flux for this position. The result was a considerably hardened spectrum which did not agree with the direct scalar measurement. Although this problem has been by no means solved experimentally, it is believed that the two scalar-flux measurements taken at 5 and 7.5 cm and the zero-degree angular-flux measurement at 3 cm, which are in agreement, indicate the best value of the spectrum at the present time. The fact that they agree although the flux shape is different at the three positions is not unexpected; the DB^2 leakage correction to the spectrum is negligible for the heavily poisoned lithium hydride. The angular-flux spectrum at zero degrees and the softer scalar-flux spectrum measurement at 3 cm are shown in Fig. 62. The spectrum calculated by Parks[24] with the scattering law predicted for lithium hydride by the code SUMMIT[8] is also shown. The optical levels in lithium hydride mentioned previously are broadened to fit the existing experimental data of Woods, et al.,[25] for inelastic scattering of 0.05- to 0.2-ev neutrons. No acoustic modes are included in the frequency spectrum, the inclusion of which should tend to soften the calculated spectrum somewhat. The spectrum calculated with the lithium hydride bound-atom kernel is only slightly different from that predicted with Nelkin's bound-hydrogen kernel for water. A further discussion of the scattering law is given in Section VII.

In Fig. 63, the scalar spectrum inferred by Verbinski from an angular-flux measurement at 7.5 cm from the source side of the lithium hydride slab is shown, together with various fits to the experimental data. It is believed that these experimental data do not constitute a good estimate of the scalar flux. The Purohit relationships are not considered exact enough in the energy regions where the neutron energy loss on collision depends strongly upon the scattering law. This situation is known to exist for water and is probably also true for lithium hydride. The free-hydrogen result is also shown in Fig. 63. Above 1-ev neutron energy, the spectrum in all cases can be calculated quite well by either the Corngold[26] asymptotic expansion or the transport code NIOBE.[27]

On the experimental side, it was decided that it would be useful to try to fill in the gap in the spectrum measurements in lithium hydride from 300 ev to 200 kev. Lithium-glass detectors were being investigated by ORNL, but this method was quite tedious. Therefore, the high-pressure BF_3 detection system installed at our 50-m flight station was tried in conjunction with ORNL on a series of introductory studies. This system worked far

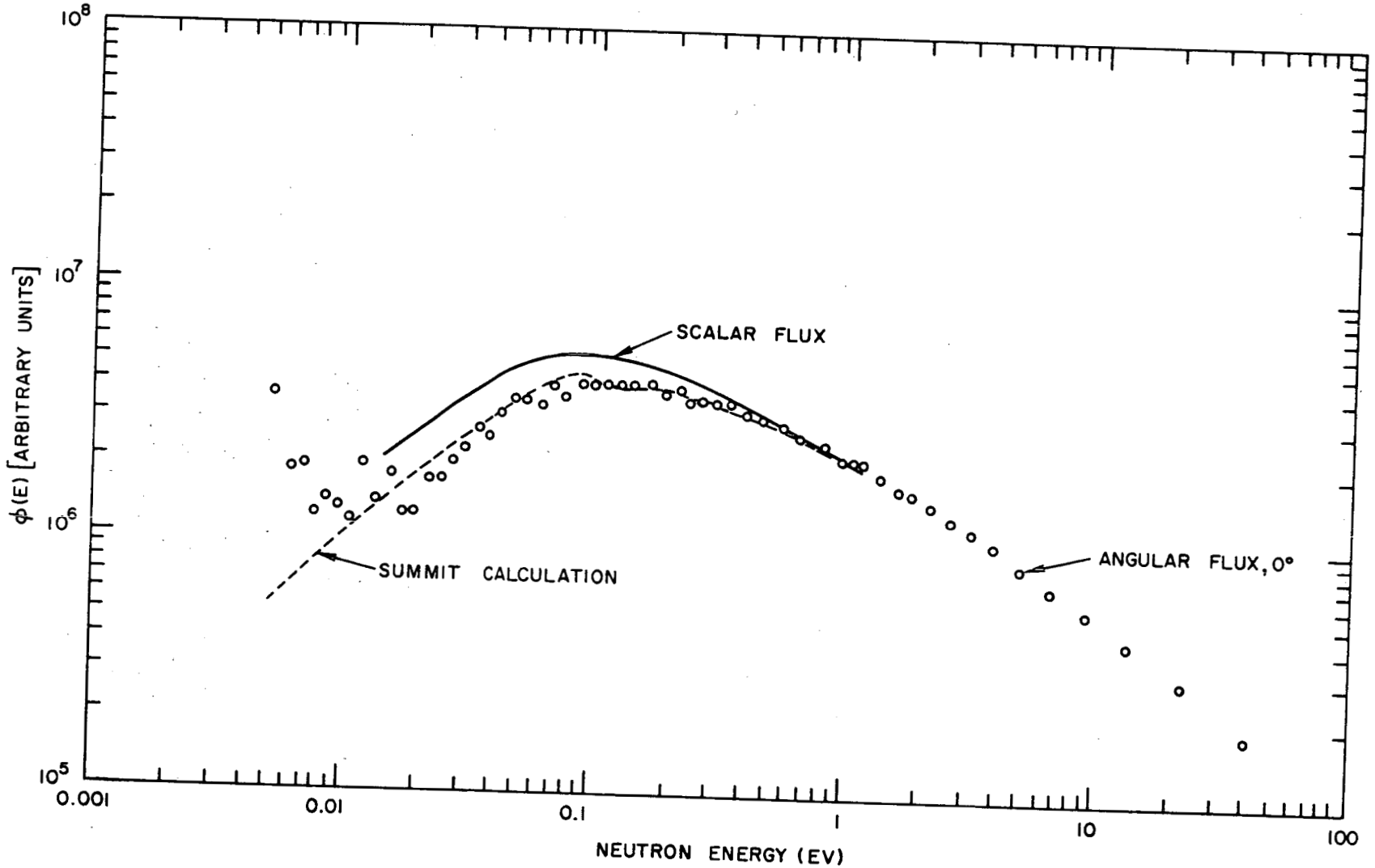

Fig. 62--Zero-degree angular-flux and scalar-flux spectra measured at 3 cm in lithium hydride compared with theoretical calculations by SUMMIT

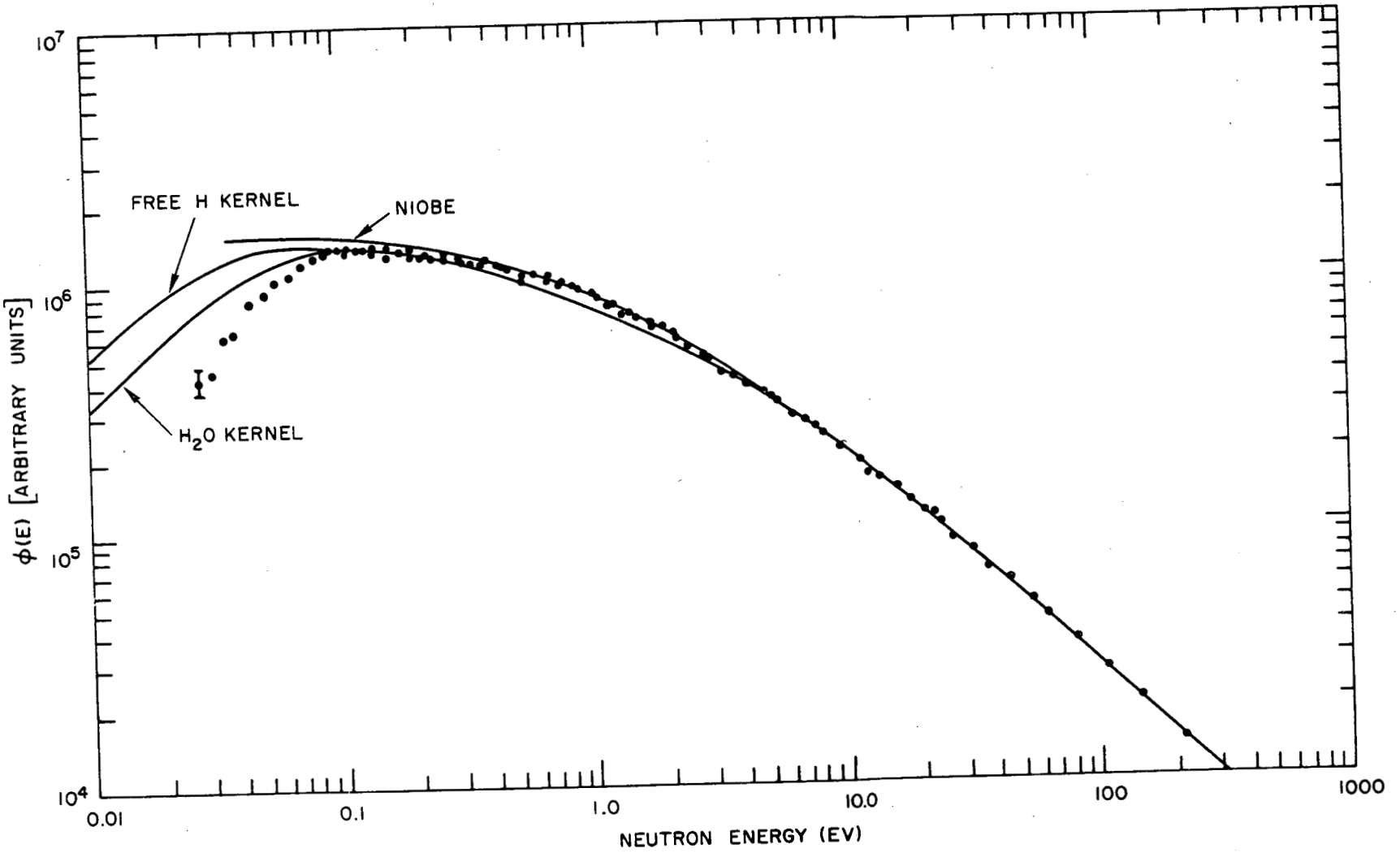

Fig. 63--Scalar-flux spectrum calculated from the zero-degree angular flux at 7.5 cm in lithium hydride compared with various theories

better than was anticipated, remaining extremely sensitive up to well above 100-kev neutron energy while being inherently gamma-insensitive. This discovery means that neutron spectra can now be measured through rather thick shields (>50 to 100 g/cm^2) in two energy bites, using BF_3 detectors from 0.01 ev to 200 kev and liquid scintillators from 200 kev to 13 Mev. The data for this experiment are being reduced by ORNL.

VII. SCATTERING LAW

7. 1. INTRODUCTION

The theoretical portion of the integral thermalization program has concerned the formulation of analytical descriptions of the scattering laws for low-energy neutrons. Comparisons have been made between the predictions of these scattering laws and available differential scattering data. In addition, the theoretical scattering laws have been used to calculate thermal-neutron spectra, which then were also compared with available experimental data.

The scattering law $S(\alpha, \beta)$ is related to the partial differential cross section $d^2\sigma/dEd\Omega$ by the following equation:

$$\frac{d^2\sigma}{dEd\Omega} = \frac{\sigma_b}{4\pi} \frac{\vec{k}}{k_0} \frac{e^{-(\beta/2)}}{T} S(\alpha, \beta), \tag{26}$$

where $\vec{k}_0$ and $\vec{k}$ are the initial and final momenta, respectively, of the neutrons, T is the temperature, σ_b is the bound-atom cross section of the scattering nucleus, and

$$\alpha = \frac{(\vec{k} - \vec{k}_0)^2}{2MT} , \tag{27}$$

$$\beta = \frac{1}{2} \frac{(k^2 - k_0^2)}{T} . \tag{28}$$

Here the nuclear mass, M, is measured in units of the neutron mass, and temperature and energy are given in the same units.

Most theoretical calculations of the scattering law proceed on the assumption that $S(\alpha, \beta)$ can be written in the form

$$S(\alpha, \beta) = \int_{-\infty}^{\infty} \exp[-\alpha w(t) + i\beta t] \, dt ,$$

where w(t) is a function depending only on the dynamics of the scattering system. This is the so-called Gaussian approximation. For harmonically vibrating systems which are isotropic, the form of $S(\alpha, \beta)$ given by Eq. (26) is exact. However, most systems that one encounters in reactor applications are not isotropic and Eq. (26) is only approximate. The SUMMIT[8] code for computing $S(\alpha, \beta)$ for crystalline materials is designed to treat in a rigorous manner anisotropies of the type exhibited by graphite. Thus, for graphite it is possible to test the validity of the Gaussian approximation by direct calculation.

Another physical approximation implied by writing $S(\alpha, \beta)$ in the form of Eq. (26) is that the effects of interference on the neutron scattering are small. For scattering processes which involve large momentum transfers, this approximation is known to be a good one. Furthermore, since most solid moderators are in a polycrystalline form, the interference effects tend to be cancelled to a very large extent. For the inelastic-scattering cross sections of aluminum and magnesium, the calculations of Marshall and Stewart[28] show that the use of the incoherent approximation leads to an error of less than 6%, even for neutron wavelengths as large as 9 Å. Although at the moment we cannot say anything more quantitative about this problem, it seems reasonable to assume that interference effects are negligible for the purpose of calculating thermal-neutron spectra.

In the following subsections, the current extent of our ability to describe the inelastic scattering of neutrons by several of the moderators of interest is discussed. In addition, the extent to which the theoretical models for computing $S(\alpha, \beta)$ are successful in predicting measured thermal-neutron spectra is described. In many cases, the theoretical $S(\alpha, \beta)$ has been derived from information other than that produced by neutron-scattering experiments. For these cases, it is important to determine how well the models predict the measured energy-angle distributions of singly scattered neutrons. In other cases, the results of neutron-scattering measurements have been used to construct models which enable us to extrapolate beyond the ranges of energy and momentum transfer actually observed in the experiments. Zirconium hydride and lithium hydride are examples of cases where such a procedure has been carried out. The models for scattering by graphite, and to a large extent for scattering by H_2O, provide examples of models constructed from evidence obtained by non-neutronic techniques.

7.2. GRAPHITE

Measurements of the differential scattering cross section, $\sigma(\vec{k} - \vec{k}_0)$, for neutrons scattered from an initial momentum $\vec{k}_0$ to a final momentum $\vec{k}$ have been made for graphite at several temperatures.[29] These data have

been examined with the object of determining the confidence with which the frequency distribution, $\rho(\omega)$, of the phonons can be derived. Egelstaff represents the experimental data by tabulating $S(\alpha, \beta)/\alpha$ versus α for a given value of β. Egelstaff and Schofield[30] point out that the frequency spectrum can be obtained by forming $p(\beta)/\beta^2 = \lim_{\alpha \to 0} S_s(\alpha, \beta)/\alpha$, where S_s is the self part of the scattering law, $S_s(\alpha, \beta)$ being that part of $S(\alpha, \beta)$ which is independent of dynamical correlations between different atoms. (The remaining part of S, S_d, arises from correlations between the motion of different atoms. Such correlations are reflected as interference effects in the scattering of neutrons. Except for low values of α, such effects are presumably unimportant for scattering by polycrystalline materials.)

In Figs. 64 through 67, some of the experimental data of Egelstaff at 300°, 653°, and 893°K are plotted. From these data, it is clear that the problem of determining $p(\beta)/\beta^2$ lies in the selection of the range of α values to be used in the extrapolation to $\alpha = 0$. We have fitted the data by a linear least-squares fit to the values of $S(\alpha, \beta)/\alpha$ for values of α greater than 0.1 and 0.2. Frequently, quite different values of $p(\beta)/\beta^2$ are obtained, depending on the low cut-off value assumed for α. This is illustrated in Table 3, which gives values of $S(\alpha, \beta)/\alpha$ at zero α for graphite at 300°K. In most cases, the data give values of $S(\alpha, \beta)/\alpha$ at $\alpha = 0$ which differ in general by less than 30%, depending on whether the minimum value of α considered is $\alpha = 0.1$ or $\alpha = 0.2$. (For $\beta = 0.2$ and 0.3, however, the data are not very accurate.) Similar results are obtained for the data at temperatures of 653° and 893°K.

Table 3

VALUES OF $p(\beta)/\beta^2 = \lim_{\alpha \to 0} [S(\alpha, \beta)/\alpha]$ FOR SEVERAL VALUES OF β AND CUT-OFF VALUES OF $\alpha = 0.1$ AND $\alpha = 0.2$

($T = 300°K$)

	Cut-off for α		Diff.		Cut-off for α		Diff.
β	0.1	0.2	(%)	β	0.1	0.2	(%)
0.2	1.1338	1.5764	-39.0	1.0	0.0904	0.08559	+5.3
0.3	0.3230	0.61164	-89.4	1.2	0.2102	0.16464	+21.7
0.4	0.5078	0.52262	-2.9	1.4	0.1661	0.12722	+23.4
0.5	0.4731	0.47161	+0.3	1.6	0.1375	0.10257	+25.4
0.6	0.3935	0.40949	-4.1	1.8	0.1031	0.08807	+14.6
0.8	0.1064		-----	2.0	0.0861	0.06040	+29.8

It is very difficult to construct a complete frequency distribution, $\rho(\omega)$, from the measurements. Nevertheless, for the purpose of reactor spectrum calculations, Egelstaff has inferred a frequency spectrum from

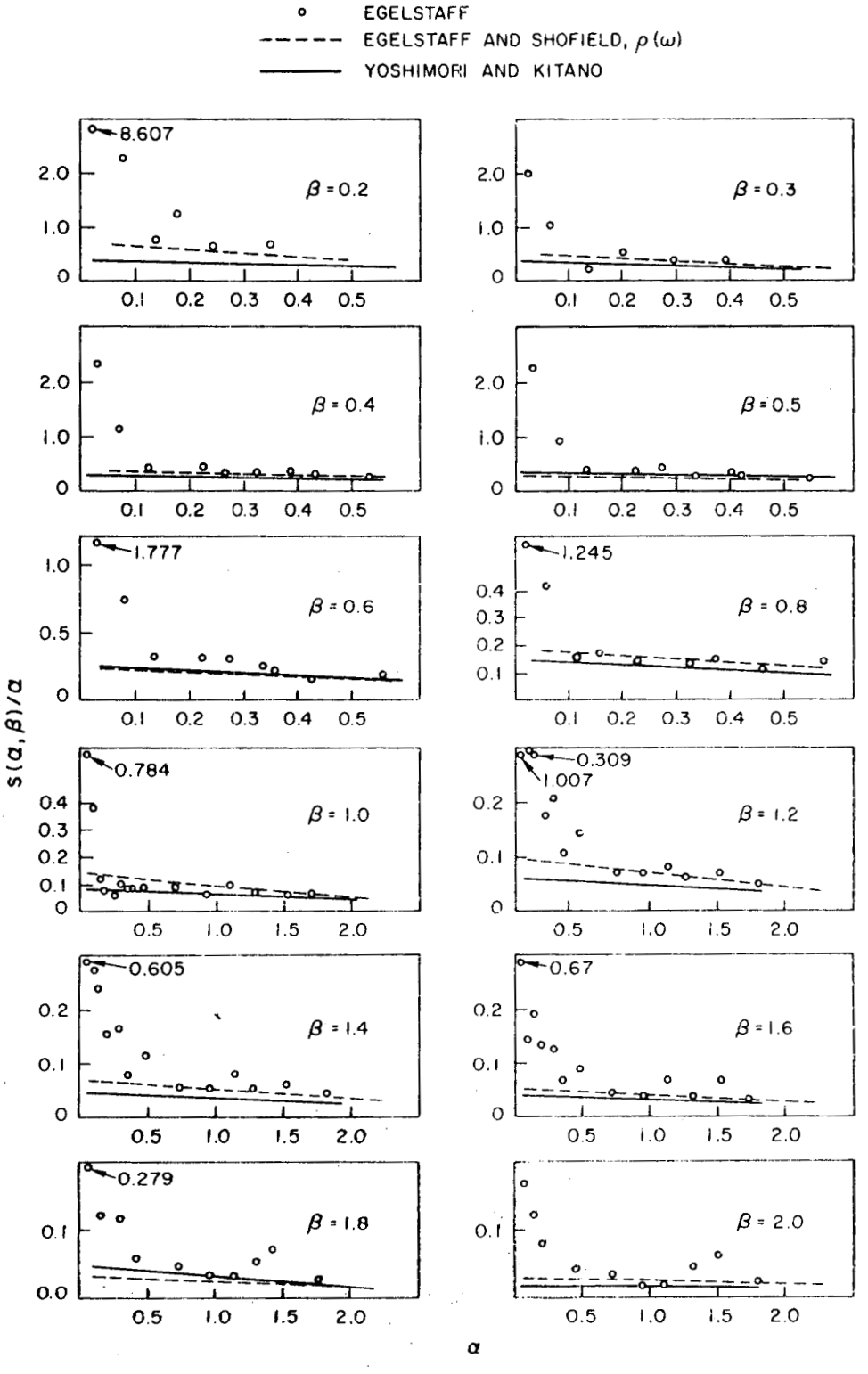

Fig. 64--Variation of $S(\alpha, \beta)/\alpha$ with α for different values of β at 300°K

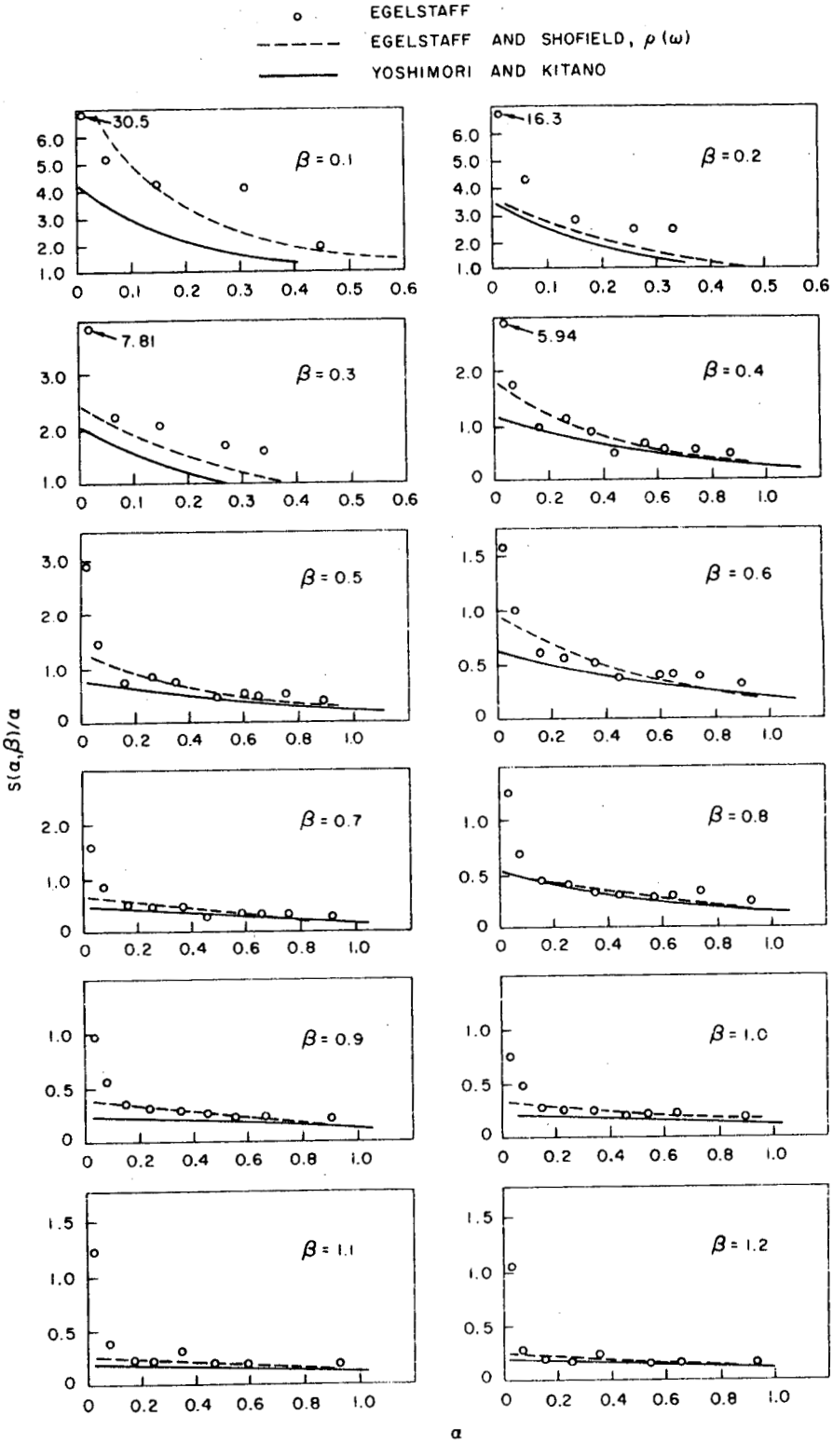

Fig. 65--Variation of $S(\alpha, \beta)/\alpha$ with α for different values of β at 635°K

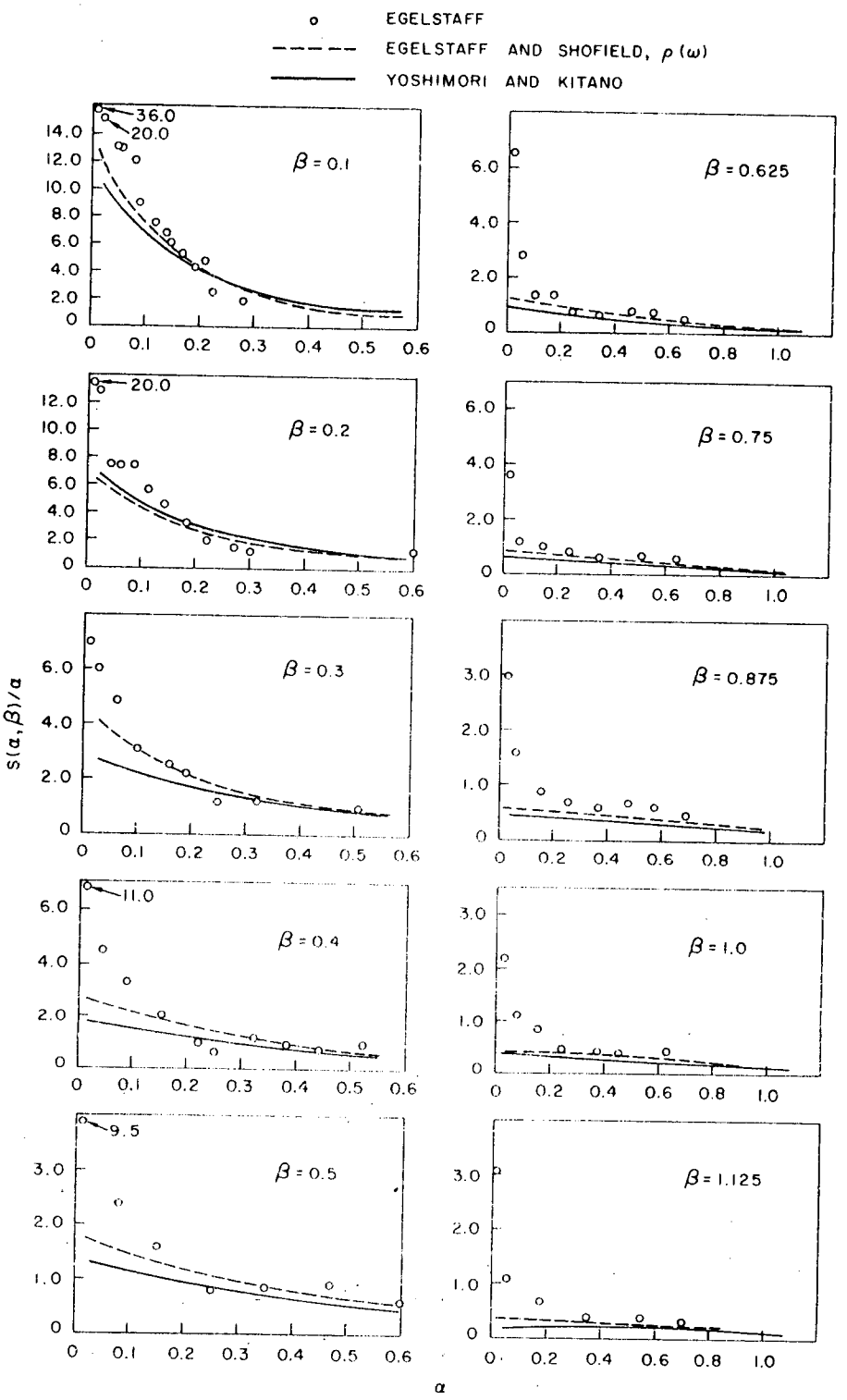

Fig. 66--Variation of $S(\alpha, \beta)/\alpha$ with α for different values of β at 893°K

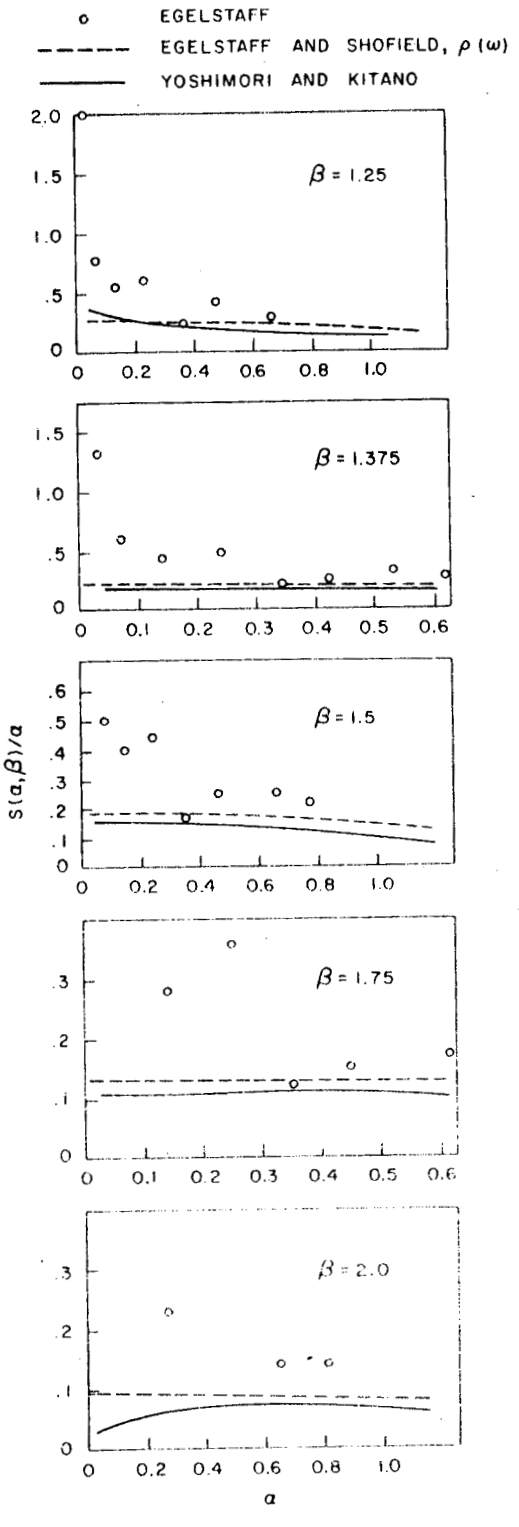

Fig. 67--Variation of $S(\alpha, \beta)/\alpha$ with α for different values of β at 893°K

the experiments.[31] He takes $\rho(\omega)$ to be constant for ω values from 300° to 2100°K and proportional to ω for ω values lower than 300°K. We would concur with the low frequency estimate of Egelstaff; however, information relating to frequencies $\omega \geq 0.1$ ev is either completely absent or of a statistically poor quality.

In addition to these direct measurements of frequency distribution, several authors have derived frequency distributions of the phonons in graphite in order to calculate the specific heat. From these theoretically computed frequency distributions, we have computed values of $S(\alpha, \beta)/\alpha$ for various values of α and β and have compared these values with the experimental measurements. The calculations were performed using frequency distributions derived by Yoshimori and Kitano[32] (Y + K), the Egelstaff-Schofield distribution (EG + S), and a Debye spectrum having the same $\overline{T}$ as Y + K. ($\overline{T} = (1/2)\int_0^\theta \rho(\omega)\, \omega \coth \omega/2T\, d\omega = 1170$°K.) These results are shown in Fig. 64 by the solid, dashed, and dotted lines, respectively. (The results for the Debye distribution lie so near the line $S(\alpha, \beta)/\alpha = 0$ as to be unobservable.) The Y + K and EG + S distributions fit the experimental data reasonably well in the ω range for which measurements have been performed.

The present scattering-law data for graphite are adequate to permit deduction of a reasonable description of the frequency distribution of phonons in graphite only at low values of ω, say, $\omega < 0.01 < 0.1$ ev. Therefore, it is important to determine the sensitivity of the neutron spectrum in poisoned graphite to vibration spectra which differ principally only at high values of ω.

In Fig. 68 is shown the calculated percentage difference between the spectrum calculated with the $\rho(\omega)$ of Y + K and (1) the spectrum calculated with the EG + S $\rho(\omega)$, and (2) the spectrum computed from the free-gas model. In all cases, the graphite is uniformly poisoned with boron to produce a 2200 m/sec macroscopic cross section of 0.136 barn per carbon atom ($C/U \cong 5000$). We chose the $\rho(\omega)$ of Y + K as the reference case, since this $\rho(\omega)$ led to calculated neutron spectra which were in excellent agreement with the measurements of Parks, et al.[33]

As expected, a free-gas representation of graphite at 300°K is very unsatisfactory. At a few tenths of an electron volt, the spectra computed with the EG + S $\rho(\omega)$ are too soft by some 12%. This is due to the selection of a high-frequency cut-off for the optical modes in graphite which is too small; although the Egelstaff scattering-law data allowed estimation of the low-frequency part of the vibration spectrum, they did not provide information concerning the optical modes.

In order to further illustrate the sensitivity of neutron spectra to lattice dynamics, we have considered the case of thermalization by a Debye

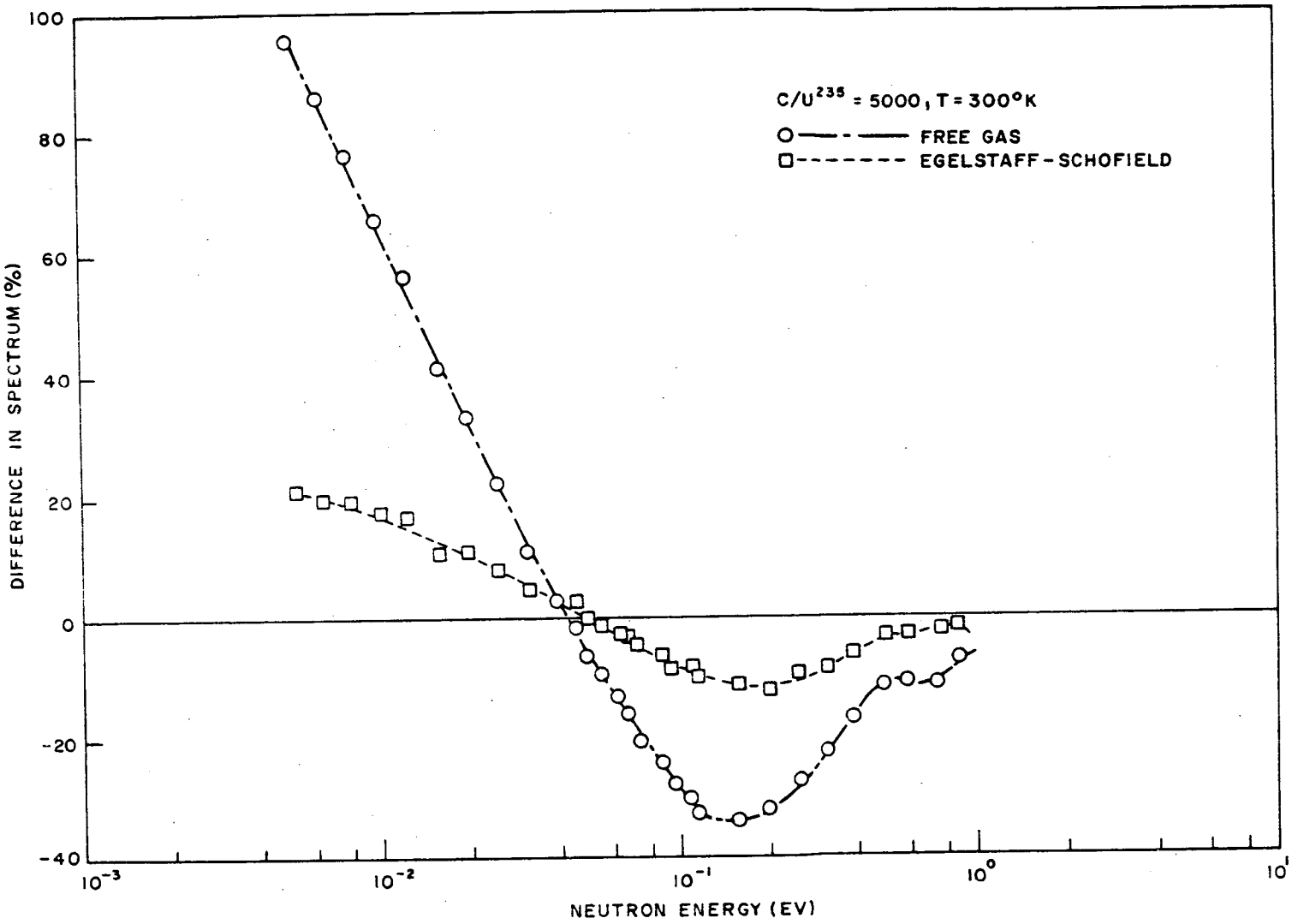

Fig. 68--Calculated percentage difference between spectra using the p(ω) of Y & K and the p(ω) of EG & S and also between p(ω) of Y & K and the free-gas model

crystal of mass 12 with $\rho(\omega) = (3/\theta_D^3)\omega^2$. Figure 69 shows that by using a $\theta_D = 1920^\circ K$, which makes $\overline{T} = 1170^\circ K$ (the same $\overline{T}$ as pertains for Y + K graphite), one obtains a significantly harder spectrum than for the case of Y + K graphite. An abnormally large number of high-frequency modes is responsible for this.

From all these considerations, we conclude that the frequency distribution of Y + K appears ideally suited for any thermalization problem in graphite. It is not necessary, however, to have as much detail in the frequency distribution as is contained in the Y + K $\rho(\omega)$, but it is necessary to have a good high-frequency cut-off and a proper split between the optical and low-frequency modes.

All of the above calculations have been performed under the assumption that the lattice vibrations of graphite are isotropic. On the other hand, in other investigations, the anisotropic nature of graphite has been treated in a realistic way. (8, 33, 34) Since a considerable amount of computer time is involved in the computation of a scattering kernel which includes the effects of anisotropy, it is of considerable interest to determine what effect the computationally convenient assumption of isotropic graphite will have on the thermal-neutron spectrum and on $S(\alpha, \beta)$.

Thermal-neutron spectra in a homogeneous medium of poisoned graphite have been computed for several different poison concentrations, corresponding to C/U^{235} atom ratios in the range from 1000 to 20,000 at $300^\circ K$ for anisotropic and isotropic graphite. For all cases, the isotropic spectra are slightly softer than for the anisotropic case. The maximum percentage difference in the spectrum is only 1% at a few tenths of a volt for $300^\circ K$ for a C/U^{235} atom ratio of 5000 (see Fig. 70). A C/Pu^{235} atom ratio of 5000 has a maximum percentage difference of only 1.2% (see Fig. 71). On the other hand, an 8% difference exists in the total inelastic scattering cross section near 0.1 ev. The effect of the crystalline anisotropy amounts to as much as 10% in $S(\alpha, \beta)$. These investigations are continuing for the case of higher temperatures and for larger values of α.

7.3. ZIRCONIUM HYDRIDE

The thermalization of neutrons by zirconium hydride has been investigated. Studies were made to determine to what extent a model based on harmonic lattice vibrations is consistent with the experimental evidence. It was determined that this model does not lead to agreement with the observed neutron spectrum, nor to agreement with the observations of Woods, et al, (25) on neutron scattering with energy transfers greater than 0.15 ev.

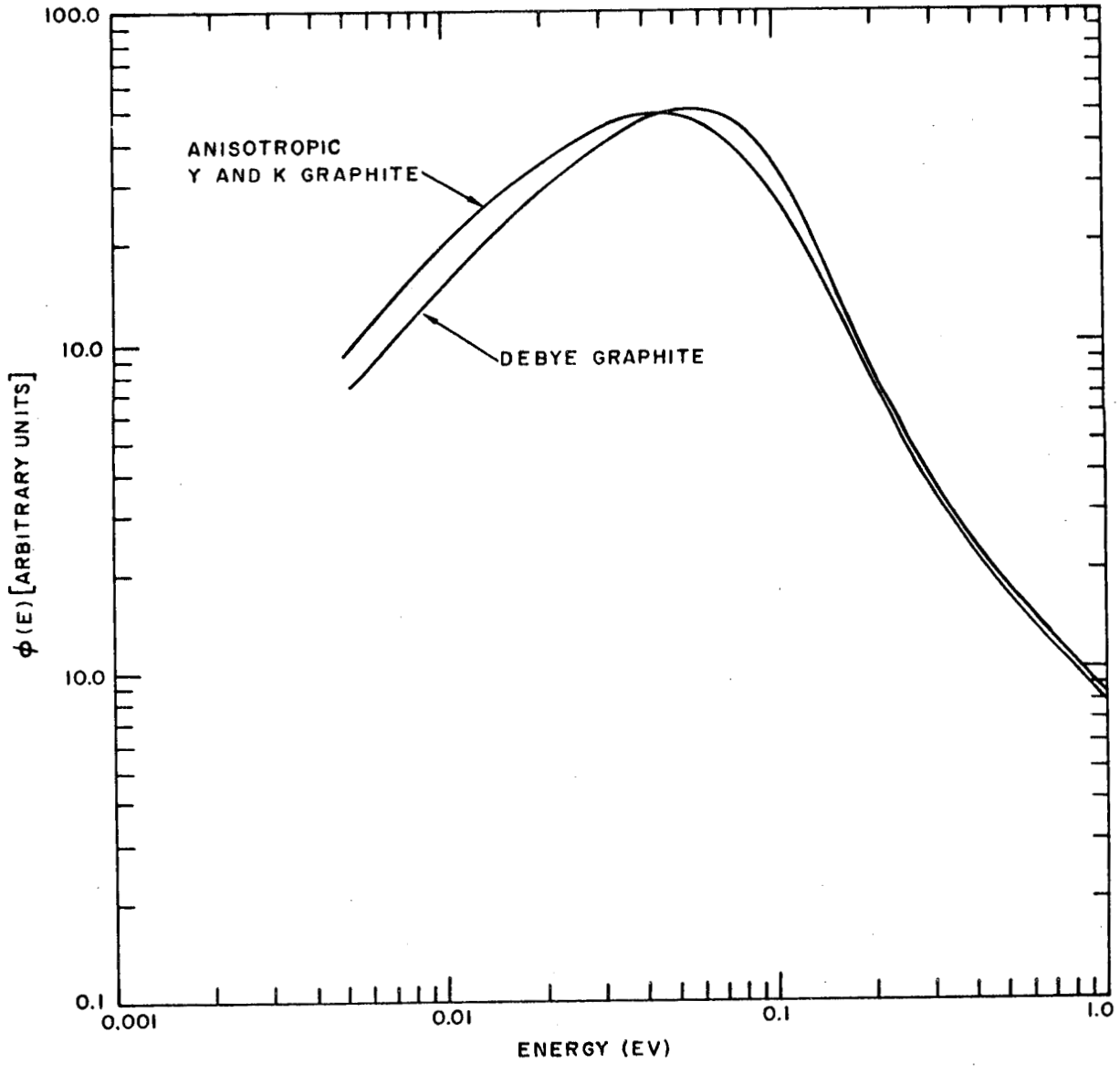

Fig. 69--Calculated spectra showing the difference between anisotropic Y & K graphite and Debye graphite

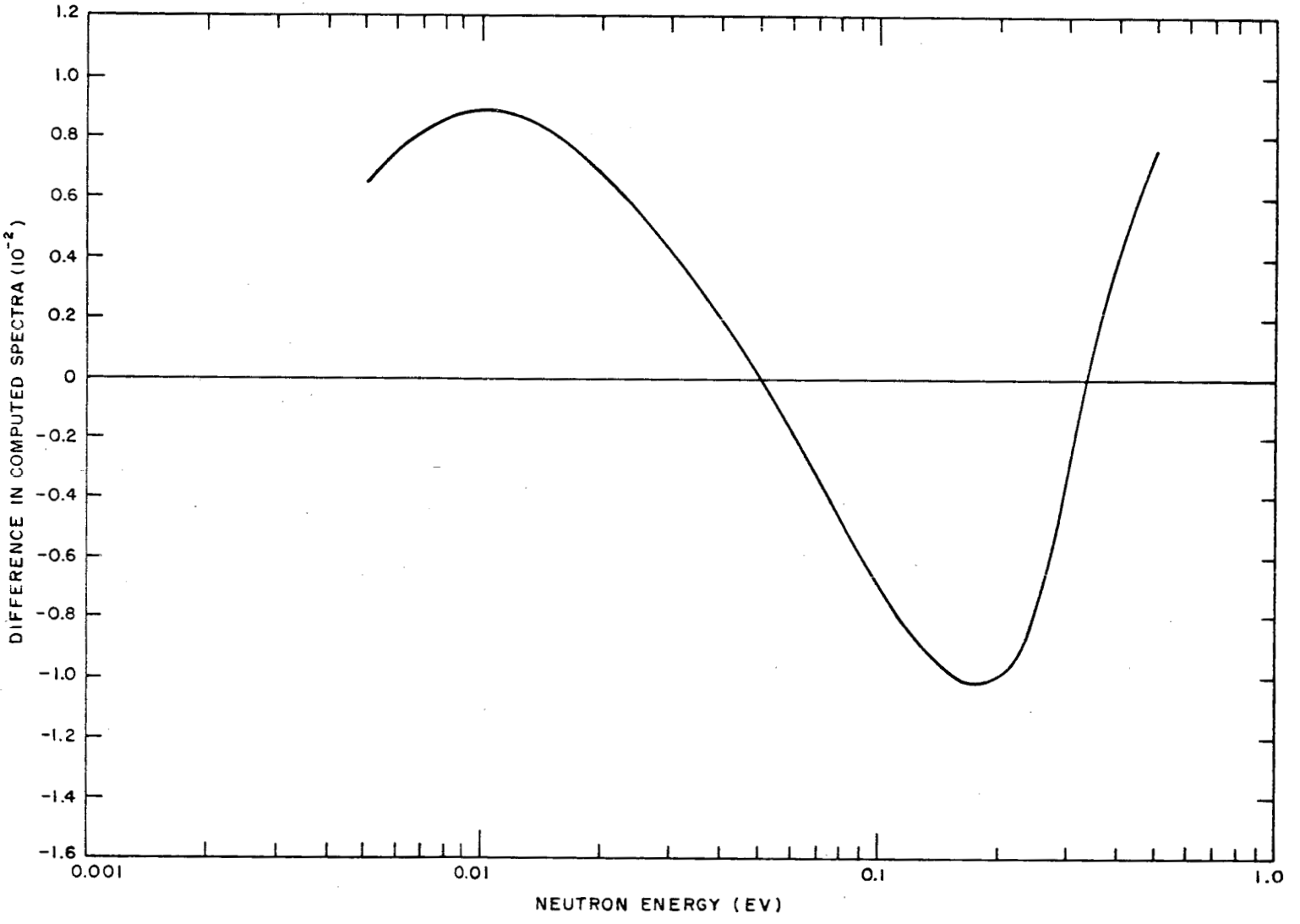

Fig. 70--Per cent difference in spectra for isotropic and anisotropic graphite with a C/U^{235} atom ratio of 5000

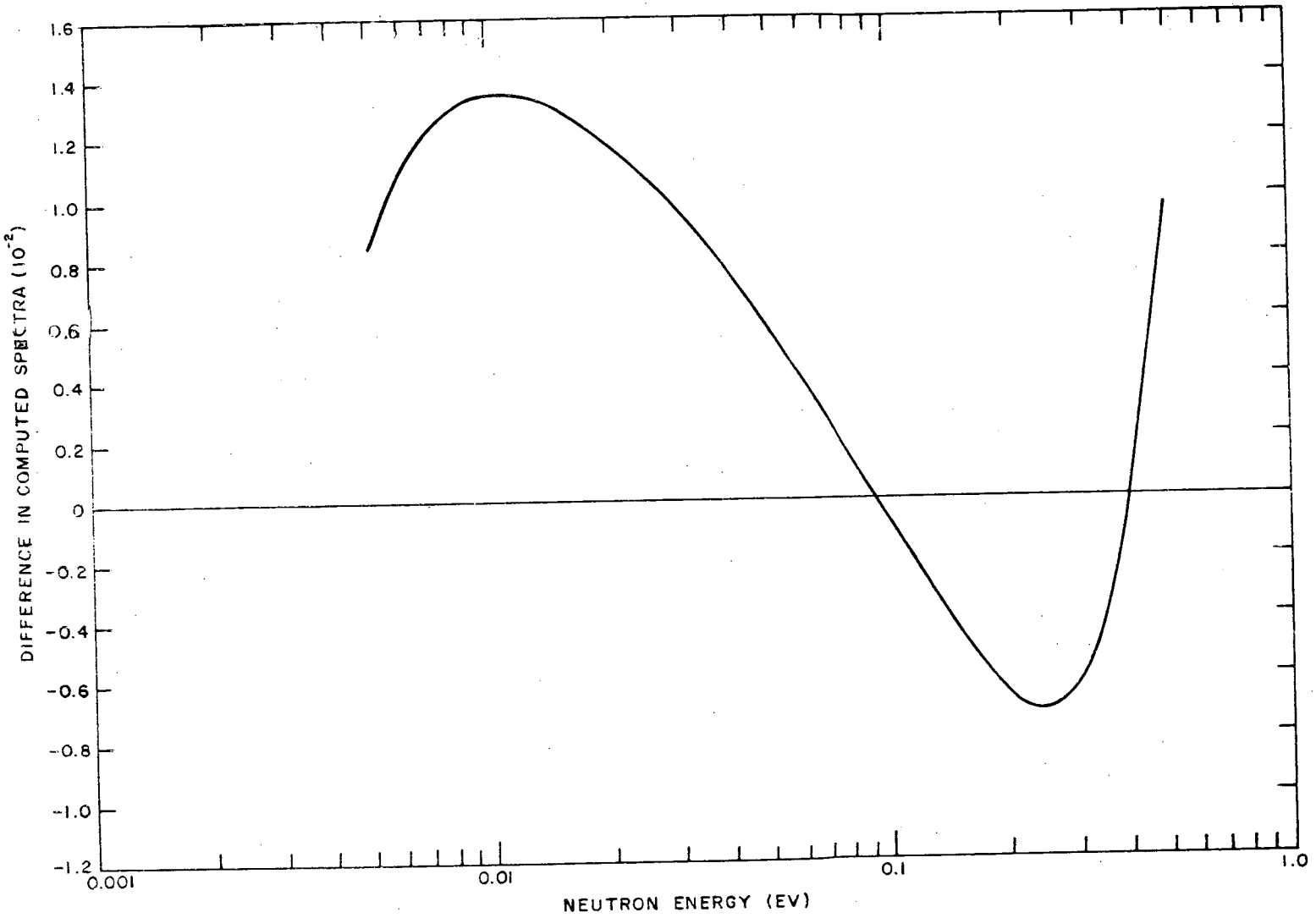

Fig. 71--Per cent difference in spectra for isotropic and anisotropic graphite with a C/Pu^{235} atom ratio of 5000

The hydrogen atom is assumed to execute isotropic harmonic vibrations. The spectrum $\rho(\omega)$ of vibrations is assumed to be of the form

$$\rho(\omega) = \frac{1}{2\pi\sigma^2} \exp\left[-\frac{(\omega - \omega_0)^2}{2\sigma^2}\right] ,$$

where the values

$$\omega_0 = 0.136 \text{ ev} ,$$

$$\sigma^2 = 7.2 \times 10^{-5} (\text{ev})^2$$

are estimated from Woods' data. Conclusions based on these values of the parameters are not affected by the uncertainties that exist in the parameters themselves.

The $\rho(\omega)$ defined above was used as input to the code SUMMIT,[8] and a scattering kernel was generated. The kernel was calculated for 100 energies extending up to 0.52 ev. Using this kernel, spectrum calculations were performed for a zirconium hydride moderator poisoned with 4.95 barns/hydrogen atom at 2200 m/sec, with the following sources:

1. $\text{source} = \text{erf}\sqrt{\frac{E}{kT_{\text{eff}}}}$,

2. $\text{source} = \int_{0.52}^{\infty} \sigma_H(E' \rightarrow E) \frac{1}{E'} dE'$,

where $\sigma_H(E' \rightarrow E)$ is the kernel for an isotropic oscillator with a level spacing equal to 0.136 ev,

3. Same as source 2 except that it is corrected for the finite width of the level at 0.136 ev.

The results of these calculations are shown in Figs. 72, 73, and 74, respectively. The figures also show the experimental results. The conclusions drawn from these results are (1) that the model of harmonic lattice vibrations used here is inadequate to explain the observed spectrum, and (2) that the calculated spectrum is insensitive to the difference in the energy-dependent shapes of the sources considered. In Fig. 75, source shapes 2 and 3 used for the calculations described above are shown. Figure 76 shows comparisons of the quantity $\sqrt{E_0}\,(d^2\sigma/dEd\Omega)\,(E_0 \rightarrow 0, \theta)$ times the normalizing constant (E_0 being the incident energy) with the

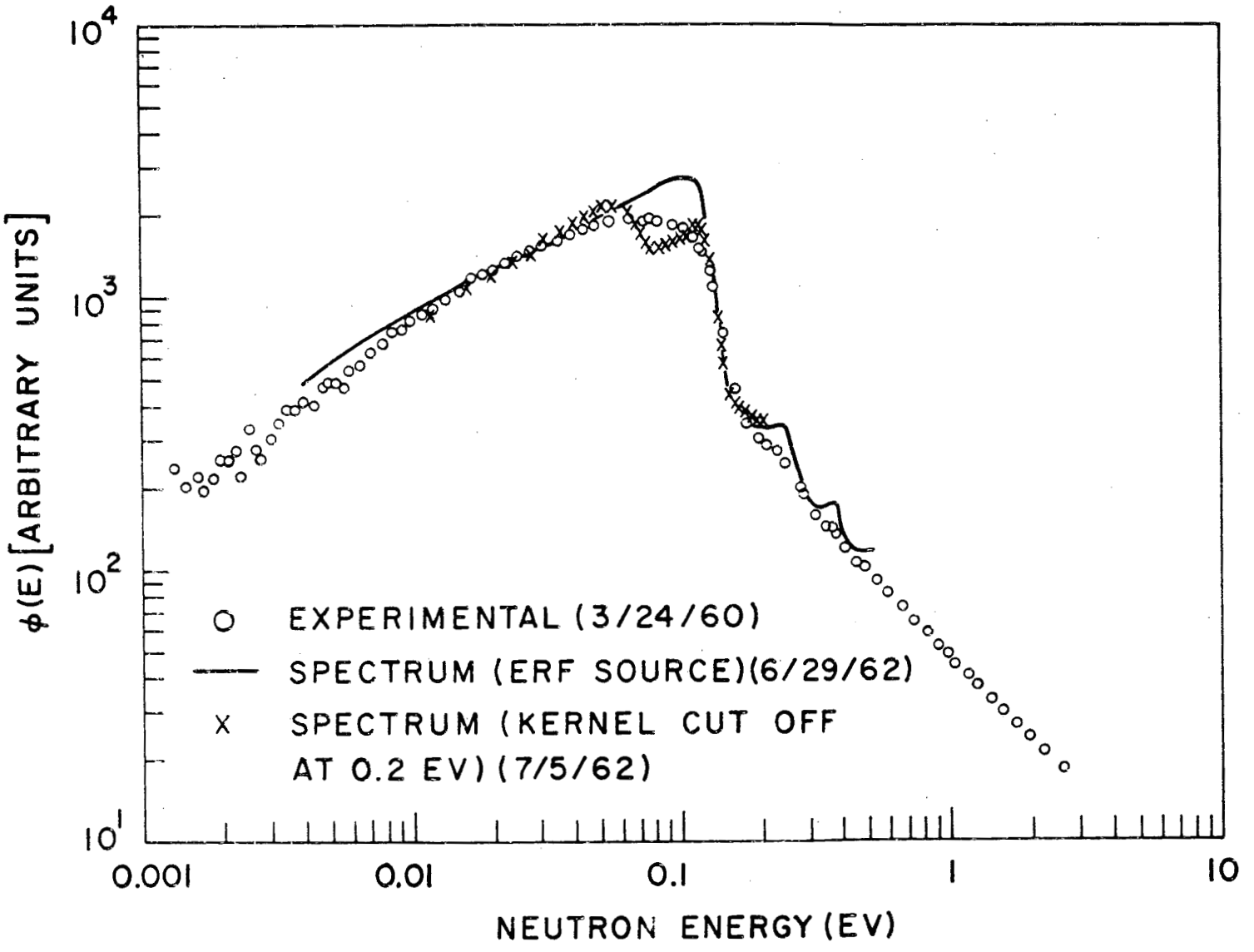

Fig. 72--Measured spectrum in $ZrH_{1.5}$ compared with theoretical spectra using an error-function source and with the kernel cut off at 0.2 ev.

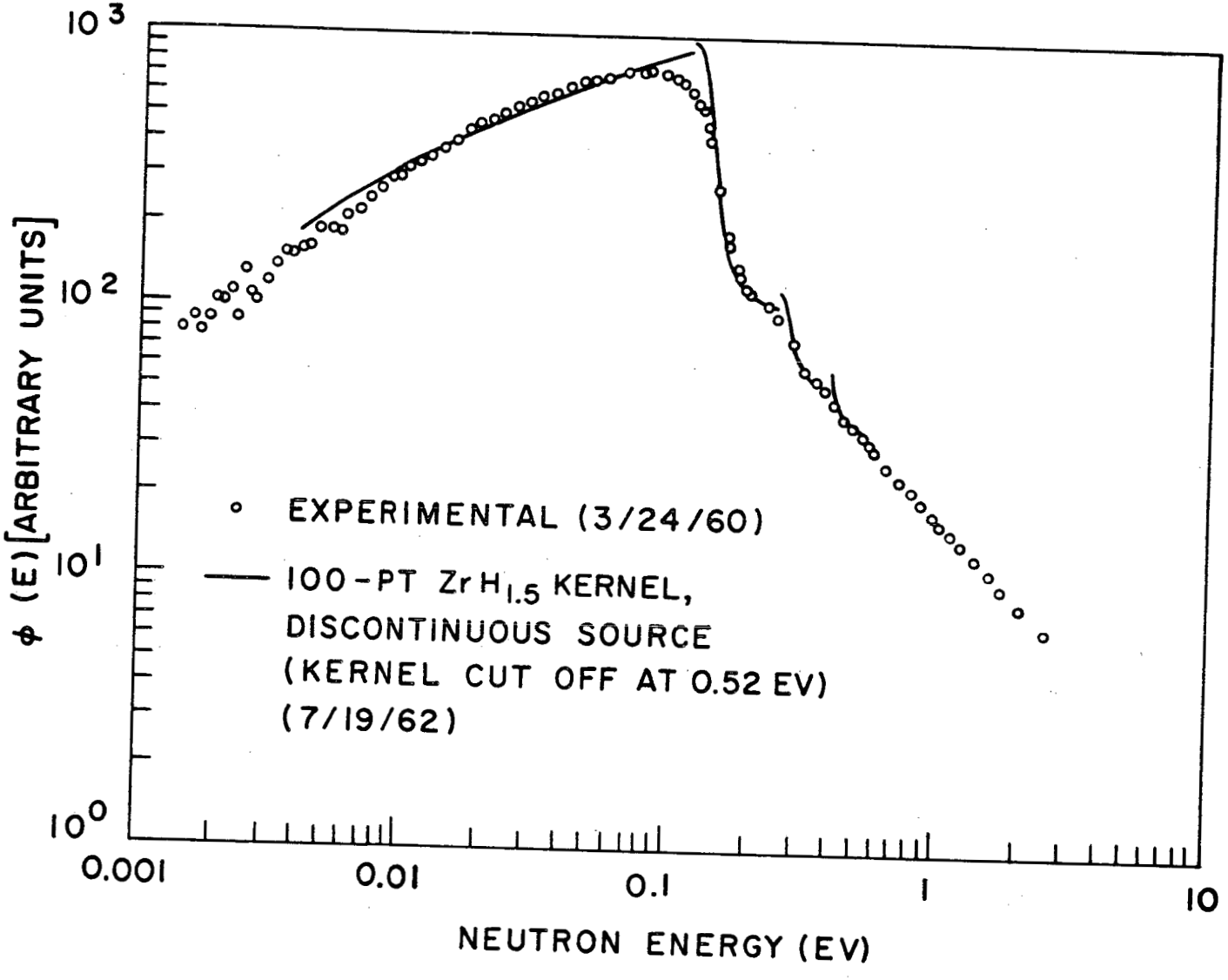

Fig. 73--Measured $ZrH_{1.5}$ spectrum compared with theoretical spectrum using a discontinuous source

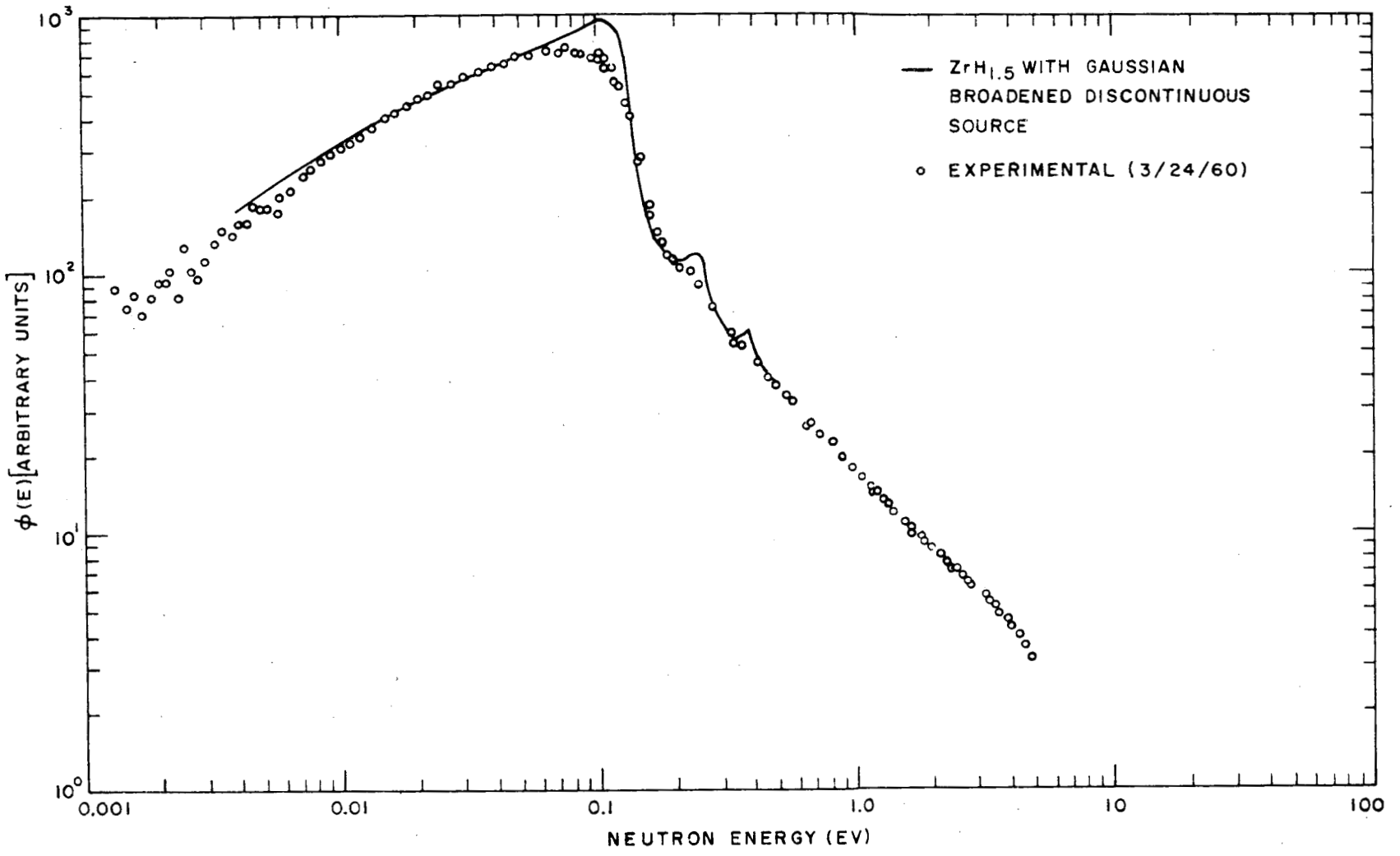

Fig. 74--Measured $ZrH_{1.5}$ spectra compared with theoretical spectrum using a Gaussian broadened discontinuous source

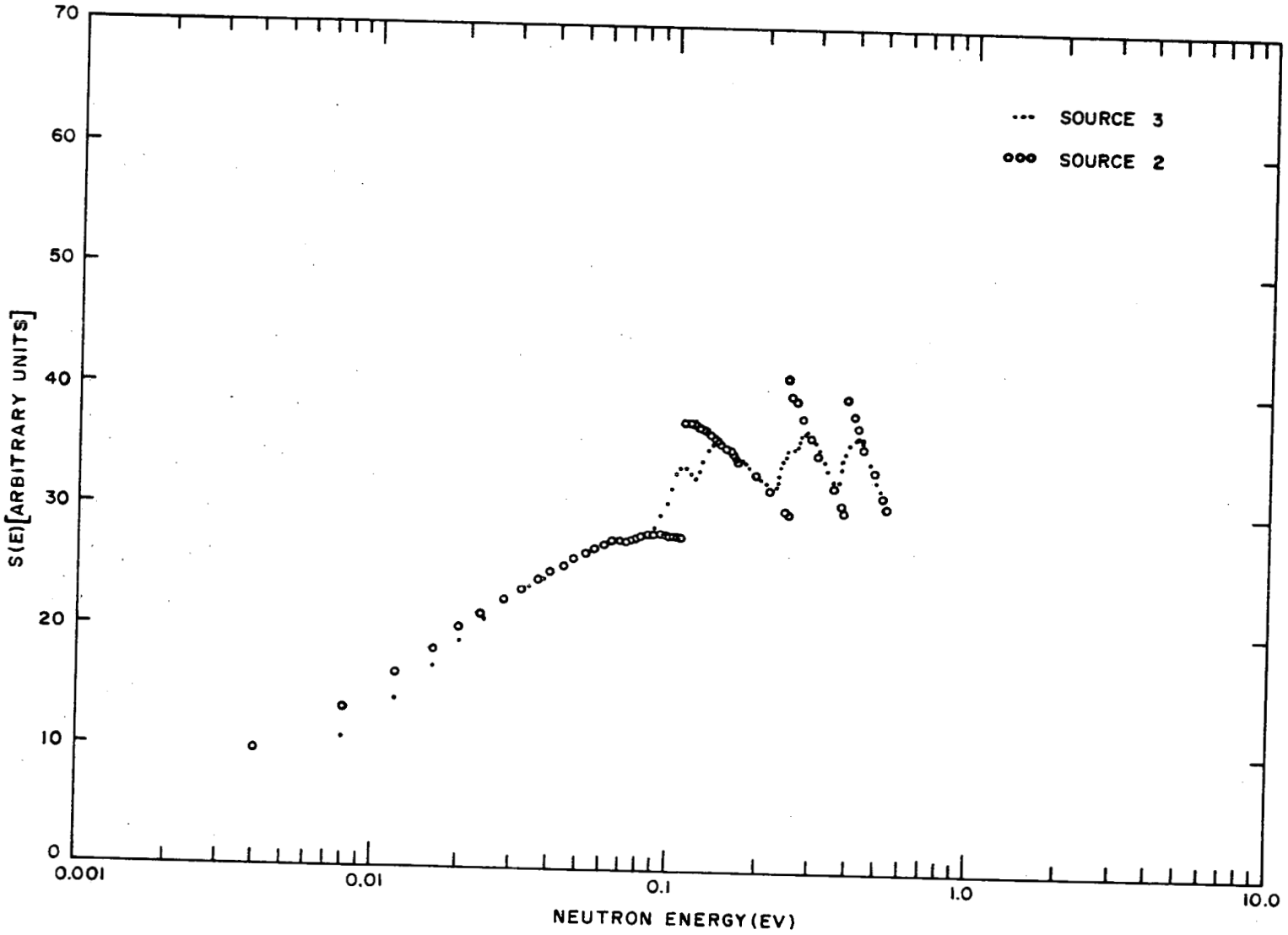

Fig. 75--$ZrH_{1.5}$ spectra calculated using sources (2) and (3)

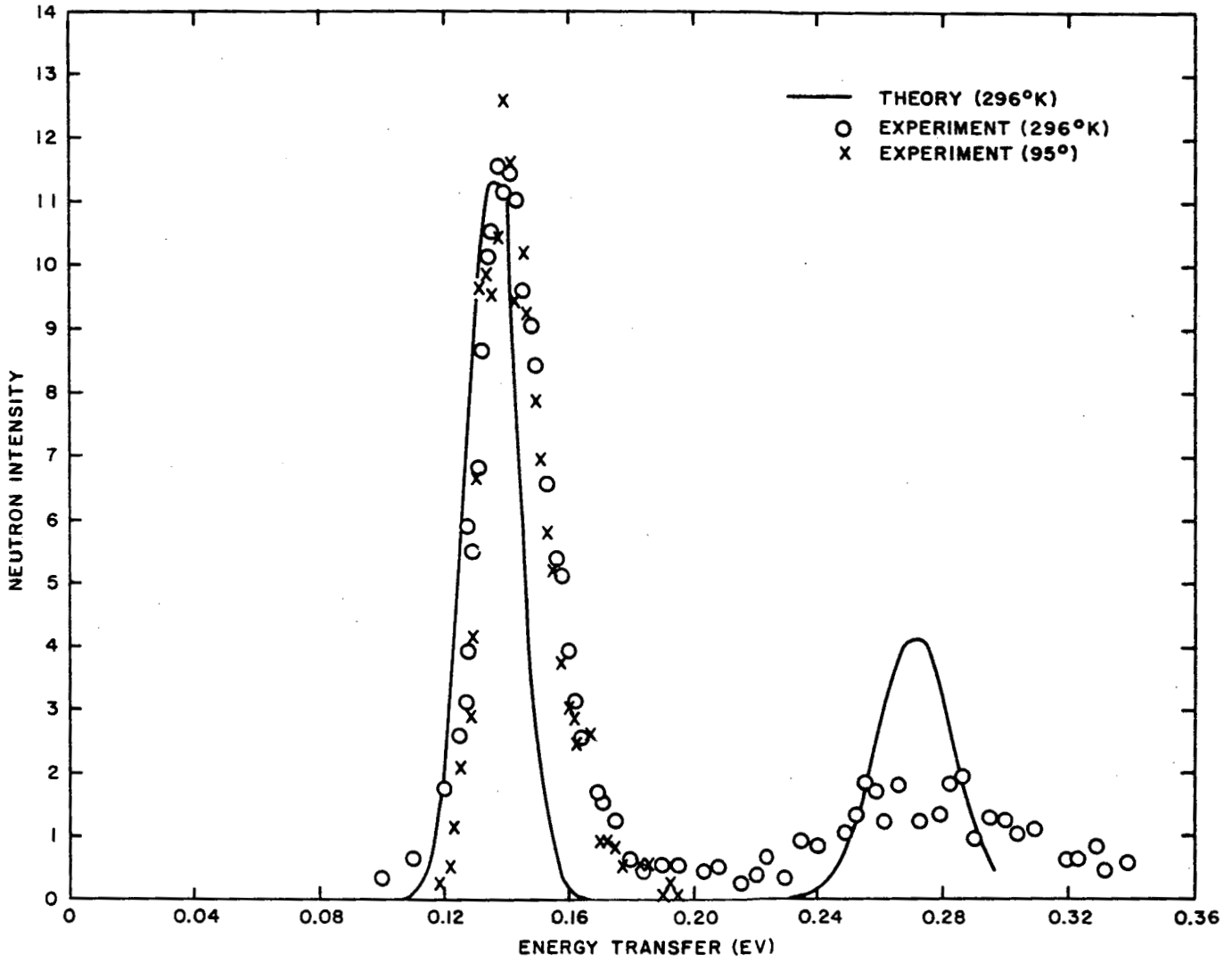

Fig. 76--Comparison of experiment and theory for neutron intensity versus energy transfer

observations of Woods. The model was chosen to fit the observations reasonably well only in the vicinity of the peak at about 0.136 ev. The calculation does not agree with the observations for $E_0 > 0.15$ ev. This is possibly due to anharmonicity of the atomic vibrations in zirconium hydride. Although it cannot be ignored that instrumental effects tend to broaden and lower the peak corresponding to the two-phonon excitation around 0.272 ev, both neutron spectra and scattering data suggest the existence of rather large effects arising from anharmonic lattice vibrations.

The idea that anharmonic effects should be manifested in neutron experiments is substantiated by measurements of the diffusion of hydrogen atoms in nonstoichiometric compositions of hydrogen and zirconium. The activation energy for diffusion is measured to be about 0.5 ev. This energy is not very large compared with the first two excited states of the zirconium hydride harmonic oscillator model. This does not imply, however, that diffusion is the mechanism for the level broadening in zirconium hydride. The time scale for diffusive processes is much too long to account for the observed line width in neutron-scattering experiments. It seems reasonable that the broadening is the result of anharmonic effects of a nondiffusive nature. At the moment, it is not known how to take account of such effects in a quantitative way.

7.4. WATER

During the past year, new experimental evidence has been developed whose explanation unquestionably requires an alteration of the physical basis of Nelkin's model[35] for the scattering of neutrons by water. Consequently, we have not attempted to develop further the theory for the scattering of neutrons by water. However, Egelstaff[36] has recently presented experimental results which strongly suggest that the effects on neutron thermalization of the vibrations of the hydrogen atoms in the H_2O molecule are considerably underestimated by the current Nelkin model. The changes suggested by the recent Egelstaff data can be treated within the framework of either of the IBM-7090 codes THERMIDOR[7] and GAKER.[4] The quantitative determination of the magnitude of these effects will be investigated in the near future as part of the program for analyzing the scattering-law measurements for H_2O. In Section VI of this report, we have made some preliminary comparisons between calculated spectra obtained using Egelstaff's suggested modification of the Nelkin kernel and the original kernel. The energies for each degree of freedom and the effective masses are given in Table 4.

7.5. LITHIUM HYDRIDE

A scattering kernel for lithium hydride has been calculated with the

Table 4

A COMPARISON OF THE ASSIGNED MASSES FOR THE ORIGINAL AND MODIFIED NELKIN KERNEL

Degree of Freedom	Energy (ev)	Nelkin Masses	Egelstaff Masses
Translational	kT	18	18
Hindered rotational	0. 06	2. 32	5. 15
Vibrational	0. 205	5. 84	4
Vibrational	0. 48	2. 92	2

aid of the data of Woods, et al.[25] The procedure for obtaining the kernel consisted in guessing a frequency distribution, $\rho(\omega)$, which, when used to calculate the inelastic scattering, would give a reasonable fit to the experimental data. The results of this procedure are shown in Fig. 77. In this figure, $E_{zero} = E_0$ is the initial neutron energy, and

$$\text{Sig(cos)} = \frac{k_0}{k} \frac{d^2\sigma}{dEd\Omega} (E_0, E_f, \cos\theta) \ .$$

In the calculations, E_f is taken to be 0. 003 ev, which is about the mean energy of neutrons which scatter down to energies less than that corresponding to the Bragg cut-off energy of the beryllium filter. To obtain better agreement with the experimental results, it will be necessary to increase the number of vibrational modes between 0. 11 and 0. 15 ev relative to the number of vibrational modes between 0. 06 and 0. 11 ev.

The experimental data which we have used to construct our kernel give no information about the vibrational modes in lithium hydride having energies of less than 0. 06 ev. Consequently, such modes have not been included in the calculation of the kernel. The absence of the low-energy modes in the $\rho(\omega)$ from which the scattering kernel was calculated will have an effect on the calculated neutron spectrum which is in a direction opposite to that of the effect resulting from the fact that the $\rho(\omega)$ we have used underestimates the mean energy in the modes with energies above 0. 06 ev. That these effects are counter effects is significant in view of the fact that the agreement between the measured and calculated neutron spectrum (see Fig. 63) in lithium hydride is reasonably good.

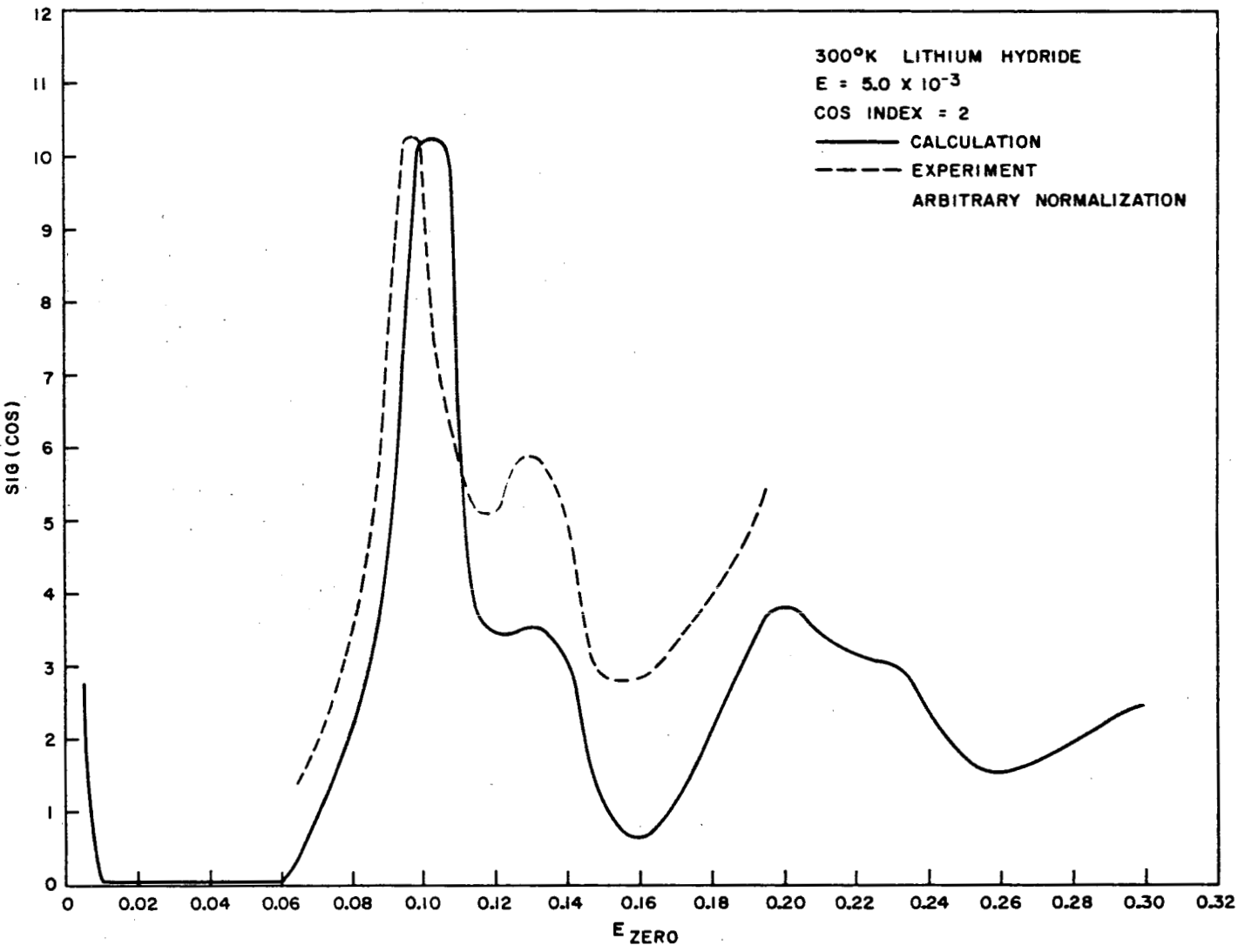

Fig. 77--Fit to experimental data using a "best guess" frequency distribution for computing kernel

VIII. NONSTATIONARY PROBLEMS

8.1. TIME-DEPENDENT THERMALIZATION SPECTRA

A large theoretical and experimental effort has been devoted to the calculation and measurement of stationary neutron spectra in different media and geometries. Very little attention, however, has been given to the analysis of spectra produced by time-dependent sources. More work in this field would seem to be justified for a number of reasons:

1. In the well-known diffusion cooling experiment, the decay constant of the asymptotic spectrum in different moderators is measured as a function of the size of the assembly. The question of the existence of such a well-defined decay constant has arisen for very small assemblies.[37] It seems to be worthwhile to clarify this problem experimentally as well as theoretically.

2. The time-of-flight method of measuring stationary spectra with a pulsed neutron source relies on the shortness of the die-away time of the neutron population in the assembly after each pulse as compared with the time-of-flight. It would be useful to know more about the actual transients in order to extend the method to systems where it is not quite possible to satisfy this condition and where, consequently, the mean-emission-time corrections are important.

3. Finally, it seems to be quite interesting to calculate transient and asymptotic spectra with different theoretical scattering kernels in order to find out how these predicted spectra agree with experiment.

The theoretical aspect of this program has been partially carried out. Only space-independent problems have been considered so far.[38] However, these have included one (spatial) mode solution for finite media where the leakage is taken into account by means of a fictitious $B^2D(E)$ absorption term.

Transient and asymptotic spectra have been computed for different moderators and scattering kernels by means of the time-moments method.[39] The source used in these calculations is of the form

$$S(E,t) = \text{const.}\ \delta(t - t_0)(avt_0)^{2(1-b)/\gamma}\ e^{-avt_0}\left(\frac{E_0}{E}\right)^{-b/\gamma}\frac{1}{E}\ , \qquad (29)$$

with

$$a = \frac{\xi}{\gamma}\,\Sigma_s + B^2\bar{D}\,, \qquad b = \frac{B^2\bar{D}}{a}\,,$$

where t, v, E are time, velocity, and energy, and Σ_s, ξ, γ, B^2, D have their usual meanings. This is an approximate expression for the slowing-down spectrum[40] produced at time t_0 by a burst of neutrons of energy E_0 injected into the moderator at t = 0. t_0 is chosen to produce the maximum of S(E, t) at 1 ev. A plot of S for a graphite moderator is shown in Fig. 78 for two values of B^2. With this source, the exact time moments $\psi_n(E) = \int_0^\infty \psi(E,t)t^n\,dt$ for a 1/v poisoned medium were calculated by the iteration procedure described in Ref. 39 using the thermal-spectra code GATHER. The time-dependent flux was then obtained from the following equation:

$$e^{-\alpha_p t}\,\psi(E,t) = \phi_0(E)\,e^{-\alpha_0 t} + e^{-\alpha_1 t}\sum_{n=0}^{N} a_n(E)L_n(\alpha_1,t)\,, \tag{30}$$

with

$$a_n(E) = \Delta_0^n\left[\frac{\psi_{m(E)}}{m!}\,\alpha_1^{m+1} - \phi_0\left(\frac{\alpha_1}{\alpha_0}\right)^{m+1}\right]. \tag{31}$$

Here, $L_n(x)$ refers to the Laguerre polynomial of n^{th} degree, Δ_0^n stands for the finite differences of order n,

$$\Delta_0^n y_m = \sum_{m=0}^{n}\binom{n}{m}y_m(-1)^m\,, \tag{32}$$

and $\alpha_p = v\Sigma_{a(\text{poison})}$. $\phi_0(E)$ is the asymptotic spectrum which describes the neutron distribution at long times after a source burst (i. e., the first energy mode in the modal expansion), and α_0 is the corresponding decay constant. Both can be obtained from the time moments of large order by the relations

$$\alpha_0 = \lim_{K\to\infty}\frac{K\psi_{K-1}(E)}{\psi_K(E)}\,, \tag{33}$$

$$\phi_0(E) = \lim_{K\to\infty}\frac{\psi_K(E)\alpha_0^{K+1}}{K!}\,. \tag{34}$$

The numbers N and K depend on the rate of convergence of the method. Typical values are 10 and 20.

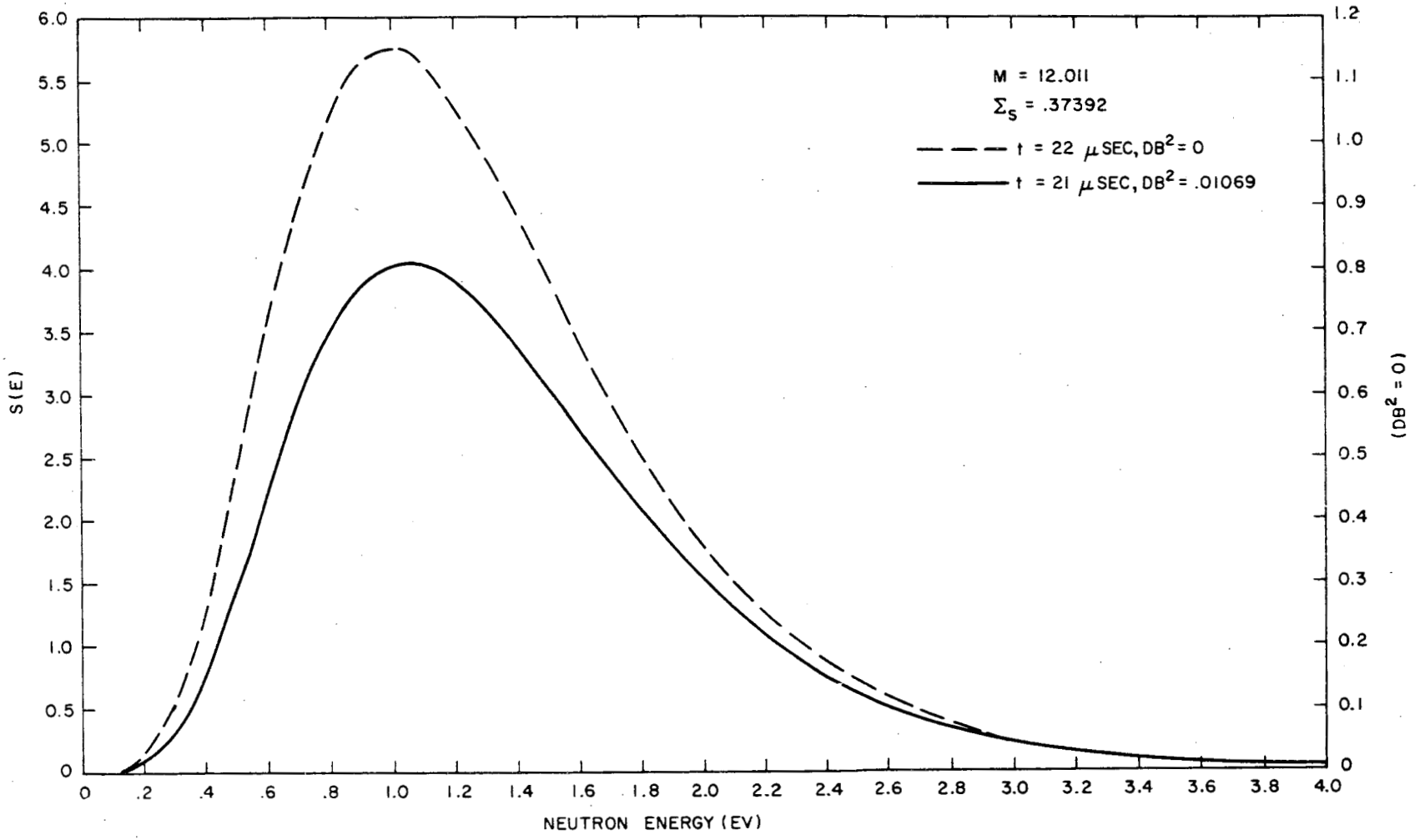

Fig. 78--Plot of S(E, t) for a graphite moderator

Equation (33) can also be put in the form of a variational principle:

$$\alpha_0 = K \frac{\int E e^{-E/kT} \psi_{K-1} \psi_K \, dE}{\int E e^{-E/kT} \psi_K^2 \, dE} . \qquad (33a)$$

Very accurate values of α_0 and $\phi_0(E)$ can be calculated with the L-code[41] even for highly anisotropic scattering. In the special case of an infinite medium ($B^2 = 0$) with $1/v$ absorption, $\Sigma_a = \alpha_m/v$, Eqs. (33) and (34) become unnecessary, because then $\alpha_0 = \alpha_p + \alpha_m$, $\phi_0(E)$ now being a Maxwellian of known normalization. The coefficient α_1 is arbitrary (between certain limits) and may be adjusted to give the best convergence. The values used were $\alpha_1 = 2\alpha_0$ for $E \leq kT$ and $\alpha_1 = \alpha_0$ for $E << kT$.

Computed transient spectra in an infinite medium of graphite (for $\Sigma_a = 0$) are shown in Figs. 79 and 80. The origin of the time scale is the slowing-down time, t_0, of Eq. (29). All curves represent the flux divided by a Maxwellian at room temperature and are normalized to a total density of 1 at $t = t_0$. The curves of Fig. 79 were calculated with a free-gas kernel of mass 12, whereas those of Fig. 80 correspond to a crystalline model.[24] It is seen that the difference between the two sets is considerable, both in time scale and in shape. This shows that the transients corresponding to the crystalline model can hardly be fitted by a gas kernel with some equivalent mass. In fact, an increase of the mass over 12 would leave the shape of the curves practically unchanged. Only their time scale would increase proportionally to the mass. More or less the same can be said of the finite-medium spectra given in Figs. 81 and 82 (for $B^2 = 0.01184$ cm^{-2} and $\Sigma_a = 0$). However, there is the additional feature of the well-known diffusion cooling effect. The asymptotic spectra, $\phi_0(E)$, deviate progressively from a Maxwellian at room temperature and become quite different when the leakage term becomes significant. This deviation is shown by the crossover of the curves and is much larger for the crystalline model than for the free-gas model. The diffusion-cooled asymptotic spectra were calculated with Eqs. (33) and (34). For the free-gas model, the result appeared to be well converged and smooth. For the crystalline model, however, the asymptotic spectrum shows dips in the vicinity of the Bragg cut-off. Hence further calculations are required with more mesh points in this energy region.

From the preceding calculation, it is seen that the measurement of asymptotic spectra in graphite should yield quite interesting results. This experiment will be performed in the near future with the aid of a chopper now being reassembled following some modifications to the synchronizing system. The measurement of the short time transients, however, is still under study. Probably the best method for performing this experiment

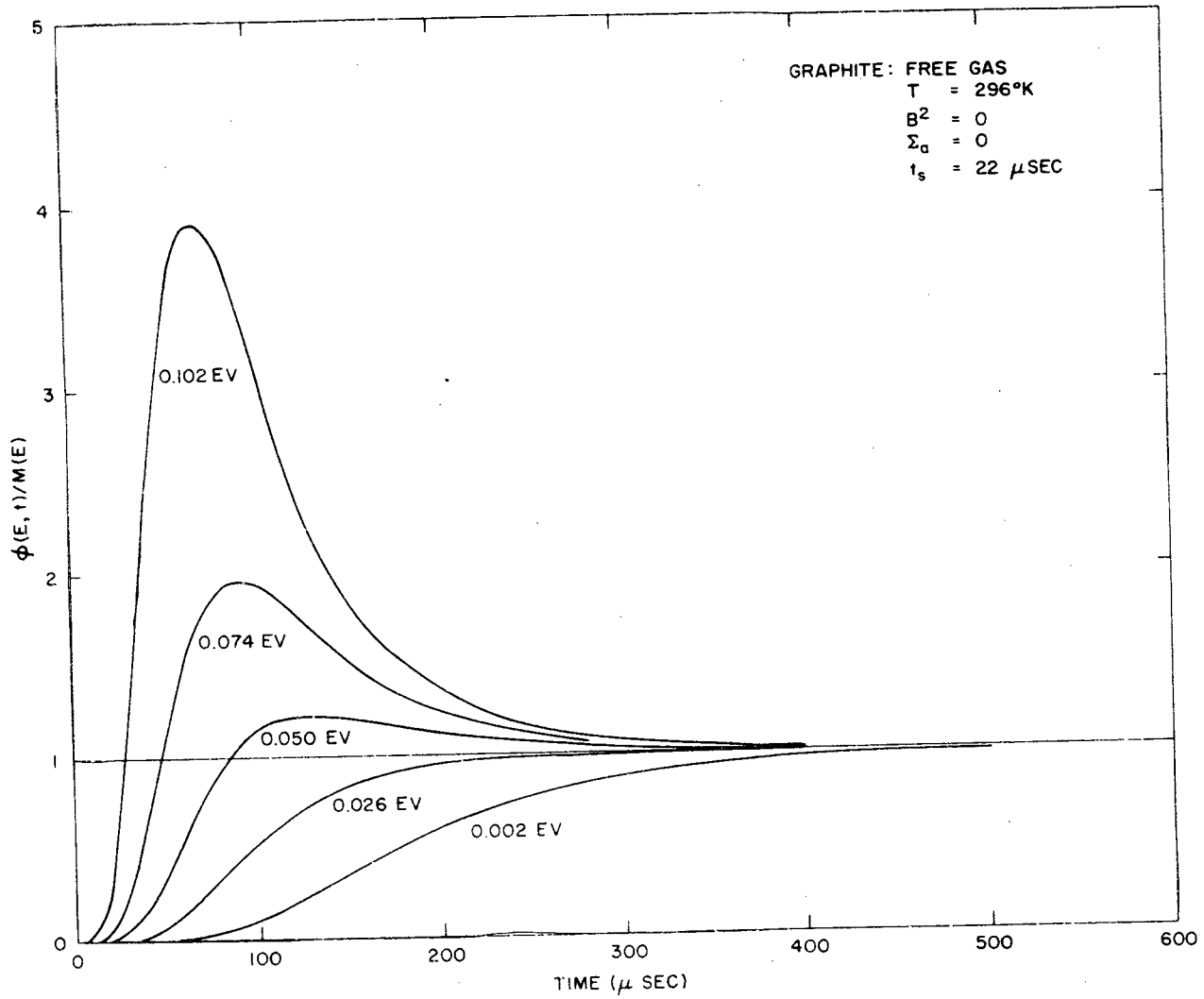

Fig. 79--Computed transient spectra in an infinite medium of graphite (free-gas model)

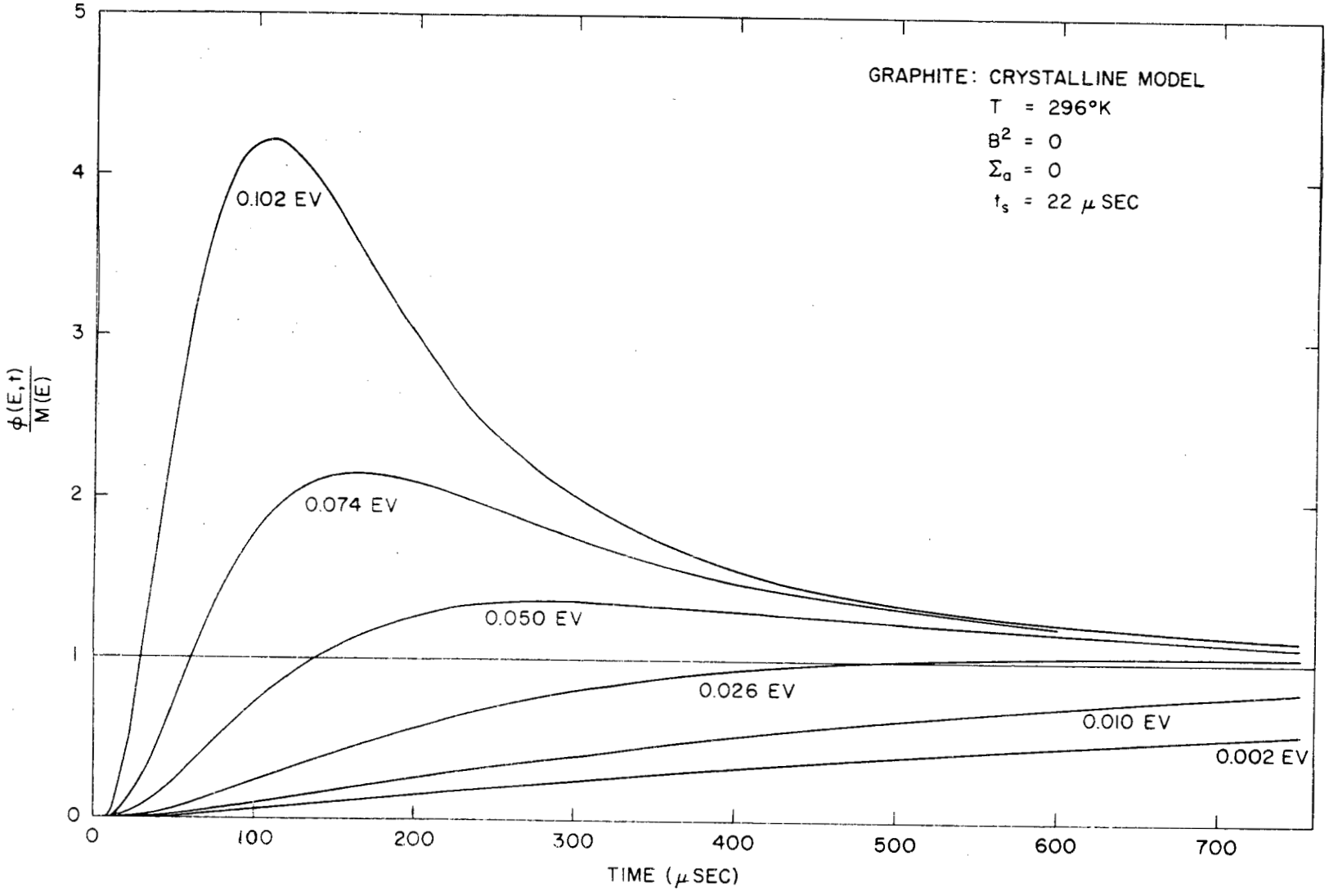

Fig. 80--Computed transient spectra in an infinite medium of graphite (crystalline model)

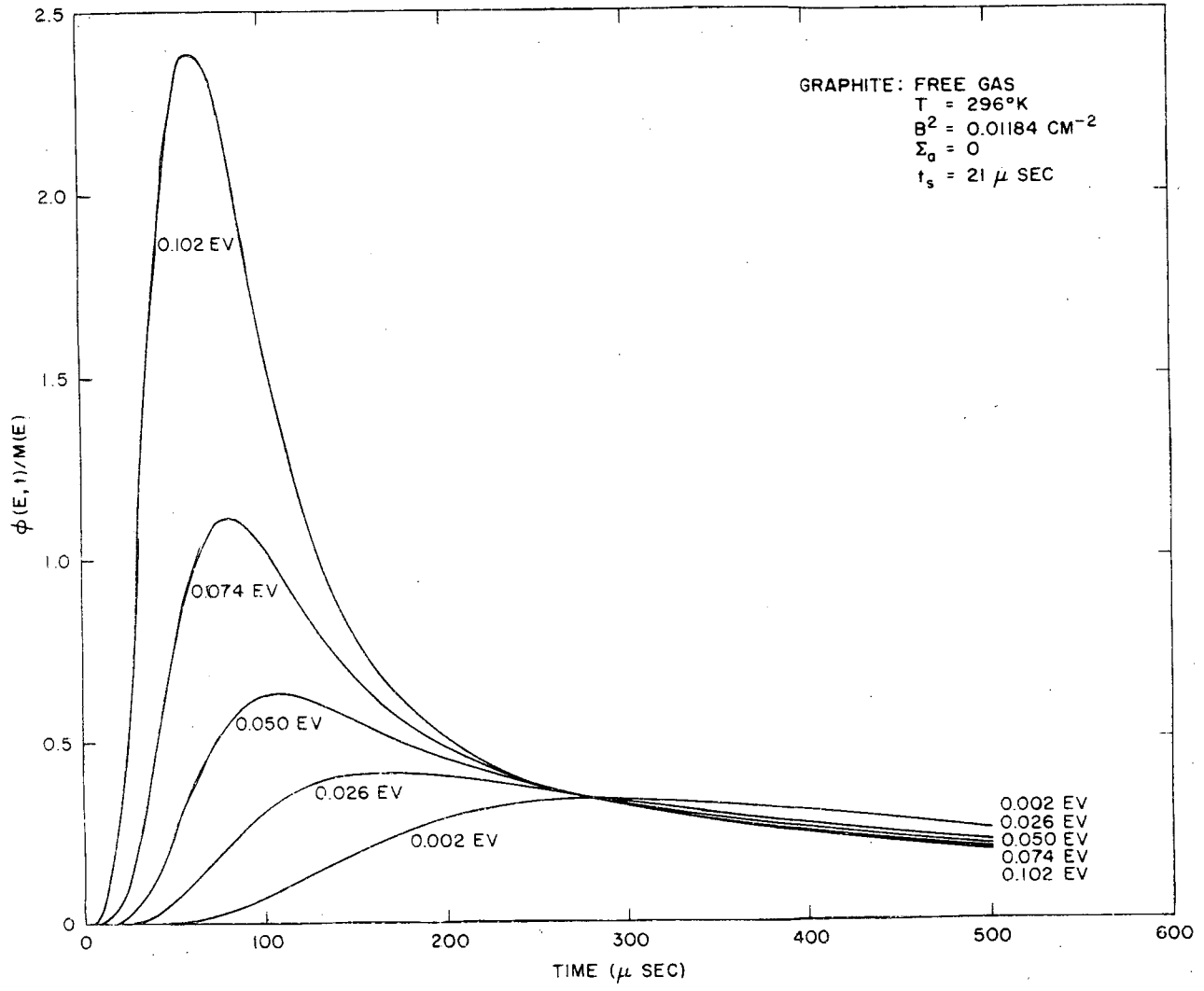

Fig. 81--Computed transient spectra in a finite medium of graphite (free-gas model)

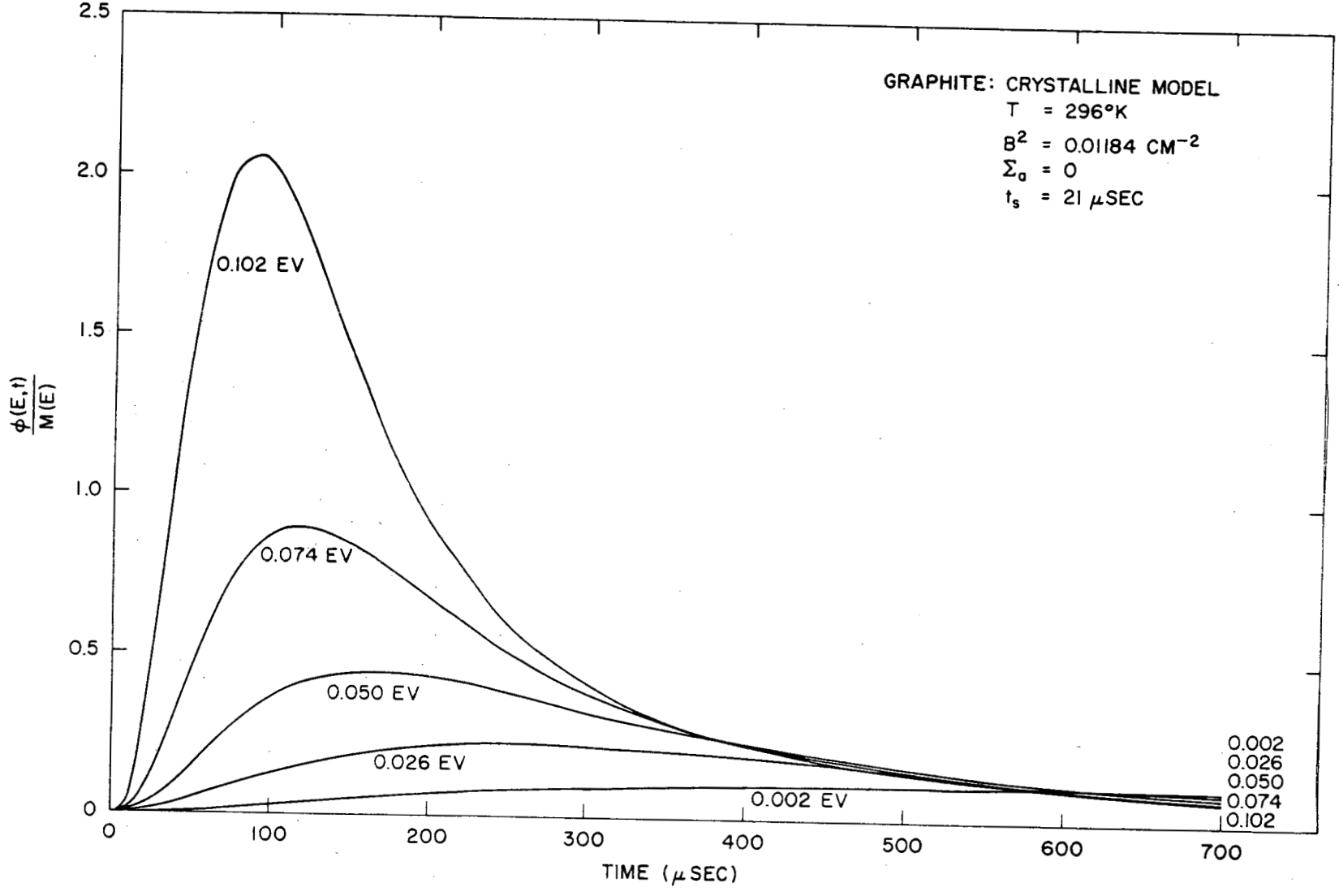

Fig. 82--Computed transient spectra in a finite medium of graphite (crystalline model)

would be to use a crystal monochromator and to record (for instance with a TMC time analyzer) the time-dependent flux corresponding to a fixed energy, after a burst of fast neutrons has been induced in the assembly. Because of the relatively long time scale involved, this technique seems to apply quite favorably to the case of graphite. This new method seems to have a number of advantages over the conventional approach which has been used recently by Poole and others.

8. 2. DIFFUSION PARAMETERS

During the past years, an extensive study has been conducted of the diffusion parameters of water by means of pulsed techniques and the General Atomic Linac. Techniques for extracting the normal-mode decay constant from the measured die-away data and for determining the over-all experimental accuracy have been developed. The same diffusion parameters may also be deduced from diffusion-length measurements in water poisoned with a 1/v absorber; these were measured by Koppel and Starr while at BNL.[42] The results from both classes of experiments have been compared, and conclusions have been reached on the relative merit of the two experiments for these determinations. It would appear that both techniques give Σ_a and D_0 quite well, the pulsed technique being superior for Σ_a measurements. The diffusion-cooling constant is hard to obtain accurately from the pulsed measurements and can possibly be better obtained by poisoned-media diffusion studies. A general review of the status of this work is given in Appendix III.

8. 3. EIGENVALUE PROBLEM DERIVED FROM THE BOLTZMANN EQUATION FOR NEUTRONS APPROACHING THERMAL EQUILIBRIUM

Consider the linear homogeneous Boltzmann equation describing the transport of thermal neutrons in its most general form:

$$\left[\frac{1}{v}\frac{\partial}{\partial t} + H\right] f(r, \Omega, E, t) = 0 , \tag{35}$$

where

$$Hf(r, \Omega, E, t) = \left[\Sigma_{tot} + \Omega\cdot\nabla\right] f(r, \Omega, E, t)$$

$$- \int f(r, \Omega', E', t)\, \Sigma(E' \to E, \Omega' \to \Omega)\, dE' d\Omega' . \tag{36}$$

Substituting into this equation solutions of the form

$$f(r, \Omega, E, t) = \phi(r, \Omega, E)\, e^{-\lambda t} \tag{37}$$

leads to the eigenvalue problem

$$-\lambda\phi(r, \Omega, E) = vH\phi(r, \Omega, E) \; . \tag{38}$$

Considerable attention has been given recently to this problem.[37][43] The most interesting conclusions reached from this analysis are that, in general, for given spatial and angular boundary conditions, the set of discrete eigenfunctions satisfying Eq. (36) is not complete (as was believed previously), and that the sequence of eigenvalues (λ) has a finite upper bound. This bound appears to be related to the existence of an unbounded transit time of the neutrons. For a medium which is bounded in every dimension, the infinite transit time corresponds to neutrons of infinitesimal velocity, and the bound is given by the limit of the collision rate as the neutron velocity approaches zero:

$$\lambda_b = \lim_{v \to 0} (\Sigma_{tot} v) \; .$$

For a medium which is infinite in one or more dimensions, there is an infinite transit time for any finite neutron velocity and the bound is the slowest collision rate at any energy, i. e. ,

$$\lambda_b = (\Sigma_{tot} v)_{min} \; .$$

Now the interesting question arises, what happens to the lowest-order eigenfunction and eigenvalue, ϕ_0 and λ_0, when the size of the assembly becomes very small. Because of the increased leakage probability, λ_0 is expected to increase; it cannot, however, surpass λ_b. It appears that for assemblies of very small dimensions (of the order of a mean free path), Eq. (38) has no regular solution at all, and consequently that the asymptotic time behavior of the neutron density in these assemblies cannot be described by an exponential expression of the form of Eq. (37).

It is possible to restore completeness of the set of eigensolutions of Eq. (38) by introducing distributions in the sense of Schwartz. This has been shown explicitly for the energy-independent[44][45] and for the space-independent problem[46][47] and probably also holds in the general case. Only by using this technique is it possible to solve the nonhomogeneous Boltzmann equation by the conventional approach of modal expansion, where now the sum over discrete modes is complemented by an integral over a continuum of eigendistributions.

IX. CODES

Modifications to existing codes and the description of a new code for the spectral analysis of experimental data are given in this section.

9.1. THERMOS

THERMOS is a one-dimensional, integral transport-theory code[4] used in spectral calculations of cell and slab geometry. The major modifications to THERMOS this past year are listed chronologically below:

1. The maximum number of space points was increased from 20 to 50 for the isotropic scattering version of the code.
2. A diagonal P_1 component of the scattering kernel was added to the 20-space-point code.
3. The anisotropic source component was included in the 20-space-point code.

THERMOS was modified to allow up to a 50-point spatial mesh, the number of velocity groups being left at 30. This change required fairly major modifications to the existing code (20-point spatial mesh, 30 velocity groups), since the size of a large matrix used in the basic iteration became too large to be contained in the core memory of the IBM 7090. The iteration is of the form

$$R_{n,i} = \sum_k H_{k,i} \; T_{i,n,k} \; ,$$

where the matrix, T, has maximum subscript values of 30, 50, 50. H is the birth-rate density, T is a kernel describing the transport properties of the flux solution, and R is the resolvent kernel (see Eq. (62)). In the 50-point version of THERMOS, $T_{i,n,k}$ is written on a magnetic tape in blocks corresponding to the values of i. During the iteration, T is read back from the tape block by block, using the buffering features of the IBM 7090. The one problem run to convergence for 50 space points required about 200 iterations (as compared with about 50 iterations for the 20-space-point problems) and about 1 hr of computer time. The results of the 50-point isotropic code indicated no appreciable improvement over or change from the 20-point isotropic version in the calculation of one-dimensional spectra.

The modification of THERMOS to include linear anisotropic scattering was made by Honeck.[48] His description, which follows, first derives the general integral transport equation. The angular flux is then expanded in Legendre polynomials and a set of coupled integral equations is obtained. THERMOS solves the lowest-order equation in the set, i.e., for isotropic scattering. The set is then truncated to include linear anisotropic scattering, and two coupled integral equations are obtained. If the anisotropic-scattering matrix is diagonal (no angle-energy correlation), the coupled equations can easily be reduced to a single integral equation of the type THERMOS solves, but with an effective transport kernel. The assumption of no angle-energy correlation for water (Nelkin water) is quite good.

9.1.1. The Integral Transport Equation

The integral transport equation in slab geometry is written:

$$\left[\mu \frac{\partial}{\partial x} + \Sigma(x, E)\right] \phi(x, E, \mu) =$$

$$S(x, E, \mu) + \int d\mu' \int dE' \Sigma_s(E' \to E, \mu' \to \mu) \cdot \phi(x, E', \mu) \equiv H(x, E, \mu) . \qquad (39)$$

This equation is converted to an integral equation by means of the integrating factor $(1/\mu)\, e^{-\lambda(x, x', E)/\mu}$:

$$\phi(x, E, \mu) = \frac{1}{\mu} \int_{-\infty}^{x} dx' e^{-\lambda(x, x', E)/\mu} H(x', E, \mu) \qquad x' < x, \ \mu > 0 , \qquad (40)$$

$$= \frac{1}{-\mu} \int_{x}^{\infty} dx' e^{+\lambda(x, x', E)/\mu} H(x', E, \mu) \qquad x' > x, \ \mu < 0 ,$$

$$\lambda(x, x'', E) \equiv \left| \int_{x'}^{x} dy \Sigma(y, E) \right| . \qquad (41)$$

Expand each of the angular dependent functions in Legendre polynomials. For example,

$$\phi(x, E, \mu) = \sum_{n=0}^{\infty} \frac{2n + 1}{2} \phi_n(x, E) P_n(\mu) . \qquad (42)$$

Insert the expansions of type (42) into (40) and operate on (40) with $\int_{-1}^{1} d\mu P_\ell(\mu)$:

$$\phi_\ell(x, E) = \sum_{n=0}^{\infty} \frac{2n+1}{2}\left[\int_{-1}^{0} d\mu P_\ell(\mu) \frac{1}{-\mu} \int_x^\infty dx' e^{+\lambda/\mu} + \int_0^1 d\mu P_\ell(\mu)\frac{1}{\mu} \int_{-\infty}^{x} dx' e^{-\lambda/\mu}\right] P_n(\mu) H_n(x', E) . \quad (43)$$

By changing μ to $-\mu$, the first term in the bracket can be shown to be $(-1)^{\ell+n}$ times the second term in the bracket:

$$\phi_\ell(x, E) = \sum_{n=0}^{\infty} \frac{2n+1}{2}\left[\int_{-\infty}^{x} dx' + (-1)^{\ell+n} \int_x^\infty dx'\right] \cdot \int_0^1 d\mu \frac{1}{\mu} P_\ell(\mu) P_n(\mu) e^{-\lambda/\mu} H_n(x', E) . \quad (44)$$

The last integral can be put in a form which defines the $E_n(x)$ functions:

$$\int_0^1 d\mu \frac{1}{\mu} P_\ell(\mu) P_n(\mu) e^{-\lambda/\mu} = \int_1^\infty \frac{dy}{y} P_\ell\left(\frac{1}{y}\right) P_n\left(\frac{1}{y}\right) e^{-\lambda y} . \quad (45)$$

The final form is then

$$\phi_\ell(x, E) = \sum_{n=0}^{\infty} \frac{2n+1}{2}\left[\int_{-\infty}^{x} dx' + (-1)^{\ell+n} \int_x^\infty dx'\right] \int_1^\infty \frac{dy}{y} P_\ell\left(\frac{1}{y}\right) P_n\left(\frac{1}{y}\right) e^{-\lambda y} H_n(x', E)$$

$$= \sum_{n=0}^{\infty} \int_{-\infty}^{\infty} dx' T_{\ell n}(x, x', E) H_n(x', E) . \quad (46)$$

The present form of THERMOS solves the $\ell = n = 0$ equation

$$\phi_0(x, E) = \int_{-\infty}^{\infty} dx' T_{00}(x, x', E) H_0(x' E) . \quad (47)$$

The next higher-order equation, which includes linear anisotropic scattering in the $H_1(x, E)$ term, is

$$\phi_0(x, E) = \int dx' T_{00}(x, x', E) H_0(x', E) + \int dx' T_{01}(x, x', E) H_1(x', E) , \quad (48a)$$

$$\phi_1(x, E) = \int dx' T_{10}(x, x', E)\, H_0(x', E) + \int dx' T_{11}(x, x', E)\, H_1(x', E) , \tag{48b}$$

$$H_0(x, E) = \int_0^\infty dE'\, \Sigma_{s0}(E' \to E)\phi_0(x, E') , \tag{49}$$

$$H_1(x, E) = \int_0^\infty dE' \Sigma_{s1}(E' \to E)\phi_1(x, E') ,$$

$$T_{00} = \frac{1}{2} E_1(\lambda) , \tag{50}$$

$$T_{01} = \frac{3}{2} E_2(\lambda) \qquad x' < x ,$$
$$= -\frac{3}{2} E_2(\lambda) \qquad x' > x , \tag{51}$$

$$T_{10} = \frac{1}{3} T_{01} , \tag{52}$$

$$T_{11} = \frac{3}{2} E_3(\lambda) , \tag{53}$$

$$E_n(\lambda) = \int_1^\infty \frac{dy}{y^n} e^{-\lambda y} . \tag{54}$$

The solution of Eqs. (48a) and (48b) requires four times as much work as the solution of Eq. (47). Since the present version of THERMOS has taken up to 1 hr for one case (admittedly an extreme case), the factor of four clearly yields an excessive amount of computer time.

9.1.2. Approximate Method for a Diagonal $\Sigma_{s1}(E' \to E)$

The linear scattering kernel for water, $\Sigma_{s1}(E' \to E)$, as given by Nelkin is nearly diagonal, that is, there is little angle-energy correlation in the scattering. Most of the anisotropy in water occurs in the elastic peak. Then

$$H_1(x, E) = \Sigma_{s1}(x, E)\phi_1(x, E) . \tag{55}$$

Equation (48b) can then be formally solved:

$$\phi_1(x, E) = \int dx'' R(x, x'', E) \int dx' T_{10}(x'', x', E) H_0(x', E) \quad , \tag{56}$$

where R is the resolvent kernel given by

$$R(x, x'', E) = \sum_{k=0}^{\infty} G^{(k)}(x, x'', E) \quad , \tag{57}$$

$$G^{(k)}(x, x'', E) = \int dx' \Sigma_{sl}(x', E) T_{11}(x, x', E)\, G^{(k-1)}(x', x'', E) \quad , \tag{58}$$

$$G^{(0)}(x, x'', E) = \delta(x - x'') \quad , \tag{59}$$

$$G^{(1)}(x, x'', E) = \Sigma_{sl}(x'', E) T_{11}(x, x'', E) \quad . \tag{60}$$

The number of terms in the k sum in Eq. (57) depends on the convergence of the $G^{(k)}$. Since T_{11} is of the order of $1/\Sigma_t$, each term is reduced by Σ_{sl}/Σ_t. The maximum value of water is $\Sigma_{sl}/\Sigma_t = 2/3$, and ten terms in (57) would be accurate to about 1.5%. For most of the energy range, Σ_{sl}/Σ_t is small. If the resolvent kernel is computed for each group, an average of about five terms would be necessary. This would take the same amount of time as five iterations of Eq. (47).

Having solved for $\phi_1(x, E)$, insert (56) into (48a):

$$\phi_0(x, E) = \int dx' T_{eff}(x, x', E) H_0(x', E) \quad , \tag{61}$$

$$T_{eff}(x, x', E) \equiv T_{00}(x, x', E) + \int dx''' T_{01}(x, x''', E) \Sigma_{sl}(x''', E) \cdot \int dx''' R(x''', x'', E) T_{10}(x'', x', E) \quad . \tag{62}$$

The kernel T_{eff} is then the effective isotropic scattering transport kernel.

The modifications still necessary to THERMOS are:

1. Compute T_{01}, T_{10}, and T_{11} in addition to T_{00}.
2. Compute the resolvent kernel, R, and the effective kernel, T_{eff}.

3. Having solved for $\phi_0(x, E)$, compute $\phi_1(x, E)$ from (56).
4. Equation (40) is currently used to compute the emergent spectra at any position or angle, but only $H_0(x', E)$ is used. Extend the calculation to include the H_1 term,

$$H(x', E, \mu) = \frac{1}{2} H_0(x', E) + \frac{3}{2} \mu H_1(x', E) . \qquad (63)$$

Items 3 and 4 above take very little time. The addition of items 1 and 2 will increase computation time by less than a factor of two.

The inclusion of an anisotropic source was also accomplished by H. C. Honeck.[49] His derivation follows.

9.1.3. Slowing-down Source (Anisotropic Approximation)

The slowing-down sources to the thermal region ($E < E^*$) are defined by

$$S_n(x, E) = \int_{E^*}^{\infty} dE' \, \Sigma_{s_n} (E' \rightarrow E) \, \phi(x, E') \qquad n = 0, 1 ,$$

where the Σ_{s_n} for a free gas are given by Weinberg and Wigner,

$$\Sigma_{s_0}(E' \rightarrow E) = 4\pi s_0(E' \rightarrow E) = \frac{\Sigma_s}{(1 - \alpha)E'} ,$$

$$\Sigma_{s_1}(E' \rightarrow E) = \frac{4\pi}{3} s_1 (E' \rightarrow E) = \frac{\Sigma_s}{(1 - \alpha)E'} \left[\frac{A + 1}{2} \sqrt{\frac{E}{E'}} - \frac{A - 1}{2} \sqrt{\frac{E'}{E}} \right],$$

$$\alpha = \left(\frac{A - 1}{A + 1} \right)^2 .$$

We need to know the flux moments $\phi_0(x, E)$ and $\phi_1(x, E)$ in

$$\phi(x, E, \mu) = \frac{1}{2} \phi_0(x, E) + \frac{3}{2} \phi_1(x, E)\mu .$$

Assume for neutron energies above E^* that (1) diffusion theory is applicable, (2) the flux is separable in space and energy, (3) the spatial distribution is given by indium-foil activity, f(x), and (4) all cross sections are constant, and $\Sigma_a = 0$. Then

$$\phi(x, E, \mu) = \phi(E) \left[\frac{1}{2} f(x) - \frac{3}{2} \mu D f'(x) \right] ,$$

where D is the diffusion coefficient and f' is the gradient of f. The energy dependence is given by the equation

$$(-DB^2 + \Sigma_s)\,\phi(E) = \Sigma_s \int_E^{E/\alpha} \frac{dE'}{E'}\,\phi(E') .$$

Let $\phi(E) = \phi E^{-k}$; then

$$k = \frac{(1 - \alpha^k)/(1 - \alpha)}{1 + \frac{DB^2}{\Sigma_s}} \quad , \quad \phi(E) = \phi^* \left(\frac{E^*}{E}\right)^k .$$

The angular components are

$$\phi_0(x, E) = \phi^* \left(\frac{E^*}{E}\right)^k f(x) ,$$

$$\phi_1(x, E) = -\phi^* \left(\frac{E^*}{E}\right)^k Df'(x) .$$

The sources are

$$S_0(x, E) = \frac{\Sigma_s}{(1 - \alpha)}\,\phi^* f(x) \int_{E^*}^{E/\alpha} \frac{dE'}{E'} \left(\frac{E^*}{E'}\right)^k$$

$$= \frac{\Sigma_s}{(1 - \alpha)k}\,\phi^* f(x) \left[1 - \left(\frac{\alpha E^*}{E}\right)^k\right], \tag{64}$$

$$S_1(x, E) = \frac{-\Sigma_s}{(1 - \alpha)}\,\phi^* Df'(x) \int_{E^*}^{E/\alpha} \frac{dE'}{E'} \left(\frac{E^*}{E'}\right)^k \left[\frac{A + 1}{2}\sqrt{\frac{E}{E'}} - \frac{A - 1}{2}\sqrt{\frac{E'}{E}}\right.$$

$$= -\frac{\Sigma_s}{(1 - \alpha)}\,\phi^* Df'(x) \left\{\frac{A + 1}{2} \int_{E^*}^{E/\alpha} \frac{dE'}{E'} \left(\frac{E^*}{E'}\right)^k \left(\frac{E}{E'}\right)^{1/2}\right.$$

$$\left. - \frac{A - 1}{2} \int_{E^*}^{E/\alpha} \frac{dE'}{E'} \left(\frac{E^*}{E'}\right)^k \left(\frac{E'}{E}\right)^{-1/2}\right\} ,$$

$$= -\frac{\Sigma_s}{(1-\alpha)}\phi^* Df'(x)\left\{\frac{A+1}{2k+1}\sqrt{\frac{E}{E^*}}\left[1-\left(\frac{\alpha E^*}{E}\right)^{k+1/2}\right],\right.$$

$$\left.-\frac{A-1}{2k-1}\sqrt{\frac{E^*}{E}}\left[1-\left(\frac{\alpha E^*}{E}\right)^{k-1/2}\right]\right\}. \qquad (65)$$

The appropriate functions of v used in THERMOS are

$$\phi(E)dE = \phi(v)dv = vN(v)dv = \frac{1}{2}N(v)dE; \qquad N(v) = 2\phi(E),$$

$$S(E)dE = S(v)dv = S(v)\frac{dE}{2v}; \qquad N^* = 2\phi^*,$$

$$S'(v) = S(v)/v = 2S(E),$$

$$S'(v)/N^* = \frac{S(E)}{\phi^*},$$

$$S'_0(x,v) = \frac{\Sigma_s N^* f(x)}{(1-\alpha)k}\left[1-\left(\frac{\gamma v^*}{v}\right)^{2k}\right], \quad \gamma = \sqrt{\alpha} = \frac{A-1}{A+1},$$

$$S'_1(x,v) = \frac{-\Sigma_s N^* Df'(x)}{(1-\alpha)}\left\{\frac{A+1}{2k+1}\left(\frac{v}{v^*}\right)\left[1-\left(\frac{\gamma v^*}{v}\right)^{2k+1}\right]\right.$$

$$\left.-\frac{A-1}{2k-1}\left(\frac{v^*}{v}\right)\left[1-\left(\frac{\gamma v^*}{v}\right)^{2k-1}\right]\right\}.$$

In the part of THERMOS where these sources are computed, the value of N^* is set equal to $1/E^*$.

9.2. DSN

The only new modification to the General Atomic version of DSN[50, 51, 52] to permit spectral calculations for one-dimensional assemblies has been the inclusion of an anisotropic component of volume source. This modification is also to be included in a later version of DSN which will include higher-order terms in the scattering matrix.[9]

The anisotropic volume source used in DSN is calculated according to the prescriptions used in THERMOS, Eqs. (64) and (65). Sources in each group are multiplied by the group width to correspond to DSN

conventions. The P_0 and P_1 components of the source are multiplied by

$$f_0(x) = \mathrm{erf}(x) ,$$

$$f_1(x) = \left(1 - \frac{1}{x^2}\right) \mathrm{erf}(x) + \frac{2}{\sqrt{\pi}} \frac{e^{-x^2}}{x} , \qquad (66)$$

respectively, where $x^2 = E/\overline{E}$ and $\overline{E}$ is the effective proton temperature, to account for the energy dependence of the free-gas scattering law used to describe scatterings above the thermal cut-off energy. The f_1 term in Eq. (66) was obtained by Nelkin, who integrated the P_1 component of the free-gas scattering kernel. A separate code, DSZ, was written to calculate the source terms, Eqs. (64) and (65), multiplied by f_0 and f_1, respectively. Values of cross sections and diffusion coefficients for the sources are calculated from epithermal (1.4 ev) data.

9.3. CORC

The previous annual summary report (GA-2544) included descriptions of the codes CERBERUS and CLAUDIUS, which correct time-of-flight data for coincidence losses and perform exponential fits, respectively. These codes have been combined with a third, ORPHEUS, which performs harmonic analysis of spatial flux distributions. The combined programs are called CORC.

CORC accepts up to 256 time points, 50 space points, 6 harmonics, and 50 values of the extrapolation distance used in the harmonic fit. Within these limits, CORC makes it possible in one computer run to correct the analyzer data for several space points, do an exponential fit to the data for each of these space points, do a spatial harmonic fit for each time point, and do an exponential fit in time of the amplitudes of the spatial harmonic fit. With the old codes, three runs were needed. Options are provided to do all or part of the above.

By replacing three codes with CORC, the necessary card handling has been reduced to a minimum. CORC will accept the punched output of the old codes, and for the case of CERBERUS and CLAUDIUS uses the same input cards with slight modifications.

ORPHEUS fits the output of CERBERUS, flux (i, k), to

$$\text{flux}\ (i,k) = \sum_{j=1}^{nt} b_j \sin\left[\frac{j\pi(X_i + \delta)}{h + 2\delta}\right]$$

for each time point k, $NF \leq k \leq NL$, and all space points i. δ is the extrapolation distance and h the thickness of the assembly in centimeters. The fit is made over the region $(h + 2\delta)$.

Let (1) $\phi(X_i)$ equal flux (i, k), i. e., consider any time point in general; (2) nt equal the number of harmonics; and (3) MS equal the number of space points. Then define

$$c(i,j) = \sin \frac{j(X_i + \delta)}{h + 2\delta}$$

$$a(j,k) = \sum_{i=1}^{MS} c(i,j)\, c(i,k)$$

$$g(j,k) = a^{-1}(j,k) ,$$

$$\begin{cases} j = 1, \cdots, nt \\ i = 1, \cdots, MS \\ k = 1, \cdots, nt \\ j = 1, \cdots, k \end{cases}$$

and

$$[a(k,j) = a(j,k)] .$$

Then

$$b_j = \sum_{\ell=1}^{MS} \phi(X_\ell) \sum_{i=1}^{nt} g(j,i)\, c(\ell,i) = \sum_{\ell=1}^{MS} \phi(X_\ell)\, d(j,\ell) ,$$

where

$$d(j,\ell) = \sum_{i=1}^{nt} g(j,i)\, c(\ell,i) \quad \begin{cases} j = 1, \cdots, nt \\ \ell = 1, \cdots, MS . \end{cases}$$

The sum of the residuals squared is

$$R = \sum_{i=1}^{MS} \left[\phi(X_i) - \sum_{j=1}^{nt} b_j c(i, j) \right]^2 ,$$

$$\chi^2 = \frac{R}{(MS - nt)} ,$$

and the standard deviations of the b_j are $\sigma^2(b_j) = g(j, j)\chi^2$.

9.4. ECTOPLASM

This general-purpose time-of-flight spectral data-reduction code has been described in GA-2544. ECTOPLASM is used to convert raw time-of-flight data taken in pulsed spectrum experiments to a normalized neutron-energy flux. Only additions to the code are given here, namely:

1. A statistical channel-grouping procedure has been superimposed in the usual energy grouping.
2. Provision for including the counter sensitivity in a tabular form has been made.

The first modification was made so that channel groupings can be done using a statistical criterion in addition to the usual energy-resolution ($\Delta E/E$) criterion. The fractional deviation of a group of channels is given by

$$\frac{\delta N_{i-j}}{N_{i-j}} = \frac{\sqrt{\sum_{k=i}^{j} c_k + \left(\frac{\rho_c}{\rho_b} \frac{m_c}{m_b} \right)^2 \sum_{k=i}^{j} b_k}}{\sum c_k - \frac{\rho_c}{\rho_b} \frac{m_c}{m_b} \sum b_k} ,$$

if the simplest form for the net intensity is used:

$$N_{i-j} = \sum_{k=i}^{j} c_k - \frac{\rho_c}{\rho_b} \frac{m_c}{m_b} \sum_{k=i}^{j} b_k ,$$

where ρ_c = the number of beam pulses during the data run,

ρ_b = the number of beam pulses during the background run,

m_c = the corrected number of monitor counts per beam pulse for the data run,

m_b = the corrected number of monitor counts per beam pulse for the background run,

$\sum_{k=i}^{j} c_k$ = the sum of the counts observed in channels i to j for the data run,

$\sum_{k=i}^{j} b_k$ = the sum of the counts observed in channels i to j for the background run,

N_{i-j} = the number of counts observed in channels i to j, corrected for background, source intensity, and different sampling times for signal and background.

After the energy grouping has been done, $\delta N/N$ is compared with an input number Δ (10% is typical), and grouping continues until $\delta N/N \leq \Delta$. This method often rejects the data for a good part of the low-energy portion of the spectra.

The output of current versions of ECTOPLASM includes a log-log plot of the grouped flux (normalized to a maximum value of 1.0) versus the energy (on a fixed scale of 0.001 to 19 ev).

The early versions of ECTOPLASM used polynomial fits to the energy-dependent counter response function, i.e., the counter sensitivity. For the new accelerator, the remeasured 16- and 50-m flight-path sensitivities have been included in a tabular form, since conserving memory space is no longer important. Linear interpolation is used, enough detail being given in the tables to ensure high spectral accuracy.

The code has also been modified to handle data taken with the 1024-channel TMC analyzer.

9.5. SPAN*

The SPectrum ANalysis (SPAN) code is an IBM-7090 FORTRAN code for computing Westcott parameters for an experimental thermal-neutron spectrum. The code also performs the following functions:

1. Smooths the experimental data with a multipoint quadratic smoothing formula.
2. Locates the position of all maxima and minima of the spectrum, both before and after smoothing.

*The work described in this section was performed by H. C. Honeck at BNL.

3. Fits the high-energy tail to the forms λ/E^k, λ/E, and $(\lambda/E)[1+(C/E)]$, both before and after smoothing.

4. Computes various integral and average properties of the spectrum.

9.5.1. Westcott Parameters

Westcott has characterized thermal-neutron spectra by the form

$$\phi(E) \doteq A\left[\frac{E}{E_t^2}\, e^{-E/E_t} + \frac{\lambda}{E}\,\alpha(\mu E_t)\right] ,$$

$$\alpha(\mu E_t) = 0 \qquad E < \mu E_t ,$$

$$= 1 \qquad E \geq \mu E_t ,$$

where ϕ is the neutron flux, E is the neutron energy (ev), A is the absolute flux level, E_t is the most probable energy, λ is the level of the $1/E$ tail, and μ is a cut-off selected so that the epithermal $1/v$ absorption rate for this representation is the same as for the real spectrum. The parameters A, E_t, and λ are determined from an experimental spectrum by a least-squares fit over a suitable energy range. A and E_t are found from a linear fit to

$$\ln\frac{\phi(E)}{E} = \ln\frac{A}{E_t^2} + \left(-\frac{1}{E_t}\right)E \qquad E_1 \leq E \leq E_2 ,$$

and λ is found by a constant fit to

$$E\phi(E) = \lambda \qquad E_3 \leq E \leq E_4 .$$

Here, E_3 and E_4 are input parameters. The values of E_1 and E_2 depend on the number of points used in the fit. The quantity μ is defined as

$$\int_0^\infty dE\,\frac{1}{v}\,\phi(E) = A\int_0^\infty dE\,\frac{1}{v}\left[\frac{E}{E_t^2}\, e^{-E/E_t} + \frac{\lambda}{E}\,\alpha(\mu E_t)\right] .$$

Defining the joining function, $\Psi(E)$,

$$\Psi(E) = \phi(E) - A\,\frac{E}{E_t^2}\, e^{-E/E_t} ,$$

then

$$\int_0^\infty dE \frac{1}{v} \Psi(E) = A\lambda \int_{\mu E_t}^\infty dE \frac{1}{v} \frac{1}{E}$$

or

$$\mu = \frac{1}{E_t} \left[A\lambda\sqrt{T_0}/2 \int_{E_5}^\infty dE \frac{1}{v} \Psi(E) \right]^2 ,$$

where $T_0 = 0.0253$ ev and $v = \sqrt{E/T_0}$. The lower limit of zero has been replaced by E_5 defined such that $\Psi(E)$ is always positive above E_5. This definition of E_5 assures that only the epithermal absorption rates are matched and not the total absorption rates of the two spectra. Accurate evaluation of this (and other) integrals is complicated by the fact that the experimental flux has statistical fluctuations, the energy points are not uniformly distributed, and the number of reliable very-low-energy fluxes is too small for computing the integrals down to zero energy. The following three subsections describe the techniques used to improve the accuracy of integration.

9.5.2. Low-energy Flux

At energies well below E_t, the flux can be represented by a power series whose lowest-order term is E. The form used for least-squares fitting is

$$\frac{\phi(E)}{E} = a + b\,E .$$

At these very low energies, many of the experimental fluxes have very large uncertainties; therefore, points below an energy E_6 (an input parameter) are ignored. The number of experimental points above E_6 used for the low-energy fit is arbitrary, but 5 to 7 points is typical.

9.5.3. Smoothing of the Flux

Much of the statistical fluctuation of the flux points can be eliminated by smoothing techniques. In this process, a quadratic is fit (in a least-squares sense) to a number of points (usually between 5 and 9) adjacent to the point being smoothed. The value of the flux at this point is replaced by that predicted from this quadratic. Actually, the quantity $E\phi(E)$ is smoothed and the process is repeated twice at all points. The assumption behind the smoothing process is that in a small region about the point being smoothed, the actual flux can be represented by a quadratic form.

9.5.4. Integration Table

A consequence of the low-energy fit and smoothing is that it is possible to evaluate the flux at all energies by quadratic interpolation (or extrapolation near the end points of the energy range). The code thus determines the flux at a series of equally spaced velocity intervals and sets up an integration table of fluxes. An accurate Simpson's rule integration can then be performed with a Richardson extrapolation:

$$I = \frac{32}{30} I_1 - \frac{2}{30} I_2 ,$$

where I denotes the value of the integral, I_1 denotes the value obtained using Simpson's rule at all points, and I_2 denotes the value obtained using Simpson's rule at every other point.

9.5.5. Least-squares Fitting

Calculation of the Westcott parameters and smoothing of the flux is accomplished by least-squares linear or quadratic fits. If the form to be fit is $y = a + bx + cx^2$, and if N points are to be used, the least-squares equations are

$$A_0 a + A_1 b + A_2 c = B_0 ,$$

$$A_1 a + A_2 b + A_3 c = B_1 ,$$

$$A_2 a + A_3 b + A_4 c = B_2 ,$$

where

$$A_k = \sum_{n=1}^{N} x_n^k \qquad B_k = \sum_{n=1}^{N} x_n^k y_n .$$

In addition to solving for the coefficients a, b, and c, the errors Δa, Δb, and Δc are determined from

$$\Delta a = \epsilon_{rms} \sqrt{C_a / D} ,$$

$$\Delta b = \epsilon_{rms} \sqrt{C_b / D} ,$$

$$\Delta c = \epsilon_{rms} \sqrt{C_c / D} ,$$

$$\epsilon_{rms} = \left\{ \frac{1}{N-2} \sum_{n=1}^{N} (a + bx_n + cx_n^2 - y_n)^2 \right\}^{1/2} ,$$

where C_a, C_b, C_c are the cofactors of a, b, and c in the determinant A, and D is the value of the determinant A.

9.5.6. Quantities Computed by SPAN

The following quantities and their errors are computed by SPAN:

1. The location and value of all maxima and minima of the flux--by least-squares quadratic fitting.

2. The parameter E_t and the peak value of the flux from a Maxwellian fit.

3. The coefficients in the three forms for the high-energy tail of flux:

$$\phi(E) = \lambda/E ,$$

$$\phi(E) = \lambda/E^k ,$$

$$\phi(E) = \frac{\lambda}{E} \left(1 + \frac{C}{E}\right) .$$

(The above quantities are computed both before and after the quantity $E\phi(E)$ has been smoothed.)

4. The Westcott parameters A, E_t, λ, and μ.

5. The following integrals and averages, computed using the flux table at equally spaced velocity intervals:

$$1/v \text{ ABS} = \int_0^{E_c} dE \frac{1}{v} \phi(E) = 2T_0 \int_0^{v_c} dv \, \phi(E) = \int_0^{v_c} dv \, N(v) ,$$

$$\bar{v} = \left[\int_0^{E_c} dE \, \phi(E) \Big/ \int_0^{E_c} dE \frac{1}{v} \phi(E) \right] ,$$

$$= \int_0^{v_c} dv \, v\phi(E) \Big/ \int_0^{v_c} dv \, \phi(E) ,$$

$$= \int_0^{v_c} dv\, v\, N(v) \Big/ \int_0^{v_c} dv\, N(v) \quad ,$$

$$\overline{v}^2 = \int_0^{E_c} dE\, v\phi(E) \Big/ \int_0^{E_c} dE\, \frac{1}{v}\phi(E) \quad ,$$

$$= \int_0^{v_c} dv\, v^2\phi(E) \Big/ \int_0^{v_c} dv\, \phi(E) \quad ,$$

$$= \int_0^{v_c} dv\, v^2\, N(v) \Big/ \int_0^{v_c} dv\, N(v) \quad ,$$

$$\overline{E} = \int_0^{E_c} dE\, E\, \phi(E) \Big/ \int_0^{E_c} dE\phi(E) \quad ,$$

$$= T_0 \int_0^{v_c} dv\, v^3\phi(E) \Big/ \int_0^{v_c} dv\, v\, \phi(E) \quad .$$

Here, $v = \sqrt{E/T_0}$, $T_0 = 0.0253$ ev, N(v) is the neutron density, and E_c is an arbitrary cut-off energy (up to five different cut-offs can be used). The first line of each equation is the definition, the second line is the form used in the code, and the third line is written in terms of neutron density.

6. A table is printed which lists the energy points, the experimental flux, the flux after one smoothing, the flux after two smoothings, the flux after two smoothings normalized to unity at 1 ev, and the joining function.

9.5.7. Inclusion in ECTOPLASM

The SPAN code will be included in the standard time-of-flight spectral data-reduction code as an optional subroutine, so that smoothed and fitted data can be presented directly with the experimental results.

INPUT DATA

Item	Format	Symbol	Description
1.	12A6	HOL(N),	72-character title card
2.	14I5	IDENT,	Identification number

Item	Format	Symbol	Description
2. (cont.)		NX,	Number of experimental flux points
		MLEP;	Number of points used in the low-energy fit, usually 5 to 9
		MSM,	Number of points (odd) used for the quadratic smoothing
		IX,	Number of points (a multiple of 4) in the integration table
		LCMX,	Number of cut-off energies used ($\leq$5)
		MPK,	Number of points used in the quadratic fit to locate maxima and minima, usually 5 to 9
3.	7E10.5	EMIN,	Point below which experimental points are ignored
		EHE,	Energy (ev) at which 1/E region starts
		ESTAR,	High-energy limit (ev) for integration table; must be larger than largest value of ECT(N)
		ETOP,	Point above which points are ignored
4.	7E10.5	(ECT(N), N=1, LCMX)	The cut-off energies (ev) for the integrations
5.	--	--	The energy points, flux values, and title cards for the spectrum in the format produced by ECTOPLASM

X. THE SPATIAL DEPENDENCE OF THE THERMAL-NEUTRON SPECTRUM ACROSS A TEMPERATURE AND ABSORPTION DISCONTINUITY*

One of the more troublesome problems which can be encountered in the design of modern, high-power-density reactors is the power spikes that occur in fueled regions near absorption and temperature discontinuities. In water-moderated systems, this phenomenon usually occurs near control-rod channels when the control element is withdrawn and in fueled regions near the core-reflector interface. For ceramic-fueled and ceramic-moderated systems, i. e., graphite or beryllium oxide reactors, the exotic term water-gap-peaking does not exist; however, the perturbations to the power distribution are as acute as in a water system. If these power spikes are not removed, the resulting decrease in performance of the reactor system can be severe.

Generally, ceramic reactors are not designed with large† unpoisoned moderator sections in the core. Consequently, power spikes resulting from the diffusion of thermal neutrons from regions of low poisoning** to regions of high poisoning are confined to the core-reflector interface. This is the case for reactors of the Peach Bottom, DRAGON, Pebblebed, and Rover type.†† Consequently, there is a general interest concerning the results of this experiment performed more than one year ago at the Linac for the Peach Bottom reactor project.

In this experiment, the chopped-beam time-of-flight technique was used to measure the thermal-neutron spectrum as a function of distance from a plane boundary separating contiguous regions with different

---

*This work was supported in part by the Atomic Energy Commission under Contract AT(04-3)-314, in part by the Empire State Atomic Development Associates, Inc., and in part by General Atomic private research funds.

†For this problem, the term large should be given to normalized lengths, where the normalizing length is the inelastic mean free path at 0.0253 ev (2200 m/sec).

**The term poisoning refers to the number of absorber barns per moderating atom at 2200 m/sec. For example, $N_b\sigma_a$ (2200 m/sec)/N_c = 0.4 barns/carbon atom is the poisoning in the experiment under discussion.

††Several military-application reactors have the same problem but cannot be mentioned here for security reasons.

temperature and absorption properties. The absorption discontinuity is characteristic of that which exists across the core-reflector interface of the Peach Bottom reactor, namely, 0.4 barns per carbon atom in the core and essentially zero absorption in the unpoisoned graphite reflector. The temperature discontinuity at the core-reflector interface of the Peach Bottom reactor is something like 600°K. However, in this experiment it was not possible to maintain the discontinuity to more than 200°K.

The experimental arrangement (see Fig. 83) and the method for obtaining the thermal spectrum have been described in GA-2544. A pulsed beam of electrons passes through an evacuated beam tube and strikes a small uranium target located near the geometrical center of the graphite assembly. The (γ, n) and (γ, f) reactions produced in uranium as the electrons are stopped give an essentially point source of fast neutrons with a mean energy of about 0.5 Mev. These fast neutrons slow down and establish themselves in a highly spatially dependent thermal spectrum. In the present experiment, the cold side of the assembly was held at a temperature of about 120°F, and essentially zero poisoning, while the hot side was maintained at about 600°F. The graphite on the hot side was poisoned with thin strips of boron-loaded stainless steel to an extent sufficient to yield a microscopic cross section of 0.4 barns per carbon atom at 2200 m/sec. The small amount of self-shielding in the stainless steel can be treated in an essentially exact manner. The foils are located on 0.525-in. centers. The graphite in which the thermal spectrum was established was a cube measuring 49 in. on a side. The ideal plane of temperature discontinuity was approximately realized by means of an air gap which separated the assembly into two rectangular parallelepipeds of equal volume.

The analysis of this experiment was facilitated by the use of Carlson's one-dimensional transport-theory code DSN.[50] The energy range from zero to 1.4 ev is divided into 25 groups. The probability of scattering from one group g to another g + n was computed according to

$$\bar{\sigma}_{g,\,g+n} = \frac{\int_g dE \int_{g'} dE' \sigma(E' \rightarrow E)\phi(E')}{\int_g \phi(E')dE}, \qquad (67)$$

where the integration extends over the energy widths of the groups of interest. The scattering kernel, $\sigma(E' \rightarrow E)$ (by Parks[33]), is obtained by a rather rigorous treatment of the interaction between neutrons and the lattice vibrations of graphite. In Ref. (33) it is shown that Parks' formulation of the neutron-phonon interaction leads to excellent agreement between calculated and measured infinite-medium spectra. In addition, reasonable agreement with the measured scattering-law data for graphite has been realized.

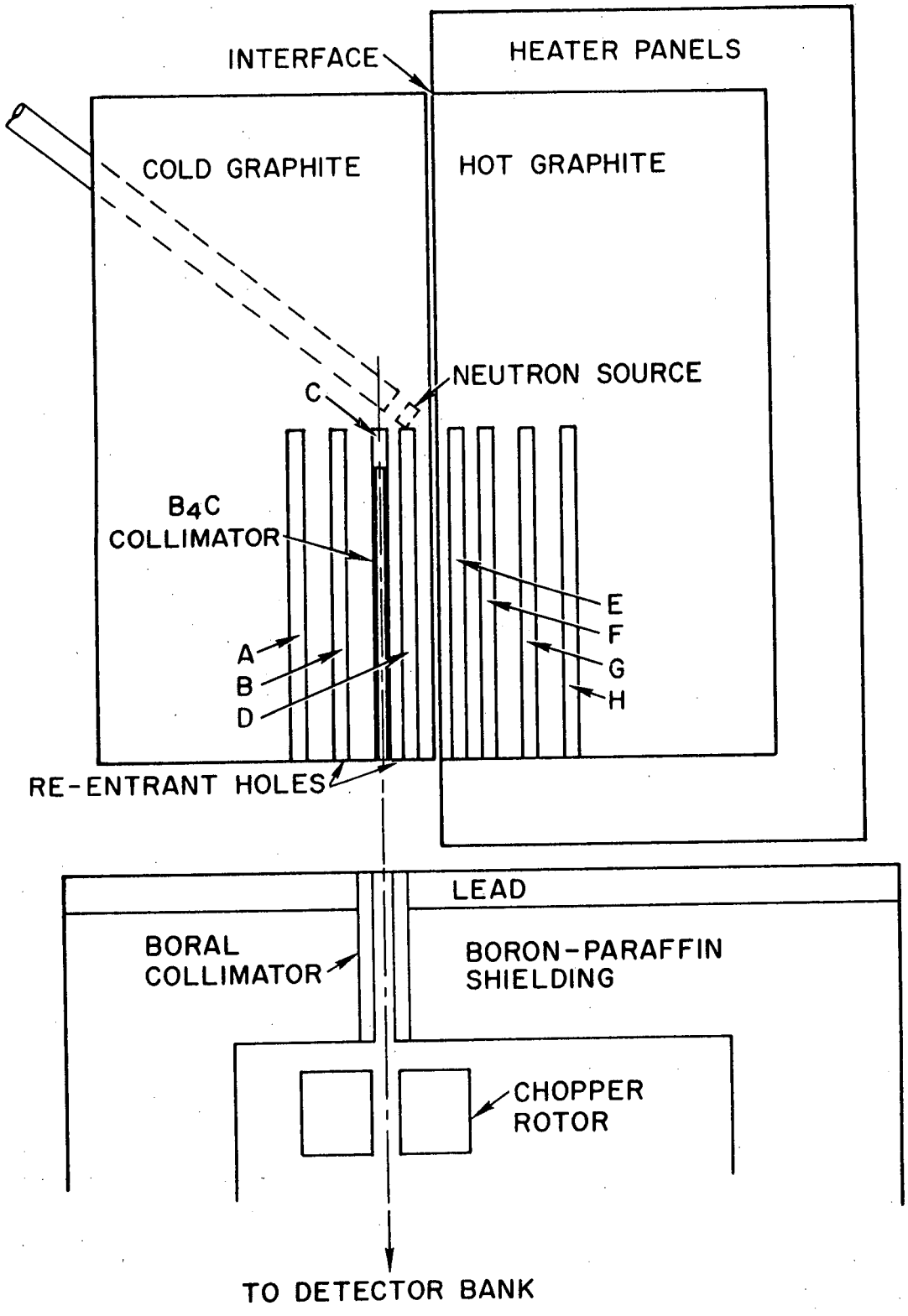

Fig. 83--Arrangement for graphite-interface experiments

The neutron flux, $\phi(E)$, which was used in Eq. (67) was obtained from a numerical solution of

$$\left[\sum_{\alpha} N_{\alpha}\sigma_{\alpha}(E) + D(E)B^2(E) + N_m\int_0^{E_{max}} \sigma(E \rightarrow E')dE'\right]\phi(E)$$

$$= N_m\int_0^{E_{max}} \sigma(E' \rightarrow E)\phi(E')dE' + S(E) ,$$

where the quantities have their usual definitions. The group cross sections for both the hot, poisoned and the cold, unpoisoned graphite were obtained by averaging over an infinite-medium spectrum characteristic of a homogeneous medium at $600^{\circ}F$ and a poisoning of 0.4 barns/carbon atom.

Although considerable confidence can be placed in the physical basis of our analysis, there are difficulties of a geometrical nature which must be considered. These stem from the fact that the configuration under consideration is a three-dimensional rather than a one-dimensional transport-theory problem. The multidimensionality and its complexities are reduced to a complexity comparable to that found in one-dimensional problems by performing a Fourier analysis of the thermal source $S(E, \vec{r})$ and the flux per unit energy $\phi(E, \vec{r})$* in two perpendicular directions parallel to the midplane of the graphite stack.

Specifically, we represent $S(E, \vec{r})$ by

$$S(E, \vec{r}) = \left[e^{-x^2/4\tau} - e^{-(|x|-2a)^2/4\tau}\right] \sum_{\substack{mn \\ 1,3,5}} a_{mn} \sin\frac{m\pi y}{a} \sin\frac{n\pi z}{a} F(E) ,$$

where a is the half-width of the assembly, including the extrapolation distance, x is the distance from the plane of the temperature discontinuity, and y and z are the perpendicular distances from two of the mutually perpendicular boundaries of the assembly which are perpendicular to the plane $x = 0$. The coefficients a_{mn} and τ are determined by comparing the spatial part of $S(E, r)$ with the measured spatial dependence of the indium-resonance flux. The quantity $F(E)dE$ is the rate at which neutrons slow down from above indium resonance into the interval dE about E by collisions with free carbon atoms at rest.

---

*The neutron energy is E and $\vec{r}$ is the position in the stack.

Following this decomposition of the source, the following sequence of one-dimensional transport-theory problems was solved:

$$D\frac{\pi^2}{a^2}(m^2+n^2)f_{nm}+\mu\frac{df_{mn}}{dx}+\Sigma_t f_{nm}=\frac{1}{2}\int\Sigma(E'\rightarrow E)\,f_{nm}(E',x',\mu')dE'$$

$$+[e^{-x^2/4\tau}-e^{-(|x|-2a)^2/4\tau}]F(E)\,.$$

Here the symbols have their usual meaning. The quantity $D(\pi^2/a^2)(m^2+n^2)$ corresponds to lateral leakage in the mode (m, n). The total angular-flux spectrum is composed of

$$f(E,\vec{r},\mu)=\sum_{nm}f_{nm}(E,x,\mu)\,a_{nm}\sin\frac{m\pi y}{a}\sin\frac{n\pi x}{a}\,.$$

For the analysis of the assembly used in this experiment, it was necessary to assume that four coefficients a_{nm} had the following values: $a_{11}=0.73801$, $a_{31}=0.43778$, $a_{33}=0.06496$, and $a_{51}=0.038514$. (The next two coefficients have values of 5.8×10^{-3} and 5×10^{-4}.)

As stated above, the energy range below 1.457 ev was divided into 25 groups of equal lethargy. In Table 5 are recorded the values of energy and lethargy for the maximum of each group and the mean energy of each interval. (The memory space required for mesh points, materials, cross sections, etc., precludes the use of a larger number of thermal groups, however desirable their use may be.) Near the interface, i.e., for 13 in. on each side of the discontinuity, mesh points were located 1 cm apart, an additional mesh point being located at the center of each experimental hole. The air gap was explicitly represented with nitrogen and oxygen filling the 1/2-in. gap at STP. The atom densities of carbon and boron on the hot, poisoned side are 7.7×10^{-2} atom/barn-cm and 4.158×10^{-5} atom/barn-cm, respectively.

Values of the fluxes, ϕ_{nm}, are given in Table 6 for the point 9-1/2 in. from the interface on the hot, poisoned side. These data are also shown in Fig. 84 as $\phi(E)$, where they are compared with the experimental values. From Table 6, the effect of increasing values of ϕ_{mn}, which is treated as an absorptive term, is clearly seen.

Figures 85, 86, and 87 give the calculated and measured spectra 1-1/2 in. on each side of the interface and 9-1/2 in. from the interface on the cold, unpoisoned side. In all cases, the measured spectra are very nearly 1/E above 1.0 ev. Hence, the calculated spectra were normalized

Table 5

VALUES OF ENERGY AND LETHARGY CHARACTERISTIC OF THE MAXIMUM FOR EACH OF THE TWENTY-FIVE GROUPS USED IN THE ANALYSIS OF SPACE-DEPENDENT EXPERIMENT

Group	Maximum of Group		Mean Energy of Group (ev)
	Energy (ev)	Lethargy	
1	1.457	15.742	1.31
2	1.1623	15.968	1.04
3	0.92717	16.194	0.833
4	0.7396	16.420	0.665
5	0.59	16.646	0.53
6	0.4707	16.872	0.423
7	0.3755	17.098	0.3375
8	0.2996	17.324	0.269
9	0.239	17.550	0.215
10	0.1906	17.776	0.171
11	0.1520	18.002	0.137
12	0.1213	18.228	0.109
13	0.09675	18.454	0.087
14	0.07718	18.680	0.0694
15	0.06157	18.906	0.0553
16	0.04911	19.132	0.0441
17	0.03918	19.358	0.0352
18	0.03125	19.584	0.0281
19	0.02493	19.810	0.0224
20	0.01989	20.036	0.0179
21	0.01587	20.262	0.0143
22	0.01266	20.488	0.0114
23	0.01010	20.714	0.0091
24	0.00805	20.940	0.00724
25	0.00642	21.166	0.00571

Table 6

CALCULATED VALUES OF $\phi_{nm}(u)$ 9-1/2 IN. FROM INTERFACE ON HOT, POISONED SIDE

Group	Group Fluxes from DSN				$E\phi(E) = f(E, 9\text{-}1/2) \cdot E$
	ϕ_{11}	ϕ_{31}	ϕ_{33}	ϕ_{51}	
1	2.9974	2.9182	2.8433	2.7722	3.7811
2	2.5641	2.4372	2.3201	2.2212	3.1955
3	2.5396	2.3598	2.1981	2.0522	3.1292
4	2.5834	2.3432	2.1336	1.9494	3.1461
5	2.6510	2.3370	2.0736	1.8496	3.1855
6	2.7964	2.3775	2.0456	1.7750	3.3058
7	3.0636	2.4873	2.0629	1.7339	3.5506
8	3.4142	2.6301	2.0950	1.7016	3.8727
9	3.7670	2.7486	2.1003	1.6469	4.1832
10	3.9474	2.7431	2.0188	1.5330	4.3043
11	3.8455	2.5662	1.8303	1.3528	4.1324
12	3.4657	2.2375	1.5553	1.1241	3.6816
13	2.8921	1.8168	1.2364	0.8772	3.0671
14	2.2620	1.3915	0.9318	0.6519	2.3642
15	1.6868	1.0212	0.6756	0.4677	1.7538
16	1.1955	0.7147	0.4684	0.3217	1.2380
17	0.8203	0.4863	0.3168	0.2164	0.84718
18	0.5452	0.3222	0.2094	0.1428	0.5625
19	0.3535	0.2086	0.1354	0.0923	0.3645
20	0.2288	0.1346	0.0872	0.0592	0.2358
21	0.1451	0.08428	0.05474	0.0371	0.1490
22	0.0902	0.05264	0.03396	0.02301	0.0927
23	0.0565	0.0334	0.02168	0.01479	0.0583
24	0.0355	0.0211	0.01379	0.0095	0.0367
25	0.06114	0.0362	0.02361	0.0762	0.0631

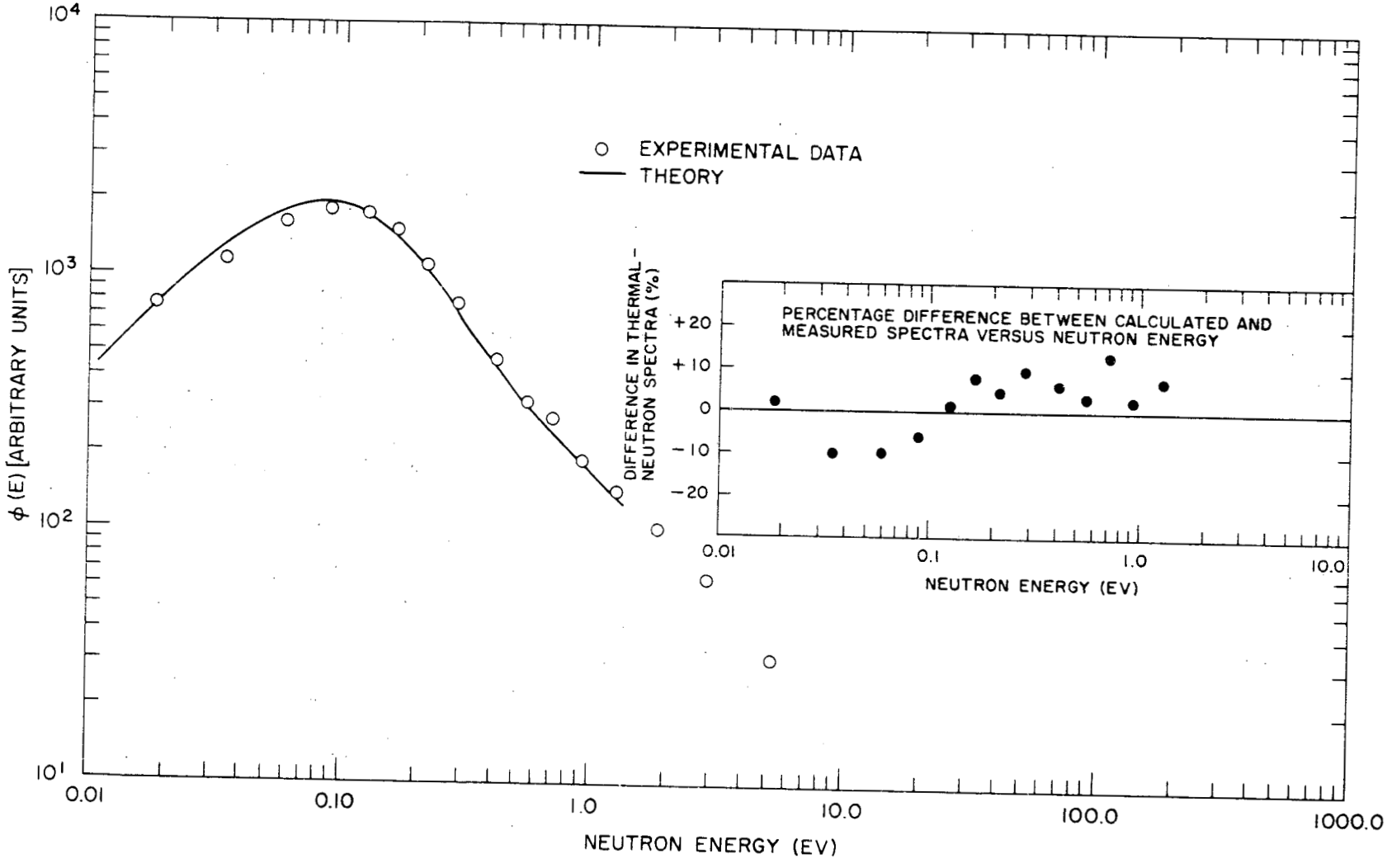

Fig. 84--Graphite spectra at 9.5 in. from interface on the hot, poisoned side

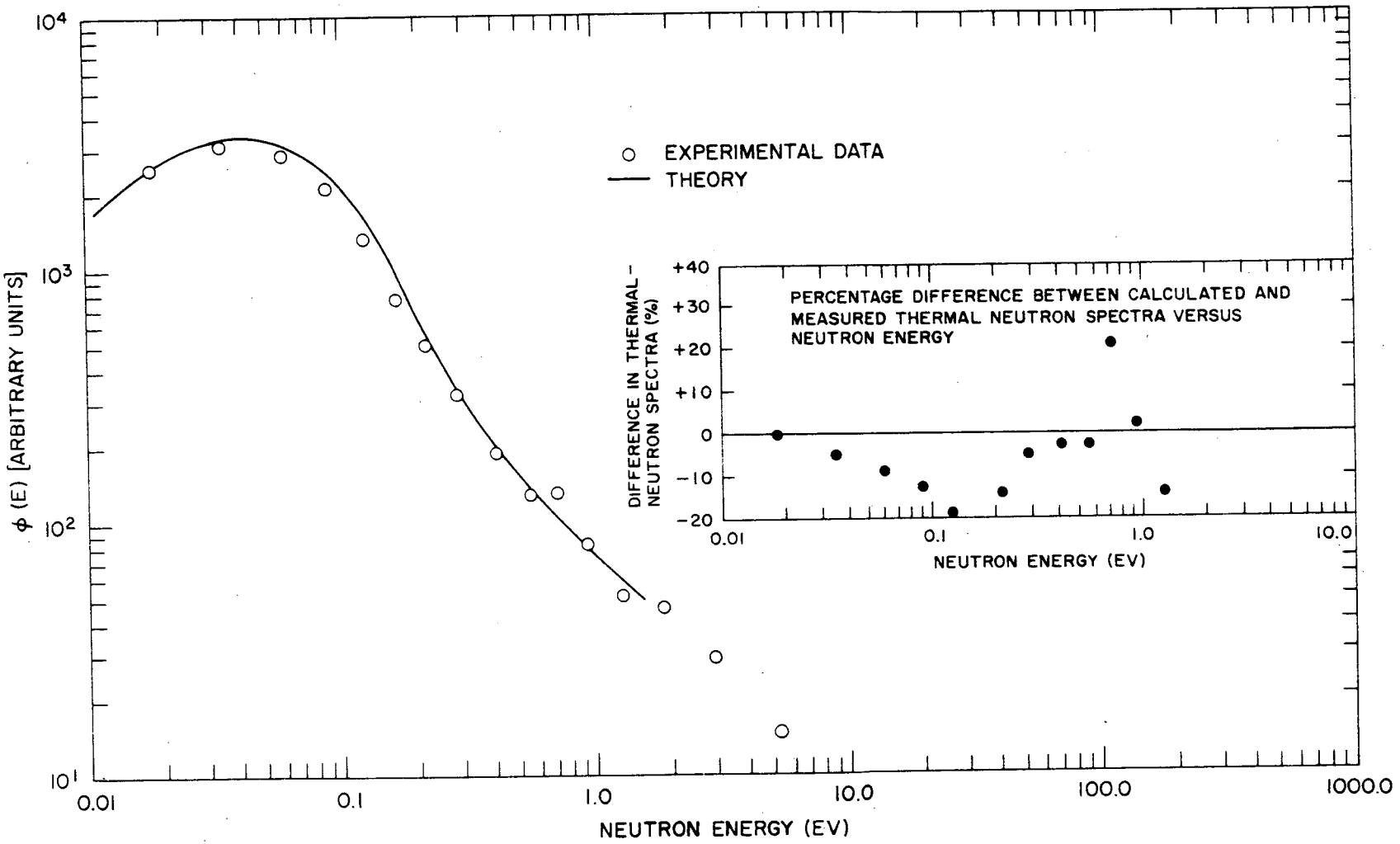

Fig. 85--Comparison of calculated and measured neutron spectra 1-1/2 in. from interface on cold (356°K), unpoisoned side

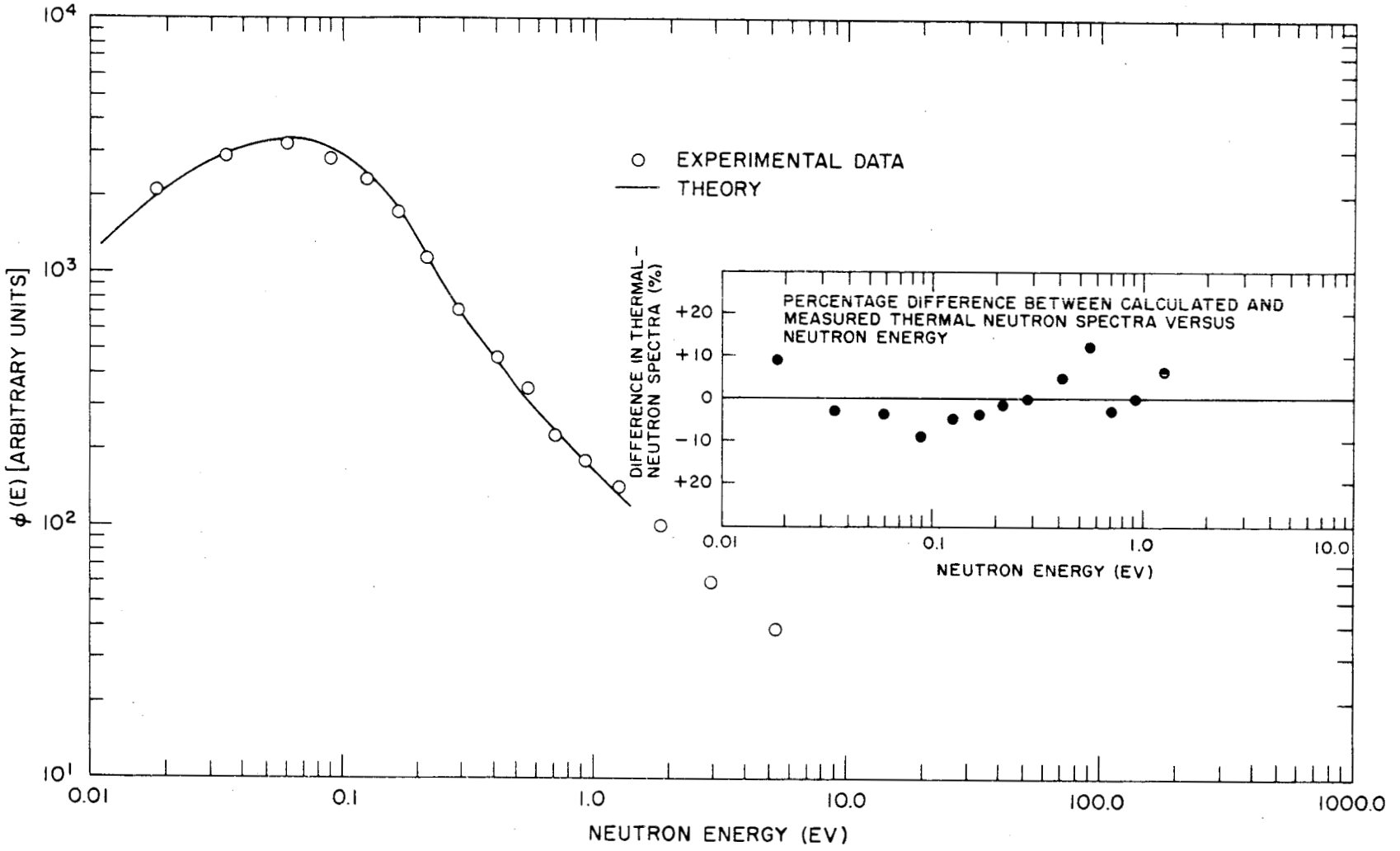

Fig. 86--Comparison of calculated and measured neutron spectra 1-1/2 in. from interface on hot (600°K), poisoned side

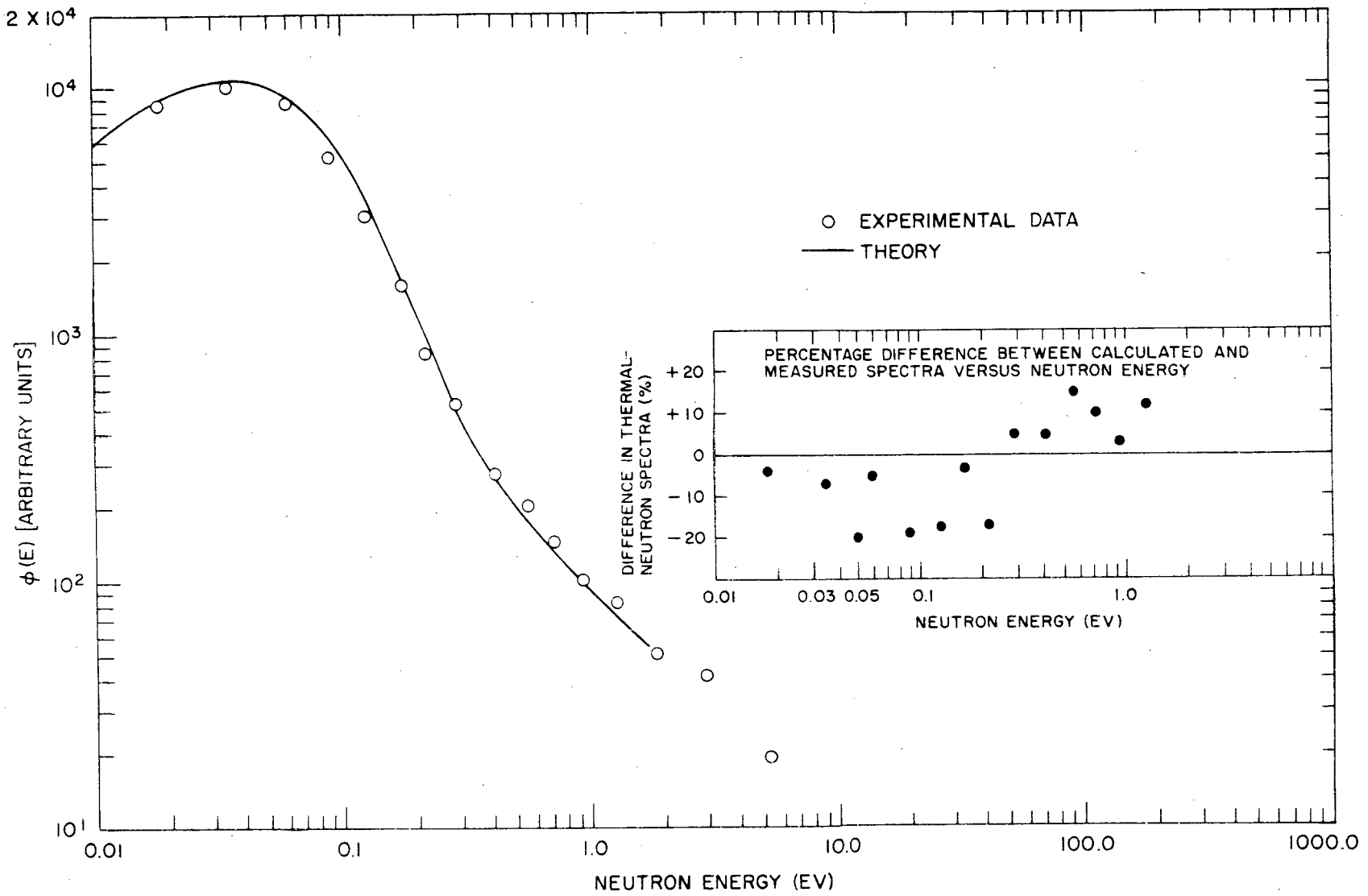

Fig. 87--Comparison of calculated and measured neutron spectra 9-1/2 in. from interface on cold (356°K), unpoisoned side

to the experiment at 1.0 ev. Since the experimental data are determined to only 15% to 20% in this energy range, some judgement was required in normalizing the calculated values to the experiments. The final decision on the normalization was made when nearly all experimental points were found to lie within ±10% of the theoretical curve.

In the right center of each figure, the percentage difference between the experimental and calculated thermal spectra is given. In general, the percentage difference between theory and experiment is only 10% to 15%. Occasionally, a point is found outside this range, but this is the exception rather than the rule. The data at the four other experimental points give the same type of comparison between theory and experiment.

To our knowledge, this is the first time an attempt has been made to measure the spatial dependence of the thermal-neutron flux across a temperature and absorption discontinuity characteristic of several reactor systems now under construction. As expected, a rather strong spatial dependence of the thermal-neutron spectrum was shown to exist across this discontinuity, and some success was achieved in our attempt to calculate the measured distributions using very standard computational procedures.

Further experiments are planned for the future should funding become available; they are certainly required. Several improvements in the experimental configuration are advisable, as is the determination of the neutron flux by activation of some thermal absorbers as a function of position. These new data would be very valuable in testing our ability to calculate not only the spectrum at any point from a temperature and absorption discontinuity, which now is consistently softer than the experimental values, but also the magnitude of the flux from one space point to another. Unfortunately, time did not allow the measurement of the relative magnitude of the thermal flux versus position.

XI. SPECTRA PRODUCED BY A SOURCE WITHOUT A HIGH-ENERGY COMPONENT

It is known that for hydrogenous moderators, the asymptotic spectrum produced far away from a high-energy neutron source still has an epithermal component. Hence, the spectrum never becomes completely thermalized, and even at a very large distance from the source there remains a $(1/E)$-like epithermal tail. This is due to the fact that because of the fast increase of the mean free path above 100 kev, the relaxation length of the uncollided flux is larger than the thermal diffusion length. In order to get rid of the epithermal component and to measure a truly thermal asymptotic spectrum, the Maxwellian-source-neutron energy must be well below 100 kev. Such a source can be easily simulated by using a cadmium curtain embedded in the moderator somewhere between the actual source and the re-entrant tube (see Fig. 88). Suppose that the neutron flux in the assembly without cadmium satisfies the equation

$$H\phi + S = 0 \quad . \tag{68}$$

Then if the cadmium curtain is added without changing anything else and if the scattering in the cadmium is neglected, the new flux will be described by the equation

$$H\phi_{Cd} + S - \phi_{Cd}\Sigma_{aCd} = 0 \quad . \tag{69}$$

Subtracting Eq. (69) from (68), it follows that

$$H(\Delta\phi) - \phi_{Cd}\Sigma_{aCd} = 0 \quad , \tag{70}$$

where

$$\Delta\phi = \phi - \phi_{Cd} \quad .$$

It is seen that the difference, $\Delta\phi$, satisfies the same equation as the original flux with the source S replaced by the term $\phi_{Cd}\Sigma_{aCd}$. Because of the shape of the cadmium cross section, this fictitious source term does not have any high-energy component. Consequently, by making two measurements--one with the curtain in place and another with the curtain removed--and taking the difference, one should obtain a true thermal asymptotic spectrum.

A preliminary investigation was made of the feasibility of the above experimental approach, using the pulsed neutron source produced by the Linac.

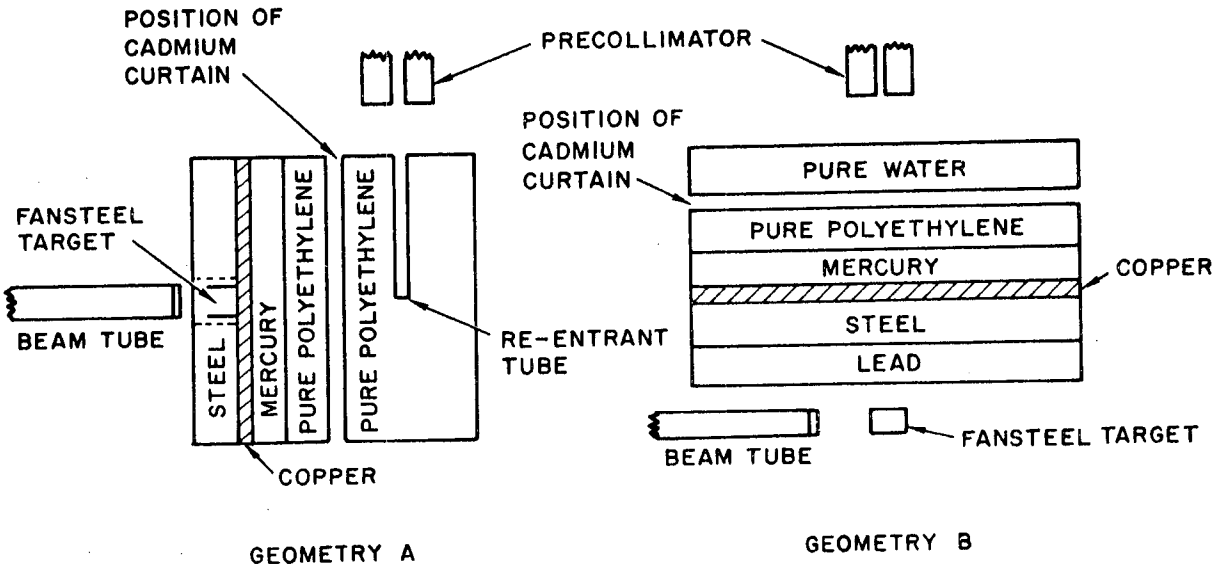

Fig. 88--Geometrical arrangement for measuring thermal asymptotic spectra

Primary fast neutrons from this source, especially those above 4 Mev, are not attenuated greatly by hydrogenous materials and thus can easily reach the location selected for the thermal-spectrum measurement. The spatial distribution of thermal neutrons diffusing to this point falls off more sharply than the fast source, or at best at the same rate. Thus, some method of slowing down the primary fast-neutron source from its essentially fission-spectrum distribution is desirable. It was decided to surround the fast source with materials having the highest possible inelastic-scattering cross sections in the million-electron-volt energy region in order to soften the primary spectrum. This can be done with little loss in intensity. The two geometries studied are shown in Fig. 88. Even with large masses of material between the source and the polyethylene thermalization region, one could produce high intensities of low-energy neutrons in the water or polyethylene regions.

In studying geometry A in Fig. 88, it was hoped to observe a pure Maxwellian spectrum at the temperature of the moderator. Geometry B is essentially a Milne-problem investigation. The spectra were measured experimentally by observing the time-of-flight distribution of counts without and with the cadmium curtain and then determining the difference between these two distributions. The data were then processed in the standard spectral reduction code ECTOPLASM to obtain the energy flux. The mean-emission-time corrections were made using as a guide the thermal-neutron die-away measurement for the case with the cadmium curtain removed. The results plotted in Figs. 89 and 90 for cases A and B,

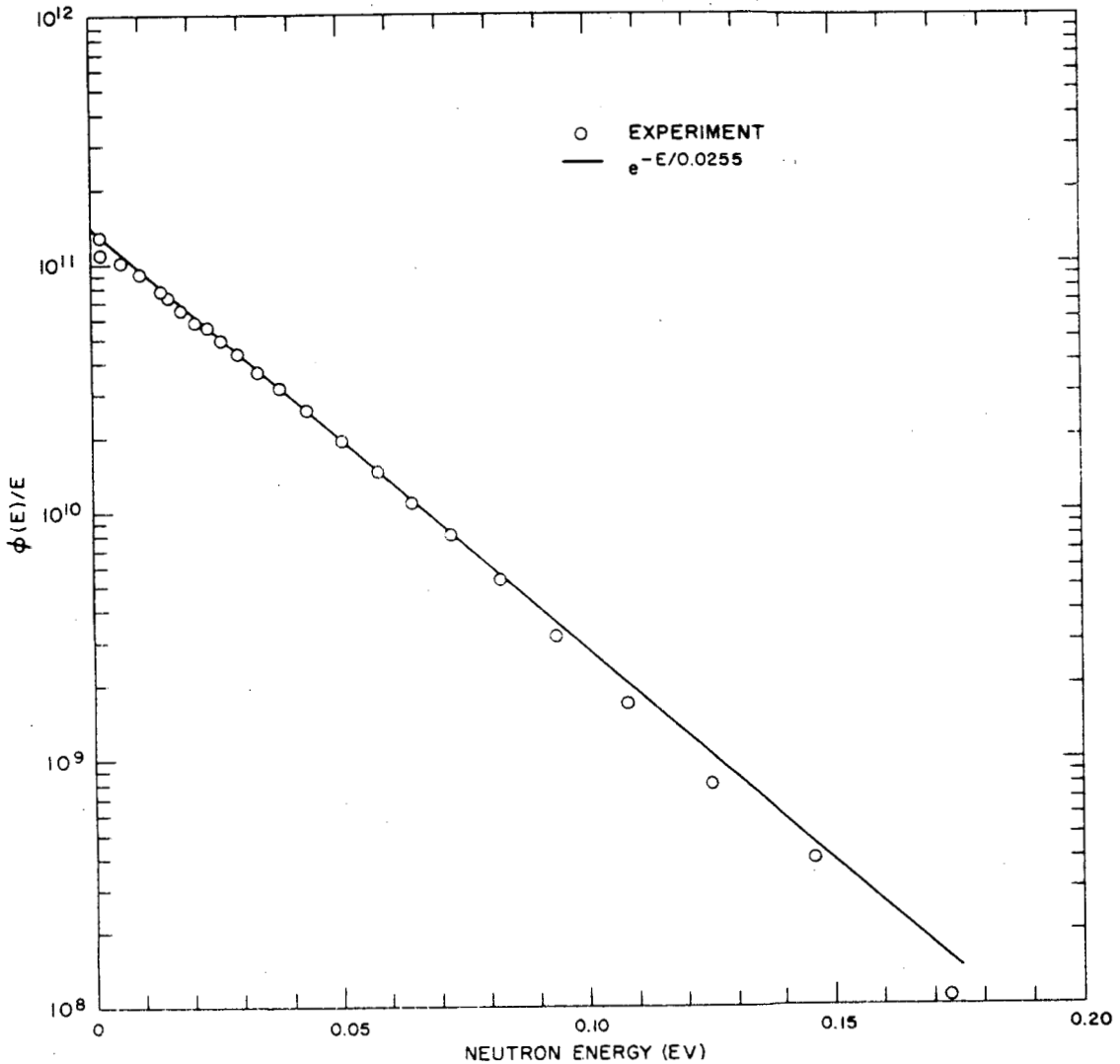

Fig. 89--$\phi(E)/E$ versus E for geometry A

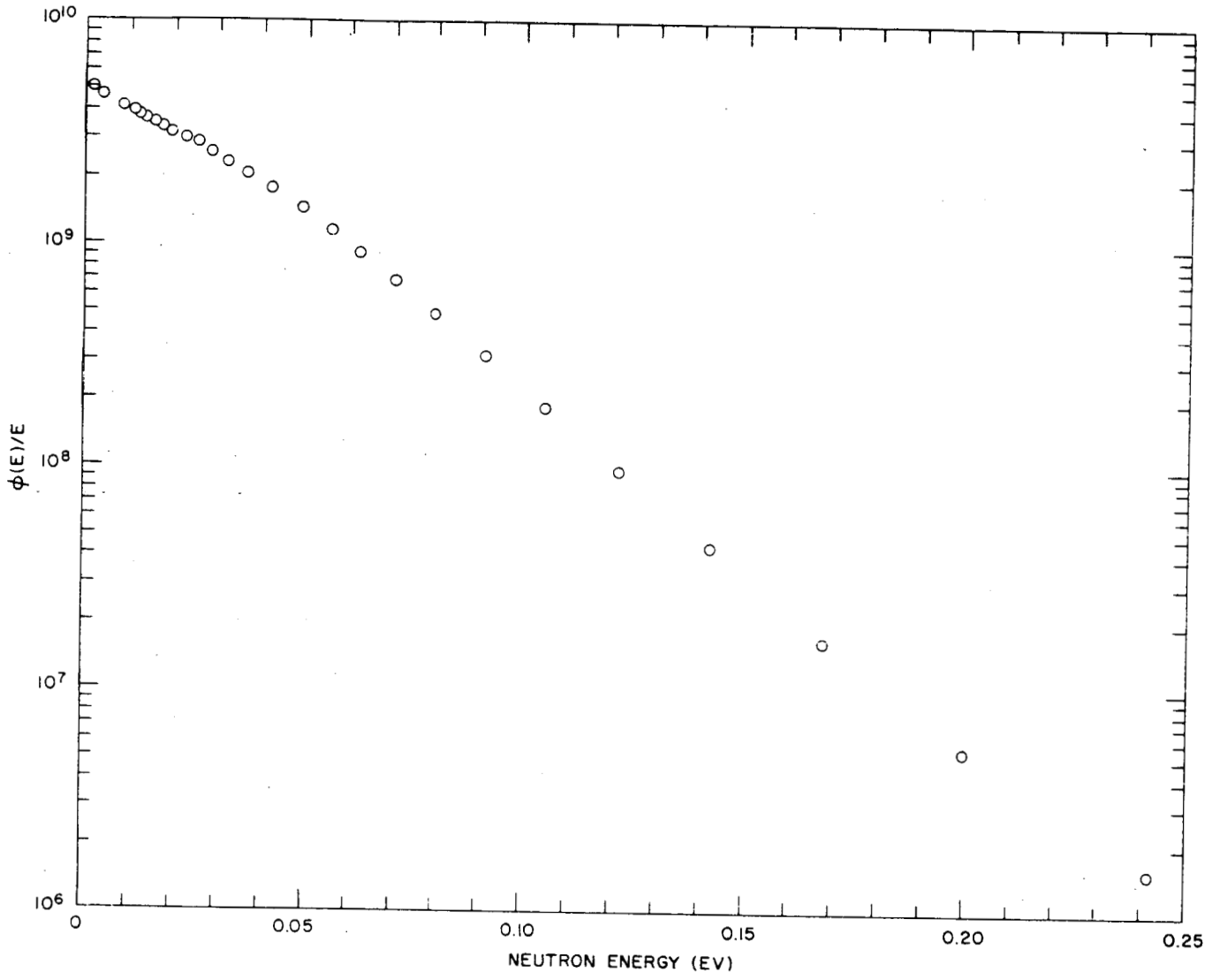

Fig. 90--$\phi(E)/E$ versus E for geometry B

respectively, show the precision obtainable in the experiment. A room-temperature Maxwellian is also shown in Fig. 89 for comparison. The geometry-A spectrum is close to a Maxwellian distribution, but is not located at quite the proper energy (corresponding to the moderator temperature). The spectrum at the surface of the water tank in geometry B is considerably harder than a room-temperature Maxwellian owing to leakage (as expected). Although these spectral results appear to be encouraging, this method is not yet completely understood. For example, one probably should not use the thermal die-away time for the thermal neutrons produced without the cadmium curtain for mean-emission-time corrections. This procedure does not measure the mean emission time of the cadmium difference spectrum, but only that of the total spectrum. A die-away measurement for the cadmium difference spectrum would be more appropriate. This die-away may well be longer and bring the result into agreement with our expectations. Use of the longer flight path (50 m) for this spectrum study may also help to solve this problem, since the mean emission time will constitute a smaller percentage correction.

Appendix I

BUILD-UP OF MODAL AMPLITUDES IN PULSED SUBCRITICAL ASSEMBLY

by

M. S. Nelkin and D. E. Parks

First assume that the effect is real, and consider how it could be analyzed. It is sufficient to consider that the spectrum as a function of time is known, and to integrate over neutron energy to derive a time-dependent diffusion equation:

$$\frac{\partial n}{\partial t} = [\,\overline{\nu v \Sigma}_f(t) - \overline{v\Sigma}_a(t)]\; n + \overline{vD}(t)\,\nabla^2 n \quad .$$

This equation has both time-dependent coefficients and a time-dependent boundary condition,

$$n(x_0(t)) = 0 \quad .$$

Ignore the time-dependent boundary condition, so that the usual modal analysis applies. For the k'th mode,

$$\frac{dn_k}{dt} = -\lambda_k(t) n \quad ,$$

where

$$\lambda_k(t) = \overline{v\Sigma}_a(t) + \overline{vD}(t) B_k^2 - \overline{\nu v E}_f(t) \quad .$$

This can be easily integrated to give

$$n_k(t) = n_k(0) \exp\left[-\int_0^t \lambda_k(t')\, dt'\right] \quad .$$

Since the spectrum will presumably get monotonically softer with time, and since the absorption and fission terms are roughly independent of time, the $\lambda_k(t)$'s will decrease monotonically to their asymptotic value.

The effect of time-dependent coefficients will therefore show up in an initially more rapid decay rather than in an initial build-up.

The effect of time-dependent boundary conditions is considerably more difficult to handle. The modes now being used are complete only for the distribution at long times. One can crudely estimate the effect by noting the lack of complete overlap between the initial fundamental mode and the final fundamental mode. What is measured is the time dependence of the final fundamental mode. The change of extrapolated boundary with time will give an effect in the right direction, since the initial fundamental mode can be thought of as slowly going over into the final fundamental mode.

Note that this description does not give a fundamental-mode amplitude building up from zero at $t = 0$, but from some finite value. This seems to fit the experiments better in any case.

Before going into the difficult mathematical problems involved with the time-dependent boundary condition, let us first investigate several possible ways in which the effect might be spurious. First, there is the possibility of room-return neutrons giving a delayed source. It seems unlikely that there are enough such neutrons or that they are sufficiently delayed to account for the effect, but the suggested experimental check of shielding the source seems worthwhile. Second, there is the possibility that the effect arises from the use of least-squares fits in the data analysis. Parks has found spurious effects arising from this sort of modal analysis in the past. This should be checked by direct examination of the spatial distribution as a function of time for early times, and by direct determination of the modal amplitudes by integration over the spatial distribution. The possibility of an important effect from time-dependent boundary conditions should be visible in the raw data if the effect really exists.

Finally, it would be interesting to see the effect in a nonmultiplying system. Without performing any calculations, it seems intuitively reasonable that the time scale for attaining the asymptotic spectrum will be shorter in the nonmultiplying case, so the build-up should take place faster. On the other hand, the difference between the initial and final spectra is larger, so the amount of the build-up may be larger.

It has been assumed in all the above that the small fission counter measures the neutron density. This is not quite true and should be looked at further, but it is not obvious in which way corrections to this assumption will go.

Appendix II

MILNE PROBLEM FOR A MULTIPLYING SYSTEM

by

D. E. Parks

GENERAL FORMULATION

Most of the rigorous results in neutron transport theory have been obtained in the constant cross-section approximation. Nelkin[53] considered the problem of the extrapolation distance in a nonabsorbing medium for the case where the neutron mean free path varies with energy.

Here we consider the problem of the extrapolation distance for an energy-dependent mean free path for the case of a homogeneous, multiplying, source-free half space. We assume the condition $k_\infty = 1$. Under this condition, the problem considered here is appropriate to the determination of the proper boundary conditions for use in the study of critical and subcritical assemblies by the methods of asymptotic reactor theory[54].

The angular flux, $f(x, E, \mu)$, is a function of the position, x, the kinetic energy, E, and the direction, $\mu = \cos^{-1}(\hat{v} \cdot \hat{z})$. The half space for $x > 0$ contains moderating material with an isotropic energy-transfer cross section $\Sigma(E \to E')$, material with absorption cross section $\Sigma_a(E)$, and a fuel with a cross section $\Sigma_f(E)$.

The transport equation for this problem is

$$\mu \frac{\partial f}{\partial x} + \Sigma_t(E) f = \frac{1}{2} \int_0^\infty \Sigma(E' \to E) \phi(x, E') dE' + \frac{X(E)}{2} \int_0^\infty \nu(E') \Sigma_f(E') \phi(x, E') dE' \quad , \tag{71}$$

where $X(E)$ is the fission spectrum, $\nu(E)$ is the number of fission neutrons resulting from fission produced by a neutron of energy E,

$$\phi(E, x) = \int_{-1}^{1} f(x, E, \mu) d\mu \quad ,$$

$$\Sigma_t(E) = \Sigma_a(E) + \int_0^\infty \Sigma(E \to E') dE' \quad ,$$

and f satisfies the boundary condition

$$f(0, E, \mu) = 0 \qquad \text{for } \mu > 0 \ .$$

For brevity's sake, we introduce the notation

$$\Sigma^*(E' \to E) = \Sigma(E' \to E) + X(E)\nu(E')\Sigma_f(E') \ ,$$

so that Eq. (71) becomes

$$\mu \frac{\partial f}{\partial x} + \Sigma_t(E)f = \frac{1}{2} \int_0^\infty \Sigma^*(E' \to E)\phi(x, E')dE' \ . \tag{72}$$

The total flux, $\phi(E, x)$, satisfies the integral equation

$$\phi(x, E) = \frac{1}{2} \int_0^\infty dx' \int_0^\infty dE'\Sigma^*(E' \to E)\ E_1\left(\frac{|x - x'|}{\ell(E)}\right)\ \phi(x', E') \ , \tag{73}$$

where

$$\ell(E) = 1/\Sigma_t(E) \ . \tag{74}$$

Later we shall show that far from the boundary, $\phi(E, x)$ will have the asymptotic form $(x + x_0)\phi_0(E)$, where $\phi_0(E)$ satisfies

$$\Sigma_t\phi_0(E) = \int_0^\infty \Sigma^*(E' \to E)\phi_0(E')dE' \ , \tag{75}$$

and x_0 is the extrapolation distance we wish to compute. In the following, we shall find a variational expression for x_0. However, we first need to derive some auxiliary relations. For this purpose, we follow closely a procedure used by Le Caine[55] for the one-velocity problem and generalized by Nelkin[53] to the multivelocity nonabsorbing case.

We introduce the functions

$$J(x) = -\int_{-1}^{1} d\mu \int_0^\infty f(x, E, \mu)\mu\phi_0^*(E)dE \ , \tag{76}$$

$$K(x) = \int_{-1}^{1} d\mu \int_0^\infty \mu^2 \frac{f(x, E, \mu)}{\Sigma_t(E)} \phi_0^*(E) \ , \tag{77}$$

where $\phi_0^*(E)$ satisfies the equation adjoint to (75):

$$\Sigma_t(E)\phi_0^*(E) = \int_0^\infty \Sigma^*(E \to E')\phi_0^*(E')dE' \quad . \tag{78}$$

Multiplying Eq. (72) by $\phi_0^*(E)$, integrating over E and μ, and using Eq. (78), we find that

$$\frac{dJ(x)}{dx} = 0 \qquad J = J_0 = \text{constant} \quad . \tag{79}$$

In a similar way, it is easily demonstrated that

$$\frac{dK}{dx} = J \qquad K = J(x + x_0) \quad . \tag{80}$$

Since the asymptotic flux behaves like $\phi(E, x) \cong A\,\phi_0(E)(x + B)$, and since the flux is almost isotropic for large x, we can compute K(x) from (77) by letting $f \to (1/2)\,\phi(x, E)$. This gives K(x) for large x as

$$K(x) = \frac{A\bar{\ell}}{3}(x + B) \quad ,$$

where

$$\bar{\ell} = \int_0^\infty \ell(E)\phi_0(E)\phi_0^*(E)dE \quad ; \tag{81}$$

and we have chosen the normalization

$$\int_0^\infty \phi_0(E)\phi_0^*(E)dE = 1 \quad . \tag{82}$$

If we use Eq. (80), we must have $A = 3J/\bar{\ell}$ and $B = x_0$. If we chose A = 1, we have

$$K(x) = \frac{\bar{\ell}}{3}(x + x_0) \quad , \tag{83}$$

$$\phi(x, E) \sim \phi_0(E)(x + x_0) \quad . \tag{84}$$

We are now ready to obtain the explicit expression for x_0.

Combining the integral relation

$$f(0, E, \mu) = -(2\mu)^{-1} \int_0^\infty dx \int_0^\infty dE' \Sigma^*(E' \to E) \exp\left(\frac{x}{\mu \ell(E)}\right) \phi(x, E') \quad (85)$$

$$\mu > 0$$

with the definition

$$K(0) = \frac{\overline{\ell}}{3} x_0 = \int_0^\infty dE \int_{-1}^0 d\mu \ell(E) \mu^2 f(0, E, \mu) \phi_0^*(E) \quad (86)$$

gives

$$x_0 = \frac{3}{2\overline{\ell}} \int_0^\infty \int_0^\infty \int_0^\infty dE dE' dx \Sigma^*(E' \to E) E_3\left(\frac{x}{\ell(E)}\right) \phi(x, E') \phi_0^*(E) \quad . \quad (87)$$

We now separate the linear term in x by introducing

$$q(x, E) = \phi(x, E) - x\phi_0(E) \quad . \quad (88)$$

Substituting (88) into (73) yields

$$q(x, E) = \frac{1}{2} \ell(E) \phi_0(E) E_3\left(\frac{x}{\ell(E)}\right) + \frac{1}{2} \int_0^\infty dx' \int_0^\infty$$

$$\cdot\, dE' \Sigma^*(E' \to E) E_1\left(\frac{|x - x'|}{\ell(E)}\right) q(x', E') \quad . \quad (89)$$

To see that the asymptotic form of $\phi(x, E)$ is given by $(x + x_0)\phi_0(E)$, as stated earlier, we note that far from the boundary we can neglect the inhomogeneous term in (89) and extend the spatial integral on the right-hand side over all space. The resulting equation allows $\phi_0(E)$ as a solution.

Finally, we substitute (88) into (87) to obtain the desired relation

$$x_0 = \frac{3}{\ell}\left[\frac{\overline{\ell^2}}{8} + \int_0^\infty \int_0^\infty \int_0^\infty dE dE' dx \frac{1}{2} \ell(E) \Sigma^*(E' \to E) E_3\right.$$

$$\left. \cdot \left(\frac{x}{\ell(E)}\right) q(x, E') \phi_0^*(E)\right] \quad , \quad (90)$$

where

$$\overline{\ell^2} = \int \ell^2(E)\phi_0(E)\phi_0^*(E)dE \quad . \tag{91}$$

THE VARIATIONAL SOLUTION

We shall now construct a variational expression for the triple integral appearing in Eq. (90). To do this we define the function $\Psi(x, E)$ and the operator S by

$$\Psi(x, E) = Sq(x, E) = \int_0^\infty \Sigma^*(E' \to E)q(x, E')\, dE' \quad . \tag{92}$$

If in addition we define the operator O by

$$OF = \frac{1}{2}\int_0^\infty \int_0^\infty dx'dE'\Sigma^*(E' \to E)E_1\left(\frac{|x - x'|}{\ell(E')}\right)F(E', x') \quad , \tag{93}$$

then the following equation for Ψ follows by operating on both sides of Eq. (89) with the operator S:

$$\Psi = O\Psi + g \quad , \tag{94}$$

where

$$g = g(E, x) = \int_0^\infty \frac{1}{2}\,\ell(E')\phi_0(E')E_3\left(\frac{x}{\ell(E')}\right)\Sigma^*(E' \to E)dE' \quad . \tag{95}$$

We now introduce the operator O^+ such that

$$O^+F(x, E) = \frac{1}{2}\int_0^\infty \int_0^\infty dx'dE'\Sigma^*(E' \to E)E_1\left(\frac{|x - x'|}{\ell(E)}\right)F(x', E') \tag{96}$$

and a function $\Psi^+(x, E)$ which satisfies

$$\Psi^+ = O^+\Psi^+ + g^+ \quad , \tag{97}$$

where g^+ is a known function of E and x.

Let us now consider the functional

$$I\{\overline{\Psi},\ \overline{\Psi}^{+}\} = \frac{(\overline{\Psi}, g^{+})(\overline{\Psi}^{+}, g)}{(\overline{\Psi}^{+},\ \overline{\Psi} - O\overline{\Psi})} \quad , \tag{98}$$

where by (A, B) we mean

$$(A, B) = \int_0^\infty \int_0^\infty dx dE A(x, E) B(x, E) \quad .$$

We can easily verify that I is stationary with respect to small variations of $\overline{\Psi}$ and $\overline{\Psi}^{+}$ about Ψ and Ψ^{+}, and that the stationary value

$$I\{\Psi,\ \Psi^{+}\} = (\Psi, g^{+}) = (\Psi^{+}, g) \quad . \tag{99}$$

Since, however, the operator O is not symmetrizable, we cannot be assured that the stationary value of I is either a maximum or a minimum.

By choosing

$$g^{+}(x, E) = \frac{1}{2}\,\ell(E) E_3\left(\frac{x}{\ell(E)}\right)\phi_0^{*}(E) \tag{100}$$

and using (99), we see that (98) becomes a stationary expression for the triple integral appearing in Eq. (90). If in Eq. (98) we use as trial functions the asymptotic solutions of (94) and (97), i. e., if we take

$$\overline{\Psi}(x, E) = \frac{\phi_0(E)}{\ell(E)} \qquad \overline{\Psi}^{+}(x, E) = \phi_0^{*}(E) \quad , \tag{101}$$

then we find that

$$x_0 = \frac{3}{8}\frac{\overline{\ell^2}}{\overline{\ell}} + \frac{1}{3}\,\overline{\ell} \quad . \tag{102}$$

This result is formally identical to the result obtained by Nelkin for the nonabsorbing case. The only difference is in the spectrum over which the averages in Eq. (102) are to be performed.

Appendix III

COMPARISON OF DIFFUSION PARAMETERS OBTAINED FOR WATER BY THE PULSED AND THE POISONING TECHNIQUES

by

J. U. Koppel and W. M. Lopez

INTRODUCTION

The measurement of neutron die-away times in pulsed assemblies of decreasing size and the measurement of diffusion lengths in media of increasing poison concentration are known[56] to be closely related experiments. This is most easily seen from the space-, time-, and energy-dependent Boltzmann equation in the diffusion-theory approximation

$$-Dv\,\Delta n(v,r,t) + \frac{\partial n(v,r,t)}{\partial t} = -(\Sigma_s + \Sigma_a)\, n(v,r,t)\, v + \int n(v',r,t)\, v'\Sigma\,(v' \to v)dv' \,. \tag{103}$$

The (asymptotic) solution corresponding to the experiment mentioned above is of the type

$$n(v, r, t) = e^{iB\cdot r - \alpha t}\, N(v) \,, \tag{104}$$

where B^2 is usually called the geometrical buckling of the assembly, α being the decay constant measured for different values of B^2. The (asymptotic) solution applying to the second experiment is

$$n(v, r) = e^{-\kappa r}\, N(v) \,, \tag{105}$$

where κ is the inverse of the diffusion length. Obviously, Eq. (105) is a special case of (104), with $\alpha = 0$ and $B = i\kappa$. Thus, κ^2 is equivalent to a negative buckling.

Now, inserting (104) in (103) yields

$$(B^2 Dv - \alpha + \Sigma_a v)\, N(v) = -\Sigma_s v\, N(v) + \int N(v')\, v'\Sigma\,(v' \to v)dv' \,, \tag{106}$$

which is an eigenvalue problem with either B^2 or α being the eigenvalue.

It is seen that the time-dependent problem can be reduced to a stationary one just by introducing a fictitious 1/v poison with cross section $-\alpha/v$. Integrating Eq. (106) over all energies and considering only 1/v absorbers, it is found that

$$B^2 \overline{Dv} + \alpha_0 - \alpha = 0 , \tag{107}$$

with

$$\alpha_0 = \Sigma_a v \qquad \overline{Dv} = \frac{\int N(v) v D dv}{\int N(v) dv} .$$

For $B^2 = 0$ (pulsed infinite medium), the solution of Eq. (106) is a Maxwellian and $\alpha = \alpha_0$. For $B^2 > 0$, the spectrum N(v) is shifted to lower energies (diffusion cooling), whereas for $B^2 < 0$ it is shifted to higher energies (diffusion hardening). Thus, $\overline{Dv}$ is a continuous function of B^2 and can be expanded in the power series:

$$\overline{Dv}\,(B^2) = D_0 - CB^2 + FB^4 - \cdots , \tag{108}$$

where C is known as the diffusion-cooling constant. Substituting (108) into (107), we have

$$\alpha - \alpha_0 = B^2 D_0 - CB^4 + FB^6 - \cdots . \tag{109}$$

Of course, the relation between $\alpha - \alpha_0$ and B^2 can also be expressed by the inverse series

$$B^2 = \frac{\alpha - \alpha_0}{D_0} + C' \left(\frac{\alpha - \alpha_0}{D_0} \right)^2 + \cdots . \tag{110}$$

It is easily seen that

$$C' = \frac{C}{D_0^2} . \tag{111}$$

The shape of the function relating α and B^2 is shown in Fig. 91. It follows from the foregoing discussion that the portion of the curve lying in the first quadrant can be measured by the pulsed technique. The intercept α_0 corresponds to the decay in an assembly of infinite dimensions. The

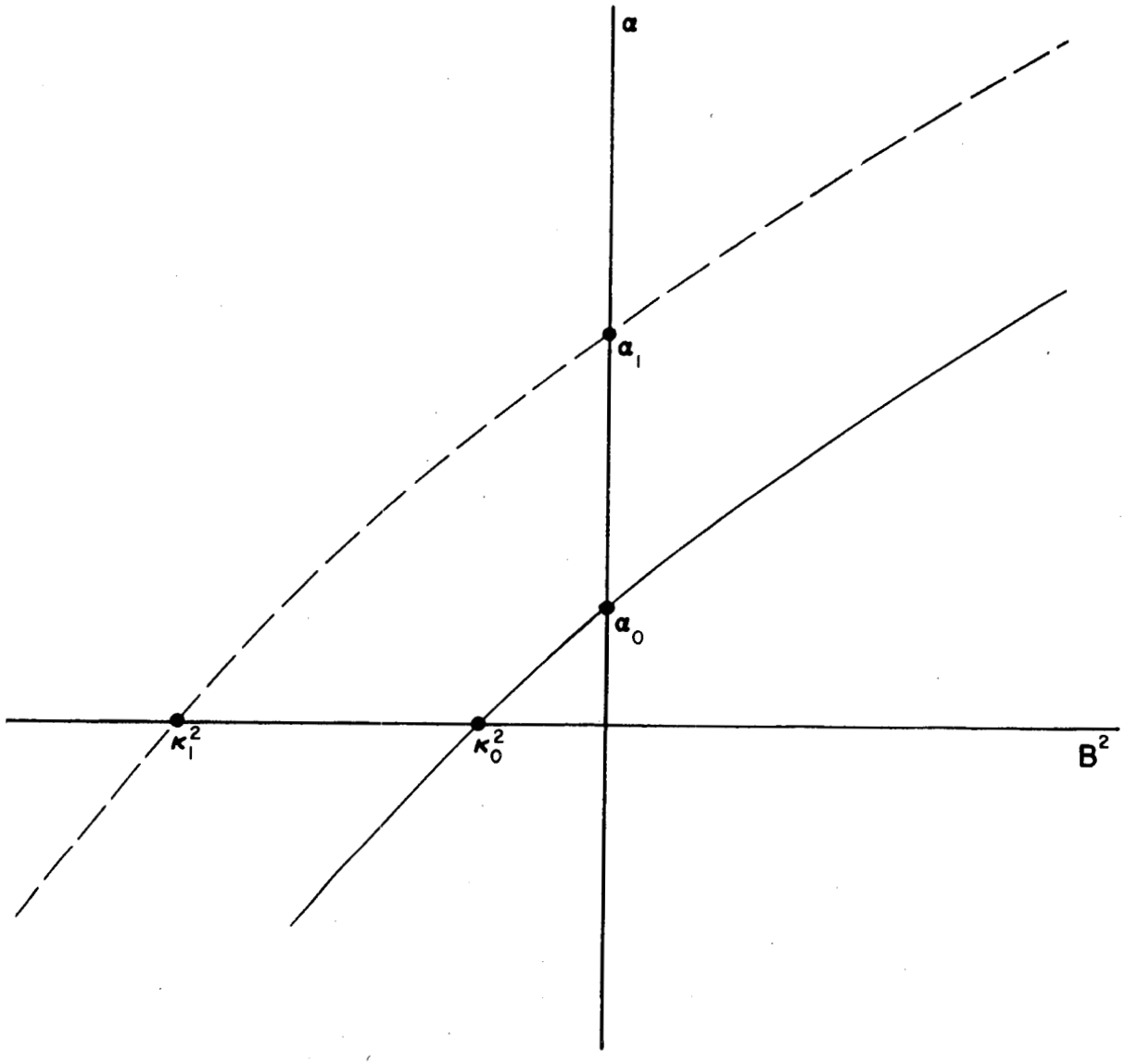

Fig. 91--General shape of the function relating α and B^2

intercept κ_0^2 is the inverse of the diffusion length in the unpoisoned medium. If a 1/v poison is now uniformly added to the medium, the curve of Fig. 91 will be shifted in the direction of positive α without having its shape changed. As the magnitude of the shift, $\Delta\alpha = v\Delta\Sigma_a$ (where $\Delta\Sigma_a$ is the increase in absorption) is known, the measurement of the diffusion length for increasing poison concentration yields points of the curve of Fig. 91 which lie in the third quadrant. Only the small segment between the intercepts cannot be measured by either of the techniques mentioned above.

INTERPRETATION OF EXPERIMENTAL DATA

The parameters of the function $\alpha = f(B^2)$ which are of physical interest are $\alpha_0 = v_0\Sigma_a(v_0)$ (intercept at $B^2 = 0$), D_0 (slope at $B^2 = 0$), and C (one-half times the second derivative at $B^2 = 0$). α_0 and D_0 can be obtained with good accuracy by both methods, and the values measured are in fair agreement with each other and with theory.[41] For C, however, there is a large discrepancy between different published values.* We believe that this is largely due to the different ways used to analyze data, and simply reflects the inherent difficulty of determining the curvature of an unknown function defined by a set of experimental points with finite standard deviation. The usual way to determine the two parameters mentioned is to fit the experimental points by a least-squares technique to an expression like Eq. (109) or (110) truncated after two or three terms. As the higher-order terms are obviously not zero, the result of the analysis will depend on the range covered by the experiment. It appears that for a given experimental error of the measured points, there is an optimum range beyond which no further accuracy is gained in the determination of the three diffusion parameters. In fact, as more terms have to be retained in order to fit larger B^2 intervals, the uncertainty in the first three coefficients remains roughly constant. Thus, a three-parameter fit of the optimum interval seems to be as good as a fit to more parameters over a wider range of B^2. It is possible to get an idea of the error involved in truncating the fit by plotting the coefficients obtained for a decreasing number of points, and thus dropping progressively those points of maximum buckling. The plots obtained for the two ways of fitting, (109) and (110), should approach roughly the same limit, obviously with a continuously increasing uncertainty. On the other hand, in order to determine the number of terms of (109) or (110) to be retained for the best fit of given experimental data, a good criterion is to compute the empirical variance

$$X = \frac{\Sigma(y_i - y_{calc})^2}{n - m}$$

*For a complete list of values see Refs. 42 and 57.

and to retain that number of terms which makes X minimum. y_i and y_{calc} are the measured and the calculated values of either α or κ^2, n is the number of points, and m is the number of parameters.

COMPARISON OF RECENT MEASUREMENTS IN WATER

We are going to show briefly how the foregoing considerations apply to the results of two recent measurements of Σ_a, D_0, and C for water.[42][57] The first is a pulsed experiment, while the second uses the stationary method.

Since the publication of the work of Lopez and Beyster,[57] more data have been obtained by its authors, which have extended the buckling range from 0.6 to 1.5 cm^{-2}. The results for the complete range are shown in Fig. 92 and Table 7. Cases 1 and 2 refer to different ways of computing the bucklings. In Case 1, the extrapolation distance was assumed to be constant and given by

$$d = 2.131 \frac{D_0}{\bar{v}} ,$$

with

$$\bar{v} = \frac{2}{\sqrt{\pi}} 2.2 \times 10^5 \text{ cm/sec} .$$

In Case 2, d was assumed to vary with B^2 according to the formula $d' = [r/(r - d)]\, d$, r being the radius of an equivalent sphere with the same buckling:

$$B^2 = \left(\frac{\pi}{r + d'}\right)^2 = \left(\frac{\pi}{a + 2d'}\right)^2 + \left(\frac{\pi}{b + 2d'}\right)^2 + \left(\frac{\pi}{c + 2d'}\right)^2 .$$

The technique of dropping points is illustrated by Tables 8a and 8b and Figs. 93 and 94. From Table 9 it is seen that the three-parameter fit of the 0 - 0.6 cm^{-2} interval is in fair agreement with the four-parameter fit of the 0 - 1.6 cm^{-2} interval (X is minimum for M = 4). It is also seen that the uncertainties of Σ_a, D_0, and C are practically the same for these two fits.

The experiment reported in Ref. 42 has already been analyzed in the manner we are suggesting here. The results are reproduced in Figs. 95, 96, and 97, and Tables 10, 11a, and 11b.* The error bars of the least-

*The figures given in Table 11 are slightly different from those appearing in Ref. 42, because in the present analysis α_0 was recalculated for each B^2 interval.

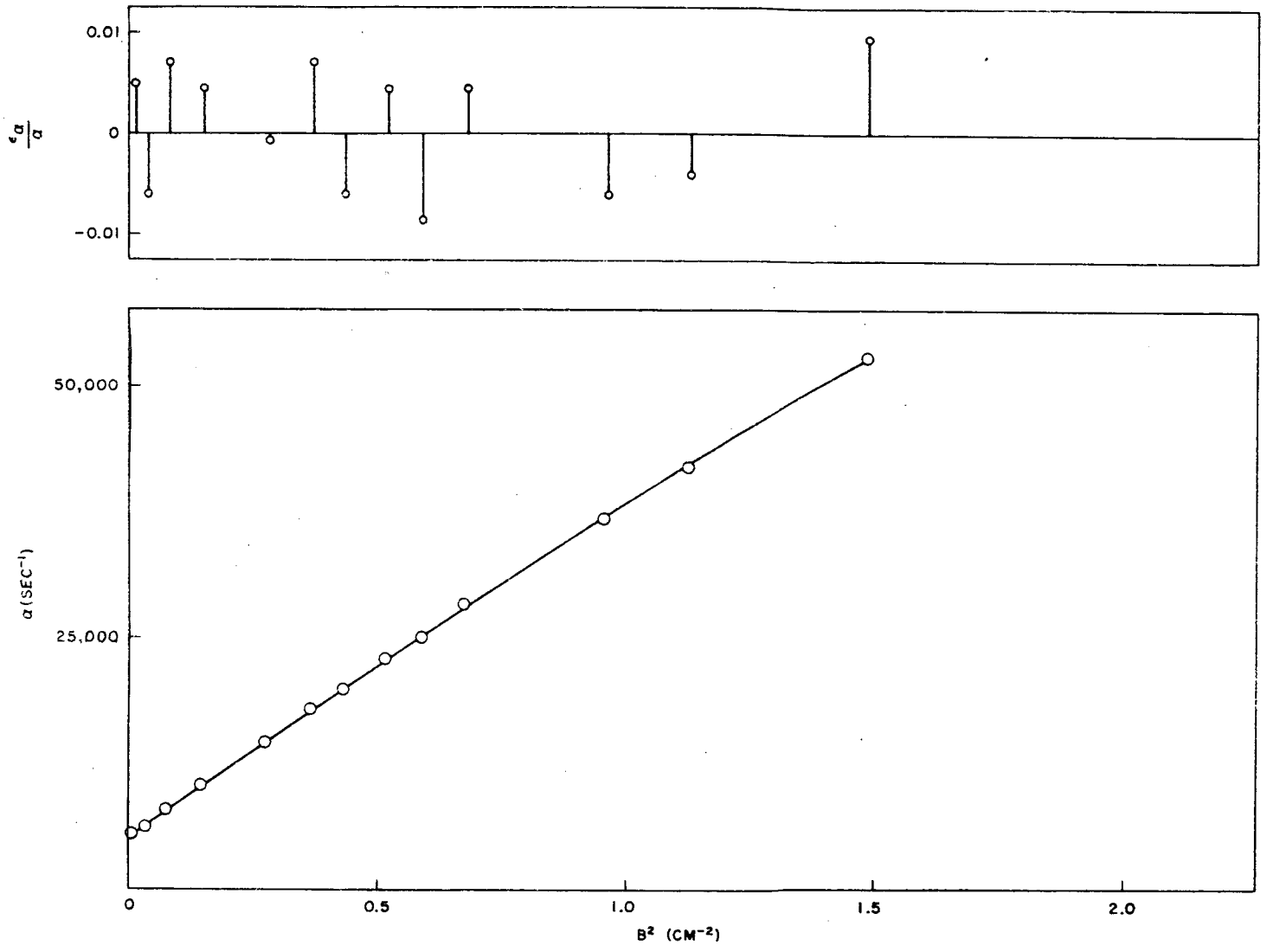

Fig. 92--Results of the pulsed experiment (Ref. 57)

Table 7

EXPERIMENTAL DATA OF LOPEZ AND BEYSTER

Size (cm)	α (sec^{-1})	B^2 (cm^{-2})	
		Case 1	Case 2
44.5×44.5×48.9	5336	0.01372	0.01370
28.6×31.1×60.2	5668	0.02400	0.02399
31.1×60.2×26.4	5722	0.02598	0.02594
31.1×60.2×19.1	6147	0.03769	0.03775
31.1×60.2×16.5	6437	0.04599	0.04599
15.2×29.7×16.5	7854	0.08341	0.08346
15.2×29.7×16.5	7904	0.08341	0.08346
76.2×76.2×10.2	7908	0.08795	0.08702
17.6×17.6×17.7	8132	0.08871	0.08847
15.2×29.7×14.6	8140	0.09232	0.09231
17.6×17.6×12.6	8989	0.1156	0.1153
17.6×17.6×12.6	9037	0.1156	0.1153
76.2×76.2×7.62	10205	0.1478	0.1471
10.2×10.2×10.2	13970	0.2538	0.2503
10.2×10.2×9.5	14330	0.2647	0.2621
10.2×10.2×8.9	14749	0.2779	0.2744
10.2×10.2×8.26	15430	0.2940	0.2903
10.2×10.2×7.62	16230	0.3139	0.3099
10.2×10.2×6.35	18116	0.3712	0.3660
10.2×10.2×5.72	19315	0.4136	0.4069
7.62×7.62×7.62	19843	0.4340	0.4288
7.62×7.62×7.62	20012	0.4340	0.4288
10.2×10.2×5.08	21547	0.4709	0.4626
7.62×7.62×6.35	21656	0.4913	0.4846
6.84×6.95×6.95	23100	0.5192	0.5117
7.62×7.62×5.72	23473	0.5338	0.5252
7.62×7.62×5.08	25168	0.5910	0.5807
5.93×6.00×5.95	28400	0.6798	0.6667
4.91×4.93×4.92	36800	0.9576	0.9308
4.49×4.49×4.47	42000	1.1292	1.0913
3.82×3.79×3.82	53000	1.4935	1.4251

Table 8a

FIT OF EQ. (109) WITH THREE PARAMETERS (PULSED-NEUTRON-SOURCE DATA)[a]

B^2_{max} (cm^{-2})	Σ_a (mb)	ϵ_σ (mb)	α_0 (sec^{-1})	ϵ_α (sec^{-1})	D_0 (cm^2/sec)	ϵ_d (cm^2/sec)	C (cm^4/sec)	ϵ_c (cm^4/sec)
				Case 1				
1.4935	327.7	1.4	4806	20	36681	193	3179	234
1.1292	326.8	1.4	4793	20	36925	221	3647	325
0.95757	326.5	1.5	4788	22	37033	265	3878	450
0.67977	326.1	1.6	4782	24	37165	347	4180	677
0.5910	325.3	1.6	4771	24	37426	368	4852	763
0.47090	325.3	1.7	4771	25	37424	418	4800	1024
				Case 2				
1.4251	327.2	1.5	4798	22	36863	215	2420	272
1.0913	326.1	1.5	4783	22	37142	243	2971	367
0.93078	325.7	1.6	4777	23	37272	289	3255	501
0.66668	325.3	1.8	4771	26	37410	374	3576	741
0.58070	324.6	1.8	4761	26	37630	404	4153	852
0.46265	324.8	1.8	4764	27	37557	458	3869	1138

[a] $T = 26.7^\circ C$.

Table 8b

FIT OF EQ. (110) WITH THREE PARAMETERS (PULSED-NEUTRON-SOURCE DATA)[a]

B^2 (cm^{-2})	Σ_a (mb)	ϵ_σ (mb)	α_0 (sec^{-1})	ϵ_α (sec^{-1})	D_0 (cm^2/sec)	ϵ_d (cm^2/sec)	C (cm^4/sec)	ϵ_c (cm^4/sec)
Case 1								
1.4935	326.5	1.4	4788	20	37078	193	4461	308
1.1292	325.9	1.4	4779	20	37271	221	4933	433
0.95757	325.7	1.5	4777	22	37309	265	5028	587
0.67977	325.7	1.6	4777	24	37310	347	5030	839
0.59100	325.0	1.6	4766	24	37586	368	5890	976
0.47090	325.1	1.7	4768	25	37519	419	5578	1251
Case 2								
1.4251	326.5	1.5	4789	22	37063	215	3052	334
1.0913	325.6	1.5	4775	22	37348	243	3726	459
0.93078	325.3	1.6	4770	23	37443	289	3976	622
0.66668	325.1	1.8	4768	26	37493	374	4114	891
0.58070	324.5	1.8	4759	26	37718	404	4805	1049
0.46265	324.8	1.8	4763	27	37589	458	4258	1338

[a] $T = 26.7^\circ C$

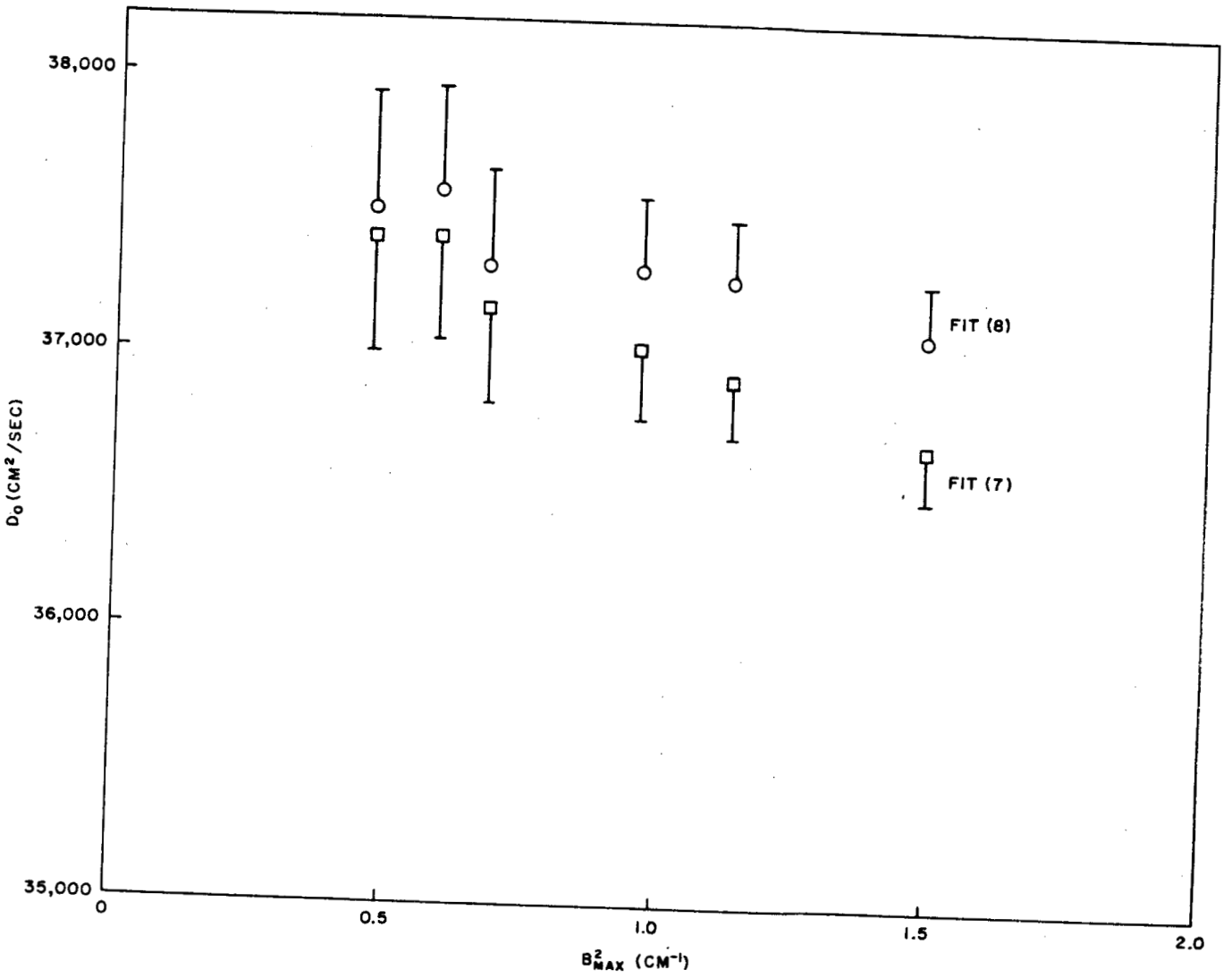

Fig. 93--Illustration of the dropping points technique for D_0 (pulsed measurement)

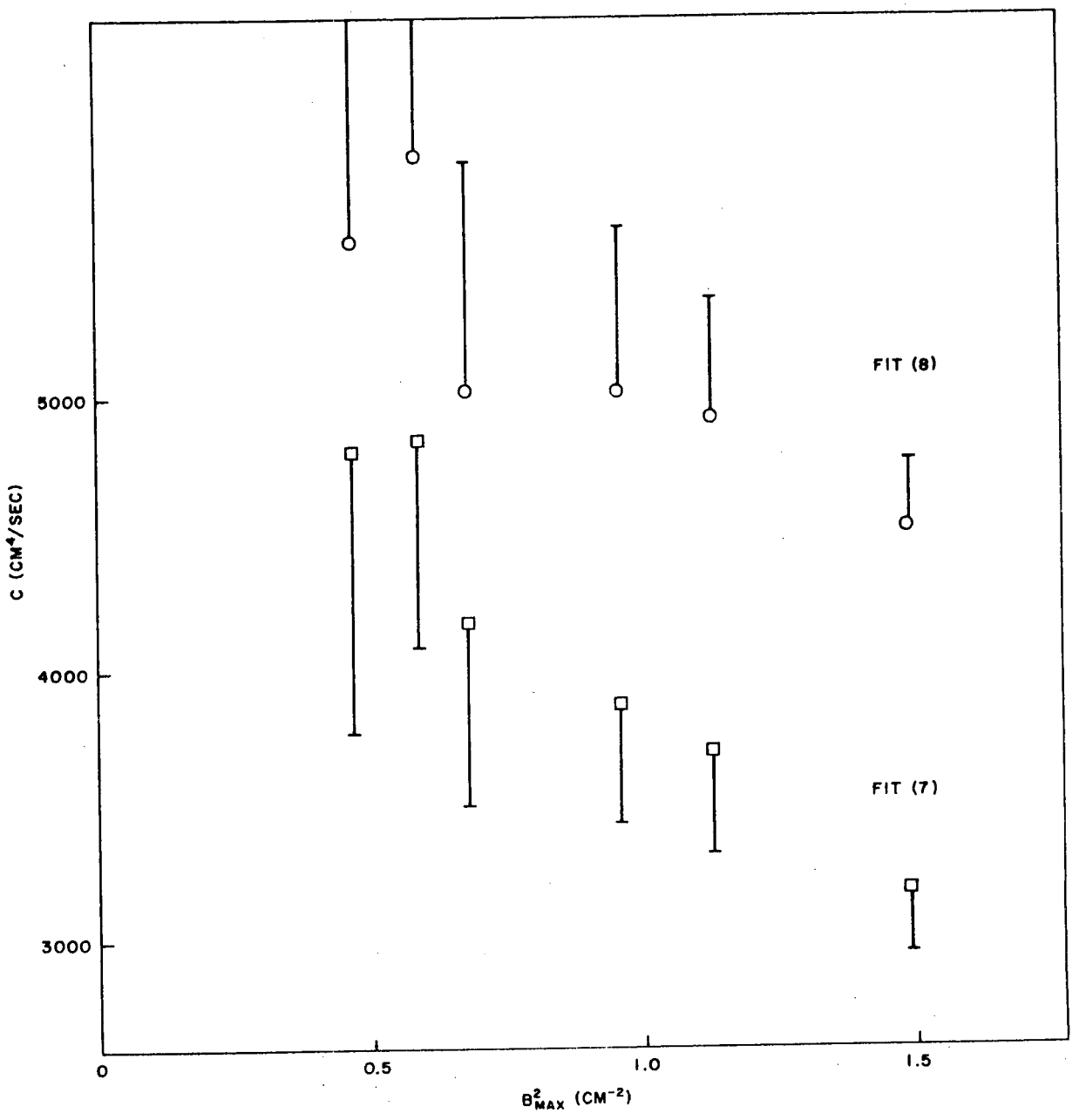

Fig. 94--Dropping points technique for C (pulsed experiment)

Table 9

FIT OF EQ. (109) WITH A VARIABLE NUMBER OF PARAMETERS (PULSED-NEUTRON-SOURCE DATA)[a]

B^2 max. (cm^{-2})	Parameters	$\alpha_0 = \Sigma_{av}$ (sec^{-1})	ϵ_α (sec^{-1})	D_0 (cm^2/sec)	ϵ_d (cm^2/sec)	C (cm^4/sec)	ϵ_c (cm^4/sec)	F (cm^6/sec)	ϵ_f (cm^6/sec)	$10^{-4}X$ (sec^{-2})
					Case 1					
1.4935	3	4806	21	36681	193	3179	234	----	----	0.6142
1.4935	4	4770	24	37476	367	5500	961	1354	550	0.5201
1.4935	5	4774	29	37389	585	5066	2423	720	3287	0.5393
0.5910	3	4771	24	37426	368	4852	763	----	----	
					Case 2					
1.4251	3	4798	22	36863	215	2420	272	----		0.6908
1.4251	4	4760	26	37715	407	4997	1103	1585	660	0.5903
1.4251	5	4768	31	37487	641	3819	2760	-219	3923	0.6079
0.5807	3	4761	26	37630	404	4153	852	----		

[a] T = 26.7°C.

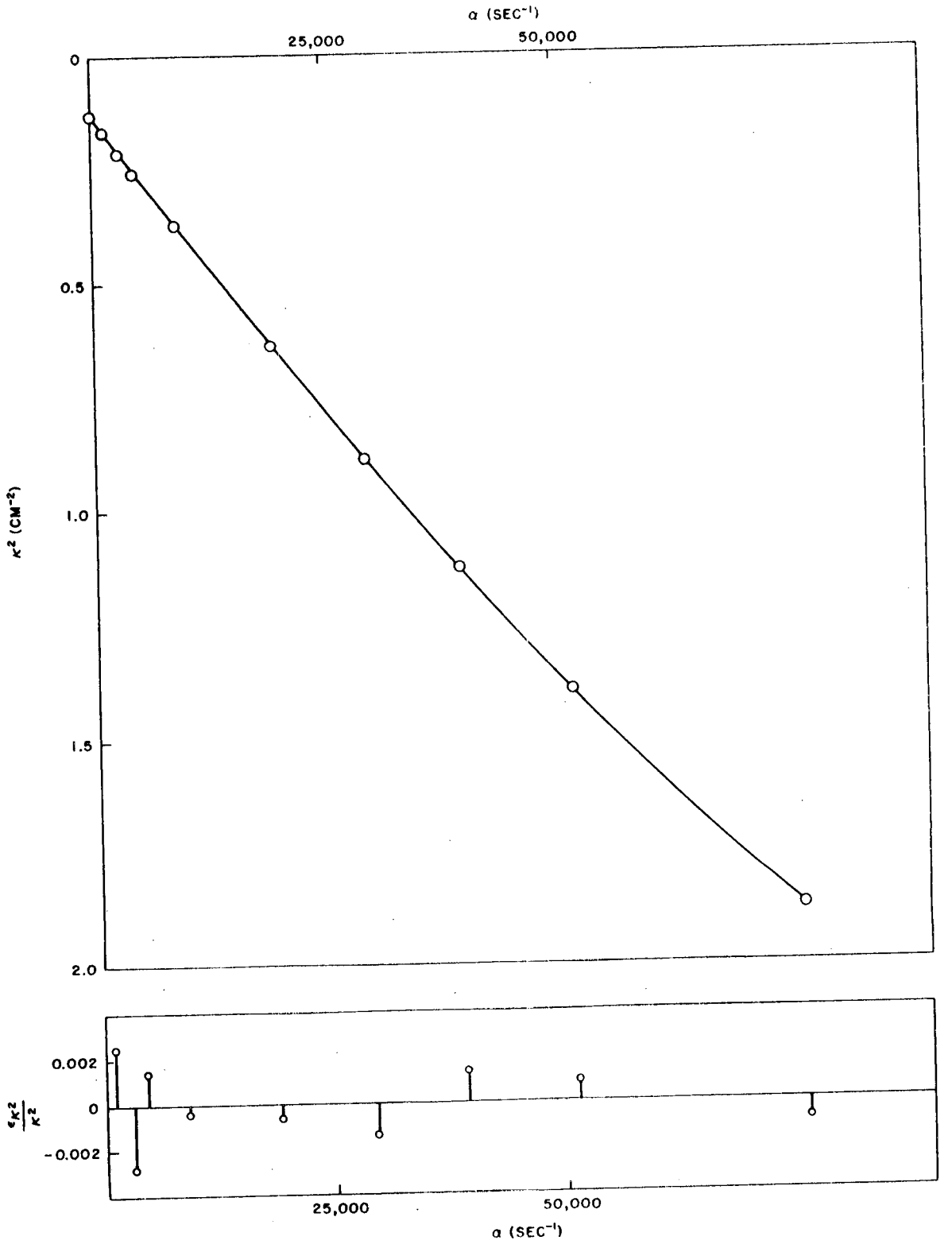

Fig. 95--Results of the poisoning experiment (Ref. 42)

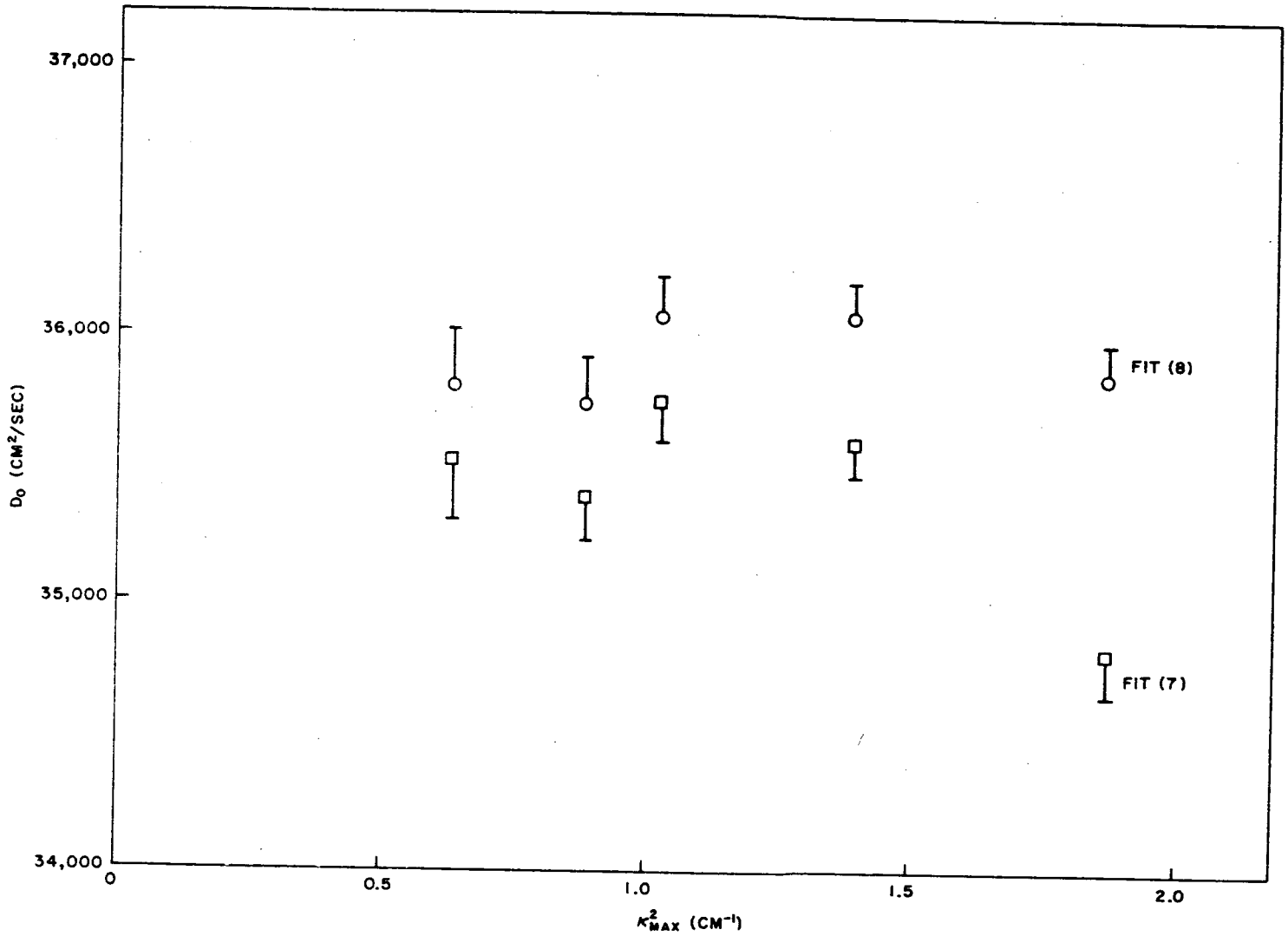

Fig. 96--Dropping points method for D_0 (poisoning experiment)

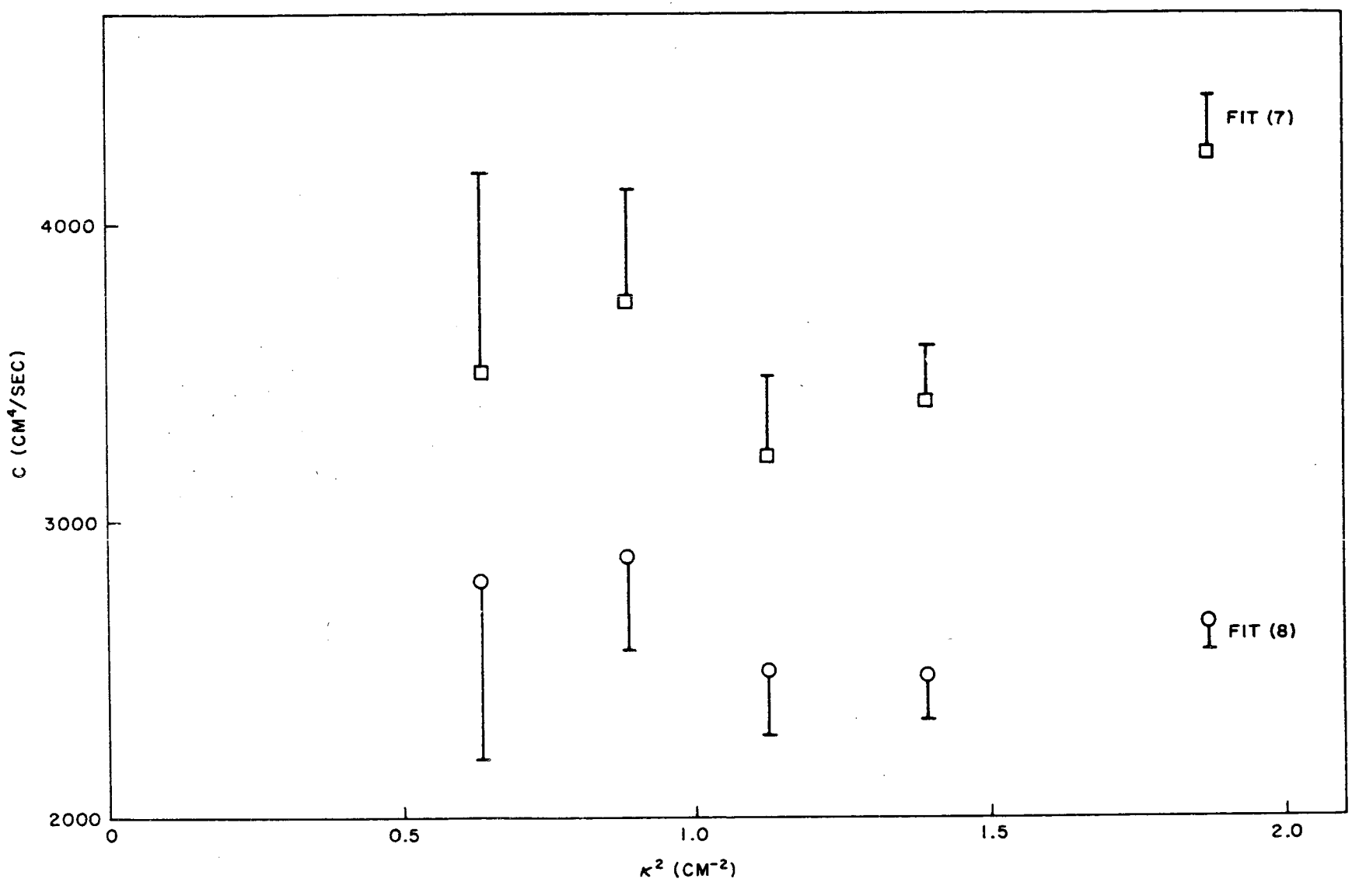

Fig. 97--Dropping points technique for C (poisoning experiment)

Table 10

EXPERIMENTAL DATA FROM REF. 42

L (cm)	κ^2 (cm^{-2})	$\Delta\Sigma_a$ (cm^{-1})	$\alpha = v\Delta\Sigma_a$ (sec^{-1})
2.754	0.1318	-----	-----
2.459	0.1653	0.005245	1153.9
2.166	0.2130	0.013870	3051.4
1.978	0.2556	0.020470	4503.4
1.639	0.3721	0.040397	8887.3
1.255	0.6348	0.087314	19209
1.063	0.8848	0.13427	29539
0.9429	1.1248	0.17895	39369
0.8469	1.3942	0.23462	51616
0.7308	1.8724	0.34655	76241

Table 11a

FIT OF EQ. (109) WITH THREE PARAMETERS (POISONING DATA)[a, b]

κ^2 max. (cm^{-2})	Σ_a (mb)	ϵ_σ (mb)	α_0 (sec^{-1})	ϵ_α (sec^{-1})	D_0 (cm^2/sec)	ϵ_d (cm^2/sec)	C (cm^4/sec)	ϵ_c (cm^4/sec)
1.8724	317.5	2.1	4663	31	34833	170	4238	187
1.3942	324.9	1.4	4771	21	35609	129	3413	179
1.1248	326.1	1.6	4790	24	35751	148	3234	253
0.8848	323.2	1.7	4747	25	35405	169	3754	367
0.6348	324.3	2.0	4763	30	35541	229	3507	674

[a] $T = 21^\circ C$.

[b] The large errors appearing in the first line show the need of retaining one more term of expansion (109) in order to fit these data.

Table 11b

FIT OF EQ. (110) WITH THREE PARAMETERS (POISONING DATA)[a]

κ^2 max. (cm^{-2})	Σ_a (mb)	ϵ_σ (mb)	α_0 (sec^{-1})	ϵ_α (sec^{-1})	D_0 (cm^2/sec)	ϵ_d (cm^2/sec)	C (cm^4/sec)	ϵ_c (cm^4/sec)
1.8724	326.6	1.4	4796	21	35874	105	2662	101
1.3942	328.6	1.5	4826	22	36079	120	2481	150
1.1248	328.6	1.7	4825	25	36074	141	2499	223
0.88481	325.8	1.7	4784	25	35754	156	2878	310
0.63481	326.2	2.0	4791	29	35808	213	2797	596

[a] $T = 21^\circ C$.

squares-fitted coefficients have been recalculated using the correct statistical expression.[58] It is seen that while Σ_a and D_0 are in good agreement* with the previous results, a large discrepancy seems to remain between the values found for C. That the uncertainty due to the extrapolation distance applying to the pulsed experiment may account at least for part of the discrepancy is seen from the following considerations. For the sake of simplicity, let us take the case of spherical assemblies. Their buckling is given by

$$B^2 = \frac{\pi^2}{R^2} ,$$

where $R = r + d$ is the extrapolated radius. Suppose that $R = R_0 + \epsilon$, where ϵ is the error of d. Then

$$B^2 = \frac{\pi^2}{R_0^2}\left[1 - 2\frac{\epsilon}{R_0} + 3\left(\frac{\epsilon}{R_0}\right)^2 - \cdots\right] . \qquad (112)$$

Substituting this expression for B^2 into the expansion (109), it follows that

$$\alpha - \alpha_0 = D_0 B_0^2\left(1 - \frac{2}{\pi}\epsilon B_0 + \frac{3}{\pi^2}\epsilon^2 B_0^2 - \cdots\right) - CB_0^4 + \cdots , \qquad (113)$$

with $B_0 = \pi/R_0$. Rearranging terms on the right side of (113) gives

$$\alpha - \alpha_0 = D_0 B_0^2 - \left(C + \frac{2}{\pi}\frac{\epsilon D_0}{B_0} - \frac{3}{\pi^2}\epsilon^2 D_0\right) B_0^4 + \cdots .$$

For ϵ = 0.1 cm and $B_0 = 1\ \text{cm}^{-1}$, the term containing ϵ to the first power introduces a correction of more than 50% of C. The term in ϵ^2 becomes significant only for much larger bucklings.

Another source of discrepancies is the weighting of the experimental points. The values of Tables 8a, 8b, and 9 were obtained with the assumption of a constant relative error in the measurement of $\alpha = f(B^2)$. The results given in Tables 11a and 11b were obtained assuming a constant relative error of κ^2. Figures 92 and 95 seem to justify both assumptions.

*The experiments reported in Refs. 42 and 57 were performed at 26.7°C and 21°C, respectively.

CONCLUSIONS

It appears that both the pulsed and the poisoning methods are suitable experiments for measuring Σ_a and the infinite-medium diffusion constant D_0. However, in view of the unavoidably increasing uncertainty in the determination of higher-order coefficients of the series (109) or (110), it seems to be preferable to compare the functions $\alpha = f(B^2)$ obtained with different experiments (and theoretical calculations) point by point rather than by the coefficients of their least-square fits.

REFERENCES

1. Egelstaff, P. A., et al., "The Thermal Neutron Scattering Law for Light and Heavy Water," Proceedings of the Symposium on Inelastic Scattering of Neutrons in Solids and Liquids, Vienna, Austria, International Atomic Energy Agency, 1961, p. 309.

2. Kottwitz, D. A., and B. R. Leonard, Jr., "The Scattering Law for Room Temperature Light Water," Proceedings of the Symposium on Inelastic Scattering of Neutrons in Solids and Liquids, Chalk River, Canada, International Atomic Energy Agency, 1962, pp. 10-14.

3. Discussion held during the Bookhaven National Laboratory Conference on Neutron Thermalization, April 30-May 2, 1962.

4. Honeck, H. C., THERMOS: A Thermalization Transport Theory Code for Reactor Lattice Calculations, Brookhaven National Laboratory Report BNL-5826, September, 1961.

5. Perkel, D. H., A Family of Thermalization Codes, General Atomic Report GAMD-754 (Rev.), July 1, 1959.

6. Perkel, D. H., ROBESPIERRE: A Program for Calculating the Nelkin Scattering Kernel for Bound Hydrogen, General Atomic Report GA-1803, August 1, 1961.

7. Brown, H. D., Jr., THERMIDOR. A FORTRAN II Code for Calculating the Nelkin Scattering Kernel for Bound Hydrogen, General Atomic Report GAMD-2622, November 10, 1961.

8. Bell, Joan, SUMMIT: An IBM-7090 Program for the Computation of Crystalline Scattering Kernels, General Atomic Report GA-2492, February 1, 1962.

9. Hinman, G. W., The DSN and GAPLSN Codes, General Atomic Report GAMD-3425, August 15, 1962.

10. Honeck, H. C., and Hiroshi Takahashi, The Angular Dependence of Thermal Neutron Spectra in Lattices, Brookhaven National Laboratory Report BNL-5924, January, 1962.

11. Young, J. C., et al., Development of Multiplying Assembly. Final Report, General Atomic Report GA-2471, June 30, 1961.

12. Nelkin, M. S., and G. B. West, Calculations of the Prompt Temperature Coefficient for TRIGA, General Atomic Report GA-1681, November 7, 1960.

13. Joanou, G. D., and J. S. Dudek, GAM-I: A Consistent P1 Multigroup Code for the Calculation of Fast Neutron Spectra and Multigroup Constants, General Atomic Report GA-1850, June 28, 1961.

14. Joanou, G., personal communication.

15. Egelstaff, P. A., personal communication.

16. Nielsen, J. R., and A. H. Woollett, "Vibrational Spectra of Polyethylenes and Related Substances," J. Chem. Phys., Vol. 26, 1957, p. 1391.

17. Goldman, D. T., and F. D. Federighi, The Calculation of Neutron Spectra for Perfect Gas, Water, and Polyethylene-Moderated Systems, Reactor Technology Report No. 19 - Physics, December, 1961, Knolls Atomic Power Laboratory Report KAPL-2000-16, January, 1962.

18. Herzberg, G., Infrared and Raman Spectra of Polyatomic Molecules, Van Nostrand, New York, 1945.

19. Hughes, D. J., et al., "Atomic Motions in Water by Scattering of Cold Neutrons," Phys. Rev., Vol. 119, 1960, p. 2.

20. Brugger, R. M., "Complication of Reduced Slow Neutron Partial Differential Scattering Cross Sections," presented at the Brookhaven National Laboratory Conference on Neutron Thermalization, April 30-May 2, 1962 (to be published in the Proceedings of the Conference).

21. Parks, D. E., Mean Time of Emission of Neutrons from Pulsed Nonmultiplying Assemblies, General Atomic Report GA-2189, October 5, 1961.

22. Brown, H. D., and D. S. St. John, Neutron Energy Spectrum in D_2O, E. I. Du Pont de Nemours and Company, Inc., Report DP-33, February, 1954.

23. Verbinski, V. V., "Low-Energy Neutron Spectra in Lithium Hydride," Trans. Am. Nuclear Soc., Vol. 5, June, 1962, p. 214.

24. Parks, D. E., The Calculation of Thermal-Neutron Scattering Kernels in Graphite, General Atomic Report GA-2438, October 10, 1961.

25. Woods, A. B., et al., "Energy Distributions of Neutrons Scattered from Graphite, Light and Heavy Water, Ice, Zirconium Hydride, Lithium Hydride, Sodium Hydride and Ammonium Chloride by the Beryllium Detector Method," Proceedings of Symposium on Inelastic Scattering of Neutrons in Solids and Liquids, Vienna, Austria, International Atomic Energy Commission, October, 1960, p. 487.

26. Corngold, N., "Thermalization of Neutrons in Infinite Homogeneous Systems," Ann. Phys., Vol. 6, 1959, p. 368.

27. Preiser, S., et al., A Program for the Numerical Integration of the Boltzmann Transport - NIOBE, ARL Technical Report 60-314, December, 1960.

28. Marshall, W., and R. Stuart, "The Scattering of Neutrons from Polycrystalline Material," Proceedings of the Symposium on Inelastic Scattering of Neutrons in Solids and Liquids, International Atomic Energy Agency, Vienna, Austria, 1961, p. 75.

29. Egelstaff, P. A., et al., "The Phonon Frequency Distribution in Graphite at Several Temperatures," Proceedings of the Symposium on Inelastic Scattering of Neutrons in Solids and Liquids, International Atomic Energy Agency, Vienna, Austria, 1961, p. 569.

30. Egelstaff, P. A., et al., "On the Evaluation of the Thermal Neutron Scattering Law," Nuclear Sci. and Eng., Vol. 12, 1962, p. 260.

31. MacDougall, J. D., "Application of Scattering Law Data to the Calculation of Thermal Neutron Spectra," presented at the Brookhaven National Laboratory Conference on Neutron Thermalization, April 30-May 2, 1962 (to be published in the Proceedings of the Conference).

32. Yoshimori, A., and Y. Kitano, "Theory of the Lattice Vibration of Graphite," J. Phys. Soc. Japan, Vol. 11, 1956, p. 352.

33. Parks, D. E., J. R. Beyster, and N. F. Wikner, "Thermal Neutron Spectra in Graphite," Nuclear Sci. and Eng., Vol. 13, 1962, p. 306.

34. Parks, D. E., The Calculation of Thermal Neutron Scattering Kernels in Graphite, General Atomic Report GA-2438, October 10, 1961.

35. Nelkin, M. S., The Scattering of Slow Neutrons by Water, General Atomic Report GA-1063, February 12, 1960.

36. Egelstaff, P. A., B. C. Haywood, and I. M. Thorson, "The Motion of Hydrogen in Water," Proceedings of the Symposium on Inelastic Scattering of Neutrons by Solids and Liquids, Chalk River, Canada, International Atomic Energy Commission, 1962.

37. Nelkin, M. S., Asymptotic Solutions of the Transport Equation for Thermal Neutrons, General Atomic Report GA-3298, July 20, 1962.

38. Koppel, J., and D. Noliboff, "Sensitivity of Transient Neutron Spectra to Different Scattering Kernels," Trans. Am. Nuclear Soc., Vol. 5, No. 2, 1962, p. 337.

39. Koppel, J. U., "Time Dependent, Space Independent Neutron Thermalization," Nuclear Sci. and Eng., Vol. 12, 1962, p. 532.

40. Koppel, J. U., "Time-Dependent Neutron Spectra," Nuclear Sci. and Eng., Vol. 8, 1960, p. 157.

41. Honeck, H., "On the Calculation of Thermal Neutron Diffusion Parameters," presented at the Brookhaven National Laboratory Conference on Neutron Thermalization, April 30-May 2, 1962 (to be published in the Proceedings of the Conference).

42. Koppel, J. U., and E. Starr, "Determination of Diffusion Hardening in Water," Nuclear Sci. and Eng., Vol. 14, 1962, p. 224.

43. Nelkin, Mark, Thermalization a la MODE, General Atomic Report GA-3122, April 25, 1962.

44. Case, K. M., "Elementary Solutions of the Transport Equation and Their Applications," Ann. Phys., Vol. 9, 1960, p. 1.

45. Mika, J. R., "Neutron Transport with Anisotropic Scattering," Nuclear Sci. and Eng., Vol. 11, 1961, p. 415.

46. Koppel; J. U., On the Solution of the Time Dependent Neutron Thermalization Problem, General Atomic Report GA-2988, March 8, 1962.

47. Koppel, J. U., A Method of Solving the Time Dependent Neutron Thermalization Problem, General Atomic Report GA-3469, August 27, 1962.

48. Honeck, H. C., GATHERMOS - A New Version of the THERMOS Code, General Atomic Report GAMD-3033, March 21, 1962.

49. Honeck, H. C., personal communication.

50. Carlson, B., C. Lee, and J. Woreton, The DSN and TDC Neutron Transport Codes, Los Alamos Scientific Laboratory Report LAMS-2346, October 16, 1959.

51. Perkel, D. H., personal communication.

52. Alexander, J. H., A New Version of DSN, General Atomic Report GAMD-2610, November 2, 1961.

53. Nelkin, Mark, Milne's Problem for a Velocity Dependent Mean Free Path, General Atomic Report GAMD-944, August 28, 1959.

54. Case, K. M., Joel H. Ferzinger, and P. F. Zweifel, "Asymptotic Reactor Theory," Nuclear Sci. and Eng., Vol. 10, 1961, p. 352.

55. Le Caine, J., "Application of a Variational Method to Milne's Problem," Phys. Rev., Vol. 72, 1947, p. 564.

56. Hurwitz, H., Jr., and M. S. Nelkin, "The Thermal Neutron Spectrum in a Diffusing Medium," Nuclear Sci. and Eng., Vol. 3, 1958, p. 1.

57. Lopez, W. M., and J. R. Beyster, "Measurement of Neutron Diffusion Parameters in Water by the Pulsed Neutron Technique," Nuclear Sci. and Eng., Vol. 12, 1962, p. 190.

58. Van der Waerden, B. L., Mathematische Statistik, Springer, 1957.